THEORETICAL CHARACTERIZATION OF CHARGE TRANSPORT IN ORGANIC MOLECULAR CRYSTALS

A Dissertation
Presented to
The Academic Faculty

by

Roel S. Sánchez-Carrera

In Partial Fulfillment
of the Requirements for the Degree
Doctor of Philosophy in the
School of Chemistry and Biochemistry

Georgia Institute of Technology
December 2008

THEORETICAL CHARACTERIZATION OF CHARGE TRANSPORT IN ORGANIC MOLECULAR CRYSTALS

Approved by:

Dr. Jean-Luc Brédas, Advisor
School of Chemistry and Biochemistry
Georgia Institute of Technology

Dr. David C. Sherrill
School of Chemistry and Biochemistry
Georgia Institute of Technology

Dr. Seth R. Marder
School of Chemistry and Biochemistry
Georgia Institute of Technology

Dr. Robert L. Whetten
School of Chemistry and Biochemistry
Georgia Institute of Technology

Dr. Bernard Kippelen
School of Electrical and Computer Engineering
Georgia Institute of Technology

Date Approved: August 8, 2008

ACKNOWLEDGEMENTS

First of all, I would like to thank my advisor Prof. Jean-Luc Brédas for his support and guidance over the past few years. Looking back, it was a privilege to work under the tutelage of Prof. Brédas. His academic and scientific leadership were a continuous source of inspiration during my years as a graduate student. Personally, I admire his eagerness to effectively disseminate new knowledge through research and education. Despite his multiple activities, he always found the time to provide me with his best advice on how to present the results of my scientific work. Undoubtedly, being a part of the Prof. Brédas group has been a great honor. Although it is sad to leave the group, I am looking forward to the future and to the development of Prof. Brédas group during the upcoming years.

The other members of my thesis committee, Professors Bernard Kippelen, Seth Marder, David Sherrill, and Robert Whetten deserve my gratitude for their support and direction throughout the development of this thesis. I had the opportunity to attend classes taught by Profs. Marder, Sherrill, and Whetten. From the "Chemistry of Electronic Materials" course taught by Prof. Marder, I acknowledge his interactive teaching style and his vast knowledge of physical-organic chemistry. Also, I recognize his leadership in the development of Georgia Tech's Center for Organic Photonics and Electronics, which provided me with a platform for collaborative and multidisciplinary research. My first "Statistical Mechanics" course taught by Prof. Whetten set the pace of my academic life at Georgia Tech; I thank him for his willingness to be part of my thesis committee. Prof. Sherrill has also been an exceptional mentor and teacher. I particularly enjoyed his two classes, "Computational Chemistry" and "Quantum Mechanics" (QM);

both courses facilitated the advancement of my doctoral research activities. Also, I appreciate the extra efforts that he made to help me succeed in my QM course and his disposition to discuss topics of computational/theoretical chemistry. While I was not able to attend any course taught by Prof. Kippelen, he has provided me with numerous physical and scientific insights, particularly during my candidacy exam and data review.

My undergraduate advisor also deserves special thanks. Prof. Ralf Warmuth (at that time in Kansas State University) was my first research mentor; he put a lot of effort and time in teaching me how to conduct physical-organic chemistry experiments. Being instructed by a great scientist at the beginning of my scientific career was one of the most valuable experiences that I ever had. Also, I am indebted to a great number of people at my undergraduate institution, the Monterrey Institute of Technology and Higher Education (or ITESM, from its Spanish name). In particular, I would like to thank Prof. Marcelo Videa Vargas for his stimulating course on "Quantum Chemistry" and Dr. Jaime Bonilla Ríos for helping me in finding financial sources for my college education.

During my graduate career I have had the opportunity of working with a number of interesting and exceptional people and I would like to collectively thank all of them for making our laboratory a great working environment. In particular, I would like to thank Dr. Veaceslav Coropceanu for his wisdom, his experience, and his continuous desire for genuine results. He deserves my special gratitude for his support and assistance over the past three years. The early days of my computational chemistry calculations were carried out in conjunction with Dr. Demetrio da Silva Filho and I am indebted to him for his

patience and guidance to assist me on the numerous technical concerns that I used to have (or that I still have). Also, I want to thank my closest collaborators within the Brédas group, specifically, Dr. Eung-Gun Kim and Dr. Pavel Paramonov (now an assistant research professor at the University of Akron). Both provided me with the best of their knowledge to investigate the electronic structure properties of organic molecular crystals from first-principles. More recently, the work done in collaboration with Dr. Indranil Rudra on constrained DFT methods and with Dr. Mari Carmen Ruiz Delgado on perfluorinated organic materials has also been a valuable experience and I thank them for our joint research contributions. Also, special thanks to Dr. Joseph Norton for proofreading the many documents of previous job applications. I would like to thank Kelly Lancaster and Dr. Prashant Jain for their friendship over the past five years. Finally, I would like to acknowledge the past and present members of the Brédas group: Dr. Georg Heimel, Dr. Terttu Hukka, Dr. Tsutomo Kawatsu, Dr. Dongwook Kim, Dr. Tommy Ohyun Kwon, PaDreyia Lawson, Dr. Amalia Leclercq, Dr. Hong Li, Shino Ohira, Kathryn Pigg, Dr. Chad Risko, Dr. Lorenz Rommaner, Seyhan Salman, Dr. John Sears, Chris Wood, Dr. Yinghua Wu, Dr. Aijun Ye, Dr. Yuanping Yi, Dr. Karin Zojer, and Prof. Egbert Zojer. For their assistance I am also thankful to Alyceson Andrews and Ginelle Tingler.

In addition, I want to thank our collaborators at the Laboratory for Chemistry of Novel Materials, in Mons, Belgium (a sister Brédas group). I am thankful to Dr. Jérôme Cornil, Dr. David Beljonne, Prof. Roberto Lazzaroni, and Angès Leclerq for providing the means for my two-month stay in Mons. I am also grateful to the past and present

members of the research group in Mons, in particular, Dr. Johannes Gierschner, Dr. Vincent Lemaur, Dr. Mathieu Linares, Nicolas Martinelli, Dr. Begoña Milián Medina, Andrea Minoia, Yoann Olivier, and Lucas Viani. While in Europe, I also visited the laboratories of Dr. Graeme Day at the University of Cambridge to further compare and evaluate the main results of my dissertation. I thank Dr. Day for his willingness to host me during my short stay in his laboratories and all his help in the molecular mechanics section of this thesis.

This thesis certainly would not have been possible without the love and encouragement of my family and friends. I would like to take the opportunity to thank my father Sigifredo, my mother Mercedes, and my three sisters, Hortensia, Erika, and Isela for their collective love and support through the years, in both México and in the United States. Also, my deepest thanks to my fiancée Luz. Her charisma and cheerfulness brought me peace and encouragement during these often very difficult years of graduate school. Her unwavering love and support have lightened up my days. In addition, I would like to thank my two closest Mexican friends at graduate school, Enrique Michel Sánchez and Gerardo Orozco Valdés, for their true friendship over the past few years.

TABLE OF CONTENTS

Page

ACKNOWLEDGEMENTS iii

LIST OF TABLES xii

LIST OF FIGURES xvi

LIST OF ABBREVIATIONS xxiv

SUMMARY xxvi

CHAPTER 1 INTRODUCTION 1

1.1 Organic semiconductors 1

1.1.1 Molecular packing in organic molecules 5

1.1.2 OTFT geometry and operation 6

1.1.3 OTFT applications 9

1.1.3.1 Electronic paper 10

1.1.3.2 RFID tags 11

1.1.3.3 Chemical sensors 12

1.2 Charge transport 12

1.2.1 Definition of charge carrier mobility 14

1.2.2 Theory of charge carrier mobility 16

1.2.2.1 Wide-band materials 17

1.2.2.2 Narrow-band materials 21

1.3 Thesis objective and outline 23

1.4 References 25

CHAPTER 2 THEORETICAL METHODS FOR ELECTRONIC STRUCTURE AND LATTICE DYNAMICS CALCULATIONS IN MOLECULAR SOLIDS 29

2.1 Electronic structure calculations 29

2.1.1 The Hamiltonian of a molecular solid 29

2.1.2 The Hartree and Hartree-Fock approximations 31

2.1.3 Density Functional Theory 33
2.1.3.1 The Hohenberg-Kohn theorems 34
2.1.3.2 The Kohn-Sham equations 37
2.1.3.3 Functionals for exchange and correlation 38

2.1.4 Quantum-mechanical methods for the solid state 41
2.1.4.1 Band theory of crystals 43
2.1.4.1.1 Band structure 45
2.1.4.1.2 Transfer integrals (electronic coupling) 47
2.1.4.1.3 Density of states 48
2.1.4.1.4 Effective mass 50

2.2 Lattice dynamics calculations 51

2.2.1 Phonons 52
2.2.1.1 The eigenvector 52
2.2.1.2 The frequencies ω(k) 53

2.2.2 Lattice dynamics for phonon calculations 53

2.2.3 Optical and acoustic phonon modes 55

2.2.4 General features of molecular mechanics force fields 57
2.2.4.1 The force field energy 58
2.2.4.2 Stretch energy 58
2.2.4.3 Bend energy 59
2.2.4.4 Torsional energy 59
2.2.4.5 Cross terms 60
2.2.4.6 van der Waals energy 60
2.2.4.7 Electrostatic energy 62

2.3 Electron-phonon interactions 63

2.3.1 Molecular dynamics simulations 65
2.3.1.1 Different types of MDS 68
2.3.1.1.1 Constant-temperature MDS 68
2.3.1.1.2 Constant-pressure MDS 69

2.4 Software 70

2.4.1 Gaussian03 70

2.4.2 ADF 70

2.4.3 VASP 71
2.4.4 CPMD 71
2.4.5 CRYSTAL06 71
2.4.6 TINKER 72
2.4.7 DMAREL 72
2.5 References 72

CHAPTER 3 LOCAL ELECTRON-PHONON COUPLING 77
3.1 Introduction 78
3.1.1 Polaron binding energy 78
3.1.2 Vibronic coupling in oligoacene cations 82
3.2 Theoretical methodology 83
3.3 Results and discussion 85
3.3.1 Photoelectron spectroscopy 85
3.3.2 Electronic structure 87
3.3.3 Relaxation energy 90
3.4 Conclusions 115
3.5 References 116

CHAPTER 4 NONLOCAL ELECTRON-PHONON COUPLING 120
4.1 Introduction 120
4.2 Theoretical methodology 121
4.3 Results and discussion 123
4.3.1 Crystallographic information 123
4.3.2 Vibrational modes in oligoacene crystals 124
4.3.3 Electronic structure calculations 134
4.3.3.1 Transfer integrals 134
4.3.3.2 Band structures 137

4.3.4 Hole- and electron-phonon coupling 144
4.3.4.1 Nonlocal electron-phonon coupling constants derived from force field methods..... 145
4.3.4.2 Nonlocal electron-phonon coupling constants derived from ab initio methods..... 149
4.3.4.3 Classical and quantum-mechanical distributions of the transfer integrals..... 163
4.3.4.4 Temperature dependence of the hole- and electron-phonon interactions..... 165
4.3.4.5 Intermolecular relaxation energies from MDS 169

4.4 Conclusions..... 172

4.5 References..... 172

CHAPTER 5 CHARGE TRANSPORT PARAMETERS OF THE PENTATHIENOACENE CRYSTAL 177

5.1 Introduction..... 177

5.2 Theoretical methodology 179

5.3 Results and discussion 181

5.3.1 Geometric structure..... 181

5.3.2 Crystal electronic structure 185

5.3.3 Local vibronic coupling 191

5.3.4 Band-like versus hopping transport 194

5.4 Conclusions..... 196

5.5 References..... 197

CHAPTER 6 CHARGE TRANSPORT PARAMETERS IN IODO-FUNCTIONALIZED ORGANIC MOLECULAR CRYSTALS 202

6.1 Introduction..... 202

6.2 Theoretical methodology 204

6.3 Results and discussion 206

6.3.1 Crystallographic information 206
6.3.2 Molecular electronic structure 209
6.3.3 Electronic-structure calculations 211
6.3.3.1 The DIB crystal 211
6.3.3.2 The DTT and DTT-2I crystals 218
6.3.4 Electron-vibration coupling 225
6.3.4.1 DIB 225
6.3.4.2 DTT and DTT-2I 231
6.4 Conclusions 235
6.5 References 237

CHAPTER 7 SUMMARY AND PERSPECTIVES 241
7.1 Synopsis 241
7.2 Future considerations 243

LIST OF PUBLICATIONS 246

LIST OF TABLES

Page

Table 3.1 First three ionization energies in naphthalene, anthracene, tetracene and pentacene obtained from ΔSCF and KT (between parentheses) calculations. All energies are given in eV. 90

Table 3.2 Adiabatic potential surfaces (AP) and normal-mode (NM) estimates of the relaxation energies λ_{rel} (meV) of the cation states D_0, D_1, and D_2 of naphthalene, anthracene, tetracene, and pentacene, related to ionization processes. 91

Table 3.3 DFT and HF estimates of frequencies, ω and relaxation energies, λ_{rel} of the cation states D_0, D_1, and D_2, related to the ionization of naphthalene. 93

Table 3.4 DFT and HF estimates of frequencies, ω and relaxation energies, λ_{rel} of the cation states D_0, D_1, and D_2, related to the ionization of anthracene. . 94

Table 3.5 DFT and HF estimates of frequencies, ω and relaxation energies, λ_{rel} of the cation states D_0, D_1, and D_2, related to the ionization of tetracene. 95

Table 3.6 DFT and HF estimates of frequencies, ω and relaxation energies, λ_{rel} of the cation states D_0, D_1, and D_2, related to the ionization of pentacene. .. 97

Table 4.1 Crystal constants and structures for oligoacenes. 124

Table 4.2 Phonon frequencies of the intermolecular optical modes in the naphthalene ($C_{10}H_8$) crystal obtained from DFT and MM calculations. Experimental results are included for comparison.[22] 126

Table 4.3 Phonon frequencies of the intermolecular optical modes in the anthracene ($C_{14}H_{10}$) crystal obtained from DFT and MM calculations. Experimental results from deuterated anthracene are included for comparison.[24]..... 129

Table 4.4 Phonon frequencies of the intermolecular optical modes in the tetracene ($C_{18}H_{12}$) crystal obtained from DFT and MM calculations. The calculated data are compared with the corresponding experimental lattice frequencies (where available)[25, 26] and with data obtained from an atom-atom intermolecular potential.[27]..... 129

Table 4.5 Phonon frequencies of the intermolecular optical modes in the pentacene ($C_{22}H_{14}$) crystal obtained from DFT and MM calculations. The calculated data are compared with the corresponding experimental lattice frequencies (where available)[28] and with data derived from an atom-atom intermolecular potential.[29] 130

Table 4.6 DFT-calculated transfer integrals in naphthalene and anthracene (meV). 137

Table 4.7 DFT-calculated transfer integrals in tetracene and pentacene (meV). ... 137

Table 4.8 Hole and electron effective masses m (in units of the free electron mass at rest, m_0) calculated at the band edges of the naphthalene crystal. 140

Table 4.9 Hole and electron effective masses m (in units of the free electron mass at rest, m_0) calculated at the band edges of the anthracene crystal. 141

Table 4.10 Hole and electron effective masses m (in units of the free electron mass at rest, m_0) calculated at the band edges of the tetracene crystal. 142

Table 4.11 Hole and electron effective masses m (in units of the electron mass at rest, m_0) calculated at the band edges of the pentacene crystal. 143

Table 4.12 Estimates of the electron (hole)-phonon coupling constants (in meV) of the 9 optical modes in the naphthalene crystal based on MM normal-mode calculations (see Figure 4.5 for a definition of pair 1, pair 2, and pair 3). 147

Table 4.13 Estimates of the electron (hole)-phonon coupling constants (in meV) of the 9 optical modes in the anthracene crystal based on MM normal-mode calculations (see Figure 4.5 for a definition of pair 1, pair 2, and pair 3). 147

Table 4.14 Estimates of the electron (hole)-phonon coupling constants (in meV) of the 9 optical modes in the tetracene crystal based on MM normal-mode calculations (see Figure 4.6 for a definition of pair 1, pair 2, pair 3, and pair 4). 148

Table 4.15 Estimates of the electron (hole)-phonon coupling constants (in meV) of the 9 optical modes in the pentacene crystal based on MM normal-mode calculations (see Figure 4.6 for a definition of pair 1, pair 2, pair 3, and pair 4). 148

Table 4.16 Estimates of the electron (hole)-phonon coupling constants (in meV) of the 105 optical modes in the naphthalene crystal based on DFT normal-mode calculations (see Figure 4.5 for a definition of pair 1, pair 2, and pair 3). 150

Table 4.17 Estimates of the electron (hole)-phonon coupling constants (in meV) of the 9 optical modes in the anthracene crystal based on DFT normal-mode calculations (see Figure 4.5 for a definition of pair 1, pair 2, and pair 3). 153

Table 4.18 Estimates of the electron (hole)-phonon coupling constants (in meV) of the 9 optical modes in the tetracene crystal based on DFT normal-mode calculations (see Figure 4.6 for a definition of pair 1, pair 2, pair 3, and pair 4). 153

Table 4.19 Estimates of the electron (hole)-phonon coupling constants (in meV) of the 213 optical modes in the pentacene crystal based on DFT normal-mode calculations (see Figure 4.6 for a definition of pair 1, pair 2, pair 3, and pair 4). 154

Table 5.1 Hole and electron effective masses m (in units of the electron mass at rest, m_0) at the band edges of the 5TA crystal. 190

Table 5.2 Calculated intramolecular reorganization energies for hole λ_h and electron λ_e transfer in the *n*TA series (energies in meV). 192

Table 6.1 DFT Estimates of the transfer integral for molecular pairs in the α-phase of DIB. 214

Table 6.2 Hole and electron effective masses m (in units of the electron mass at rest, m_0) calculated at the band edges of the α-phase of DIB. 216

Table 6.3 Hole and electron effective masses m (in units of the electron mass at rest, m_0) calculated at the band edges of the β-phase of DIB. 217

Table 6.4 DFT estimates of the transfer integral for molecular pairs in the DTT crystal (see Figure 6.2 for labeling). 221

Table 6.5 DFT estimates of the transfer integral for molecular pairs in the DTT-2I crystal. 223

Table 6.6 Hole effective masses m (in units of the electron mass at rest, m_0) calculated at the band edges of the DTT crystal. 224

Table 6.7 Hole effective masses m (in units of the electron mass at rest, m_0) calculated at the band edges of the DTT-2I crystal. 225

Table 6.8 B3LYP/6-31G(d,p) (B3LYP/3-21G(d,p) for iodine) estimates of intramolecular frequencies (ω) and polaron binding energy (relaxation energy) related to hole transport in DIB. 227

Table 6.9 B3LYP/6-31G(d,p) estimates of intramolecular frequencies (ω) and polaron binding energy (relaxation energy) related to hole transport in DTT. 232

Table 6.10 B3LYP/6-31G(d,p) (B3LYP/3-21G(d,p) for iodine) estimates of intramolecular frequencies (ω) and polaron binding energy (relaxation energy) related to hole transport in DTT-2I. 233

LIST OF FIGURES

Page

Figure 1.1 Side and front views of the XEL-1 Sony television with a screen one-eighth of an inch thick.[14] 2

Figure 1.2 Representative organic semiconductors (those with p-channel characteristics are colored in blue, while those that exhibit n-channel characteristics are colored in red): (a) pentacene, (b) copper phthalocyanine, (c) fluorinated copper phthalocyanine, (d) fluorinated naphthalene diimide, (e) poly(3-hexyl thiophene), (f) poly(2,5-bis(3-alkylthiophen-2-yl)thieno[3,2-b]thiophene), and (g) triethylsilylethynyl anthradithiophene. (Figure adapted from Reference 22). 5

Figure 1.3 Illustration of packing arrangements for anthracene: herringbone (top) and π-stacking (bottom) (only HOMO orbital interactions are shown). 6

Figure 1.4 Schematic of top (a) and bottom (b) contact organic OTFTs. (c) Relevant voltages and geometry for an OTFT, L represents the source-drain channel length and W the channel width. (Figure adapted from Reference 25). 7

Figure 1.5 (A) Idealized energy level diagram of an OTFT at $V_G = 0$ and $V_D = 0$. (B and D) Electron accumulation and electron transport in the OTFT. (C and E) Hole accumulation and hole transport in the OTFT. (Figure adapted from Reference 25). 9

Figure 1.6 (a) A 256-element electronic paper system, each pixel consists of an organic transistor with channel length < 20 μm. Details are described elsewhere.[12] (b) Photo of an RFID tag component circuit. (Figure adapted from Reference 11). 11

Figure 1.7 Electron and hole mobilities in the a-direction of a highly purified naphthalene crystal as a function of temperature. (Figure adapted from Reference 38). 14

Figure 1.8 Temperature dependence of the mobility for the limiting cases of strong and weak electron-phonon couplings, g. (Figure adapted from Reference 23). 17

Figure 1.9 A schematic representation of the shift of the Fermi distribution of the conduction electrons in the k-space of a metal under the action of an electric field F_x and the scattering processes during the relaxation after switching off F_x. (Figure adapted from Reference 42). 19

Figure 2.1 Real space arrangements for a 2D square lattice and its corresponding reciprocal space lattice. 43

Figure 2.2 Variation of the energy with respect to k for a 1D lattice of s orbitals (left) and p_x orbitals (right). The corresponding arrangement of the orbitals is also shown. 46

Figure 2.3 Illustration of the electronic splittings between the HOMO/LUMO levels of two ethylene molecules superimposed in a cofacial configuration. 48

Figure 2.4 Representation of the density of states $D(E)$ for a 1D lattice. 49

Figure 2.5 Schematic representation of the A_g and B_g phonons. For A_g phonons the axes of rotational symmetry of the two molecules in the unit cell are antiparallel, while for the B_g phonons, they are oriented parallel. (Figure adapted from Reference 19). 53

Figure 2.6 Optical and acoustic modes as $k \rightarrow 0$. (Figure adapted from Reference 20). 56

Figure 2.7 Schematic representation of the most important energetic terms of an elementary force field. (Figure adapted from Reference 25). 57

Figure 2.8 Torsional angle definition. 60

Figure 3.1 Sketch of the potential energy surfaces for the neutral state 1 and charged state 2, showing the vertical transitions, the normal-mode displacement ΔQ, and the relaxation energies $\lambda_{rel}^{(1)}$ and $\lambda_{rel}^{(2)}$. 80

Figure 3.2 Gas-phase photoelectron emission spectrum of naphthalene.[37, 41] 86

Figure 3.3 Gas-phase photoelectron emission spectrum of anthracene.[2, 38, 41] 87

Figure 3.4 Orbital energies (DFT/B3LYP) of the first three frontier occupied MO in naphthalene, anthracene, tetracene and pentacene. The blue, green and red colors are used to group the MOs by their type I, II and III, respectively (see text). 88

Figure 3.5 HF and DFT estimates of Huang-Rhys factors, S, related to the first three ionizations bands (D_0, D_1, and D_2) of naphthalene (see Table 3.3 for the energy of the vibrational modes). 99

Figure 3.6 HF and DFT estimates of Huang-Rhys factors, S, related to the first three ionizations bands (D_0, D_1, and D_2) of anthracene (see Table 3.4 for the energy of the vibrational modes). 100

Figure 3.7 DFT and HF simulations of the vibrational structure of the first ionization band of anthracene. In the DFT simulations, the BHandHLYP, B3LYP, and BLYP functionals were used. 101

Figure 3.8 DFT and HF simulations of the vibrational structure of the second ionization band of anthracene. In the DFT simulations, the BHandHLYP, B3LYP, and BLYP functionals were used. 102

Figure 3.9 DFT and HF simulations of the vibrational structure of the third ionization band of anthracene. In the DFT simulations, the BHandHLYP, B3LYP, and BLYP functionals were used. 102

Figure 3.10 DFT/(B3LYP with 30% EEX) simulations of the vibrational structure of the first ionization band of anthracene. 103

Figure 3.11 DFT/B3LYP simulations of the vibrational structure of the first three PE bands of naphthalene 105

Figure 3.12 DFT/B3LYP simulations of the vibrational structure of the first three PE bands of anthracene 106

Figure 3.13 DFT/B3LYP estimates of Huang-Rhys factors, S, related to the first three ionizations bands of naphthalene. 107

Figure 3.14 DFT/B3LYP estimates of Huang-Rhys factors, S, related to the first three ionizations bands of anthracene. 108

Figure 3.15 DFT/B3LYP estimates of Huang-Rhys factors, S, related to the first two ionizations bands of tetracene. 109

Figure 3.16 DFT/B3LYP estimates of Huang-Rhys factors, S, related to the first three ionization bands of pentacene. 110

Figure 3.17 Sketch of the normal-mode that yields the largest vibrational coupling for type-II electronic states. 112

Figure 3.18 DFT/B3LYP estimates of the relaxation energies, λ_{rel}, of the first three cation states D_0, D_1, and D_2 upon ionization *versus* the inverse of the number of carbon atoms in naphthalene, anthracene, tetracene and pentacene. As in Figure 3.4, the blue, green and red colors are used to specify the three groups of states according to their type (I, II and III, respectively). 113

Figure 3.19 Sketch of the normal modes that yield the largest vibrational couplings in naphthalene. 115

Figure 4.1 DFT calculated eigenvectors for the nine ($k = 0$) optical phonon modes in naphthalene. The phonon frequencies are also given. 127

Figure 4.2 DFT calculated eigenvectors for the nine ($k = 0$) optical phonon modes in anthracene. The phonon frequencies are also given. 131

Figure 4.3 DFT calculated eigenvectors for the nine ($k = 0$) optical phonon modes in tetracene. The phonon frequencies are also given. 132

Figure 4.4 DFT calculated eigenvectors for the nine ($k = 0$) optical phonon modes in pentacene. The phonon frequencies are also given. 133

Figure 4.5 Illustration of the naphthalene (anthracene) molecular pairs with the largest transfer integrals as reported by Cheng *et al*.[31] 135

Figure 4.6 Definition of the tetracene and pentacene molecular pairs used to compute transfer integrals. 136

Figure 4.7 The band structure of crystalline naphthalene and density of states (DOS) spectrum. The energy is set to be zero at the top of the valence band. The energies are plotted along the directions in the first Brillouin zone, connecting the points Γ=(0,0,0), Y=(0,0.5,0), A=(0.5,0.5,0), B=(0.5,0,0) and Z=(0,0,0.5). DOS in states/eV per cell. 140

Figure 4.8 The band structure of single anthracene and density of states (DOS) spectrum. The energy is set to be zero at the top of the valence band. The energies are plotted along the directions in the first Brillouin zone, connecting the points Γ=(0,0,0), Y=(0,0.5,0), A=(0.5,0.5,0), B=(0.5,0,0) and Z=(0,0,0.5). DOS in states/eV per cell. 141

Figure 4.9 The band structure of crystalline tetracene and density of states (DOS) spectrum. The energy is set to be zero at the top of the valence band. The energies are plotted along the direction in the first Brillouin zone, connecting the points Γ=(0,0,0), R=(0.5,0.5,0.5), V=(0.5,0.5,0), X=(0.5,0,0), and Y=(0,0.5,0), all in crystallographic coordinates. DOS in states/eV per cell. 142

Figure 4.10 The band structure of crystalline pentacene and density of states (DOS) spectrum. The energy is set to be zero at the top of the valence band. The energies are plotted along the directions in the first Brillouin zone, connecting the points Γ=(0,0,0), R=(0.5,0.5,0.5), V=(0.5,0.5,0), X=(0.5,0,0), and Y=(0,0.5,0), all in crystallographic coordinates. DOS in states/eV per cell. 143

Figure 4.11 DFT estimates of the hole-phonon and electron-phonon couplings in the naphthalene crystal as a function of phonon energy. 159

Figure 4.12 DFT estimates of the intermolecular relaxation energy (L) in the naphthalene crystal..... 161

Figure 4.13 DFT estimates of the intermolecular relaxation energy (L) for holes in the pentacene crystal. 162

Figure 4.14 DFT estimates of the intermolecular relaxation energy (L) for electrons in the pentacene crystal. 162

Figure 4.15 Classical and quantum-mechanical standard deviations of the hole-phonon coupling (top) and electron-phonon coupling (bottom) as a function of temperature for pair 1 (black), pair 2 (red), and pair 3 (blue) in the naphthalene crystal..... 167

Figure 4.16 Classical and quantum-mechanical standard deviations of the hole-phonon coupling (top) and electron-phonon coupling (bottom) as a function of temperature for pair 1 (black), pair 2 (red), pair 3 (blue), and pair 4 (green) in the pentacene crystal. Note: the standard deviations for holes and electrons in pairs 1 and 2 display the same evolution as a function of the temperature; therefore, the red curves appear on top of the black ones. 168

Figure 4.17 Normalized probability distribution of the transfer integrals for holes and electrons in pair 1 and pair 2 of the naphthalene crystal. The average value μ and the standard deviation σ are also reported. The vertical lines (in red) correspond to the transfer integrals of the two molecular dimers obtained from the optimized geometry at the MM3 force field level..... 171

Figure 5.1 Chemical structures of actively investigated π-conjugated organic semiconductors: (a) sexithienyl (6T), (b) bisdithienothiophene (BDT), (c) pentacene, (d) *syn*-anthradithiophene (*syn*-ADT), (e) *syn*-thienobisbenzothiophene (*syn*-TBBT), and (f) pentathienoacene (5TA)..... 178

Figure 5.2 Evolutions of the C−C bond lengths in going from the end to the center of the molecule: (top panel) DFT calculations on isolated molecules and (bottom panel) experimental crystal data. In the top panel, three data points of 6TA overlap with those of 7TA. In the bottom panel, DFT values are also given for the 5TA crystal. 183

Figure 5.3 Calculated bond length changes in isolated 5TA upon oxidation (open symbols) and reduction (filled symbols)..... 184

Figure 5.4 Wavefunctions of the frontier molecular orbitals in isolated 5TA and 7TA. 184

Figure 5.5 Crystal structure of 5TA.[10] The experimental lattice constants of the orthorhombic unit cell (*Pnma*) are a = 11.171, b = 25.098, and c = 3.8852 Å. Shown in (b) is a view from the bottom along the b-axis, where the molecules in gray belong to the top layer of the double-layered unit cell. Rolled π-stacks (displaced along the short molecular axis) are clearly seen along the c-axis. Values in parentheses refer to the DFT-optimized structure. The nearest-neighbor pairs *A*, *B*, and *C* considered for calculation of the transfer integrals are indicated by arrows. 185

Figure 5.6 Electronic band structure of the geometry-optimized 5TA crystal. Points of high symmetry in the first Brillouin zone are Γ=(0, 0, 0); X=(0.5, 0, 0); Y=(0, 0.5, 0); Z=(0, 0, 0.5); S=(0.5, 0.5, 0); T=(0, 0.5, 0.5); and U=(0.5, 0,0.5), all in crystallographic coordinates. The energy levels are shifted such that the valence band edge at the Γ-point aligns at 0 eV. The conduction band edge denoted by Λ_Z (0, 0, 0.337) is located 59 meV below the Γ-point. The wavefunctions of the crystal orbitals at the Γ -point (for the bottom molecular layer) are shown on the right, with each corresponding to a labeled arrow in the band structure plot. 187

Figure 5.7 Illustration of rolled π-stacking and of the HOMO and LUMO interaction patterns: (b) two adjacent molecules from the unit cell along the c-axis as viewed down the molecular plane normal; and (a) the HOMO and (c) LUMO wavefunctions of isolated 5TA from Figure 5.4 laid over each of the molecules in (b). The wavefunction overlap between the two molecules is significant; however, the LUMO electronic coupling is greatly reduced by the roll in the stack which, in combination with the alternating LUMO phase along the short molecular axis, creates both in-phase and out-of-phase interaction patterns. 188

Figure 5.8 Huang–Rhys factors S_i of 5TA and 7TA. The relaxation energy λ_{rel} contributed by each normal mode at frequency ω_i is obtained by $\lambda_{rel} = \hbar\omega_i S_i$. 192

Figure 5.9 Normal modes with strong vibronic coupling in cationic 5TA. The low-frequency modes at 239 and 489 cm^{-1} involve mostly sulfur atoms whereas the high-frequency modes at 1261 and 1535 cm^{-1} involve carbon atoms. All modes are in-plane. 193

Figure 6.1 a) Chemical structure of DIB. b) Crystal structure of the α-phase of DIB[28] (*Pbca* space group, a=16.9697, b=7.3242, and c=6.156 Å; the labeling of the DIB molecules as used in the calculations of the transfer integrals is also shown). c) Crystal structure of the β-phase of DIB[28] (*Pccn* space group, a=17.047, b=7.4370, and c=6.1548 Å). 207

Figure 6.2 (top) Crystal structure of DTT ($P\ 21/n$ space group, a=12.746, b=10.614, c=6.005 Å, and β=97.53°. (bottom) Crystal structure of DTT-2I ($P\ 21/n$ space group, a=13.200, b=4.140, c=19.760 Å, and β=96.354°. Chemical structures of the DTT and DTT-2I molecules are drawn in the top right corner of each crystal structure, respectively. The labeling of the DTT and DTT-2I molecules as used in the calculations of the transfer integrals is also shown. The reciprocal lattice vectors for each crystal are included as well. 208

Figure 6.3 Illustration of the frontier molecular orbitals of benzene and DIB. 209

Figure 6.4 Illustration of the frontier molecular orbitals of DTT and DTT-2I. 210

Figure 6.5 Electronic band structure of the α-phase of DIB. Points of high symmetry in the first Brillouin zone are labeled as follows: Γ=(0,0,0), X=(0.5,0,0), Y=(0,0.5,0), Z=(0,0,0.5), S=(0.5,0.5,0), and R=(0.5,0.5,0.5), all in crystallographic coordinates. The zero of energy levels corresponds to the valence band edge. The conduction band edge denoted by Δ_Y=(0,0.25,0) is located about 4 meV below the Γ-point. The right panel illustrates the corresponding density of states. 212

Figure 6.6 Electronic band structure of the β-phase of DIB. The labeling scheme for the points of high symmetry is the same as in Figure 6.5. The conduction band edge denoted by Λ_Z=(0,0,0.125) is located about 7 meV below the Γ-point. 213

Figure 6.7 Wavefunctions of (a) the four valence sub-bands; and (b) the four lowest conduction sub-bands at the Γ-point. in the α-crystalline phase (the frontier orbitals are denoted as 1). Due to the periodic boundary conditions, portions of the electron density appear as fragmented throughout the unit cell. 214

Figure 6.8 Illustration of the standard Brillouin zone directions used to generate the band structure plots of Figures 6.9 and 6.10. 219

Figure 6.9 Electronic band structure of the DTT crystal. The valence band edge is located at the Γ-point. The right panel illustrates the corresponding density of states (see text for definition of the high-symmetry k-points in the first Brillouin zone). 220

Figure 6.10 Electronic band structure of the DTT-2I crystal. The valence band edge is located at A=(0.5,0.5,0). The right panel illustrates the corresponding density of states (see text for definition of the high-symmetry k-points in the first Brillouin zone). 222

Figure 6.11 Illustration of the rotation of molecule 7 along its short molecular axis in a dimer formed by molecules 5 and 7 (see Figure 6.2 for a definition of the given molecule numbers). 223

Figure 6.12 Contributions of the vibrational modes to the polaron binding energy (relaxation energy) in DIB and benzene. 227

Figure 6.13 Evolution of the HOMO transfer integral for a DIB dimer composed of molecules 1 and 8, as a function of the dimensionless normal coordinate of the ω = 110 cm^{-1} libration mode (here, the mean-square displacement at room temperature approximately corresponds to $Q = \pm 2$ since thermal energy at room temperature is ~200 cm^{-1}). 229

Figure 6.14 DFT geometries (bond lengths are given in Å) for the neutral, radical-cation, and radical-anion states of DIB. 231

Figure 6.15 Low-frequency normal modes involving sulfur atoms in cationic DTT and DTT-2I, respectively. 233

Figure 6.16 DFT geometries (bond lengths are given in Å) for the neutral, radical-cation, and radical-anion states of DTT-2I. 234

LIST OF ABBREVIATIONS

5TA	Pentathienoacene
6T	Sexithienyl
AP	Adiabatic Potential
BZ	Brillouin Zone
DIB	1,4-diiodobenzene
DFT	Density Functional Theory
DMA	Distributed Multipole Analysis
DOS	Density of States
DTT	dithieno[3,2-*b*:2',3'-*d*]thiophene
DTT-2I	2,6-diiodo-dithieno[3,2-*b*:2',3'-*d*]thiophene
ET	Electron Transfer
EEX	Hartree-Fock Exchange
FC	Franck-Condon
FCI	Franck-Condon Integrals
GGA	Generalized Gradient Approximation
HF	Hartree-Fock
HOMO	Highest Occupied Molecular Orbital
INDO	Intermediate Neglect of Diatomic Overlap
KS	Kohn-Sham
KT	Koopmans' Theorem
L(S)DA	Local (Spin) Density Approximation

LJ	Lennard-Jones
LUMO	Lowest Unoccupied Molecular Orbital
MDS	Molecular Dynamics Simulation
MM	Molecular Mechanics
MO	Molecular Orbitals
NM	Normal Mode
OLED	Organic Light-Emitting Diode
OTFTs	Organic Thin-Film Transistors
PE	Photoelectron
RFID	Radio Frequency Identification
SCF	Self-Consistent Field
STO	Slater-type Orbital
TBA	Tight-Binding Approximation
TBBT	Thienobisbenzothiophene
TFT	Thin-Film Transistor

SUMMARY

The rapid growth in the interest to explore new synthetic crystalline organic semiconductors and their subsequent device characterization has revived the debate on the development of theoretical models to better understand the intrinsic charge transport mechanisms in organic materials. At the moment, several charge-transport theories for organic molecular crystals have been proposed and have observed a comparable agreement with experimental results. However, these models are limited in scope and restricted to specific ranges of microscopic parameters and temperatures. A general description that is applicable in all parameter regimes is still unavailable. The first step towards a complete understanding of the problem associated with the charge transport in organic molecular crystals includes the development of a first-principles theoretical methodology to evaluate with high accuracy the main microscopic charge-transport parameters and their respective couplings with *intra*- and *inter*molecular vibrational degrees of freedom.

In this thesis, we have developed a first-principles methodology to investigate the impact of electron-phonon interactions on the charge-carrier mobilities in organic molecular crystals. Well-known organic materials such as oligoacene and oligothienoacene derivatives were studied in detail. To predict the charge-transport phenomena in organic materials, we rely on the Marcus theory of electron-transfer reactions. Within this context, the nature of the intramolecular vibronic coupling in oligoacenes was studied using an approach that combines high-resolution gas-phase

photo-electron spectroscopy measurements with first-principles quantum-mechanical calculations. This further led to investigation of the electron interactions with optical phonons in oligoacene single crystals. The lattice phonon modes were computed at both density functional theory (DFT) and empirical force field levels. The low-frequency optical modes are found to play a significant role in dictating the temperature dependence of the charge-transport properties in the oligoacene crystals. A combined classical molecular dynamics and quantum-chemical study on organic molecular crystals revealed that the lattice vibrations are a key component to be taken into account when designing organic materials with improved charge mobilities.

Finally, we investigated the microscopic charge-transport parameters in the pentathienoacene, 1,4-diiodobenzene, and 2,6-diiodo-dithieno[3,2-*b*:2',3'-*d*]thiophene crystals. In the first case, a combined DFT and gas-phase ultraviolet photoelectron spectroscopy approach revealed that the intrinsic charge transport properties in the pentathienoacene crystal might be higher than that in two benchmark high-mobility organic crystals, *i.e.*, pentacene and sexithienyl. For 1,4-diiodobenzene crystal, a detailed quantum-mechanical study of the electronic and vibrational couplings indicated that its high mobility is primarily associated with the iodine atoms. In the 2,6-diiodo-dithieno[3,2-*b*:3',2'-*d*]thiophene crystal, the main source of electronic interactions were found along the π-stacking direction. For negatively charged carriers, these two halogen-functionalized molecular crystals show a very large polaron binding energy, which suggests significantly low charge-transport mobility for electrons.

CHAPTER 1

INTRODUCTION

1.1 Organic semiconductors

Technologies based on organic semiconductors may answer the always increasing demand that consumers have for large-area electronics, lightweight displays, and portable computing. Advances in scientific understanding, technology, and device performance of organic semiconductors have reached a point where molecular crystals of pentacene[1, 2] and rubrene[3, 4] have surpassed amorphous Si in performance. Organic materials are therefore of great interest for the new generation of thinner, lighter and higher resolution electronic applications. The market for organic electronics-based products is now projected to reach over $30 billion by 2015.[5] Needless to say, organic semiconductors have captured the interest of both chemical and electronics industries worldwide for good reasons. Importantly, a wide range of properties, such as solubility in different organic solvents and the color of the light emission can be fine-tuned via chemical synthesis.[6, 7] Another feature of interest includes the ease in processing, and the potential for low-cost fabrication. The combination of these attributes has fueled research and development in organic electronics in both academia and industry.

On the basic research side, organic materials represent systems in which the subtle interplay between their π-electronic structure and geometric structure has unveiled

extraordinary properties, leading to the establishment of new research areas for materials scientists.[8-10] On the applied research side, organic semiconductors have the potential to facilitate the development of large-area displays, solid-state lightening, radio frequency identification tags, or solar cells. It is expected that, one day, fascinating applications would be realized, such as wallpapers whose patterns and colors can change at the click of a switch; newspapers and books whose contents automatically update daily or on request;[11, 12] or television sets so thin and flexible that they can be rolled up and carried in a briefcase.[13] The maturity of these and other futuristic applications is not as far off as one might initially think. The Sony Corporation is now selling a television, called XEL-1, that is only about one-eighth of an inch thick; it owes its saturated colors and superlative slimness to the emerging technology of organic light-emitting diodes (OLEDs).

Figure 1.1 Side and front views of the XEL-1 Sony television with a screen one-eighth of an inch thick.[14]

The development of organic semiconductors, central to the aforementioned applications, was pioneered in the 1950s by Martin Pope and colleagues, who performed seminal studies of the ground- and excited-state electronic structure of model molecules and crystals, such as anthracene.[15] The field of organic electronics has also its root in the

1977 discovery of the conducting properties of doped polyacetylene.[16] This breakthrough earned Alan Heeger, Alan MacDiarmid, and Hideki Shirakawa the 2000 Nobel Prize in Chemistry for their "discovery and development of conductive polymers" and opened an entire new field of research. These conducting polymers have unique properties, in the way that they can combine the electrical properties of metals with the mechanical properties of polymers.

To date, a number of organic semiconductor families have been investigated; the data generated on these systems have allowed researchers around the world to draw important relations between molecular structure and structural organization in the solid state, film morphology, and electrical performance. Figure 1.2 collects the chemical structures of representative organic semiconductors. Some of these materials belonging to the oligoacenes or oligothiophene families have received much attention since single crystals with limited number of impurities can be obtained through repeated sublimation steps.[1, 3] In principle, these materials can be used to develop single-crystal organic transistors,[17-19] providing the opportunity to explore fundamental processes that determine the operation and reliability of organic electronic devices. Topics of current interest include investigating the role of the electronic interactions with vibrations and the induced electronic polarization and electrostatic effects in organic single crystals. Work along these lines is necessary to be able to estimate carrier mobilities accurately. However, the lack of processability of crystalline organic semiconductors prevents them from being easily integrated in industrial processes. For industrial applications, solution-process-able organic semiconductors are required. Therefore, to truly realize the low-cost

aspects of organic electronics, organic semiconductors should be deposited from solution via more versatile and economic techniques, such as spin coating, drop casting, or inkjet printing.[20, 21]

Despite the current progress in crystalline organic semiconductors, the promise of organic thin-film transistors (OTFTs) as to low-cost materials for disruptive technologies has triggered the production of vast libraries of synthetic organic semiconductors. OTFTs are the fundamental unit for backplane driving circuits in flexible displays and low-cost memory applications. In order for OTFTs to be successfully incorporated as driving circuits in display applications, they need to exhibit high current output, good switching speeds, and high contrast between the "on" and "off" states. These requirements are intrinsically correlated to the parameters used to characterize OTFTs, such as mobility (this quantity measures the average charge-carrier drift velocity per unit of electric field; it is usually given in units of $cm^2/V \cdot s$), the threshold voltage (which measures the voltage required to turn "on" the transistor), and on/off current ratio (a measure of contrast between the device "on" and "off" states). In section 1.1.2, a brief description of the structural design and operation of an OTFT is presented.

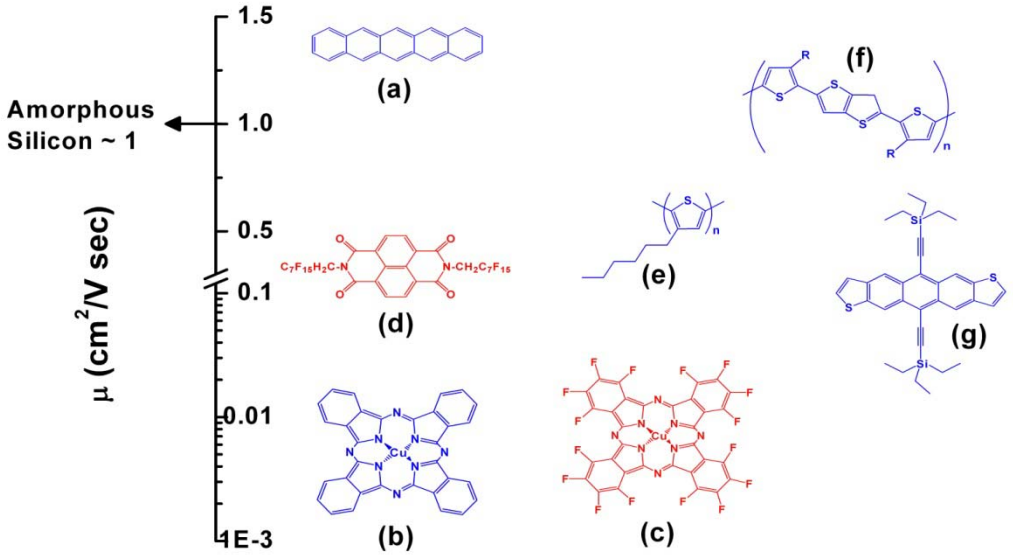

Figure 1.2 Representative organic semiconductors (those with p-channel characteristics are colored in blue, while those that exhibit n-channel characteristics are colored in red): (a) pentacene, (b) copper phthalocyanine, (c) fluorinated copper phthalocyanine, (d) fluorinated naphthalene diimide, (e) poly(3-hexyl thiophene), (f) poly(2,5-bis(3-alkylthiophen-2-yl)thieno[3,2-b]thiophene), and (g) triethylsilylethynyl anthradithiophene. (Figure adapted from Reference 22).

1.1.1 Molecular packing in organic molecules

A key factor that influences the charge mobility and the overall performance in all organic electronic devices is the intermolecular ordering of the molecules in the solid state. In general, it has been demonstrated that good electrical performance requires strong electronic coupling (a quantity that measures the strength of the electronic interactions) between adjacent molecules in the solid.[23] For example, extensive prior work in our research group has shown that the intermolecular electronic coupling is extremely sensitive to molecular packing,[23, 24] in a way that closely depends on the bonding-antibonding pattern of the frontier molecular orbitals (HOMO, highest occupied

molecular orbital, or LUMO, lowest unoccupied molecular orbital). Two common packing motifs adopted by organic molecular crystals in the solid state can yield strong intermolecular wavefunction overlap, namely, the herringbone and π-stacking arrangements (Figure 1.3). Interactions with adjacent stacks can lead to two- or three-dimensional electronic coupling in the solid.

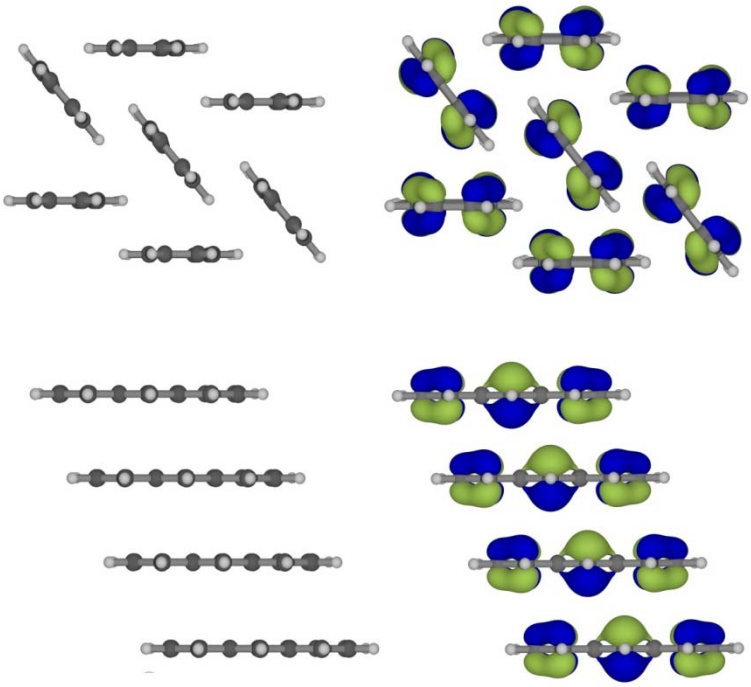

Figure 1.3 Illustration of packing arrangements for anthracene: herringbone (top) and π-stacking (bottom) (only HOMO orbital interactions are shown).

1.1.2 OTFT geometry and operation

Figure 1.4 shows two common device geometry configurations used for OTFTs. In both cases, an organic semiconductor film is deposited on a gate/insulator substrate and is contacted with metallic source and drain electrodes. The voltage applied between

the source and drain is referred to as the source-drain voltage, V_D. For a given V_D, the amount of current that flows through the semiconductor film from source to drain is a function of the voltage, V_G, applied to the gate electrode. The application of a bias on the gate induces the injection of charges into the semiconductor film. When these charges are mobile, they can move in response to the applied source-drain voltage, V_D. Under ideal conditions, if no gate voltage is applied, the conductance of the semiconductor is negligible, and the device is "off" due to lack of mobile charge carriers. On the other hand, if a gate voltage is applied, mobile charges are induced, and the transistor is "on".

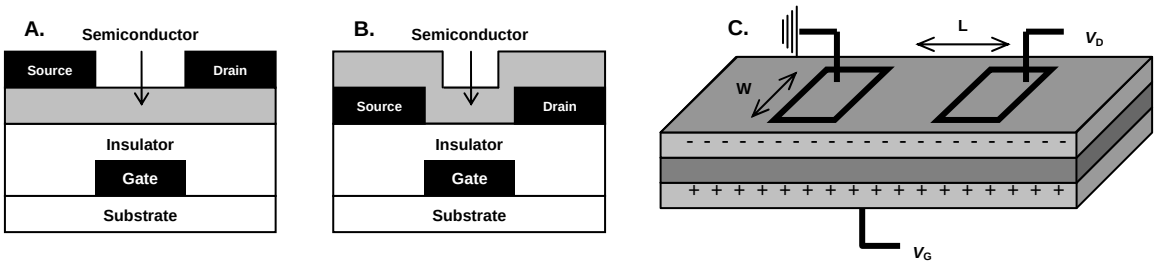

Figure 1.4 Schematic of top (a) and bottom (b) contact organic OTFTs. (c) Relevant voltages and geometry for an OTFT, L represents the source-drain channel length and W the channel width. (Figure adapted from Reference 25).

In order to understand the origin of the gate-induced charging process, a schematic electronic energy level diagram is shown in Figure 1.5. The positions of the HOMO and LUMO of the semiconductor relative to the Fermi energy (E_F) of the source and drain contacts are illustrated in Figure 1.5 (A). In the absence of gate voltage, there is no significant conduction since there are no mobile charges injected into the semiconductor. The left part of Figure 1.5 (B and D) shows the application of a positive gate voltage, which produces a strong electric field at the organic/insulator interface. The presence of this field causes the HOMO and LUMO levels of the semiconductor to shift

down in energy with respect to the Fermi levels of the metal contacts. In the particular case of a large enough gate field, electrons can flow from the metallic contacts to the LUMO level of the semiconductor; electrons are injected at the semiconductor/insulator interface. Under the application of a drain voltage, V_D, this results in an electrical current between source and drain. The same reasoning can be used to understand the effect of a negative bias in an OTFT (Figures 1.5 C and 1.5 E). Negative gate bias, V_G, causes the HOMO and LUMO levels to shift up in energy, allowing the HOMO of the semiconductor to become resonant with the contact Fermi levels. Electrons can jump from the semiconductor to the metallic contacts, leaving behind positively charged holes. These holes are able to move in response to the applied drain voltage, V_D, Figure 1.5 E.

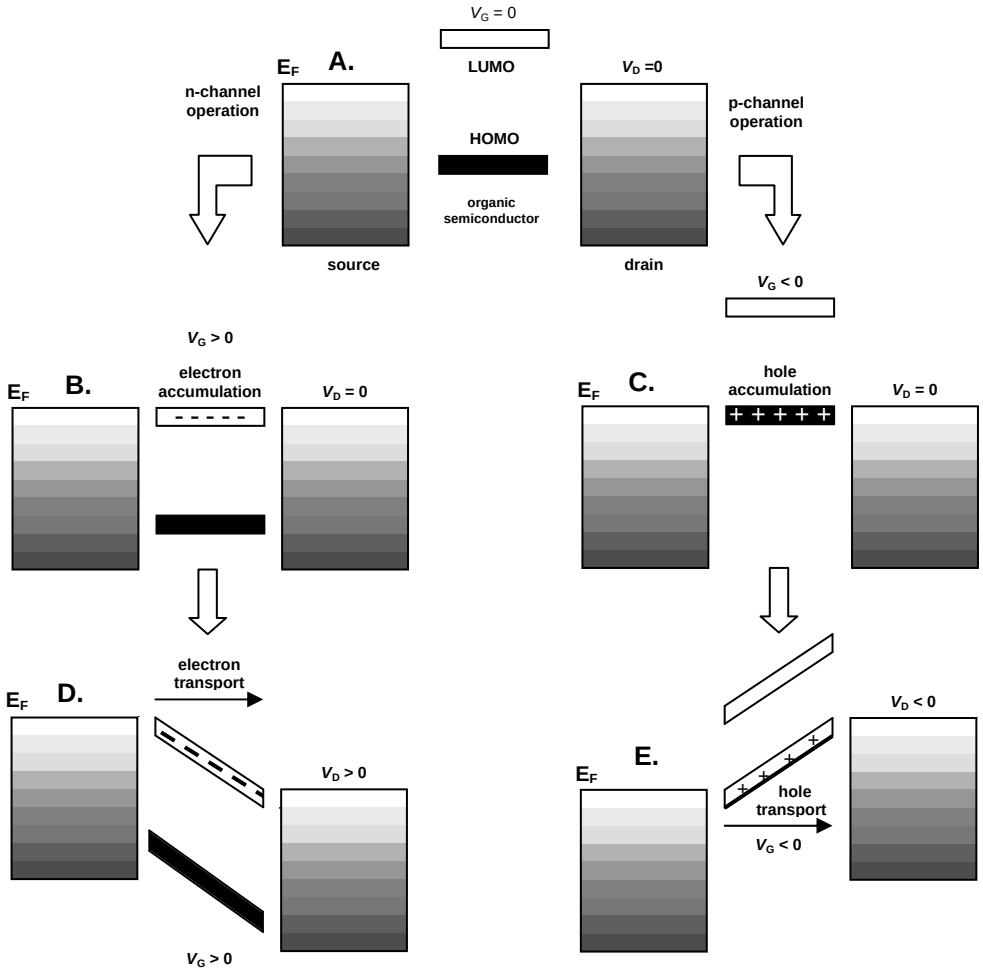

Figure 1.5 (A) Idealized energy level diagram of an OTFT at $V_G = 0$ and $V_D = 0$. (B and D) Electron accumulation and electron transport in the OTFT. (C and E) Hole accumulation and hole transport in the OTFT. (Figure adapted from Reference 25).

1.1.3 OTFT applications

Organic thin films have long been attractive for use in electronics because of their light weight, large-area applications, and a less complex fabrication process compared with their inorganic counterparts. Recent developments in device performance have rapidly expanded organic electronics niche markets, making them targets for a wider range of applications. OTFTs have been proposed for applications such as display

switches,[26] display drivers,[27] radio-frequency identification (RFID) tags,[28] and sensors.[29, 30] In the following, a brief description of some (potential) applications of OTFTs is presented.

1.1.3.1 Electronic paper

One of the earliest examples of organic semiconductor applications that was realized was active-matrix electronic paper. Organic transistors can be manufactured directly at low (ambient) temperature onto plastic films, which are mechanically flexible, lightweight, and thin. In such systems, an organic or polymer transistor backplane drives elements such as electrophoretic cells. The display elements have a memory effect and are often electric-field driven. The current drive requirements are much less than those required for an active-matrix OLED display. Electronic paper is often required to be flexible and processed over relatively large areas. In the first report on organic transistor-based electronic paper, pentacene transistors were printed on low-cost, mechanically flexible polymer substrates.[12] Although that early prototype did not display the number of pixels required for most customer applications, it set the foundations for companies to commercialize electronic paper based on polymer electronics. Companies such as E Ink, SiPix, and Polymervision, as well as such giants as Sony, IBM, Hewlett-Packard, Philips, Fujitsu, Hitachi, and many others, are continuing to develop electronic paper technology.[31, 32] The backplane for a 256-element electronic paper is shown in Figure 1.6 (a).

1.1.3.2 RFID tags

Another major application area for OTFTs is that of RFID tags. The primary driver for consideration of this application is cost; it is expected that the cost of an RFID tag fabricated using organic-printed transistors will be substantially lower than that of Si-based tags. Upon the assumption that a fully printed process is realized, it is likely that a cost advantage for printed RFIDs will exist over conventional Si chip technologies. If so, organic-based RFIDs tags can be used in the identification of individual retail goods in much the same way as barcodes are presently employed. The realization of this technology undoubtedly represents an opportunity for organic- and polymer-transistor-based components. A photo of a flexible circuit based on pentacene transistors is shown in Figure 1.6 (b).

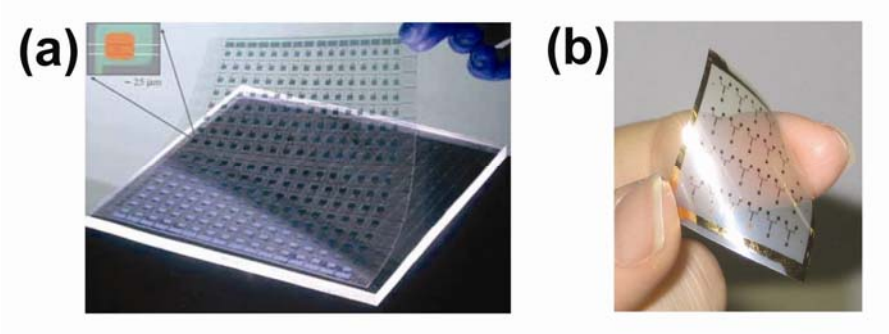

Figure 1.6 (a) A 256-element electronic paper system, each pixel consists of an organic transistor with channel length < 20 μm. Details are described elsewhere.[12] (b) Photo of an RFID tag component circuit. (Figure adapted from Reference 11).

1.1.3.3 Chemical sensors

The usage of organic and polymeric transistors for sensor applications emerges from the chemical nature of these materials and the fact that they can form weak chemical interactions with a variety of analytes.[33, 34] The semiconductor characteristics of organic materials enables the transfer of chemical information into electronic information in the solid state. A large number of organic semiconductors will permit the identification of several analytes through fingerprinting, in which a particular analyte produces a unique pattern of responses with different semiconductors. Despite the availability of chemical sensors, implementing a relatively inexpensive and highly selective portable system for detecting volatile analytes is still a challenge. Thus, OTFTs appear promising in this sense because they have demonstrated to operate as multiparametric sensors[35] and have shown a remarkable response reproducibility.[36]

1.2 Charge transport

After several decades of intensive research, the understanding of the basic charge transport mechanism in organic semiconductors remains incomplete. The complexity of the transport phenomena is generally associated with the polaronic nature of charge carriers and the strong electron-vibration interactions; in such a case, the coupling between electrons and vibrations cannot be simply treated as a perturbation.[15, 37] A challenge for theoreticians is to develop an adequate model that describes transport as a function of temperature. The time-of-flight experiments with ultrapure crystals of

naphthalene and anthracene carried out by Karl and co-workers[38, 39] have demonstrated that charge transport in organic crystals is characterized by a rapid decrease of the carrier mobility with increasing temperature and a pronounced anisotropy of the mobility along different crystallographic directions. This is illustrated in Figure 1.7 for the case of electron and hole transport along the a crystal axis of ultrapure crystals of naphthalene.[38] Similar evolution is observed along specific directions for a large number of crystals. This decrease in mobility originates from enhanced scattering processes by lattice phonons. Transport measurements on molecular single crystals indicate that charge mobilities as high as a few hundred $cm^2/V \cdot s$ can be obtained at low temperature (up to 300 $cm^2/V \cdot s$ for holes in naphthalene at 10 K).[38]

In the past, conjugated polymers and charge-transfer complexes were the main focus of charge transport studies in organic materials. For an extensive review on the topic, see for example the monographs by Pope and Swenberg[15] and Silinsh and Capek.[37] As previously mentioned, significant attention is now paid to highly ordered semiconductors, of particular interest for their high mobilities and their potential applications in molecular electronic devices.[1-4] In principle, large mobility values are associated with the improved purity of molecular crystals, which represents a drawback for large-scale applications because of the relatively high cost and complexity of the vacuum fabrication technique.[1] However, highly ordered molecular crystals provide a unique opportunity to explore the basic charge-transport processes that determine the operation and reliability of organic electronic devices. Since the key quantity that characterizes charge transport is the carrier mobility, this section starts with the definition

of the carrier mobility and is followed by the description of a theoretical model for charge transport in ordered molecular materials.

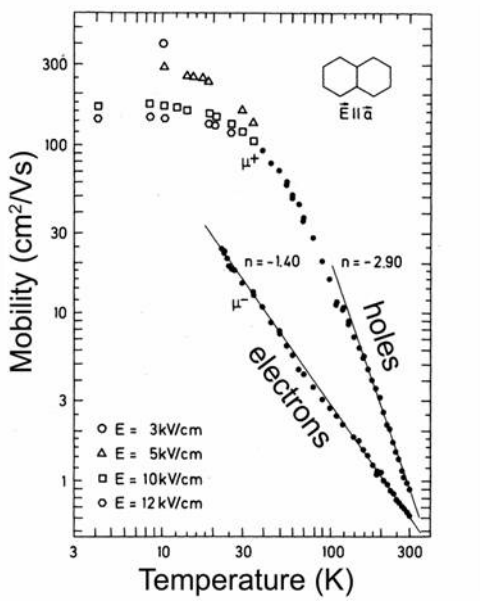

Figure 1.7 Electron and hole mobilities in the *a*-direction of a highly purified naphthalene crystal as a function of temperature. (Figure adapted from Reference 38).

1.2.1 Definition of charge carrier mobility

The mobility, μ, is related to the conductivity, σ, according to:

$$\sigma = en\mu \tag{1.1}$$

where n indicates the density of the charge carriers and e is the elementary charge. The mobility of the charge carriers in solids is often described in terms of the linear response formalism. In this case, the Kubo formula provides a general starting point for a semiclassical or fully quantum-mechanical description of the mobility. For charge carriers at thermal equilibrium moving in an electric field, the mobility is, according to Kubo's formula, given by:

$$\mu(\omega) = -\frac{e\omega^2}{2k_B T}\int_0^{\infty} \frac{\langle |r(t) - r(0)|^2 \rangle}{d} e^{-i\omega t} dt \tag{1.2}$$

with k_B Boltzmann's constant, T the temperature, t the time, ω the radial frequency (that accounts for the possible oscillating behavior of the electric field), r the total displacement vector, and $d = 1, 2, 3$ the dimensionality of the system. The brackets imply averaging over a large number of charge carriers at thermal equilibrium. Calculation of the charge carrier mobility on the basis of Equation 1.2 requires an evaluation of the average of the square displacement for all the charge carriers contributing to the conductivity. This averaging involves taking into account the contribution of all states of the charge carriers. The charge carrier states can be obtained from the Hamiltonian of the system, given by:

$$H = H_e + H_{ph} + H_{e-ph} \tag{1.3}$$

In Equation 1.3, H_e is the electronic Hamiltonian and H_{ph} is the phonon Hamiltonian. The H_{e-ph} term describes the interactions between electrons and phonons, which are associated with the dynamic fluctuations of the material. Such fluctuations correspond to nuclear vibrations of the molecule or to motions of the entire molecular unit.

In the case of normal Gaussian diffusion, the mean square displacement of a charge eventually increases with time according to:

$$\langle |r(t) - r(0)|^2 \rangle = 2dDt \tag{1.4}$$

with *D* representing the diffusion constant, *d* the dimensionality of the system, and t the time. Substitution of Equation 1.4 into Equation 1.2 gives the Einstein relation for the mobility:

$$\mu = \frac{e}{k_B T} D \tag{1.5}$$

The mobility in Equation 1.5 is frequency independent and the imaginary component is zero.

1.2.2 Theory of charge carrier mobility

The most detailed transport theories in ultrapure organic crystals are still those based on the 1D Holstein molecular model.[40, 41] According to this model, the total mobility can be expressed to a good approximation as a sum of two contributions:

$$\mu = \mu_{\text{tun}} + \mu_{\text{hop}} \tag{1.6}$$

Here, the first term is due to electron tunneling (coherent electron transfer) and dominates transport at low temperatures; the second term is related to hopping motion (incoherent electron transfer) and becomes dominant at higher temperatures. The relative contribution of each mechanism is associated with the actual values of the microscopic parameters, such as electron-phonon coupling, electronic and phonon bandwidths, and phonon energy. An illustrative example of the temperature dependence of the mobility for large ($g^2 \gg 1$) and weak ($g^2 \ll 1$) electron-phonon couplings is shown in Figure 1.8. In the case of weak electron-phonon coupling, the mobility is dominated by tunneling and displays a band-like temperature dependence in the whole range of temperatures. For the strong couplings, three different temperatures regimes are observed: (i) at low temperature, the mobility is band-like; (ii) as temperature increases, the hopping term becomes dominant, and the mobility is associated with a temperature-activated process; (iii) if the system can reach very high temperatures (where thermal energy overcomes the

polaron binding energy), the residual electron is scattered by thermal phonons and the mobility decreases again with temperature. In the next sections, the analytical results for the tunneling and hopping mobilities derived from Holstein's seminal work[40,41] are described for the case of wide- and narrow-band materials.

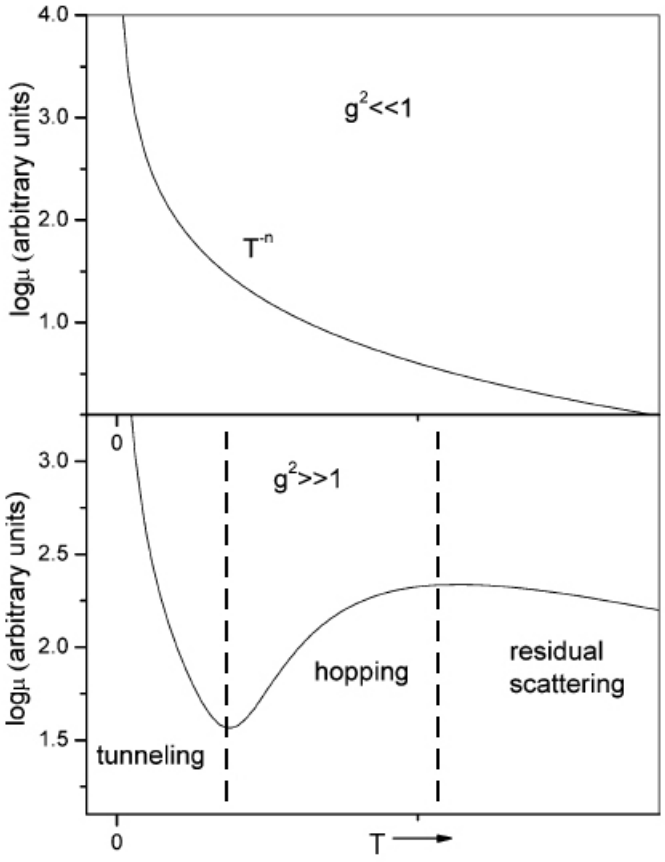

Figure 1.8 Temperature dependence of the mobility for the limiting cases of strong and weak electron-phonon couplings, g. (Figure adapted from Reference 23).

1.2.2.1 Wide-band materials

In the following, the band model for a metal will be discussed. Conceptually, this model is an important basis for understanding the band conductivity in wide-band organic semiconductors. According to band theory, all the energy states $E(k)$ of the electrons

below the Fermi energy E_F are occupied and those lying at higher energies ($E > E_F$) are empty when the temperature is low, *i.e.*, $k_B T \ll E_F$; k represents the electron wavevector, with a linear momentum defined as follows: $\hbar k = mv$. In the k-space (reciprocal space) of a simple metal, the occupied states are described by a sphere centered on the origin in the absence of any electric field F. If an electric field is applied, $F = F_x$, the electrons within the Fermi sphere can take up energy. In this case, the whole Fermi sphere shifts from the stationary equilibrium by the amount:

$$\delta k_x = -\frac{e\tau}{\hbar} F_x \tag{1.7}$$

Here, $\tau = \tau(E_F)$ is the relaxation time of those conduction electrons which have acquired the additional momentum $\hbar \delta k_x$ on the Fermi surface and relax back to thermal equilibrium after the electrical field is switched off. This relaxation process can be considered as an inelastic process, in which the electrons that occupy a state A are scattered into unoccupied states B on the Fermi surface (see Figure 1.9). This scattering process can take place with a phonon, with a lattice defect, or with an impurity.

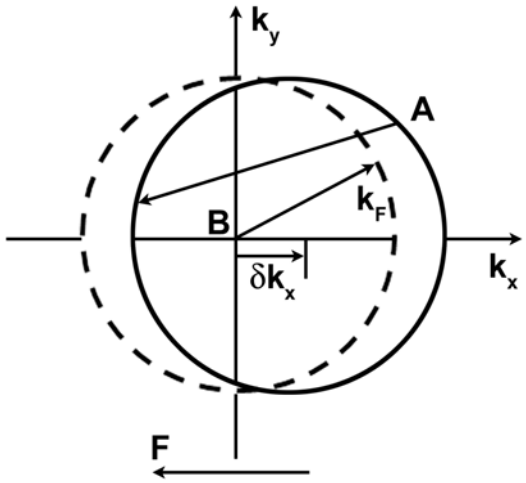

Figure 1.9 A schematic representation of the shift of the Fermi distribution of the conduction electrons in the k-space of a metal under the action of an electric field F_x and the scattering processes during the relaxation after switching off F_x. (Figure adapted from Reference 42).

For the sake of clarity, the energy states (or band energies), $E(k)$, are now considered for a one-dimensional structure of molecular units with mutual spacing a. In a simple tight-binding approach, the energy at the bottom of the conduction band can be written as:

$$E(k) = \epsilon + 2t \cdot cos(ka) \tag{1.8}$$

where ϵ is the electron site energy and t is the charge transfer integral (also referred to as electronic coupling or hopping integral).

When the width W of the energy band in Equation 1.8 is much larger than the thermal energy, k_BT, excess electrons will occupy states near the bottom of the conduction band, while holes will remain close to the top of the valence band. Near these band extrema, the energies in Equation 1.8 can be approximated via a parabolic expression with respect to k, giving:

$$E(k) = \frac{\hbar^2\left(k_x^2 + k_y^2 + k_z^2\right)}{2m^*} = \frac{\hbar^2 k^2}{2m^*} \tag{1.9}$$

with the effective mass m^* of the charge carriers equal to:

$$\frac{1}{m^*} = \frac{1}{\hbar^2} \cdot \frac{d^2E}{dk^2} = \frac{2a^2|t|}{\hbar^2} \tag{1.10}$$

Once the effective mass, m^*, has been defined, it is useful to make a few more remarks with respect to Figure 1.9. First, an additional momentum transferred by the electric field F_x to the whole Fermi sphere is defined as:

$$m^* \delta v(E_F) = \hbar \delta k_x \tag{1.11}$$

Secondly, the stationary additional velocity of the electrons then becomes with Equation 1.7:

$$\delta v_x = -\frac{e\tau(E_F)}{m^*} \cdot F_x \tag{1.12}$$

Therefore, in the band model, the charge carrier mobility μ and the conductivity σ are:

$$\mu_{\text{tun}} = \frac{e\tau(E_F)}{m^*} = \frac{2ea^2|t|}{\hbar^2}\tau(E_F) \tag{1.13}$$

and

$$\sigma = \frac{e^2\tau(E_F)}{m^*} \cdot n \tag{1.14}$$

Note, that the mobility expression in Equation 1.13 is only valid in the case where the energy of the charge carriers depends quadratically on their wavevector k according to Equation 1.9. This condition is not fulfilled when charge carriers undergo strong interactions with phonons or scattering on structural imperfections. This restricts the applicability of the band-like mobility expression to structurally ordered systems where the charges undergo weak scattering. Weak scattering implies that the bandwidth, W,

should be equal to $4|t|$ and that the relaxation time largely exceeds the $\hbar/W$ ratio, *i.e.*, $\tau \gg \hbar/W$. In this context, t is thus a key factor to understand the charge transport properties in organic molecular crystals at low temperature, when the charges adopt a band-like motion.

1.2.2.2 Narrow-band materials

In the narrow band limit, when a strong vibrational coupling exists ($g^2 \gg 1$), the mobility is given as a sum of coherent (μ_{tun}) and incoherent (μ_{hop}) contributions. First the hopping part of the mobility is considered. In this case, μ_{hop}, can be obtained from Equation 1.5, where $D = a^2\kappa_{\text{ET}}$; κ_{ET} is the hopping rate between adjacent sites. According to the 1D Holstein model,[41] the hopping rate is given by:

$$\kappa_{\text{ET}} = \frac{t^2}{\hbar^2\omega_0}\left[\frac{\pi}{g^2 \operatorname{csch}\left(\frac{\hbar\omega_0}{2k_BT}\right)}\right]^{1/2} exp\left[-2g^2 \tanh\left(\frac{\hbar\omega_0}{4k_BT}\right)\right] \tag{1.15}$$

where $\hbar\omega_0$ represents the energy of an optical phonon and is characterized by a coupling constant g. In the classical limit for which $\hbar\omega_0 \ll k_BT$, the hyperbolic tangents get replaced by their argument, and κ_{ET} assumes a standard Arrhenius type expression:

$$\kappa_{\text{ET}} = \frac{t^2}{\hbar}\left[\frac{\pi}{2E_{pol}k_BT}\right]^{1/2} exp\left(-E_{pol}/2k_BT\right) \tag{1.16}$$

where E_{pol}, the polaron binding energy, is equal to $\hbar\omega_0 g^2$. By substituting Equations 1.15 and 1.16 into Equation 1.5, the analytical expressions for the general and classical mobilities in the hopping mechanism are obtained. They write, respectively:

$$\mu_{\text{hop}} = \frac{ea^2t^2}{k_B T\hbar^2\omega_0}\left[\frac{\pi}{g^2\text{csch}\left(\frac{\hbar\omega_0}{2k_BT}\right)}\right]^{1/2} exp\left[-2g^2\tanh\left(\frac{\hbar\omega_0}{4k_BT}\right)\right] \tag{1.17}$$

and

$$\mu_{\text{hop}} = \frac{ea^2t^2}{k_B T\hbar}\left[\frac{\pi}{2E_{pol}k_BT}\right]^{1/2} exp\left(-E_{pol}/2k_BT\right) \tag{1.18}$$

The coherent part of the mobility at low temperatures and in the narrow band limit (*i.e.*, $t \sim k_BT$) is given by (compare with Equation 1.13):

$$\mu_{\text{tun}} = \frac{2ea^2}{k_BT}\frac{\tau(T)}{\hbar^2}t^2(T) \tag{1.19}$$

with

$$t(T) = t \cdot exp\left[-g^2\coth\left(\frac{\hbar\omega_0}{2k_BT}\right)\right] \tag{1.20}$$

By inserting Equation 1.15 into Equation 1.19 and by defining $t(T)$ in terms of the hopping rate κ_{ET}, *i.e.*, $1/t(T) = 2\kappa_{\text{ET}}$, the general expression of the tunneling mobility is obtained:

$$\mu_{\text{tun}} = \frac{ea^2\omega_0}{k_BT}\left[\frac{g^2\text{csch}\left(\frac{\hbar\omega_0}{2k_BT}\right)}{\pi}\right]^{1/2} exp\left[-2g^2\text{csch}\left(\frac{\hbar\omega_0}{2k_BT}\right)\right] \tag{1.21}$$

Note that, because of the assumption that the band is narrow, Equation 1.21 does not depend on t, and its application is restricted to temperatures such that $k_BT > 4t(T)$.

1.3 Thesis objective and outline

Despite the extensive use of the Holstein molecular model to derive qualitative interpretations of experimental data, their model cannot fully describe the charge transport mechanisms in organic materials. In fact, it has been demonstrated that in organic crystals the modulations of the transfer integral with acoustic and optical phonons can be of the same order of magnitude as the value of the transfer integral itself.[43, 44] Thus, more general models need to be considered. Recently, Coropceanu *et al.*[23] reviewed extensions of the 1D Holstein molecular model to charge transport theory in organic materials. This review clearly shows that a full knowledge of the microscopic charge transport parameters is the first step toward the development of a comprehensive understanding of transport in organic semiconductors. Under this theoretical approach, the primary emphasis of this thesis includes the development of a first-principles theoretical methodology to evaluate with high accuracy the main microscopic charge-transport parameters and their respective couplings with intra- and intermolecular vibrational degrees of freedom (electron-phonon interactions). This molecular approach contrasts with many models developed earlier for organic materials where the electronic and electron-phonon (vibration) interactions have been described on a phenomenological basis and from a macroscopic perspective, thereby masking the impact of the actual chemical/molecular structures of the systems on charge transport.

In Chapter 2, a brief review of the electronic structure methods essential in the understanding of the physics of molecular solids is presented. The discussion starts with

the theoretical basis of a single-particle description of the molecular crystal. This will be done by starting with the exact Hamiltonian for a solid and introducing approximations in its solution. This is followed by a description of the tools used for understanding the motion of atoms in crystals through the language of phonons. The dynamical matrix is introduced; it is shown that the frequencies are obtained from the eigenvalues of the dynamical matrix and that the atomic motions are given by the eigenvectors. Finally, a discussion on the role of electron-phonon interactions and their impact on the microscopic charge transport parameters is presented.

In Chapters 3 and 4, the local and nonlocal electron-phonon interactions in oligoacene crystals are addressed using an approach based on density functional theory. Within this framework, a description of the vibronic coupling interactions in oligoacene cations and the electron-phonon coupling in organic molecular crystals is investigated. It was found that the description of charge transport in organic semiconductors requires that both local and nonlocal electron-phonon couplings be considered.

Chapter 5 is devoted to the electronic and vibronic coupling in oligothienoacenes with a focus on the pentathienocene crystal. In Chapter 6, a detailed quantum-mechanical study of the electronic and vibrational couplings in crystals of small iodine-substituted organic molecules is reported. In both cases, it was found that either the iodine atoms or π-π interactions play a significant role in dictating the charge transport properties of these crystalline systems.

Finally, in Chapter 7, a comprehensive summary of the first-principles methodology that was developed to characterize the intra- and intermolecular electron-phonon interactions is presented. Its scope and current applications are also described.

1.4 References

(1) Jurchescu, O. D.; Baas, J.; Palstra, T. T. M. *Applied Physics Letters* **2004**, *84*, 3061.

(2) Reese, C.; Chung, W. J.; Ling, M. M.; Roberts, M.; Bao, Z. N. *Applied Physics Letters* **2006**, *89*, 202108.

(3) Podzorov, V.; Menard, E.; Borissov, A.; Kiryukhin, V.; Rogers, J. A.; Gershenson, M. E. *Physical Review Letters* **2004**, *93*, 086602.

(4) Sundar, V. C.; Zaumseil, J.; Podzorov, V.; Menard, E.; Willett, R. L.; Someya, T.; Gershenson, M. E.; Rogers, J. A. *Science* **2004**, *303*, 1644.

(5) IDTechEx *Organic Electronic Forecasts, Players, Opportunities, 2005-2025*, June 2005.

(6) Anthony, J. E. *Chemical Reviews* **2006**, *106*, 5028.

(7) Anthony, J. E. *Angewandte Chemie-International Edition* **2008**, *47*, 452.

(8) Brédas, J. L.; Beljonne, D.; Coropceanu, V.; Cornil, J. *Chemical Reviews* **2004**, *104*, 4971.

(9) Heeger, A. J.; Kivelson, S.; Schrieffer, J. R.; Su, W. P. *Reviews of Modern Physics* **1988**, *60*, 781.

(10) Su, W. P.; Schrieffer, J. R.; Heeger, A. J. *Physical Review Letters* **1979**, *42*, 1698.

(11) Dodabalapur, A. *Materials Today* **2006**, *9*, 24.

(12) Rogers, J. A.; Bao, Z.; Baldwin, K.; Dodabalapur, A.; Crone, B.; Raju, V. R.; Kuck, V.; Katz, H.; Amundson, K.; Ewing, J.; Drzaic, P. *Proceedings of the National Academy of Sciences of the United States of America* **2001**, *98*, 4835.

(13) Howard, W. E. *Scientific American* **2004**, *290*, 76.

(14) Ebling, M. C., Mark. *Pervasive Computing, IEEE* **2008**, *7*, 8.

(15) Pope, M.; Swenberg, C. E.; Pope, M. *Electronic processes in organic crystals and polymers*, 2nd ed.; Oxford University Press: New York, 1999.

(16) Chiang, C. K.; Fincher, C. R.; Park, Y. W.; Heeger, A. J.; Shirakawa, H.; Louis, E. J.; Gau, S. C.; Macdiarmid, A. G. *Physical Review Letters* **1977**, *39*, 1098.

(17) Aleshin, A. N.; Lee, J. Y.; Chu, S. W.; Kim, J. S.; Park, Y. W. *Applied Physics Letters* **2004**, *84*, 5383.

(18) Butko, V. Y.; Chi, X.; Lang, D. V.; Ramirez, A. P. *Applied Physics Letters* **2003**, *83*, 4773.

(19) de Boer, R. W. I.; Klapwijk, T. M.; Morpurgo, A. F. *Applied Physics Letters* **2003**, *83*, 4345.

(20) Sirringhaus, H. *Advanced Materials* **2005**, *17*, 2411.

(21) Sirringhaus, H.; Kawase, T.; Friend, R. H.; Shimoda, T.; Inbasekaran, M.; Wu, W.; Woo, E. P. *Science* **2000**, *290*, 2123.

(22) Loo, Y. L. *Aiche Journal* **2007**, *53*, 1066.

(23) Coropceanu, V.; Cornil, J.; da Silva Filho, D. A.; Olivier, Y.; Silbey, R.; Brédas, J. L. *Chemical Reviews* **2007**, *107*, 926.

(24) Brédas, J. L.; Calbert, J. P.; da Silva Filho, D. A.; Cornil, J. *Proceedings of the National Academy of Sciences of the United States of America* **2002**, *99*, 5804.

(25) Newman, C. R.; Frisbie, C. D.; da Silva Filho, D. A.; Brédas, J. L.; Ewbank, P. C.; Mann, K. R. *Chemistry of Materials* **2004**, *16*, 4436.

(26) Dodabalapur, A.; Bao, Z.; Makhija, A.; Laquindanum, J. G.; Raju, V. R.; Feng, Y.; Katz, H. E.; Rogers, J. *Applied Physics Letters* **1998**, *73*, 142.

(27) Sirringhaus, H.; Tessler, N.; Friend, R. H. *Science* **1998**, *280*, 1741.

(28) Bao, Z.; Locklin, J. J. *Organic field-effect transistors*; CRC Press: Boca Raton, 2007.

(29) Crone, B. K.; Dodabalapur, A.; Sarpeshkar, R.; Filas, R. W.; Lin, Y. Y.; Bao, Z.; O'Neill, J. H.; Li, W.; Katz, H. E. *Journal of Applied Physics* **2001**, *89*, 5125.

(30) Crone, B. K.; Dodabalapur, A.; Sarpeshkar, R.; Gelperin, A.; Katz, H. E.; Bao, Z. *Journal of Applied Physics* **2002**, *91*, 10140.

(31) Graham-Rowe, D. *Nature Photonics* **2007**, *1*, 248.

(32) Granmar, M.; Cho, A. *Science* **2005**, *308*, 785.

(33) Assadi, A.; Gustafsson, G.; Willander, M.; Svensson, C.; Inganas, O. *Synthetic Metals* **1990**, *37*, 123.

(34) Laurs, H.; Heiland, G. *Thin Solid Films* **1987**, *149*, 129.

(35) Torsi, L.; Dodabalapur, A.; Sabbatini, L.; Zambonin, P. G. *Sensors and Actuators B-Chemical* **2000**, *67*, 312.

(36) Crone, B.; Dodabalapur, A.; Gelperin, A.; Torsi, L.; Katz, H. E.; Lovinger, A. J.; Bao, Z. *Applied Physics Letters* **2001**, *78*, 2229.

(37) Silins, E.; Cápek, V. *Organic molecular crystals : interaction, localization, and transport phenomena*; American Institute of Physics: New York, 1994.

(38) Karl, N. *Synthetic Metals* **2003**, *133*, 649.

(39) Karl, N.; Marktanner, J. *Molecular Crystals and Liquid Crystals* **2001**, *355*, 149.

(40) Holstein, T. *Annals of Physics* **1959**, *8*, 325.

(41) Holstein, T. *Annals of Physics* **1959**, *8*, 343.

(42) Schwoerer, M.; Wolf, H. C. *Organic molecular solids*; Wiley-VCH: Weinheim, 2007.

(43) Troisi, A.; Orlandi, G. *Journal of Physical Chemistry A* **2006**, *110*, 4065.

(44) Troisi, A.; Orlandi, G.; Anthony, J. E. *Chemistry of Materials* **2005**, *17*, 5024.

CHAPTER 2

THEORETICAL METHODS FOR ELECTRONIC STRUCTURE AND LATTICE DYNAMICS CALCULATIONS IN MOLECULAR SOLIDS

In this chapter, a brief review of the electronic structure methods essential in the understanding of the physics of molecular solids is presented. The discussion starts with the exact Hamiltonian for a solid and introducing approximations in its solution. This is followed by a description of the tools used for understanding the motion of atoms in crystals through the language of phonons. Finally, the computational methodologies used to investigate the impact of the electron-vibration interactions on charge transport are presented.

2.1 Electronic structure calculations

2.1.1 The Hamiltonian of a molecular solid

A theory for a stationary system of nuclei and interacting electrons is intrinsically quantum-mechanical, and is based on solving the time-independent Schrödinger equation of the form:

$$H\Psi([R;r]) = E\Psi([R;r]) \tag{2.1}$$

where H is the Hamiltonian of the system, containing the kinetic and potential energy operators; E is the energy of the system; $\Psi([R;r])$ is the wavefunction of the system; $[R]$

are the positions of the nuclei, and $[r]$ are the variables that describe the coordinates of the electrons. Two electrons at r_i, r_j repel one another, producing a potential energy term:

$$\frac{e^2}{|r_i - r_j|} \tag{2.2}$$

where e is the electronic charge. An electron at r is attracted to each positively charged nucleus at R, producing a potential energy term:

$$\frac{Ze^2}{|R - r|} \tag{2.3}$$

where Z is the charge of the nucleus. The total external potential experienced by an electron due to the presence of the nuclei is:

$$V(r) = -\sum_I \frac{Z_I e^2}{|R_I - r|} \tag{2.4}$$

Two nuclei at positions R_i and R_j also repel one another giving rise to a potential energy term:

$$\frac{Z_i Z_j e^2}{|R_i - R_j|} \tag{2.5}$$

Typically, it can be assumed that the nuclei move more slowly in space than the electrons, so that Ψ has a dependence on the electronic degrees of freedom alone. This is known as the Born-Oppenheimer approximation. Its validity rests on the huge difference of mass between nuclei and electrons, making the former behave like classical particles. In this case, the quantum-mechanical term for the kinetic energy of the nuclei can be omitted and their kinetic energy can be taken into account as a classical contribution. If the nuclei are considered to be at rest, the Hamiltonian of the system becomes (note that in the following equations $4\pi\varepsilon_0 = 1$):

$$H = -\sum_i \frac{\hbar^2}{2m_e}\nabla_{r_i}^2 - \sum_{iI} \frac{Z_I e^2}{|R_I - r_i|} + \frac{1}{2}\sum_{i\neq j} \frac{e^2}{|r_i - r_j|} + \frac{1}{2}\sum_{I\neq J} \frac{Z_I Z_J e^2}{|R_I - R_J|} \quad (2.6)$$

The last term in the previous equation is a constant and the electronic Hamiltonian writes:

$$H_e = -\sum_i \frac{\hbar^2}{2m_e}\nabla_{r_i}^2 - \sum_{Ij} \frac{Z_I e^2}{|R_I - r_i|} + \frac{e^2}{2}\sum_{i\neq j} \frac{1}{|r_i - r_j|} \quad (2.7)$$

Even with the proposed Born-Oppenheimer approximation, solving for $\Psi([r])$ remains an extremely difficult task, due to the many body nature of the electronic interactions. Each electron is affected by the motion of every other electron in the system; this is known as the "correlation" of their motion. In addition, two electrons of the same spin can exchange their positions, in which case Ψ must change sign. It is possible to produce a simpler picture by describing the system as a collection of classical nuclei and single quantum-mechanical particles that reproduce the behavior of the electrons: this is the single particle picture. In the following sections, the equations for the equivalent one-electron picture will be derived.

2.1.2 The Hartree and Hartree-Fock approximations

In the Hartree approximation, the electrons are considered as non-interacting particles, and the total wavefunction can be approximated by a product of orthonormal wavefunctions, namely:

$$\Psi^H([r_i]) = \phi_1(r_1)\phi_2(r_2)\cdots\phi_N(r_N) \quad (2.8)$$

Such an expression is known as the Hartree product. Unfortunately, this total wavefunction does not satisfy the antisymmetry principle with respect to the exchange of two electron coordinates. Therefore, the next level of sophistication is to try to

incorporate the half-integer spin nature of electrons into the wavefunction $\Psi([r])$. This is known as the Hartree-Fock (HF) approximation. Combining then Hartree-type wavefunctions to form a properly antisymmetrized wavefunction for the system, the following determinant, first introduced by Slater[1], is obtained:

$$\Psi^{HF}([r_i]) = \frac{1}{\sqrt{N!}} \begin{vmatrix} \phi_1(r_1) & \phi_1(r_2) & \cdot & \cdot & \cdot & \phi_1(r_N) \\ \phi_2(r_1) & \phi_2(r_2) & \cdot & \cdot & \cdot & \phi_2(r_N) \\ \vdots & \vdots & & & & \vdots \\ \cdot & \cdot & & & & \cdot \\ \phi_N(r_1) & \phi_N(r_2) & \cdot & \cdot & \cdot & \phi_N(r_N) \end{vmatrix} \tag{2.9}$$

where N is the total number of electrons. This determinant has the desired property, since interchanging the position of two electrons is equivalent to interchanging the corresponding columns in the determinant, which in turn changes its sign.

The total energy of the HF wavefunction is:

$$E^{HF} = \langle \Psi^{HF} | H | \Psi^{HF} \rangle \tag{2.10}$$

$$= \sum_i \langle \phi_i \left| \frac{-\hbar^2 \nabla_r^2}{2m_e} + \frac{Ze^2}{|R-r|} \right| \phi_i \rangle + \frac{e^2}{2} \sum_{i \neq j} \langle \phi_i \phi_j \left| \frac{1}{|r-r'|} \right| \phi_i \phi_j \rangle$$

$$- \frac{e^2}{2} \sum_{i \neq j} \langle \phi_i \phi_j \left| \frac{1}{|r-r'|} \right| \phi_j \phi_i \rangle$$

The last term on the right hand side of Equation 2.10 represents the "exchange" term, which describes the effects of exchange between electrons.

Then, the single-particle HF equations take the form:

$$\left[\frac{-\hbar^2 \nabla_r^2}{2m_e} + \frac{Ze^2}{|R-r|} + V_i^H(r) + V_i^X(r) \right] \phi_i(r) = \epsilon_i \phi_i(r) \tag{2.11}$$

The Hartree $V_i^H(r)$ and exchange $V_i^X(r)$ potentials give the electron-electron interaction $V_i^{HF}(r)$ in the Hartree-Fock approximation:

$$V_i^{HF}(r) = V_i^H(r) + V_i^X(r) \tag{2.12}$$

The first term in the previous equation is the total Coulomb operator and represents the electrostatic interaction of an electron in a spatially-averaged one-electron potential of all other electrons. The second term is the exchange operator; it has a pure quantum origin and prevents two electrons with parallel spins to be at the same position in space.

2.1.3 Density Functional Theory

Density Functional Theory (DFT) provides a general framework to deal with the ground-state energy of the electrons in many-atom systems. The basic ideas of DFT are contained in a series of seminal papers of Hohenberg, Kohn, and Sham;[2, 3] these authors showed that the density of particles in the ground-state of a quantum many-body system can be considered as a "basic variable", and that all properties of the system can be considered to be a unique *functional* of the ground-state density (it is important to note that a *function* generates a number from a set of variables; a *functional* produces a number from a function, which in turn depends on variables).

Conceptually, the focus changes in DFT from a many-body Schrödinger Equation 2.1, which involves a many-body wavefunction Ψ, to one that focuses on the single particle density $\rho(r)$, a quantity that is related to Ψ via the following equation:

$$\rho(r) = N \int dr_1 dr_2 \cdots dr_{N-1} |\Psi(r, r_1, r_2, \cdots, r_{N-1})|^2 \tag{2.13}$$

The density ρ in this case is a much simpler quantity than Ψ because it depends on three spatial coordinates (x, y, z) or (r, θ, ϕ). In other words, the numerical complexity of a calculation that uses ρ as the basic variable depends only linearly on the number of grid points that are needed to represent the density ρ. Ultimately this number is expected to increase linearly with system size, thus the computational cost of calculations based on ρ should depend only linearly on system size.

2.1.3.1 The Hohenberg-Kohn theorems

The first Hohenberg-Kohn theorem states that: for any system of interacting particles in an external potential $V_{ext}(r)$, the potential $V_{ext}(r)$ is determined uniquely, except for a constant, by the ground-state particle density $\rho(r)$. To prove this theorem, two different external potentials $V_{ext}(r)$ and $V'_{ext}(r)$, which lead to the same electron density $\rho(r)$ are considered. The two external potentials lead to two different Hamiltonians, H and H', which have different ground-state wavefunctions, Ψ and Ψ', and different ground-state energies, E_0 and E'_0, with $E_0 \neq E'_0$. However, it is hypothesized that both wavefunctions give rise to the same electron density. Since Ψ and Ψ' are different, Ψ' can be used as a trial wavefunction for H, and the virtue of the variational principle, it follows that:

$$E_0 = \langle \Psi | H | \Psi \rangle < \langle \Psi' | H | \Psi' \rangle \tag{2.14}$$

This inequality follows in the case of non-degenerate ground state. The last term in Equation 2.14 can be written as:

$$E_0 < \langle \Psi' | H | \Psi' \rangle = \langle \Psi' \left| H' \right| \Psi' \rangle + \langle \Psi' \left| H - H' \right| \Psi' \rangle \tag{2.15}$$

or, because the two Hamiltonian operators differ only in the external potential:

$$E_0 < E_0' + \int \rho(r)\{V_{ext} - V_{ext}'\}\, dr \tag{2.16}$$

On the other hand if E_0' is considered exactly in the same way, the same equation is found with the unprimed and primed quantities being interchanged:

$$E_0' < E_0 + \int \rho(r)\{V_{ext}' - V_{ext}\}\, dr \tag{2.17}$$

Adding Equations 2.16 and 2.17 yields a contradictory inequality:

$$E_0 + E_0' < E_0' + E_0 \tag{2.18}$$

This establishes the desired result: there cannot be two different external potentials which give rise to the same non-degenerate ground-state charge density.

Since the complete ground-state energy is in principle (as shown above) a functional of the ground-state electron density, so must be its individual components:

$$E_0[\rho_0] = T[\rho_0] + E_{ee}[\rho_0] + E_{Ne}[\rho_0] \tag{2.19}$$

where $T[\rho_0]$ represents the kinetic energy of the system, and $E_{ee}[\rho_0]$ and $E_{Ne}[\rho_0]$ are the electron-electron and nuclear-electron electrostatic interactions, respectively. The sum of the kinetic and electron-electron terms represents the Hohenberg-Kohn functional:

$$F_{HK}[\rho_0] = T[\rho_0] + E_{ee}[\rho_0] \tag{2.20}$$

In this case, if an arbitrary density $\rho(r)$ is given, one can obtain the sum of the kinetic energy and the electron-electron interaction by means of the ground-state wavefunction Ψ and the density $\rho(r)$, that is:

$$F_{HK}[\rho] = T[\rho] + E_{ee}[\rho] = \langle \Psi | T + V_{ee} | \Psi \rangle \tag{2.21}$$

Equation 2.21 is the most important equation in DFT; if $F_{HK}[\rho]$ were known, the Schrödinger equation could be solved exactly.

The second Hohenberg-Kohn theorem states that $F_{HK}[\rho]$, the functional that is used to calculate the ground-state energy of the system, will generate the lowest energy if and only if the input density is the true ground-state density, ρ_0. In the present context, this theorem can be expressed as:

$$E_0 \leq E[\tilde{\rho}] = T[\tilde{\rho}] + E_{Ne}[\tilde{\rho}] + E_{ee}[\tilde{\rho}] \tag{2.22}$$

This means that for any trial density $\tilde{\rho}(r)$ the energy obtained from the functional given in Equation 2.19 represents an upper bound to the true ground-state energy E_0. The proof for this inequality can be demonstrated by means of the variational principle, *i.e.*, any trial density $\tilde{\rho}(r)$ defines its own Hamiltonian and wavefunction, $\widetilde{H}$ and $\widetilde{\Psi}$, respectively. This wavefunction is now used as the trial wavefunction for the Hamiltonian generated from the true external potential V_{ext}. Therefore,

$$\langle \widetilde{\Psi} | H | \widetilde{\Psi} \rangle = T[\tilde{\rho}] + V_{ee}[\tilde{\rho}] + \int \tilde{\rho}\,(r) V_{ext} dr = E[\tilde{\rho}] \geq E_0[\rho_0] = \langle \Psi | H | \Psi \rangle \tag{2.23}$$

which is the desired result for this second theorem.

2.1.3.2 The Kohn-Sham equations

Kohn and Sham proposed that the ground-state density of the original interacting system is equal to that of some chosen non-interacting system. This leads to independent-particle equations for the non-interacting system than can be considered as soluble, if all the difficult many-body terms are incorporated into an *exchange-correlation functional of the density*. For such a system of non-interacting electrons, the kinetic energy is defined as follows:

$$T_S = -\frac{1}{2}\sum_i^N \langle \varphi_i | \nabla^2 | \varphi_i \rangle \tag{2.24}$$

This kinetic energy term forms part of the Hamiltonian operator that does not contain any electron-electron interactions, which writes:

$$H_S = -\frac{1}{2}\sum_i^N \nabla_i^2 + \sum_i^N V_s(r_i) \tag{2.25}$$

where $V_s(r)$ represents an effective local potential. Accordingly, the ground-state wavefunction associated with this Hamiltonian is represented by a Slater determinant:

$$\Theta_S = \frac{1}{\sqrt{N!}}\begin{vmatrix} \varphi_1(x_1) & \varphi_1(x_2) & \cdot & \cdot & \cdot & \varphi_1(x_N) \\ \varphi_2(x_1) & \varphi_2(x_2) & \cdot & \cdot & \cdot & \varphi_2(x_N) \\ \vdots & \vdots & & & & \vdots \\ \cdot & \cdot & & & & \cdot \\ \varphi_N(x_1) & \varphi_N(x_2) & \cdot & \cdot & \cdot & \varphi_N(x_N) \end{vmatrix} \tag{2.26}$$

where the orbitals φ_i are usually termed *Kohn-Sham orbitals*, or KS orbitals. In this case, the non-interacting kinetic energy is not equal to the true kinetic energy of the interacting system. Kohn and Sham accounted for that difference by defining the following functional $F(\rho)$:

$$F[\rho(r)] = T_S[\rho(r)] + J[\rho(r)] + E_{XC}[\rho(r)] \quad (2.27)$$

where $J[\rho(r)]$ represents the classical Coulomb integral of the electron-electron term and $E_{XC}[\rho(r)]$ is the *exchange-correlation energy* defined as:

$$E_{XC}[\rho] = (T[\rho] - T_S[\rho]) + (E_{ee}[\rho] - J[\rho]) = T_C[\rho] + E_{ncl}[\rho] \quad (2.28)$$

The residual part of the true kinetic energy, T_C is simply added to the non-classical electrostatic contributions, E_{ncl}. The exchange-correlation energy E_{XC} is the functional that contains everything that is unknown, *i.e.*, the non-classical effects of self-interaction correction, exchange and correlation, and a portion belonging to the kinetic energy.

Thus, the total energy for the system can be expressed as:

$$E[\rho(r)] = T_S[\rho] + J[\rho] + E_{XC}[\rho] + E_{Ne}[\rho] \quad (2.29)$$

In this expression, the only term for which no explicit form can be given is E_{XC}; if it were known, the exact ground-state energy and density of the many-body electron problem could be found by solving the KS equations for independent particles. If an approximate form for E_{XC} is derived, the KS method provides in this case a practical approach to calculating the ground-state properties of the many-body electron system.

2.1.3.3 Functionals for exchange and correlation

The crucial quantity in the KS approach is the exchange-correlation energy, which is expressed as a functional of the density, $E_{XC}[\rho]$. In practice, approximations are necessary to specify E_{XC}. The first approximation that has been extensively used is the local density approximation (LDA); central to this model is the concept of a hypothetical

uniform electron gas, extensively used to describe metals in the solid-state physics community. In such a system, the electrons move on a positive background charge distribution so that the ensemble is electrically neutral. The exchange-correlation energy, E_{XC} is expressed in the following form:

$$E_{XC}^{LDA}[\rho] = \int \rho(r)\varepsilon_{XC}\big(\rho(r)\big)dr \tag{2.30}$$

where $\varepsilon_{XC}\big(\rho(r)\big)$ represents the exchange-correlation energy per particle of a uniform electron gas of density $\rho(r)$. The unrestricted case can be developed through the incorporation of spin into Equation 2.30; this is known as the local spin-density approximation (LSDA).

Extensions to the purely local approximation have included the consideration of the gradient of the charge density, $\nabla\rho(r)$, in order to account for the non-homogeneity of the true electron density. In other words, the LDA formalism is represented by the first term of a Taylor expansion of the uniform density; a better approximation to the exchange-correlation functional is expected by extending the series with the next lowest term. Functionals that include the gradients of the charge density are known as GGAs (gradient generalized approximations). These functionals represent the current machinery of density functional theory and can be written as:

$$E_{XC}^{GGA}[\rho_\alpha, \rho_\beta] = \int f\big(\rho_\alpha, \rho_\beta, \nabla\rho_\alpha, \nabla\rho_\beta\big)dr \tag{2.31}$$

with α and β indicating the electronic spin. The most popular GGA exchange functional was developed by Becke (B88),[4] and the popular ones for the correlation functional include: Perdew(P86),[5] Perdew and Wang (PW91),[6] and Lee, Yang, and Parr (LYP).[7]

How to improve on current approximations for the exchange and correlation functional is an area of intense research. Many variants of the GGA functional have been proposed, sometimes including empirical fitting. Also, the so-called hybrid functionals that incorporate both HF and DFT energies have been proposed as an alternative to obtain a more accurate expression for the exchange-correlation energy. The derivation of the hybrid functionals can be understood by looking at an equivalent expression for the exchange-correlation energy of the KS scheme as shown in Equation 2.32. The equation describes the non-classical contribution of the electron-electron interactions for different values of λ (where λ represents a coupling constant):

$$E_{XC} = \int_0^1 E_{ncl}^{\lambda} d\lambda \tag{2.32}$$

The $\lambda = 0$ case, $E_{ncl}^{\lambda=0}$, corresponds to exchange only (no correlation) and can be computed exactly, if the KS orbitals are available. In the $\lambda = 1$ case, the non-classical contributions are those of a fully interacting system, containing exchange and correlation contributions. To evaluate the integral exactly, intermediate values of λ are needed. This information is not available, and approximations are required. The simplest way to solve the integrand E_{ncl}^{λ} is to assume that it is a linear function of λ. That is:

$$E_{XC}^{HH} = \frac{1}{2} E_{XC}^{\lambda=0} + \frac{1}{2} E_{XC}^{\lambda=1} \tag{2.33}$$

If one uses the LDA exchange-correlation functional for the second right-hand-side term in Equation 2.33, it represents the *half-and-half* combination of exact exchange and density functional exchange-correlation as introduced by Becke.[8] The next step taken by Becke[9] was to introduce semiempirical coefficients to determine the weight of the various

components of the exchange-correlation energy expression. This description is implemented in the following equation:

$$E_{XC}^{B3} = E_{XC}^{LSDA} + a\left(E_{XC}^{\lambda=0} - E_{X}^{LSDA}\right) + bE_{X}^{B} + cE_{C}^{PW91} \quad (2.34)$$

In this equation, there are three parameters: *a* specifies the amount of exact exchange in the functional, while *b* and *c* control the contributions of exchange and correlation gradient corrections to the local density approximation. In the given equation, Becke's[4] 1988 exchange functional and Perdew and Wang's[6] 1991 correlation functional are employed. These three empirical parameters were chosen such that the atomization and ionization energies as well as the proton affinities included in the G2 data base[10] were optimally reproduced (note that the G2 data base consists of 55 experimentally well-characterized molecules). The values are: *a*=0.20, *b*=0.72, and *c*=0.81. Currently, the most popular hybrid functional is known as B3LYP.[11] While being very similar in nature to the one previously discussed (Equation 2.34), in B3LYP, the PW91 is replaced by the LYP functional. The B3LYP exchange-correlation energy expression is defined as follows (with *a*, *b*, and *c* as indicated above):

$$E_{XC}^{B3LYP} = (1-a)E_{X}^{LSDA} + aE_{XC}^{\lambda=0} + bE_{X}^{B88} + cE_{C}^{LYP} + (1-c)E_{C}^{LSDA} \quad (2.35)$$

2.1.4 Quantum-mechanical methods for the solid state

The quantum-mechanical methods used to model the behavior of solid-state systems are somewhat differ from those used to investigate individual molecules. First, it is important to define the crystalline system. A perfect crystal is constructed by stacking copies of a repeating unit (the unit cell) in a systematic way (according to translational

symmetry elements) without overlapping and without gaps. Therefore, the structure of a crystal can be defined by specifying the size and shape of the unit cell and the positions of the atoms within it. The unit cell is mainly characterized by three lattice vectors a, b, and c and the angles between them. There are fourteen different types of basic unit cells; these are named the *Bravais lattices*. Common Bravais lattices include the simple cubic, body-centered cubic and face-centered cubic lattices. In addition, the unit cell is characterized by the symmetric arrangements of the atoms. The particular combination of the symmetry elements within the crystal defines its *space group*. There are 230 different space groups. If there is symmetry within the unit cell, then it is only necessary to specify the *asymmetric unit*, which represents the unique part of the crystalline structure; the positions of the remaining atoms are then generated using the appropriate symmetry operators.

The foundation for describing the electronic structure of a crystal is the use of the reciprocal lattice, which is the inverse of the real lattice. The reciprocal lattice vectors are defined by:

$$a^* = \frac{2\pi(b \times c)}{a \cdot (b \times c)}; \quad b^* = \frac{2\pi(a \times c)}{b \cdot (a \times c)}; \quad c^* = \frac{2\pi(a \times b)}{c \cdot (a \times b)} \tag{2.36}$$

Note that the denominator in each case is equal to the volume of the unit cell. It is the fact that a^*, b^*, and c^* have units of 1/length that gives rise to the terms "reciprocal space" and "reciprocal lattice". A simple illustrative example of reciprocal space is that of a 2D square lattice where the two vectors a and b are orthogonal and of length equal to the lattice spacing, a. The reciprocal vectors a^* and b^* are directed along the same directions as a and b, respectively, and have a length $1/a$ (see Figure 2.1).

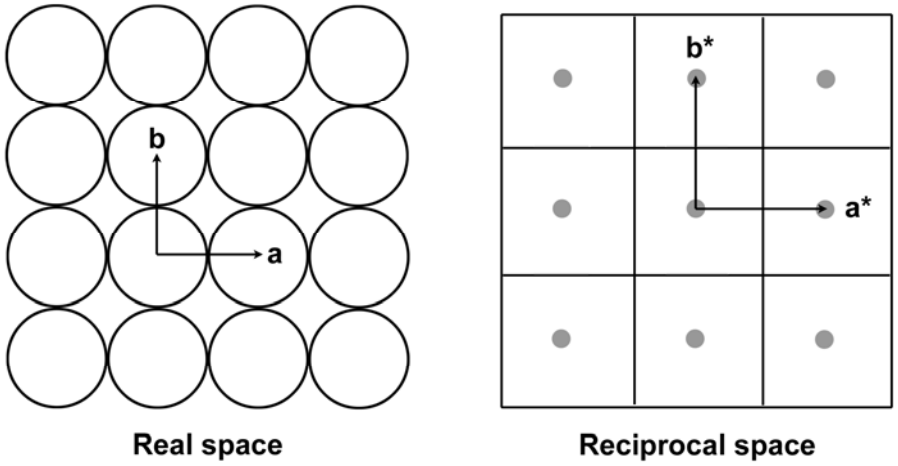

Figure 2.1 Real space arrangements for a 2D square lattice and its corresponding reciprocal space lattice.

Similarly, as in the real-space lattice, where the lattice is constructed from the unit cells, the reciprocal lattice can be constructed form a series of primitive cells, which completely fill the space without any gaps or overlapping. These primitive cells, called *Wigner-Seitz cells*, play the same role in the reciprocal space as does the unit cell in the real-space lattice. In an electronic structure setting, the Wigner-Seitz cell of a reciprocal lattice is more commonly referred to as the *first Brillouin zone* (BZ). The reciprocal lattice vectors that connect all equivalent points in reciprocal space are defined by:

$$G = m_1 a^* + m_2 b^* + m_3 c^*; \quad m_1, m_2, m_3 \text{ are integers} \tag{2.37}$$

2.1.4.1 Band theory of crystals

Solid-state materials have a variety of electronic, chemical and physical properties. Therefore, a variety of methods have been developed to study these materials. One of them is *band theory*. In this method atomic orbitals are combined to give the

equivalent of molecular orbitals, under the assumption that the effect of orbital overlap is to modulate but not change completely the initial atomic levels. In order to describe band theory, a 1D lattice will be considered. The periodicity of the lattice means that the electronic density has to be identical at equivalent points on the lattice. Thus, there must be a relationship between the wavefunction at point x and at an equivalent point elsewhere in the lattice, $x + na$, where n is an integer. For systems with one-dimensional periodicity, the following relationship is observed:

$$|\psi^k(x)|^2 = |\psi^k(x + a)|^2 \tag{2.38}$$

where a is the length of the unit cell in direct space. In this case, *Bloch's theorem* provides the phase relation of the wavefunctions at periodically related points:

$$\psi^k(x + a) = e^{ika}\psi^k(x) \tag{2.39}$$

In this equation, k actually represents the electron wavevector (and is a vector in reciprocal space). By taking into account the Tight-Binding Approximation (TBA), orbitals that are very similar to atomic levels (*i.e.*, wavefunctions that are tightly bound to the atoms, hence the term "tight-binding") can be used as a basis for expanding the crystal wavefunctions. For example, suppose that the s orbitals in a given 1D lattice are labeled by χ_n, where the nth orbital is located at the position $x = na$; then, an acceptable crystal wavefunction that satisfies the Bloch requirement is:

$$\psi^k = \sum_n e^{ika}\chi_n \tag{2.40}$$

2.1.4.1.1 Band structure

Now, it is important to evaluate the form of the crystal wavefunction as it varies with the reciprocal-space vector k. The first scenario corresponds to $k = 0$ (center of the first BZ), where all the exponential terms are equal to 1 and the overall wavefunction becomes a simple additive linear combination of the atomic orbitals:

$$\psi^{k=0} = \sum_n \chi_n = \chi_0 + \chi_1 + \chi_2 + \cdots \tag{2.41}$$

Another situation to consider is when $k = \pi/a$ (edge of the first BZ). The $\exp(ix)$ term can be written as $cos(x) + isin(x)$. When $k = \pi/a$, the sine terms are zero, leaving only the $cos(n\pi)$ terms, which can be expressed more generally as $(-1)^n$. Therefore, the wavefunction is:

$$\psi^{k=\pi/a} = \sum_n (-1)^n \chi_n = \chi_0 - \chi_1 + \chi_2 - \cdots \tag{2.42}$$

The energy varies in a cosine-like manner as shown by Figure 2.2. Wavefunctions for values of $0 \leq k \leq \pi/a$ have energies intermediate between those of the $k = 0$ and $k = \pi/a$ situations.

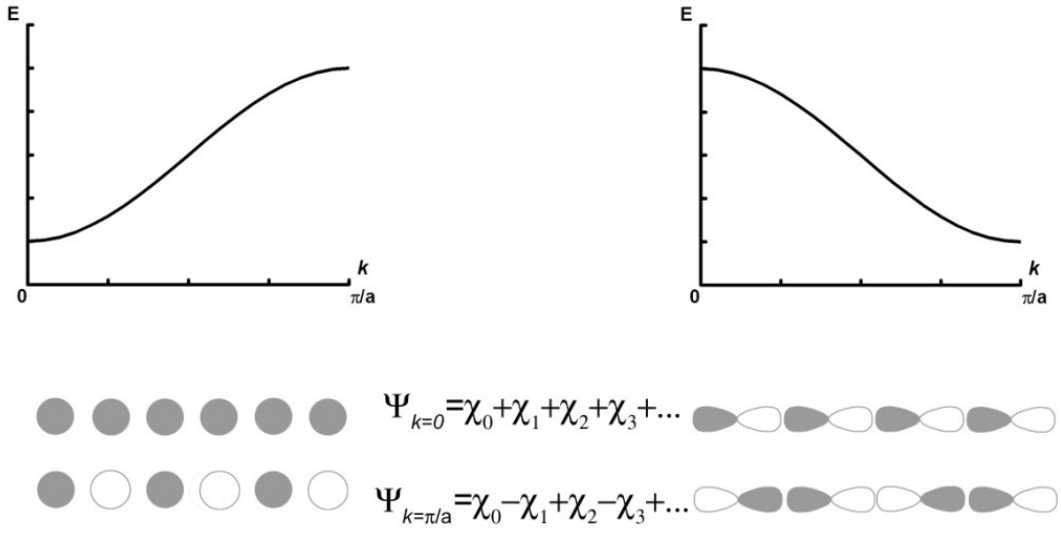

Figure 2.2 Variation of the energy with respect to k for a 1D lattice of s orbitals (left) and p_x orbitals (right). The corresponding arrangement of the orbitals is also shown.

The plot of energy *versus* k is named the *band structure*; the *bandwidth* (W) is the difference in energy between the lowest and highest levels in the band. A very common way to represent the band structure for lattice structures is to plot how the energy evolves as a function of k along certain directions of high symmetry within the first BZ. In such a diagram, Roman or Greek capital letters are used to label specific values of k, which have a particular symmetry. In principle, the calculation needs to be performed for all k vectors in the BZ. However, in practice, a discrete sampling over the BZ is used. Obviously, the denser the set of k vectors, the more accurate the calculation. Various schemes have been suggested for selecting suitable sets of k vectors, which can give excellent approximations to properties like charge density and total electronic energies. Among the different methodologies, the k-sampling method of Monkhorst and Pack is particularly popular.[12]

2.1.4.1.2 Transfer integrals (electronic coupling)

The electronic properties of solid-state materials are in general associated with the study of intermolecular transfer integrals and bandwidths. Within a simple TBA, the total bandwidth (W) results from the interaction of the frontier molecular orbitals (HOMO or LUMO) of all molecules within a molecular crystal. For instance, in the case of an infinite one-dimensional stack of molecules, $W = 4t$, where t represents the transfer integral (electronic coupling).[13, 14] A number of computational methods[15-17] have been developed to estimate the transfer integrals. This parameter can be defined by the matrix element $t = \langle \Psi_i | H | \Psi_j \rangle$, where H is the electronic Hamiltonian of the system and Ψ_i and Ψ_j are the unperturbed HOMOs (LUMOs) of the individual molecular units. Another approach is to use Koopman's theorem (KT),[18] that is to rely on the one-electron approximation. In this context, the absolute value of the transfer integral for electron [hole] transfer can be obtained from the energy difference:

$$t = \frac{\epsilon_{L+1[H]} - \epsilon_{L[H-1]}}{2} \tag{2.43}$$

where $\epsilon_{L[H]}$ and $\epsilon_{L+1[H-1]}$ are the energies of the LUMO and LUMO+1 [HOMO and HOMO-1] levels taken from the closed-shell configurations of the neutral state of a dimer. Figure 2.3 shows an isolated ethylene molecule, and a cofacial ethylene dimer along with their respective HOMO and LUMO electronic splittings. Finally, another useful method to calculate transfer integrals is the band-fitting method which is based on the TBA. In this case, the transfer integrals are obtained by fitting the energy bands to a tight-binding function of the type: $E(k) = E_0 + \sum_{ij} E_{ij} exp\left(-ik \cdot R_{ij}\right)$, which is a k dependent function with several adjacent transfer integrals as band-dependent parameters.

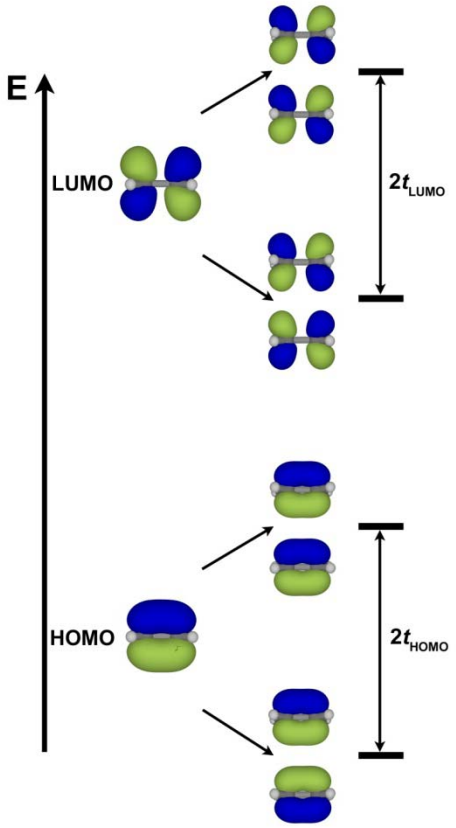

Figure 2.3 Illustration of the electronic splittings between the HOMO/LUMO levels of two ethylene molecules superimposed in a cofacial configuration.

2.1.4.1.3 Density of states

A useful concept in analyzing the band structure of solids is the evolution of density of electronic states as a function of energy. For example, the integral of the density of states up to the Fermi level (energy level of the highest occupied state) is equal to the number of electrons and the integral of the density of states multiplied by the energy is the total electronic energy:

$$N_{electrons} = \int_{-\infty}^{E_F} D(E)dE \tag{2.44}$$

$$E_{tot} = \int D(E)EdE \tag{2.45}$$

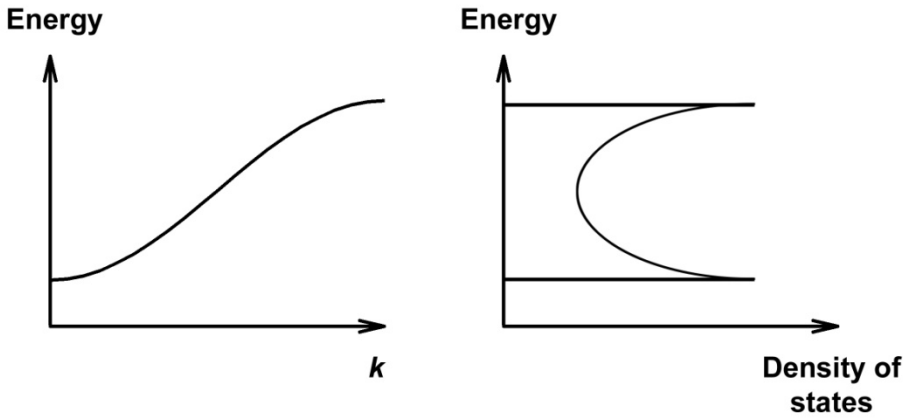

Figure 2.4 Representation of the density of states $D(E)$ for a 1D lattice.

Figure 2.4 shows a 1D situation where the energy varies in cosine-like manner with k, the density of states is greatest at the top and bottom of the band. The density of states is inversely proportional to the slope of the energy *versus* k curve; the flatter the band, the greater the density of states at that particular energy. To some extent, the density of states can be considered as an orbital energy diagram, but it does not provide a well-defined individual energy level description. Nevertheless, it is often possible to determine from which atomic orbitals a particular section of the DOS is mainly derived.

2.1.4.1.4 Effective mass

Another useful concept in analyzing the band structure of solids is the effective mass. The relation between the charge carrier energy, $E(k)$, and the wavevector k is known as the "dispersion relation". Near the minima and maxima in the band structure, this relationship tends to be approximately parabolic, *i.e.*, $E(k) \propto k^2$ (see Equation 1.9). By taking into account Equation 1.9, the second derivative of $E(k)$ with respect to components of the vector k, denoted by k_i and k_j, can be written as follows:

$$\frac{1}{m^*} = \frac{1}{m_{ij}(k)} = \frac{1}{\hbar^2}\frac{\partial^2 E(k)}{\partial k_i \partial k_j} \tag{2.46}$$

This expression indicates that the effective mass m^* is inversely proportional to the curvature of the band, with a steeply curved band having a small mass, hence the reference to heavy or light bands and effective masses. The dimensions of this expression are $1/\text{mass}$. Since the curvature of the bands will be different in different directions, the effective mass represents a second-rank tensor given by:

$$\frac{1}{m^*} = \begin{pmatrix} \frac{\partial^2 E}{\partial k_i^2} & \frac{\partial^2 E}{\partial k_i \partial k_j} & \frac{\partial^2 E}{\partial k_i \partial k_k} \\ \frac{\partial^2 E}{\partial k_j \partial k_i} & \frac{\partial^2 E}{\partial k_j^2} & \frac{\partial^2 E}{\partial k_j \partial k_k} \\ \frac{\partial^2 E}{\partial k_k \partial k_i} & \frac{\partial^2 E}{\partial k_k \partial k_j} & \frac{\partial^2 E}{\partial k_k^2} \end{pmatrix} \tag{2.47}$$

2.2 Lattice dynamics calculations

In all molecular crystals, there are two types of vibrations which can be distinguished: the intramolecular vibrations, also known as internal modes, and the external vibrations (lattice vibrations), where the molecules as a whole oscillate around their equilibrium positions. Usually, only the external vibrations are called phonons. In the case of external vibrations, the molecules (treated as rigid bodies) experience either translational or librational (slow oscillation) motions, or mixed translation-libration oscillations. The frequency, $\omega(k)$, of these vibrations can be represented as a function of wavevector k due to crystal symmetry. The phonon frequencies in organic molecular crystals are typically lower than the energies of the internal modes, and also significantly smaller than the phonon energies in covalently-bonded inorganic crystals such as Si. This is a direct result of both the large masses and the large moments of inertia of the organic molecules. An important consequence of the small frequency value for the phonons in molecular crystals is their thermal excitation: in thermal equilibrium at room temperature, the probability that the phonon states are occupied in organic molecular crystals is larger than in covalently bound inorganic crystals. Therefore, thermally-excited phonons play an important role in describing the interaction of charge carriers in molecular solids. Note that in some instances internal and external modes can mix, making the overall description more complex.

2.2.1 Phonons

Phonons in organic materials are generally described as oscillatory displacements of the molecules from their equilibrium positions in the periodic crystal lattice. In molecular crystals, there exists $6Z$ intermolecular modes and ($3N$-$6Z$) intramolecular modes, where N indicates the number of atoms and Z the number of molecules in the primitive unit cell. Thus, there are 3 translational and 3 rotational degrees of freedom ($6Z$ degrees of freedom) per molecule. Every phonon is characterized by the eigenvector of the displacement of the molecules and its frequency $\omega(k)$.

2.2.1.1 The eigenvector

The eigenvector of the displacement defines the direction of the translation or the direction of the axis of rotation of the molecules. The eigenvectors must obey the symmetry of the crystal. There exist four possible symmetries for the eigenvectors in organic molecular crystals: A_g, B_g, A_u, and B_u. Eigenvectors are of type A if they are self-identical under a C_2 (180° rotation) symmetry operation, and are termed symmetric; those of type B reverse their signs under C_2 and are called antisymmetric (Figure 2.5). Eigenvectors are denoted by an index *g* when they are self-identical under inversion (i), while those with index *u* change their sign under i.

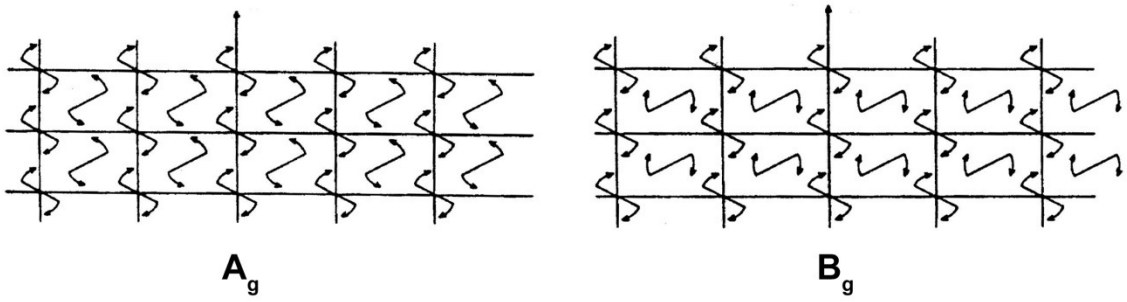

Figure 2.5 Schematic representation of the A_g and B_g phonons. For A_g phonons the axes of rotational symmetry of the two molecules in the unit cell are antiparallel, while for the B_g phonons, they are oriented parallel. (Figure adapted from Reference 19).

2.2.1.2 The frequencies $\omega(k)$

At each point $\omega(k)$ along a dispersion relation curve, all the molecules oscillate with the same frequency ω and with the same amplitude, but with phase differences that are defined by the wavevector k. For example, at the Γ point ($k = 0$), the molecules with the same orientation oscillate in phase in all the unit cells.

2.2.2 Lattice dynamics for phonon calculations

For the formulation of the lattice dynamics in a molecular crystal, only six equations of motion per single molecule are required (if all the molecules in the unit cell are connected by symmetry operations): three for translation and three for rotation. The translational-rotational displacements $u\binom{l}{\kappa}$ of the κth molecule in the lth unit cell are given by propagating plane waves:

$$u\binom{l}{\kappa} = U\binom{l}{\kappa} exp\{i[k \cdot r - \omega(k)t]\} \tag{2.48}$$

where $\omega(k)$ is the frequency of the phonon with wavevector k; u is a vector with six components u_i, and r is the position of the lth unit cell. Here, the u_i terms for i = 1, 2, 3 refer to the translational displacements and for i = 4, 5, 6 refer to the rotational displacements. For the formulation of the equations of motion, the "force constants" are required. They can be derived from the overall lattice energy Φ. Within the harmonic approximation, Φ is given by:

$$\Phi = \frac{1}{2}\sum_{l\kappa\alpha}\sum_{l'\kappa'\beta}\Phi_{\alpha\beta}\binom{ll'}{\kappa\kappa'}u_\alpha\binom{l}{\kappa}u_\beta\binom{l'}{\kappa'} \tag{2.49}$$

where the coefficients $\Phi_{\alpha\beta}\binom{ll'}{\kappa\kappa'}$ represent the force constants, *i.e.*, the second derivative with respect to a displacement of molecule κ or κ' in unit cell l in the Cartesian directions α and β, evaluated at the equilibrium lattice geometry:

$$\Phi_{\alpha\beta}\binom{ll'}{\kappa\kappa'} = \left[\frac{\partial^2\Phi}{\partial u_\alpha\binom{l}{\kappa}\,\partial u_\beta\binom{l'}{\kappa'}}\right]_0 \tag{2.50}$$

With these expressions, the equations of motion for molecule $\binom{l}{\kappa}$ become:

$$M_\kappa\ddot{u}_\alpha\binom{l}{\kappa} = -\sum_{l'\kappa'j}\Phi_{\alpha\beta}\binom{ll'}{\kappa\kappa'}u_\beta\binom{l'}{\kappa'} \tag{2.51}$$

Here, the M_κ term for κ = 1, 2, 3 refers to the masses of the molecules and for κ = 4, 5, 6 to their moments of inertia up on rotation around the principal axes of the inertial tensor.

Writing Equation 2.51 in terms of the proposed solution (Equation 2.48) and simplifying yields:

$$\omega^2(k)w_\alpha(\kappa) = \sum_{\beta\kappa} D_{\alpha\beta}\begin{pmatrix} k \\ \kappa\kappa' \end{pmatrix} w_\beta(\kappa') \tag{2.52}$$

Here, $w_\alpha(\kappa)$ is a reduced displacement, $w_\alpha(\kappa) = \sqrt{M_\kappa}u_\alpha(\kappa)$, and $D_{\alpha\beta}\begin{pmatrix} k \\ \kappa\kappa' \end{pmatrix}$ is the *dynamical matrix*, whose elements are defined as:

$$D_{\alpha\beta}\begin{pmatrix} k \\ \kappa\kappa' \end{pmatrix} = \frac{1}{\sqrt{M_\kappa M_{\kappa'}}} \sum_{l'} \Phi_{\alpha\beta}\begin{pmatrix} 0l' \\ \kappa\kappa' \end{pmatrix} exp\big(ik \cdot r(l')\big) \tag{2.53}$$

Equation 2.52 generates a set of equations that are linear and homogeneous; it follows from a well-known theorem in algebra that, for the equations to be soluble, the determinant formed from the coefficients must vanish:

$$\left| D_{\alpha\beta}\begin{pmatrix} k \\ \kappa\kappa' \end{pmatrix} - \omega^2(k)\delta_{\alpha\beta}\delta_{\kappa\kappa'} \right| = 0 \tag{2.54}$$

Equation 2.54 allows the evaluation of the modes of vibration for a particular molecular crystal, *i.e.*, the eigenvalues of the dynamical matrix are the squares of the phonon frequencies for a particular wavevector.

2.2.3 Optical and acoustic phonon modes

As $|k| \to 0$, the exponential term in Equation 2.53 becomes unity; then the dynamical matrix writes:

$$D_{\alpha\beta}\begin{pmatrix} k = 0 \\ \kappa\kappa' \end{pmatrix} = \frac{1}{\sqrt{M_\kappa M_{\kappa'}}} \sum_{l'} \Phi_{\alpha\beta}\begin{pmatrix} 0l' \\ \kappa\kappa' \end{pmatrix} \tag{2.55}$$

The matrix defined by Equation 2.55 is singular and three of the eigenvalues, ω^2, are zero. These are the *acoustic modes*, which for $k = 0$ correspond to translations of the crystal in the directions $\alpha = x, y, z$ (it is because of their relation to the velocity of the

sound through a crystal that these modes are referred to as acoustic). The remaining $3n-3$ (n, number of molecules in the primitive unit cell) are the *optical modes*, since as $|k| \to 0$, the frequencies are in the optical (infrared) part of the spectrum.

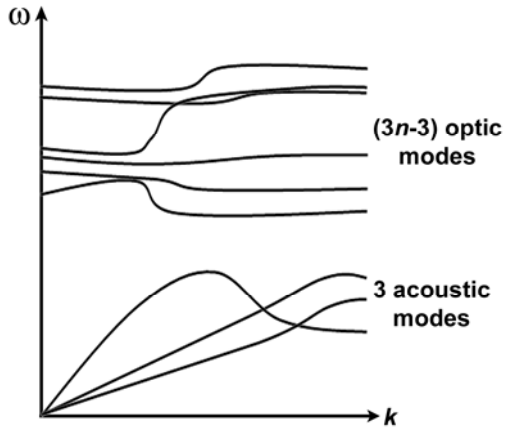

Figure 2.6 Optical and acoustic modes as $|k| \to 0$. (Figure adapted from Reference 20).

Because of the presence of weak intermolecular interactions, calculating the vibrational modes (*i.e.*, determining the phonon frequencies $\omega(k)$ in Equation 2.54) by means of quantum-chemical methods in organic molecular crystals is a rather difficult proposition. The reason is that conventional first-principles methods fail to predict noncovalent interactions adequately.[21, 22] Current investigations on the lattice dynamics of organic molecules are mainly based on force-field methods (also known as molecular mechanics), in which the electronic motions are ignored and the lattice energy term Φ (essential for lattice dynamics calculations) is calculated as a function of the nuclear positions only. In this thesis, lattice dynamics studies were performed at both DFT and empirical force-field levels. For the latter approach, the rigid-body approximation, in which the intramolecular geometries are frozen, was used. In the following section, a

brief description of the force-field method is presented. A particular emphasis is paid to the description of the intermolecular energy terms (*i.e.*, non-bonded interactions), which reproduce the intermolecular interactions in the crystal.

2.2.4 General features of molecular mechanics force fields

In MM methods, the energy of the system is described via a force field, an expression made of a sum of energetic terms involving bonded and non-bonded interactions. Bonded interactions include bond stretching, angle bending, and torsional terms, while the non-bonded interactions contain the van der Waals and electrostatic terms (see Figure 2.7). All of the energetic terms involved in the force field depend on constants that have been derived from experiments or parameterized via quantum-mechanics calculations to reproduce selected features of a set of molecules.[23,24]

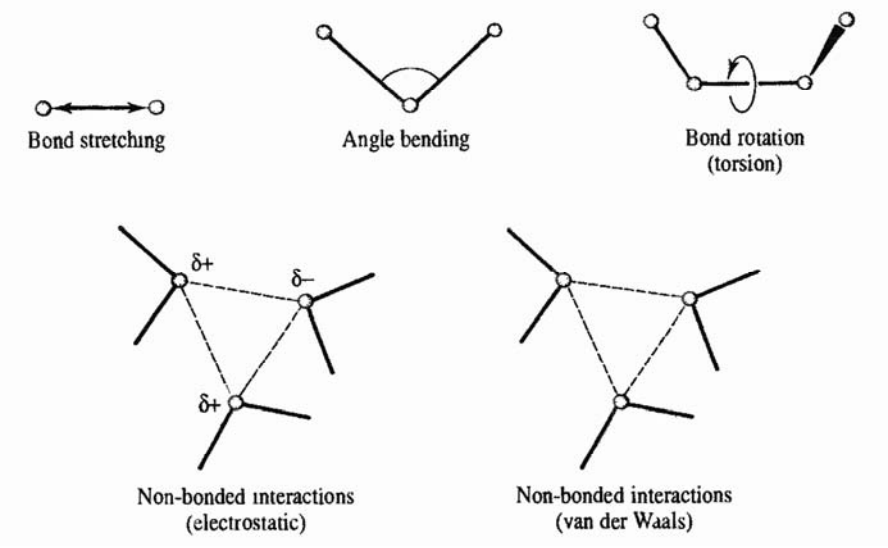

Figure 2.7 Schematic representation of the most important energetic terms of an elementary force field. (Figure adapted from Reference 25).

2.2.4.1 The force field energy

The force field energy is written as a sum of Taylor series expansions for stretches for every pair of bonded atoms, and adds additional potential energy terms coming from bending, torsional energy, van der Waals energy, electrostatics, and cross terms:

$$E = E_{str} + E_{bend} + E_{tors} + E_{vdw} + E_{el} + E_{cross} \tag{2.56}$$

2.2.4.2 Stretch energy

E_{str} is the energy function for stretching a bond between two atom types A and B. The stretching potential for a bond between atoms A and B is given by a Taylor series around an equilibrium bond length, R_0:

$$E_{str}(R^{AB} - R_0^{AB}) = E(0) + \frac{dE}{dR}(R^{AB} - R_0^{AB}) + \frac{1}{2}\frac{d^2E}{dR^2}(R^{AB} - R_0^{AB})^2 \tag{2.57}$$

However, this expansion has an incorrect limiting behavior: at large distances, higher powers of $(R^{AB} - R_0^{AB})$ dominate, leading $E_{str}(R^{AB} - R_0^{AB})$ to go to positive or negative infinity. A function with a correct limiting behavior is the Morse potential:

$$E_{str}(R - R_0) = D\left[1 - e^{-\sqrt{k/2D}(R-R_0)}\right]^2 \tag{2.58}$$

where D is the dissociation energy and k the stretching constant of the bond. This potential shows a very slow convergence in the geometry optimization; therefore the Taylor expression (Equation 2.57) is usually preferred.

2.2.4.3 Bend energy

E_{bend} is the energy required for bending the bond angle formed by three atoms A-B-C, where there is a bond between A and B, and between B and C. Similarly to E_{str}, E_{bend} is usually expanded as a Taylor series around an equilibrium bond angle and terminated at second order, giving the harmonic approximation:

$$E_{bend}(\theta^{ABC} - \theta_0^{ABC}) = k^{ABC}(\theta^{ABC} - \theta_0^{ABC})^2 \tag{2.59}$$

2.2.4.4 Torsional energy

E_{tors} is the energy change associated with rotation around a B-C bond in a four atom sequence A-B-C-D. The torsional angle τ is shown in Figure 2.8. It is the angle between two planes defined by atoms A, B, and C and by B, C, and D. The expression for the torsional energy is not expanded in a Taylor series (as done for the E_{str} and E_{bend}) because τ can go far from equilibrium. Fourier series are used instead:

$$E_{tors}(\tau^{ABCD}) = \sum_{n=1} V_n^{ABCD} cos(n\tau^{ABCD}) \tag{2.60}$$

The $n = 1$ term describes a rotation which is periodic by 360°, the $n = 2$ term is periodic by 180°, the $n = 3$ term is periodic by 120° and so on. The V_n constants determine the size of the barrier for rotation around the B-C bond.

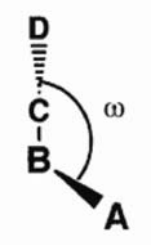

Figure 2.8 Torsional angle definition.

2.2.4.5 Cross terms

The presence of cross terms in a force field reflects coupling between the internal coordinates. The components in E_{cross} are usually written as products of Taylor-like expansions in the individual coordinates. The most important among the cross terms is the stretch/bend term which for an A-B-C sequence may be written as:

$$E_{str/bend} = k^{ABC}(\theta^{ABC} - \theta_0^{ABC})[(R^{AB} - R_0^{AB}) + (R^{BC} - R_0^{BC})] \quad (2.61)$$

Other cross terms might include stretch-stretch, bend-bend, stretch-torsion, bend-torsion, etc. Force fields models vary depending on what cross terms they use.

2.2.4.6 van der Waals energy

E_{vdw} describes the repulsion or attraction between atoms that are not directly bonded. At short range, this interaction is strongly repulsive, while at intermediate range the interaction is attractive. At large interatomic distances E_{vdw} is zero. The attraction part of this potential can be understood in terms of the quantum-mechanical electron correlation effect, in which a fluctuation of the electrons on one atom produces a

temporary dipole that induces a complementary dipole on the other atom. The attractive force associated with this potential is commonly referred to as dispersion or London force. In general, van der Waals energies are computed for atoms which are connected by no less than two atoms. Interactions between closer atoms are already taking into account by the stretching and/or bending terms.

E_{vdw} is very positive at small distances, close to an exponential function, and at intermediate to long ranges, the attraction is proportional to $1/R^6$. One of the models which obey these general requirements is the Lennard-Jones (LJ) potential, which takes the following form between two atoms:

$$E_{LJ}(R) = 4\varepsilon\left[\left(\frac{\sigma}{R}\right)^{12} - \left(\frac{\sigma}{R}\right)^{6}\right] \tag{2.62}$$

The LJ potential contains just two adjustable parameters: the collision diameter σ (the separation for which the energy is zero) and the well depth ε. From electronic structure theory it is known that the repulsion is due to the overlap of the electronic wavefunctions, and that the electron density dies off approximately exponentially with the distance from the nucleus. Therefore the R^{-12} term in the LJ potential can be appropriately replaced by an exponential expression giving rise to a new E_{vdw} function, also known as Buckingham potential:

$$E_{vwd}(R) = A \cdot exp(-BR) - \frac{C}{R^6} \tag{2.63}$$

where A, B, and C are adjustable parameters of the Buckingham potential.

2.2.4.7 Electrostatic energy

Electronegative elements tend to attract charge density, giving rise to an unequal distribution of charge in a molecule. This charge distribution can be represented in a number of ways; one common approach is to represent the charge distribution as an arrangement of fractional point charges throughout the molecule. If the charges are restricted to occupy the nuclear centers, they are referred to as partial atomic charges. The electrostatic interaction between two molecules is then calculated as a sum of interactions between pairs of point charges, and this can be described using Coulomb's law:

$$E_{el}(r_{ij}) = \sum_{i=1}^{N_A} \sum_{j=1}^{N_B} \frac{q_i q_j}{4\pi\varepsilon_0 r_{ij}} \tag{2.64}$$

N_A and N_B are the numbers of point charges in the two molecules. Since the electrostatic potential is an observable quantity that can be determined from a wavefunction, then the objective is to derive the set of partial atomic charges that best reproduces the quantum-mechanical electrostatic potential at a series of points surrounding the molecule. The points i (1, 2,…, N_{points}) where the potential is fitted should be taken from the region where it is most important, that is, the region just beyond the van der Waals radii of the atoms involved. For example, in the CHelpG algorithm[26] (used in this thesis) a cubic grid of points is used and all grid points that lie within the van der Waals radius of any atom are discarded, together with those that lie further than 2.8 Å away from any atom. While the atom-centered charge models present many advantages, they are based on the assumption that the charge density about each atom is spherically symmetrical. However, an atom's valence electrons are often distributed in a manner that is far from spherical,

especially in molecules that contain π electron clouds above aromatic rings. One way to represent such an anisotropy of the molecular charge includes the use of distributed multipoles. In this model, point charges, dipoles, quadrupoles and higher multipoles are distributed through the molecule. The distributed multipoles can be determined in several ways; one of the best-known examples is the distributed multipole analysis (DMA)[27, 28] of the charge density. The DMA method calculates the multipoles from a quantum-mechanics wavefunction defined in terms of Gaussian basis functions.

2.3 Electron-phonon interactions

The origin and physical consequences of electronic and electron-phonon interactions can be easily understood on the basis of the TBA. In this case, the corresponding Hamiltonian writes in second quantization form:[29,30]

$$H_e = \sum_m \epsilon_m a_m^+ a_m + \sum_{mn} t_{mn} a_m^+ a_n \tag{2.65}$$

Here, a_m^+ and a_m are the creation and annihilation operators, respectively, for an electron on lattice site m; ϵ_m is the electron site energy, and t_{mn} the transfer integral. In this case, the site energy and transfer integral are defined by the following equations:

$$\epsilon_m = \langle \varphi_m(r - R_m) | H_e | \varphi_m(r - R_m) \rangle \tag{2.66}$$

$$t_{mn} = \langle \varphi_m(r - R_m) | H_e | \varphi_n(r - R_n) \rangle \tag{2.67}$$

where vector $R_m(R_n)$ represents the position of site $m(n)$. In equations 2.65, 2.66, and 2.67, a single localized molecular orbital has been considered on each site, corresponding to the HOMO or LUMO for hole or electron transport, respectively.

Based on the well-defined sensitiveness of the molecular system to the surrounding environment,[15] the electron-phonon coupling can be defined as the dependence of the system parameters on vibration (phonon) coordinates. That is, any small displacement of the atoms from their equilibrium positions affects the microscopic parameters. In organic molecular crystals, two distinct sources of electron-phonon interactions can be found. First, the site energy ϵ_m is modulated by intramolecular (internal) vibrations, leading to electron-vibration interactions with such modes. The electron-vibration coupling that arises from the overall modulations of the site energy is termed *local* coupling; it is the main interaction present in Holstein's molecular crystal model.[31, 32] The second source of electron-phonon interactions is related to the dependence of the transfer integral, t_{mn}, on the spacing and relative orientations of adjacent molecules. The modulation of the transfer integral by lattice phonons is referred to as the *nonlocal* coupling;[16, 33-35] this constitutes the major interaction in Peierls-type models.[36]

The Hamiltonian that includes the electron-phonon interactions is obtained by expanding ϵ_m and t_{mn} in a power series of phonon coordinates. Therefore, the system Hamiltonian is given by:

$$H = H_e + H_{ph} + H_{e-ph}^{local} + H_{e-ph}^{nonlocal} \tag{2.68}$$

Here, H_{ph} is the Hamiltonian of the phonon subsystem and the electron-phonon interaction $\left(H_{e-ph}\right)$ has been split into local and nonlocal contributions.

Currently, quantum-chemical approaches allow for a very accurate description of some of the main microscopic charge-transport parameters, in particular the intramolecular reorganization energy (see Chapter 3) and the electronic coupling (*vide supra*). However, the analysis has to date been mainly restricted to "frozen" systems, in which there is no coupling to the lattice dynamics. As previously mentioned, a main point of this thesis is the investigation of the coupling between the electronic and (lattice) vibrational degrees of freedom in organic materials. To evaluate the role of such electron-vibration interactions and their impact on charge-transport properties, a combined approach that uses classical molecular dynamics simulations (MDS) and quantum-mechanical calculations of the transfer integrals has been used. The main advantage of MDS is to encompass all vibrational modes of the system instead of few effective modes, as is typically done in phenomenological models.[16, 33] In the following, some basic remarks with respect to the MDS technique are presented to enable the reader to understand how the transfer integrals in organic solids are modulated by classical lattice vibrations. Further reviews on the MDS technique are given by Leach (2001)[25] and Frenkel and Smit (2002).[37]

2.3.1 Molecular dynamics simulations

The essence of MDS is to solve Newton's equations of motion for a set of atoms which are assumed to interact via a model interatomic anharmonic potential. The solutions for the equations of motion involve the use of small discrete steps, with an algorithm to generate the atomic positions and velocities at a given time step from the

positions and velocities of the previous time steps. The MDS method then generates the classical trajectories of the collection of atoms over a period of time that is long enough to be able to analyze the system with an adequate accuracy. Thus, the MDS method consists of the numerical, step by step, solution of Newton's equations of motion, which for a simple atomic system can be written as:

$$\frac{d^2 r_i(t)}{dt^2} = \frac{F_i}{m_i} \qquad F_i = -\frac{\partial V(r_i, \cdots r_N)}{\partial r_i} \tag{2.69}$$

where the force on atom i is denoted by F_i, time is denoted by t, and the mass of the i-th atom is expressed by m_i. MDS requires a calculation of the gradient of the potential energy $V(r)$, which therefore must be a differentiable function of the atomic coordinates r_i. The integration of the left part of Equation 2.69 is performed in small time steps Δt, typically 1-10 fs for molecular systems. Upon the calculation of all the forces between the atoms, Newton's equations of motion can be integrated. Algorithms have been designed for this purpose; one of those is the so-called Verlet algorithm.[38] In this algorithm, the atomic positions r and velocities v are calculated by the following equations:

$$r(t + \Delta t) = 2r(t) - r(t - \Delta t) + \frac{F(t)}{m}\Delta t^2 \tag{2.70}$$

$$v(t) = \frac{r(t + \Delta t) - r(t - \Delta t)}{2\Delta t} \tag{2.71}$$

Although this algorithm might appear to be a simplistic way of integrating the equations of motion, it turns out to give solutions that are sufficiently stable and accurate for routine use. Alternatives to the Verlet algorithm include the Leap-Frog algorithm.[39] This

algorithm evaluates the velocities at half-integer time steps and uses these velocities to compute new positions. The following relationships are used:

$$r(t + \Delta t) = r(t) + \Delta t v\left(t + \frac{\Delta t}{2}\right) \tag{2.72}$$

$$v\left(t + \frac{\Delta t}{2}\right) = v\left(t - \frac{\Delta t}{2}\right) + \Delta t \frac{F(t)}{m} \tag{2.73}$$

Leap-Frog has two advantages over the standard Verlet algorithm: it explicitly includes the velocity and does not require the calculation of differences of large numbers. However, it has the obvious disadvantage that the positions and velocities are not synchronized. This means that it is not possible to calculate the kinetic and potential energy at the same time, and therefore the total energy cannot be computed in the Leap-Frog scheme. Another method is the Beeman's algorithm,[40] which yields the same trajectories as the Verlet algorithm, but provides better estimates of the velocity. The velocities and positions are calculated from:

$$r(t + \Delta t) = r(t) + v(t)\Delta t + \frac{4F(t) - F(t - \Delta t)}{6m}\Delta t^2 \tag{2.74}$$

$$v(t + \Delta t) = v(t) + \frac{2F(t + \Delta t) + 5F(t) - F(t - \Delta t)}{6m}\Delta t \tag{2.75}$$

As a consequence of a more accurate expression for the velocity, the total energy conservation is better described under this approach, in which the kinetic energy is calculated directly from the velocities.

2.3.1.1 Different types of MDS

The MDS technique discussed in the previous section is a scheme for describing the natural time evolution of a classical system of N particles in volume V. In such simulations the total energy E is conserved, and it will generate a microcanonical (constant-*NVE*) ensemble. Many experimental measurements are made under conditions of constant temperature and pressure, and so simulations in the isothermal-isobaric ensemble are most directly relevant to experimental data. Therefore, a brief explanation on how to perform MDS under conditions of constant temperature *NVT* and constant pressure *NVP* is presented below.

2.3.1.1.1 Constant-temperature MDS

The temperature of a system is related to the time average of the kinetic energy by means of the following equation:

$$E_{kin}(t) = \frac{3}{2} N k_B T(t) \tag{2.76}$$

where,

$$T(t) = \frac{1}{3k_B N} \sum_{i=1}^{N} m_i v_i^2 \tag{2.77}$$

A simple way to alter the temperature of the system is thus to scale the velocities. In this case, the velocities are multiplied at each time step by the factor $[T_0/T(t)]^{1/2}$ where $T(t)$ is the temperature calculated from the kinetic energy and T_0 is the desired temperature. An alternative way to maintain the temperature is to couple the system to an external heat

bath that is fixed at the desired temperature.[41] The velocities are scaled at each step, such that the rate of change of temperature is proportional to the difference in temperature between the bath and the system:

$$\frac{dT(t)}{dt} = \frac{1}{\tau}\left(T_{bath} - T(t)\right) \tag{2.78}$$

τ is a coupling parameter whose magnitude determines how tightly the bath and the system are coupled together.

2.3.1.1.2 Constant-pressure MDS

Many of the methods used for pressure control are similar to those used for temperature control. For example, the pressure can be maintained at a constant value by simply scaling the volume. An alternative is to couple the system to a pressure bath, as done before for the temperature bath. The rate of change of pressure is given by:

$$\frac{dP(t)}{dt} = \frac{1}{\tau_P}\left(P_{bath} - P(t)\right) \tag{2.79}$$

τ_P is the coupling constant, P_{bath} is the pressure of the bath and $P(t)$ is the actual pressure at the time t.

2.4 Software

The electronic-structure and atomistic modeling methods discussed throughout the remainder of this dissertation are used as implemented in the following software packages:

2.4.1 Gaussian03

The Gaussian[42] series of electronic structure programs provide the energies, molecular structures, and vibrational frequencies of molecular systems, along with molecular properties derived from these basic computation types. It can be used to study molecules and reactions under a wide range of conditions, including both stable species and compounds which are difficult to observe experimentally such as short-lived intermediates and transition structures.

2.4.2 ADF

The Amsterdam Density Functional (ADF)[43] package is a software for first-principles electronic-structure calculations via DFT. The code uses Slater-type orbital (STO) basis functions and has been parallelized for calculating large chemical systems.

2.4.3 VASP

The Vienna Ab-initio Simulation Package (VASP)[44-46] allows one to perform *ab initio* quantum-mechanical molecular dynamics using pseudopotentials and a plane wave basis set. VASP is based on a finite-temperature, local-density approximation and an exact evaluation of the instantaneous electronic ground-state at each molecular dynamics step using matrix diagonalization schemes and Pulay mixing.[47, 48]

2.4.4 CPMD

CPMD (Car-Parrinello Molecular Dynamics) is a program for *ab initio* molecular dynamics. It uses a density functional method to speed up quantum-chemical computations.[49] Plane waves are used as the basis set for the valence electron wave functions and pseudo-potentials to describe the interaction between the valence electrons and the ionic cores.

2.4.5 CRYSTAL06

The CRYSTAL[50] package performs *ab initio* calculations of the ground-state energy, energy gradient, electronic wave function and properties of periodic systems. Hartree-Fock or Kohn-Sham Hamiltonians can be used. The fundamental approximation includes expanding the single-particle wave functions (crystalline orbitals) as a linear combination of Bloch functions defined in terms of local functions, which are linear combinations of Gaussian-type functions.

2.4.6 TINKER

The TINKER[51] molecular modeling software is a general package for molecular mechanics and dynamics, with some special features for biopolymers. TINKER has the ability to use any of several force fields, such as Amber, CHARMM, Allinger MM, OPLS, Liam Dang's polarizable potentials, and AMOEBA.

2.4.7 DMAREL

DMAREL[52, 53] is a lattice energy minimization program for molecular structures, using a realistic anisotropic atom-atom model for the intermolecular forces, an electrostatic model, along with anisotropic repulsion and simple dispersion models.

2.5 References

(1) Slater, J. C. *Physical Review* **1929**, *34*, 1293.

(2) Hohenberg, P.; Kohn, W. *Physical Review B* **1964**, *136*, B864.

(3) Kohn, W.; Sham, L. J. *Physical Review* **1965**, *140*, 1133.

(4) Becke, A. D. *Physical Review A* **1988**, *38*, 3098.

(5) Perdew, J. P. *Physical Review B* **1986**, *33*, 8822.

(6) Perdew, J. P.; Wang, Y. *Physical Review B* **1992**, *45*, 13244.

(7) Lee, C. T.; Yang, W. T.; Parr, R. G. *Physical Review B* **1988**, *37*, 785.

(8) Becke, A. D. *Journal of Chemical Physics* **1993**, *98*, 1372.

(9) Becke, A. D. *Journal of Chemical Physics* **1993**, *98*, 5648.

(10) Curtiss, L. A.; Raghavachari, K.; Redfern, P. C.; Pople, J. A. *Journal of Chemical Physics* **1997**, *106*, 1063.

(11) Stephens, P. J.; Devlin, F. J.; Chabalowski, C. F.; Frisch, M. J. *Journal of Physical Chemistry* **1994**, *98*, 11623.

(12) Monkhorst, H. J.; Pack, J. D. *Physical Review B* **1976**, *13*, 5188.

(13) Li, X. Y.; Tang, X. S.; He, F. C. *Chemical Physics* **1999**, *248*, 137.

(14) Pati, R.; Karna, S. P. *Journal of Chemical Physics* **2001**, *115*, 1703.

(15) Brédas, J. L.; Beljonne, D.; Coropceanu, V.; Cornil, J. *Chemical Reviews* **2004**, *104*, 4971.

(16) Hannewald, K.; Stojanovic, V. M.; Schellekens, J. M. T.; Bobbert, P. A.; Kresse, G.; Hafner, J. *Physical Review B* **2004**, *69*, 075211.

(17) Troisi, A.; Orlandi, G. *Journal of Physical Chemistry A* **2006**, *110*, 4065.

(18) Koopmans, T. *Physica* **1934**, *1*, 104.

(19) Schwoerer, M.; Wolf, H. C. *Organic molecular solids*; Wiley-VCH: Weinheim, 2007.

(20) Day, G. Lattice Dynamical Studies of Molecular Crystals with Application to Polymorphism and Structure Prediction, University College London, 2003.

(21) Grimme, S. *Journal of Computational Chemistry* **2006**, *27*, 1787.

(22) Podeszwa, R.; Bukowski, R.; Szalewicz, K. *Journal of Physical Chemistry A* **2006**, *110*, 10345.

(23) Bunte, S. W.; Sun, H. *Journal of Physical Chemistry B* **2000**, *104*, 2477.

(24) Sun, H. *Journal of Physical Chemistry B* **1998**, *102*, 7338.

(25) Leach, A. R. *Molecular modelling : principles and applications*, 2nd ed.; Prentice Hall: Harlow, England ; New York, 2001.

(26) Breneman, C. M.; Wiberg, K. B. *Journal of Computational Chemistry* **1990**, *11*, 361.

(27) Stone, A. J. *Chemical Physics Letters* **1981**, *83*, 233.

(28) Stone, A. J.; Alderton, M. *Molecular Physics* **1985**, *56*, 1047.

(29) Pope, M.; Swenberg, C. E.; Pope, M. *Electronic processes in organic crystals and polymers*, 2nd ed.; Oxford University Press: New York, 1999.

(30) Silins, E.; Cápek, V. *Organic molecular crystals : interaction, localization, and transport phenomena*; American Institute of Physics: New York, 1994.

(31) Holstein, T. *Annals of Physics* **1959**, *8*, 325.

(32) Holstein, T. *Annals of Physics* **1959**, *8*, 343.

(33) Hannewald, K.; Stojanovic, V. M.; Bobbert, P. A. *Journal of Physics-Condensed Matter* **2004**, *16*, 2023.

(34) Munn, R. W.; Silbey, R. *Journal of Chemical Physics* **1985**, *83*, 1843.

(35) Munn, R. W.; Silbey, R. *Journal of Chemical Physics* **1985**, *83*, 1854.

(36) Peierls, R. E. *Quantum theory of solids*; Clarendon Press: Oxford, 1955.

(37) Frenkel, D.; Smit, B. *Understanding molecular simulation : from algorithms to applications*, 2nd ed.; Academic: San Diego, Calif. ; London, 2002.

(38) Verlet, L. *Physical Review* **1967**, *159*, 98.

(39) Hockney, R. W.; Eastwood, J. W. *Computer simulation using particles*; McGraw-Hill: New York, 1981.

(40) Beeman, D. *Journal of Computational Physics* **1976**, *20*, 130.

(41) Berendsen, H. J. C.; Postma, J. P. M.; Vangunsteren, W. F.; Dinola, A.; Haak, J. R. *Journal of Chemical Physics* **1984**, *81*, 3684.

(42) Frisch, M. J.; Trucks, G. W.; Schlegel, H. B.; Scuseria, G. E.; Robb, M. A.; Cheeseman, J. R.; Montgomery, J., J. A. ; Vreven, T.; Kudin, K. N.; Burant, J. C.; Millam, J. M.; Iyengar, S. S.; Tomasi, J.; Barone, V.; Mennucci, B.; Cossi, M.; Scalmani, G.; Rega, N.; Petersson, G. A.; Nakatsuji, H.; Hada, M.; Ehara, M.; Toyota, K.; Fukuda, R.; Hasegawa, J.; Ishida, M.; Nakajima, T.; Honda, Y.; Kitao, O.; Nakai, H.; Klene, M.; Li, X.; Knox, J. E.; Hratchian, H. P.; Cross, J. B.; Bakken, V.; Adamo, C.; Jaramillo, J.; Gomperts, R.; Stratmann, R. E.; Yazyev, O.; Austin, A. J.; Cammi, R.; Pomelli, C.; Ochterski, J. W.; Ayala, P. Y.; Morokuma, K.; Voth, G. A.; Salvador, P.; Dannenberg, J. J.; Zakrzewski, V. G.; Dapprich, S.; Daniels, A. D.; Strain, M. C.; Farkas, O.; Malick, D. K.; Rabuck, A. D.; Raghavachari, K.; Foresman, J. B.; Ortiz, J. V.; Cui, Q.; Baboul, A. G.; Clifford, S.; Cioslowski, J.; Stefanov, B. B.; Liu, G.; Liashenko, A.; Piskorz, P.; Komaromi, I.; Martin, R. L.; Fox, D. J.; Keith, T.; Al-Laham, M. A.; Peng, C. Y.; Nanayakkara, A.; Challacombe, M.; Gill, P. M. W.; Johnson, B.; Chen, W.; Wong, M. W.; Gonzalez, C.; Pople, J. A. Gaussian 03, Revision C.02; Gaussian, Inc.: Wallingford, CT, 2004.

(43) Velde, G. T.; Bickelhaupt, F. M.; Baerends, E. J.; Guerra, C. F.; Van Gisbergen, S. J. A.; Snijders, J. G.; Ziegler, T. *Journal of Computational Chemistry* **2001**, *22*, 931.

(44) Kresse, G.; Furthmüller, J. *Comput. Mat. Sci.* **1996**, *6*, 15.

(45) Kresse, G.; Hafner, J. *Phys. Rev. B* **1993**, *47*, 558.

(46) Kresse, G.; Hafner, J. *Phys. Rev. B* **1994**, *49*, 14251.

(47) Pulay, P. *Chemical Physics Letters* **1980**, *73*, 393.

(48) Pulay, P. *Journal of Computational Chemistry* **1982**, *3*, 556.

(49) Car, R.; Parrinello, M. *Physical Review Letters* **1985**, *55*, 2471.

(50) Dovesi, R.; Saunders, V. R.; Roetti, C.; Orlando, R.; Zicovich-Wilson, C. M.; Pascale, F.; Civalleri, B.; Doll, K.; Harrison, N. M.; Bush, I. J.; D'Arco, P.; Llunell, M. CRYSTAL06 User's Manual; University of Torino: Torino, 2006.

(51) Ponder, J. W. TINKER: Software Tools for Molecular Design, 4.2 ed.; Washington University School of Medicine: Saint Louis, MO, 2004.

(52) Price, S. L.; Willock, D. J.; Leslie, M.; Day, G. DMAREL 3.02; University College London: London, 2001.

(53) Willock, D. J.; Price, S. L.; Leslie, M.; Catlow, C. R. A. *Journal of Computational Chemistry* **1995**, *16*, 628.

CHAPTER 3

LOCAL ELECTRON-PHONON COUPLING

In this chapter, the vibrational coupling in the ground and excited states of positively charged naphthalene, anthracene, tetracene, and pentacene molecules is studied. This investigation is based on a joint experimental and theoretical analysis of ionization spectra using high-resolution gas-phase photoelectron spectroscopy and first-principles correlated quantum-mechanical calculations. The discussion starts with the definition of the polaron binding energy, E_{pol}, a parameter that measures the strength of the local vibration coupling (as mentioned in the previous chapter, the local coupling essentially arises from the modulation of the site energy by intramolecular vibrations). This is followed by a brief description of the vibronic coupling in oligoacene cations. In this case, the previously used approach to calculate the vibrational couplings for the radical-cation[1] and the radical-anion[2] ground states in oligoacenes was extended to investigate their vibrational coupling in the radical-cation excited states. Theoretical and experimental results reveal that, while the main contribution to the polaron binding energy in the ground state of oligoacene systems is coming from high-energy vibrations, the excited-state relaxation energies show a significant redistribution towards lower-frequency vibrations. A direct correlation is found between the nature of the vibronic interaction and the pattern of the state electronic structure.

3.1 Introduction

3.1.1 Polaron binding energy

When only the local electron-phonon coupling in Equation 2.68 is used, the standard Holstein-type polaron model is obtained. In this case, the Hamiltonian for a single charge carrier in the lattice can be diagonalized and the resulting energy is given by:

$$E_m = \epsilon_m^{(0)} - \frac{1}{N}\sum_{kj} \hbar\omega_{kj}|g_m(k,j)|^2 + \sum_{kj} \hbar\omega_{kj}\left(n_{kj} + \frac{1}{2}\right) \tag{3.1}$$

where N denotes the total number of unit cells, and $g_m(k,j)$ the corresponding local electron-phonon coupling constant for a phonon of branch j and wavevector k. The electron (hole) is localized on a single lattice site with a stabilization energy known as the polaron binding energy, E_{pol}:

$$E_{pol} = \frac{1}{N}\sum_{kj} \hbar\omega_{kj}|g_m(k,j)|^2 \tag{3.2}$$

The polaron binding energy results from the deformations in molecular and lattice geometries that occur as the carrier localizes on a given site. This quantity is thus closely related to the reorganization energy in electron-transfer theories (*vide infra*). The contribution to the polaron binding energy arising from the internal degrees of freedom can be obtained by expanding the site energy ϵ_m in powers of molecular nomal-mode coordinates, $Q_m(j)$. In the harmonic approximation, it writes:

$$\epsilon_m(Q) = \epsilon_m^{(0)} + \sum_j V_m(j)Q_m(j) + \frac{1}{2}\sum_j M_j\omega_j^2 Q_m^2(j) \tag{3.3}$$

where M_j represents the molecular mass and $V_m(j)$ is defined as follows:

$$V_m(j) = \left(\frac{\partial \epsilon_m}{\partial Q_m(j)}\right)_{Q=0} \tag{3.4}$$

Since ϵ_m is the energy of a frontier molecular orbital, Equation 3.3 represents the adiabatic potential surface of the charged molecule obtained in the one-electron picture. Figure 3.1 shows the potential energy surfaces for electronic states 1 and 2 corresponding to the neutral state and the ground state of the charged molecule; the geometry relaxation energies upon vertical transition from the neutral state to a charged state and vice versa ($\lambda_{rel}^{(1)},\ \lambda_{rel}^{(2)}$) are given by:

$$\lambda_{rel} = \sum_j \lambda_j = \sum_j \frac{V^2(j)}{2M_j\omega_j^2} \tag{3.5}$$

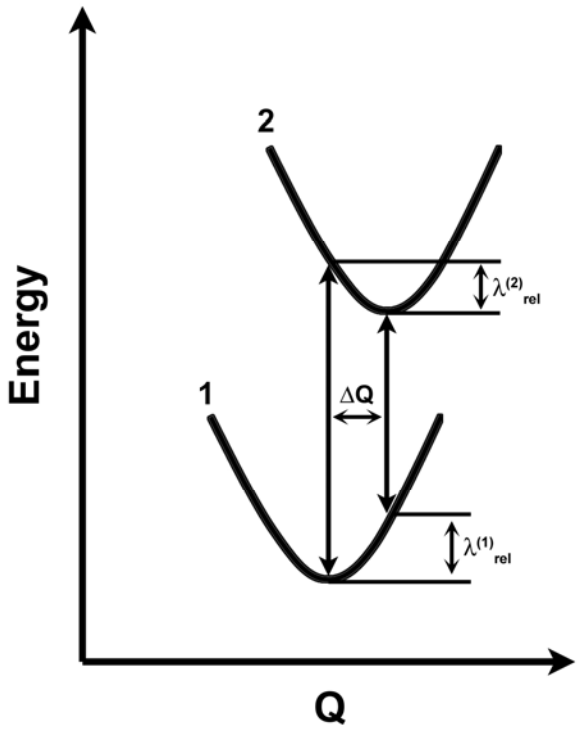

Figure 3.1 Sketch of the potential energy surfaces for the neutral state 1 and charged state 2, showing the vertical transitions, the normal-mode displacement ΔQ, and the relaxation energies $\lambda_{rel}^{(1)}$ and $\lambda_{rel}^{(2)}$.

In this case, $E_{pol} = \lambda_{rel}$, where the intramolecular contribution to E_{pol} is equal to the geometry relaxation upon charging a molecule. As well, it is useful to point out that when the coupling constant $g_m(k,j)$ in Equation 3.2 does not depend on the phonon wavevector k, that is, $g_m(k,j) = g_m(j)$, then $g_m(j)$ or simply $g(j)$ is directly related to the Huang-Rhys factor $S_j = g^2(j)$. This dimensionless factor is commonly used in molecular spectroscopy and electron transfer theory.

In general, the reorganization energy is expressed as the sum of inner and outer contributions. The inner (intramolecular) reorganization energy represents the change in equilibrium geometry of the donor and acceptor sites after the gain or loss of an

electronic charge upon an electron transfer (ET) process. The outer reorganization energy arises from the electronic and nuclear polarization of the surrounding medium. To a good approximation, it is possible to separate the reorganization energy into its inter- and intramolecular contributions in molecular systems due to the weakness of the van der Waals interactions. The intramolecular reorganization energy (λ_{reorg}) associated with an intermolecular ET reaction of the type $M_a^- - M_b \rightarrow M_a - M_b^-$, is given by:

$$\lambda_{reorg} = \lambda_{rel}^{(1)} + \lambda_{rel}^{(2)} \tag{3.6}$$

Thus, within the approximation described above, the polaron binding energy is equal to half the reorganization energy, *i.e.*, $E_{pol} = \lambda_{reorg}/2$.

An alternative approach to calculate the intramolecular reorganization energy and the contribution of vibrational modes to λ_{rel} can be obtained by expanding the potential energies of the neutral and cation states in power series of normal-mode coordinates. Within the harmonic oscillator approach, the relaxation (polaron) energy λ_{rel} is written as follows:

$$E_{pol} = \lambda_{rel} = \sum_j \lambda_j = \sum \frac{M_j \omega_j^2 \Delta Q_j^2}{2} \tag{3.7}$$

$$\lambda_j = \frac{k_j}{2} \Delta Q_j^2, \qquad S_j = \lambda_j / \hbar\omega_j \tag{3.8}$$

where ΔQ_j represents the displacement along normal-mode j between the equilibrium geometries of the neutral and charged molecules. k_j and ω_j are the corresponding force constants and vibrational frequencies; and S_j denotes the Huang-Rhys factor. The λ_j term

is commonly used to estimate the electron-vibration coupling constant of a particular normal-mode. The addition of all coupling constants for a given molecular system represents the so-called vibronic coupling.

3.1.2 Vibronic coupling in oligoacene cations

Oligoacenes play an important role in many areas of chemistry, materials science, and astrophysics. For instance, oligoacene radical-cations are thought to be responsible for interstellar infrared emission features and diffuse interstellar visible absorption bands.[3-8] Oligoacenes are also among the most studied organic materials[9-15] used as active elements in new generations of organic (opto)electronic devices. A detailed understanding of the properties of oligoacenes and their derivatives is thus of interest from both fundamental and practical points of view.

Vibronic coupling represents a key interaction that can control to a large extent many system properties such as the profile of the optical bands, superconductivity, or the efficiency of charge and energy transport.[10] Vibronic coupling in oligoacenes has been previously addressed in several theoretical and experimental studies.[1, 2, 6, 10, 16-34] The relaxation processes in the radical-cation ground state upon positive ionization of anthracene, tetracene, and pentacene have been recently investigated by using an approach that combines high-resolution gas-phase photoelectron (PE) spectroscopy measurements with first-principles quantum-mechanical calculations.[1, 2, 24] In a more recent communication,[21] it was shown that this approach can be applied as well to study

the vibronic interaction in the excited states; up to now, however, these investigations have been limited to naphthalene.

Based on results obtained for naphthalene, anthracene, tetracene, and pentacene, the dependence of the hole-vibrational interaction on the molecular size in both ground and excited states is discussed in this chapter. We also investigate how the amount of "exact" Hartree-Fock exchange (EEX)[23] included in hybrid functionals affects DFT results and the reliability of DFT calculations to reproduce experimental findings.

3.2 Theoretical methodology

Geometry optimizations for the neutral and radical-cation states of naphthalene, anthracene, tetracene, and pentacene were performed, followed by calculation of harmonic vibrational frequencies and normal modes. The calculations were achieved at the DFT level using the 6-31G** basis set, and the BLYP, B3LYP, and BHandHLYP functionals as implemented in the Gaussian 98 program.[35] For the sake of comparison, calculations have been also performed at the Hartree-Fock (HF) level with the same basis set. Spin-unrestricted wave functions were used for the investigation of the radical-cation states. All excited state calculations have been achieved by applying symmetry constraints on the wave functions.

The normal modes $Q_{1(2)}$ were obtained as a linear combination of Cartesian displacements:

$$Q_{1(2)j} = \sum_k L_{1(2)kj}\left(q_{1(2)k} - q^0_{1(2)k}\right) \tag{3.9}$$

Here, the matrix $L_{1(2)}$ connects the $3\,n\,-6$ (n is the number of atoms) normal coordinates with the set of $3n$ mass-weighted Cartesian coordinates $q_{1(2)}$; the vectors $q_1^{(0)}$ and $q_2^{(0)}$ correspond to the stationary points on the adiabatic potential surfaces of states 1 and 2, respectively. Then, the normal-mode displacements $\Delta Q_{1(2)}$ are obtained by projecting the displacements $\Delta q = q_1^{(0)} - q_2^{(0)}$ onto the normal vectors. The Huang-Rhys factors and the total relaxation energy are obtained by using Equations 3.8 and 3.9. It is important to note that the normal modes of the neutral and cation states, Q_1 and Q_2, are in general different and are related by the Duschinsky matrix, J, as:[36]

$$Q_1 = JQ_2 + \Delta Q \tag{3.10}$$

The calculations of the Huang-Rhys factors and Duschinsky matrices have been carried out with the DUSHIN program developed by Reimers.[36] For the present system the Duschinsky mixing is found to be minor, and this effect was neglected in the following analyses.

The simulation of the ionization bands has been performed in the framework of the Born-Oppenheimer and Franck-Condon (FC) approximations.[1] In cases where Duschinsky mixing can be neglected, the relative intensity of a multi-dimensional vibrational transition, involving p vibrational modes, is obtained as a simple product of one-dimensional FC integrals, $FCI(m,n) = \langle \Phi_m(Q) | \Phi_n(Q) \rangle$ (where $\Phi_m(Q)$ and $\Phi_n(Q)$ are the vibrational functions corresponding to the neutral and cation electronic states):

$$I(m_1, n_1, \ldots, m_p, n_p) = \prod_{i=1}^{p} FCI(m_1, n_1)^2 exp\left(\frac{-\hbar m_1 \omega_i}{k_B T}\right) \tag{3.11}$$

$$FCI(m_1, n_1)^2 = exp\{-S\} S^{(n-m)} \frac{m!}{n!} \left[L_m^{(n-m)}(S)\right]^2 \tag{3.12}$$

where m_i and n_i are the initial and final vibrational quantum numbers of mode Q_i, and $L_n^{(m)}$ is a Laguerre polynomial.

3.3 Results and discussion

3.3.1 Photoelectron spectroscopy

The gas-phase photoelectron spectra of naphthalene and anthracene are shown in Figures 3.2 and 3.3, respectively. In general, the spectra are similar to those previously reported;[2, 37-41] however, the use of synchrotron sources allows the individual peaks in the vibrational fine structure to have a better resolution. The first ionization band of both naphthalene and anthracene exhibits a high-frequency progression of about 1500 cm^{-1}, which lies in the region expected for C−C stretching modes. However, in contrast to anthracene, a contribution from a second vibration at about 500 cm^{-1} is also clearly resolved[21] in naphthalene. In addition, as seen from the profile of the third ionization, the interaction with this mode completely dominates the geometrical relaxation of the $^2B_{2g}$ state of naphthalene upon ionization. In striking contrast to the first and third ionization bands, the second PE band in naphthalene is rather structureless. The second ionization of

anthracene, however, exhibits a well-resolved frequency progression of about 750 cm^{-1}. A vibrational structure, although less resolved, is also seen in the third PE band of anthracene.

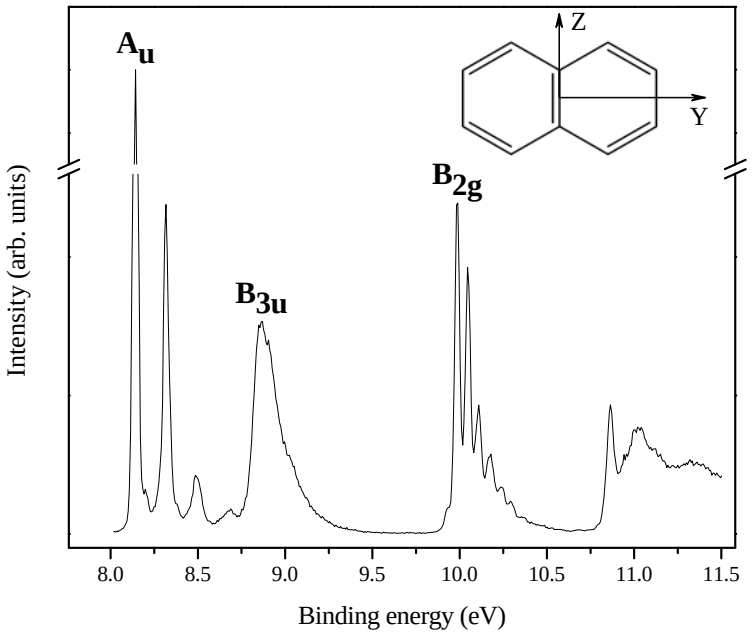

Figure 3.2 Gas-phase photoelectron emission spectrum of naphthalene.[37, 41]

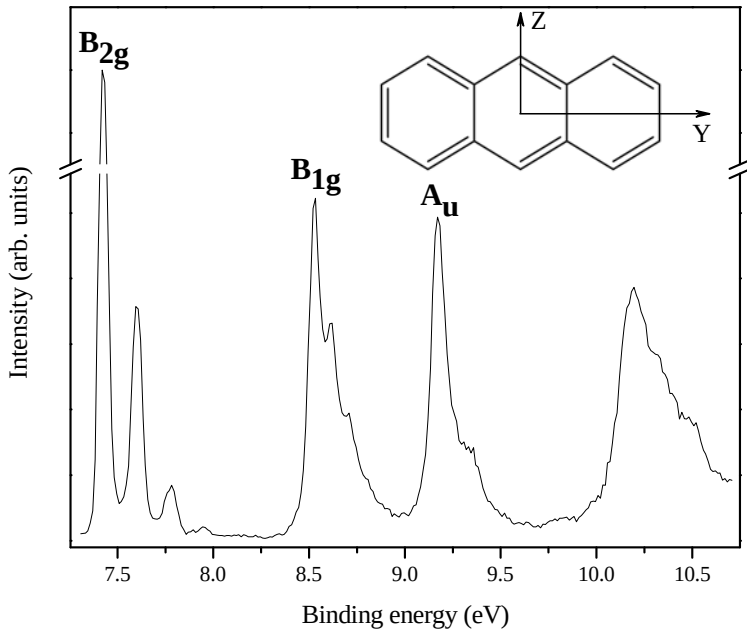

Figure 3.3 Gas-phase photoelectron emission spectrum of anthracene.[2, 38, 41]

3.3.2 Electronic structure

The vertical ionization energies of the first three photoelectron bands obtained within the framework of Koopmans' theorem[42] (KT) and at the ΔSCF (self-consistent field) level are collected in Table 3.1. The KT/HF calculations yield better absolute values for the ionization energies. However, the relative positions of the ionization peaks are better described at the KT/B3LYP level. The B3LYP molecular orbitals (MO) associated with the first three PE bands are shown in Figure 3.4.

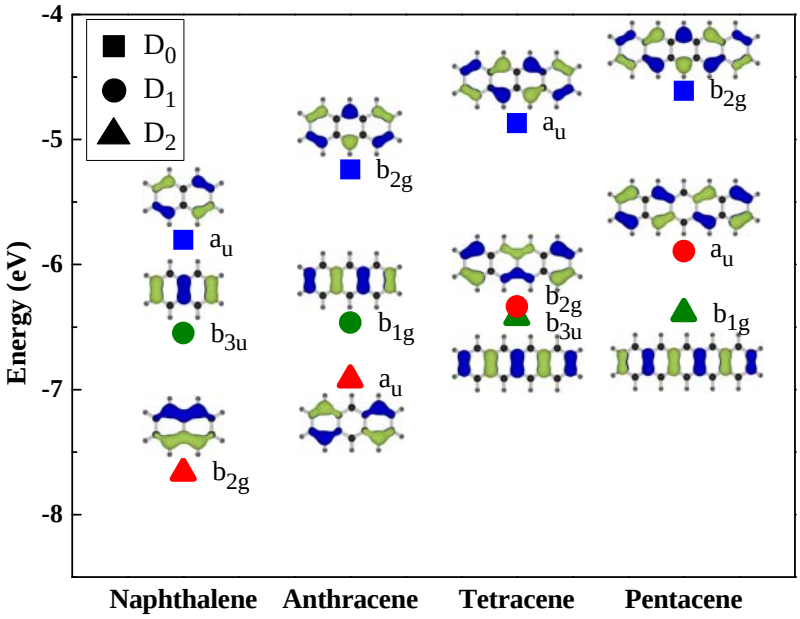

Figure 3.4 Orbital energies (DFT/B3LYP) of the first three frontier occupied MO in naphthalene, anthracene, tetracene and pentacene. The blue, green and red colors are used to group the MOs by their type I, II and III, respectively (see text).

The inspection of Figure 3.4 reveals that the electron density pattern for the highest occupied MO (HOMO) is the same (denoted here as type I) for all four molecules. The electronic structure of the HOMO-1 and HOMO-2 levels with either b_{3u} or b_{1g} symmetry also share a common pattern (type II) along the series. The HOMO-1 and HOMO-2 levels with b_{2g} and a_u symmetries are denoted as a type III. Each group of orbitals, as clearly seen from Figure 3.4, shows a characteristic dependence of their energies on the system size. The second and third ionizations in naphthalene and anthracene, according to the KT calculations, are of type II and type III, respectively; this sequence is inverted in pentacene. The KT results are conflicting for tetracene; while the KT/BLYP and KT/B3LYP calculations yield the $^2B_{2g}$ and $^2B_{3u}$ states (type III and type II) as second and third PE bands, respectively, the KT/BHandLYP and KT/HF calculations give the opposite ordering. At the ΔSCF level, the B3LYP and BHandLYP calculations

give almost identical results for the first ionization. B3LYP, however, better describes the energy spacing between the excited states. In the case of naphthalene, anthracene, and pentacene, all three functionals yield the same ordering of the cation states. For tetracene, however, as in the case of the KT calculations, the situation is less clear: the B3LYP calculations yield the $^2B_{2g}$ and $^2B_{3u}$ sequence for the second and third ionizations while the reverse ordering is obtained at the BHandLYP level. Furthermore, the results of the normal-mode calculations reveal that the optimized geometries of the $^2B_{3u}$ state obtained at both B3LYP and BHandLYP levels correspond to a transition state, which suggests a broken-symmetry effect. In contrast, the BLYP and HF calculations yield a minimum for this state. Further calculations would therefore be needed to shed more light on the ordering of the second and third radical-cation states in tetracene and on the shape of their adiabatic potential surfaces. Finally, the results clearly indicate that ΔSCF/HF calculations, in contrast to DFT calculations, totally fail to describe the PE spectra. This failure is more likely related to large spin contaminations observed in the (unrestricted) HF calculations of the radical-cation states, in particular the excited states.

Table 3.1 First three ionization energies in naphthalene, anthracene, tetracene and pentacene obtained from ΔSCF and KT (between parentheses) calculations. All energies are given in eV.

	BLYP	B3LYP	BHandHLYP	HF	Experiment
Naphthalene					
D_0 (^2A_u)	7.39 (4.89)	7.70 (5.80)	7.68 (6.75)	6.92 (7.81)	8.15[b]
D_1 ($^2B_{3u}$)	8.16 (5.59)	8.46 (6.55)	8.39 (7.53)	7.33 (8.54)	8.87[b]
D_2 ($^2B_{2g}$)	9.11 (6.51)	9.61 (7.66)	9.86 (8.92)	9.49 (10.32)	10.08[b]
Anthracene					
D_0 ($^2B_{2g}$)	6.58 (4.40)	6.89 (5.24)	6.87 (6.08)	6.14 (7.01)	7.42[c]
D_1 ($^2B_{1g}$)	7.78 (5.55)	8.13 (6.46)	8.10 (7.38)	7.03 (8.29)	8.53[c]
D_0 (^2A_u)	8.05 (5.86)	8.59 (6.92)	8.91 (8.06)	8.72 (9.35)	9.17[c]
Tetracene					
D_0 (^2A_u)	6.04 (4.09)	6.34 (4.87)	6.31 (5.63)	5.58 (6.47)	6.94[c]
D_1 ($^2B_{2g}$)	7.28 (5.35)	7.82 (6.34)	8.15 (7.37[a])	8.01 (8.52)[a]	8.30 -8.40[c]
D_2 ($^2B_{3u}$)	7.52 (5.53)	- (6.42)	- (7.29[a])	6.83 (8.13)[a]	8.40 -8.60 [c]
Pentacene					
D_0 ($^2B_{2g}$)	5.65 (3.88)	5.95 (4.61)	5.91 (5.31)	5.18 (6.08)	6.59[c]
D_1 (^2A_u)	6.72 (4.97)	7.23 (5.89)	7.54 (6.84)	7.39[a] (7.88)	7.89[c]
D_2 ($^2B_{1g}$)	7.32 (5.52)	7.74 (6.39)	7.78 (7.23)	6.67[a] (8.03)	8.27[c]

[a]In these results the ordering of D_1 and D_2 states (or/and of the respective MOs) is inversed. [b]Taken from Reference 41. [c]Derived from the data published in Reference 2.

3.3.3 Relaxation energy

The results of the DFT and HF calculations of the relaxation energies in naphthalene, anthracene, tetracene, and pentacene related to the first three PE bands, *i.e.*, the geometry relaxations in the radical-cation states D_0, D_1, and D_2, are reported in Table 3.2 for both the adiabatic potential (AP) surface and normal-mode (NM) approaches. The

partition of the reorganization energy into the contributions of each normal-mode for naphthalene, anthracene, tetracene, and pentacene are given in Tables 3.3-3.6.

Table 3.2 Adiabatic potential surfaces (AP) and normal-mode (NM) estimates of the relaxation energies λ_{rel} (meV) of the cation states D_0, D_1, and D_2 of naphthalene, anthracene, tetracene, and pentacene, related to ionization processes.

	BLYP		B3LYP		BHandHLYP		HF	
	(AP)	(NM)	(AP)	(NM)	(AP)	(NM)	(AP)	(NM)
Naphthalene								
D_0	72	70	91	91	133	130	243	236
D_1	98	92	110	103	127	119	152	141
D_2	126	122	133	128	144	141	168	165
Anthracene								
D_0	50	49	68	68	110	112	222	223
D_1	76	73	88	85	107	102	138	130
D_2	68	67	77	75	91	90	126	125
Tetracene								
D_0	38	37	56	57	97	93	217	211
D_1	49	50	59	59	-	-	132	124
D_2	63	61	-	-	78	77	128	125
Pentacene								
D_0	30	31	48	48	88	90	229	228
D_1	39	38	49	47	66	65	112	110
D_2	53	52	64	63	84	81	134	128

The calculated results are in line with recent findings by Dierkesen and Grimme[23] and indicate that the calculated value of λ_{rel} crucially depends on the amount of EEX included in the hybrid functionals. As seen from Table 3.2, the values of λ_{rel} derived at the DFT level are much smaller than the values obtained at the HF level. The DFT estimates of λ_{rel} increase with the increase in EEX contribution to the hybrid functionals: λ_{rel}(BLYP, 0% EEX) < λ_{rel}(B3LYP, 20% EEX) < λ_{rel}(BHandHLYP, 50% EEX). The results show that the dependence of λ_{rel} on the EEX amount is state dependent. For instance, the ratio λ_{rel}(HF)/ λ_{rel}(BLYP) is at least twice as large for the D_0 state than for the first two excited radical-cations states D_1 and D_2. Moreover, as seen from Table 3.3 and Table 3.4 (see also Figures 3.5 and 3.6 for naphthalene and anthracene, respectively), the contributions of each vibration to λ_{rel} do not scale in the same way for all vibrations when going from one functional to another but are rather mode-dependent.

Table 3.3 DFT and HF estimates of frequencies, ω and relaxation energies, λ_{rel} of the cation states D_0, D_1, and D_2, related to the ionization of naphthalene.

	BLYP		B3LYP		BHandHLYP		HF	
Vibrational Mode	ω (cm^{-1})	λ_{rel} (meV)	ω (cm^{-1})	λ_{rel} (meV)	ω (cm^{-1})	λ_{rel} (meV)	ω (cm^{-1})	λ_{rel} (meV)
				D_0				
1	501	4	515	3	532	3	548	2
2	752	0	777	0	806	0	821	0
3	1039	2	1072	2	1111	2	1143	4
4	1176	3	1207	4	1248	7	1296	14
5	1366	26	1420	40	1478	68	1507	148
6	1465	4	1509	4	1567	4	1627	6
7	1569	31	1635	39	1712	46	1779	61
8	3151	0	3232	0	3331	0	3399	0
				D_1				
1	503	14	517	16	533	19	545	18
2	708	30	734	35	763	41	783	55
3	967	19	998	19	1033	20	1045	27
4	1164	6	1197	7	1239	7	1286	6
5	1362	0	1418	1	1482	1	1526	7
6	1439	5	1482	5	1536	5	1585	2
7	1535	16	1602	20	1681	25	1740	24
8	3150	1	3231	1	3330	1	3399	1
				D_2				
1	492	59	506	61	522	65	535	71
2	748	4	774	4	804	4	826	3
3	1035	0	1067	0	1105	0	1131	0
4	1176	3	1207	3	1248	3	1296	5
5	1410	24	1471	21	1538	16	1587	9
6	1465	0	1510	0	1568	0	1629	0
7	1587	31	1655	39	1738	51	1815	74
8	3153	1	3235	0	3333	0	3403	1

Table 3.4 DFT and HF estimates of frequencies, ω and relaxation energies, λ_{rel} of the cation states D_0, D_1, and D_2, related to the ionization of anthracene.

	BLYP		B3LYP		BHandHLYP		HF	
Vibrational Mode	ω (cm^{-1})	λ_{rel} (meV)	ω (cm^{-1})	λ_{rel} (meV)	ω (cm^{-1})	λ_{rel} (meV)	ω (cm^{-1})	λ_{rel} (meV)
				D_0				
1	385	0	396	0	408	0	416	0
2	612	0	626	0	644	0	661	0
3	741	0	766	0	795	0	813	0
4	1025	0	1057	0	1096	0	1125	1
5	1177	3	1207	4	1245	6	1285	19
6	1254	1	1291	3	1332	7	1352	22
7	1377	16	1426	27	1473	51	1466	111
8	1495	7	1545	9	1607	15	1665	32
9	1546	21	1611	25	1689	32	1756	37
10	3147	0	3228	0	3327	0	3395	0
				D_1				
1	387	7	398	8	411	10	419	7
2	614	2	629	2	648	2	667	3
3	706	32	730	39	759	49	777	66
4	966	12	996	11	1028	11	1023	19
5	1174	3	1206	4	1247	4	1293	3
6	1274	0	1315	0	1362	0	1385	2
7	1390	2	1453	3	1526	7	1566	12
8	1455	3	1499	2	1554	0	1607	1
9	1523	11	1591	14	1673	18	1734	17
10	3147	0	3229	0	3328	0	3396	1
				D_2				
1	383	11	394	11	407	12	417	14
2	617	7	633	8	653	9	674	10
3	746	0	772	0	803	0	828	0
4	1023	1	1055	1	1091	1	1113	1
5	1176	4	1207	4	1247	5	1294	10
6	1251	18	1291	19	1338	20	1369	21
7	1406	0	1465	0	1531	1	1587	7
8	1487	4	1538	6	1601	10	1659	17
9	1551	21	1618	25	1698	31	1771	43
10	3150	0	3232	0	3330	0	3399	1

Table 3.5 DFT and HF estimates of frequencies, ω and relaxation energies, λ_{rel} of the cation states D_0, D_1, and D_2, related to the ionization of tetracene.

	BLYP		B3LYP		BHandHLYP		HF	
Vibrational Mode	ω (cm^{-1})	λ_{rel} (meV)	ω (cm^{-1})	λ_{rel} (meV)	ω (cm^{-1})	λ_{rel} (meV)	ω (cm^{-1})	λ_{rel} (meV)
				D_0				
1	308	0	318	0	327	0	334	0
2	612	0	634	0	649	0	671	0
3	740	0	766	0	795	0	812	0
4	851	0	872	0	914	0	937	3
5	1018	0	1030	1	1087	1	1113	5
6	1172	2	1190	2	1241	7	1279	34
7	1213	4	1235	7	1290	14	1324	36
8	1372	1	1426	9	1467	9	1455	7
9	1388	10	1438	6	1499	30	1535	79
10	1449	0	1492	2	1547	0	1610	0
11	1504	8	1571	5	1621	13	1677	24
12	1532	12	1591	22	1675	18	1745	22
13	3112	0	3174	0	3294	0	3363	0
14	3121	0	3180	0	3302	0	3369	0
15	3144	0	3205	0	3325	0	3392	0
				D_1				
1	306	3	315	3	-	-	334	4
2	603	2	617	2	-	-	661	4
3	745	0	771	0	-	-	780	68
4	839	0	867	0	-	-	894	2
5	1016	0	1048	0	-	-	1014	12
6	1164	1	1196	2	-	-	1284	2
7	1199	0	1232	0	-	-	1320	1
8	1373	14	1425	15	-	-	1544	3
9	1398	0	1453	1	-	-	1557	11
10	1452	2	1496	2	-	-	1575	0
11	1521	22	1578	26	-	-	1677	5
12	1537	4	1604	8	-	-	1732	11
13	3115	0	3197	0	-	-	3372	0
14	3121	0	3204	0	-	-	3378	1
15	3146	0	3228	0	-	-	3393	1
				D_2				
1	309	5	-	-	325	3	331	5
2	609	3	-	-	634	1	642	0
3	711	29	-	-	801	0	824	0
4	819	1	-	-	898	0	913	1
5	965	7	-	-	1084	0	1105	0
6	1167	2	-	-	1235	2	1264	1
7	1211	0	-	-	1273	0	1308	4

8	1379	0	-	-	1480	16	1511	21
9	1391	1	-	-	1518	4	1576	16
10	1437	3	-	-	1554	3	1614	5
11	1493	1	-	-	1646	34	1696	52
12	1516	8	-	-	1686	11	1763	20
13	3118	0	-	-	3296	0	3366	0
14	3125	0	-	-	3303	0	3373	0
15	3145	0	-	-	3327	0	3395	1

Table 3.6 DFT and HF estimates of frequencies, ω and relaxation energies, λ_{rel} of the cation states D_0, D_1, and D_2, related to the ionization of pentacene.

	BLYP		B3LYP		BHandHLYP		HF	
Vibrational Mode	ω (cm^{-1})	λ_{rel} (meV)	ω (cm^{-1})	λ_{rel} (meV)	ω (cm^{-1})	λ_{rel} (meV)	ω (cm^{-1})	λ_{rel} (meV)
				D_0				
1	256	1	263	1	272	1	277	1
2	597	0	613	0	633	0	650	0
3	739	0	764	0	793	0	808	1
4	780	0	807	0	837	1	855	5
5	1015	0	1046	0	1081	1	1099	6
6	1169	1	1200	2	1237	8	1269	56
7	1197	4	1227	7	1266	13	1303	17
8	1297	0	1339	1	1382	2	1385	0
9	1374	0	1425	1	1478	4	1497	0
10	1392	9	1440	18	1493	37	1525	98
11	1470	0	1516	0	1572	1	1626	5
12	1503	11	1560	11	1627	14	1682	27
13	1526	4	1590	7	1668	8	1739	9
14	3119	0	3201	0	3300	0	3368	0
15	3142	0	3224	0	3322	0	3390	0
				D_1				
1	255	1	262	1	270	1	276	2
2	592	0	607	0	626	0	644	0
3	743	0	770	0	800	0	820	0
4	778	0	805	0	835	0	854	1
5	1014	0	1045	0	1079	0	1096	1
6	1167	1	1198	1	1237	1	1280	1
7	1196	0	1228	0	1268	0	1309	2
8	1278	3	1318	4	1363	7	1378	17
9	1391	7	1446	2	1506	1	1558	28
10	1397	2	1452	10	1520	15	1567	0
11	1467	2	1514	2	1573	3	1629	6
12	1519	13	1578	17	1643	21	1690	26
13	1522	9	1586	9	1668	13	1746	24
14	3119	0	3201	0	3302	0	3371	0
15	3145	0	3226	0	3325	0	3392	0
				D_2				
1	257	4	264	6	273	6	277	3
2	595	3	610	3	629	2	645	3
3	713	24	738	31	766	44	781	73
4	753	2	778	2	805	2	808	1
5	969	5	999	4	1031	3	1002	10
6	1165	1	1198	1	1239	1	1280	3
7	1197	0	1229	0	1270	0	1302	2

8	1309	0	1354	0	1406	0	1425	0
9	1380	0	1440	0	1510	1	1543	13
10	1399	2	1456	3	1517	3	1552	2
11	1447	2	1490	2	1544	1	1588	0
12	1484	3	1545	5	1623	10	1685	11
13	1522	4	1588	5	1669	6	1736	6
14	3122	0	3204	0	3305	0	3376	1
15	3144	0	3225	0	3324	0	3391	1

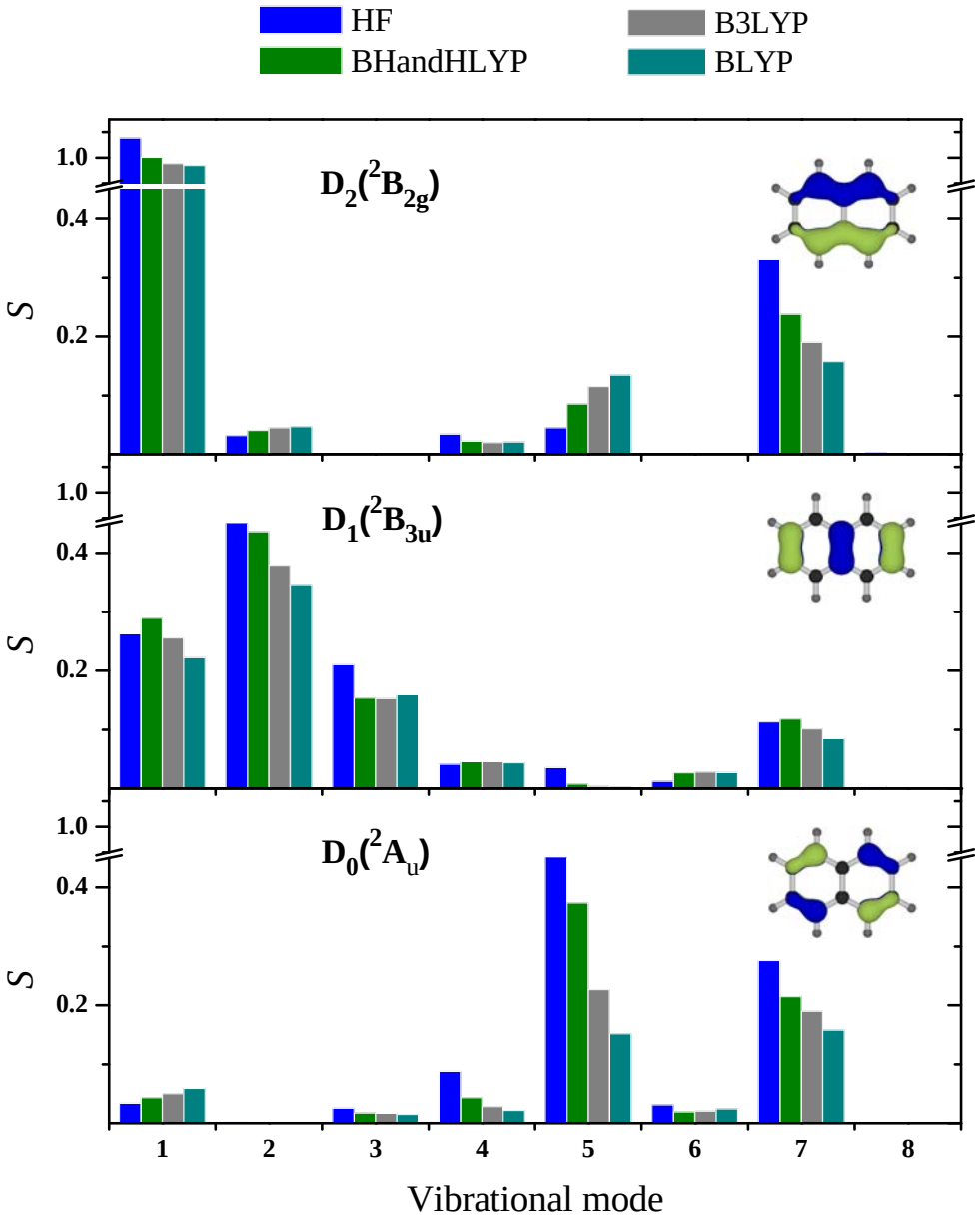

Figure 3.5 HF and DFT estimates of Huang-Rhys factors, *S*, related to the first three ionizations bands (D_0, D_1, and D_2) of naphthalene (see Table 3.3 for the energy of the vibrational modes).

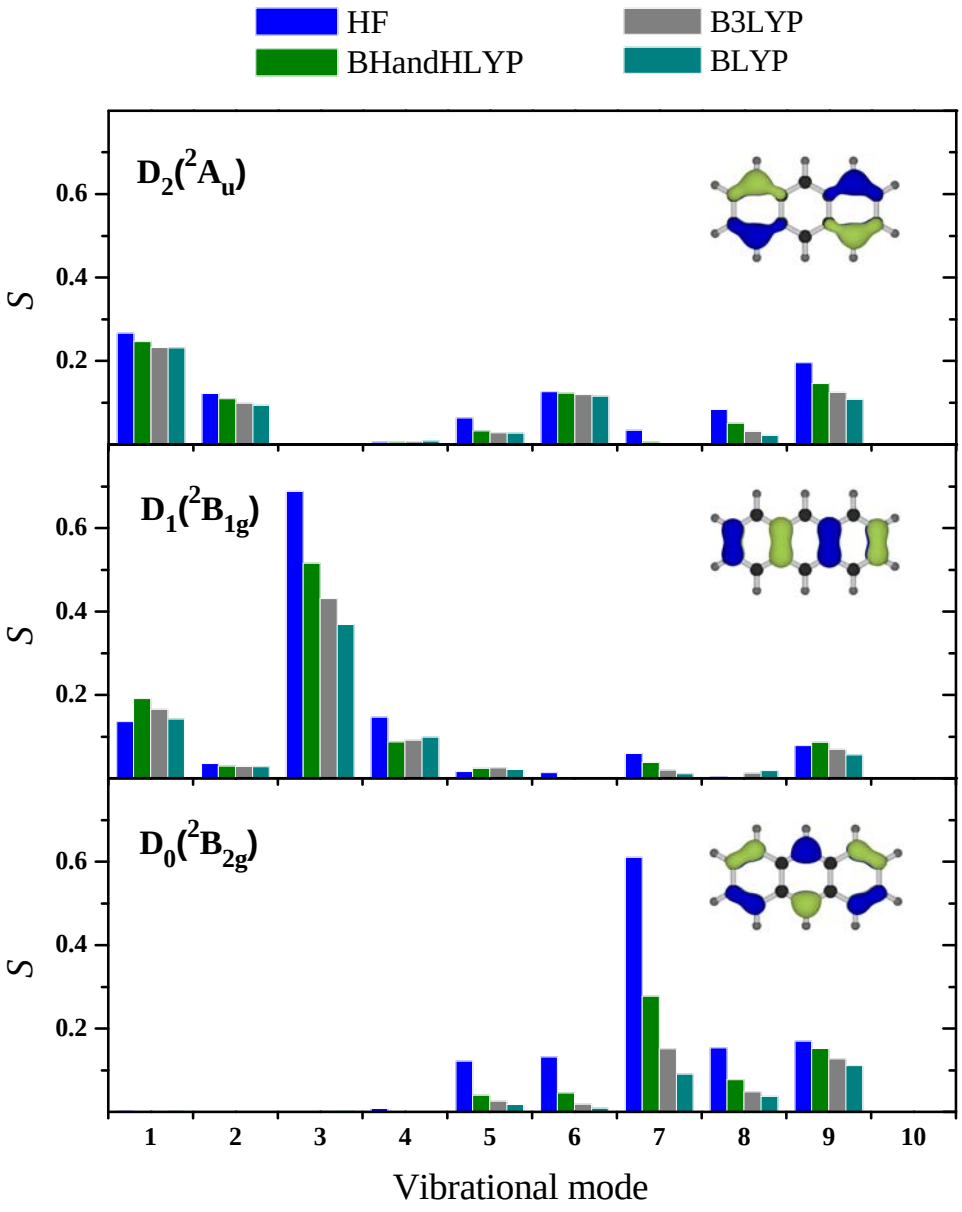

Figure 3.6 HF and DFT estimates of Huang-Rhys factors, *S*, related to the first three ionizations bands (D_0, D_1, and D_2) of anthracene (see Table 3.4 for the energy of the vibrational modes).

The relaxation energies obtained at the HF level and DFT level with different functionals (see Table 3.2) show different dependences as a function of system size. For instance, the BLYP values of λ_{rel} for the D_0 state decreases by over a factor of two when

going from naphthalene to pentacene. The variation of λ_{rel} becomes smaller, however, as the amount of the EEX included in hybrid functionals increases; at the HF level, λ_{rel} is practically independent of molecular size. This trend shown by the HF estimates is clearly in contradiction with the experimental data.[2] The simulations of the PE spectra indicate that the best agreement between theory and experiment is obtained at the B3LYP level. As an illustrative example, Figures 3.7-3.9 show the simulated spectrum for the D_0 D_1 and D_2 states of anthracene using the results derived from HF and DFT methods.

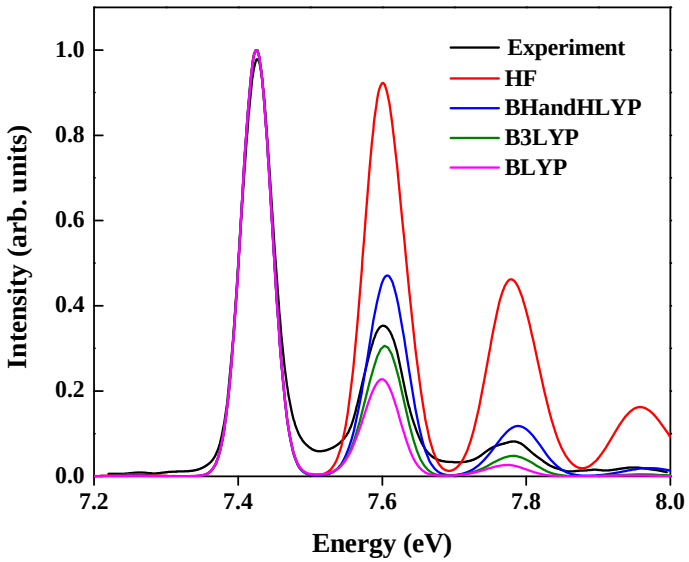

Figure 3.7 DFT and HF simulations of the vibrational structure of the first ionization band of anthracene. In the DFT simulations, the BHandHLYP, B3LYP, and BLYP functionals were used.

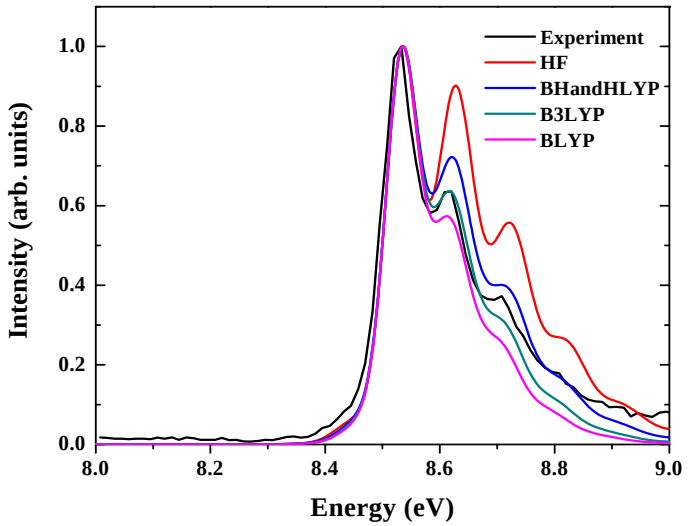

Figure 3.8 DFT and HF simulations of the vibrational structure of the second ionization band of anthracene. In the DFT simulations, the BHandHLYP, B3LYP, and BLYP functionals were used.

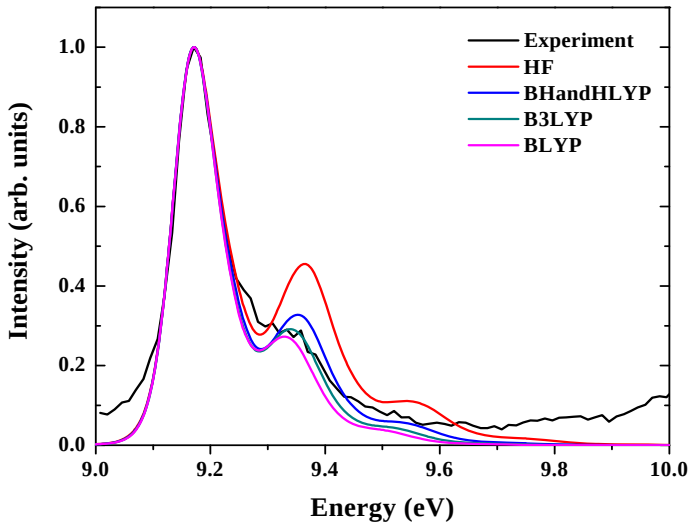

Figure 3.9 DFT and HF simulations of the vibrational structure of the third ionization band of anthracene. In the DFT simulations, the BHandHLYP, B3LYP, and BLYP functionals were used.

As seen from Figure 3.7, DFT/BHandHLYP overestimates the intensity of the high-energy vibrational peaks, meaning that BHandHLYP overestimates the hole-vibration coupling constants (and consequently λ_{rel}); in contrast, BLYP functional underestimates λ_{rel}. The vibrational couplings derived at HF level completely fail to describe the shape of the experimental band. While the results obtained at the B3LYP level reproduce well the shape of the PE band, the intensity of the second peak is also slightly underestimated. These results suggest that an increase of EEX amount could lead to more accurate description of the vibrational couplings. Indeed our calculations indicate that increasing the EEX admixture into the B3LYP functional from 20% to 30% leads to a better agreement between the simulated and the experimental bands (see Figure 3.10). Unfortunately, this modification to the functional does not generally lead to an improved description of the excited states. Therefore, further discussions are limited to the B3LYP results.

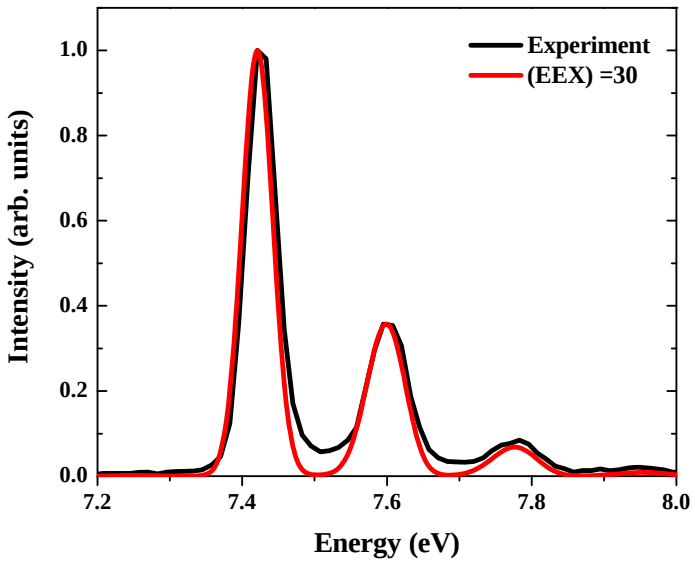

Figure 3.10 DFT/(B3LYP with 30% EEX) simulations of the vibrational structure of the first ionization band of anthracene.

The results of the Frank-Condon simulations of the shape of first three PE bands in naphthalene and anthracene using DFT/B3LYP frequencies and Huang-Rhys factors are shown in Figures 3.11 and 3.12, respectively. In general, the positions and shapes of the peaks are very well reproduced. The overall agreement between the simulated and experimental spectra increases the confidence in the reliability of DFT/B3LYP-derived vibronic constants and relaxation energies. The hole-vibrational coupling constants (Huang-Rhys factors) related to the first three PE bands in naphthalene, anthracene, tetracene, and pentacene are shown in Figures 3.13-3.16, respectively.

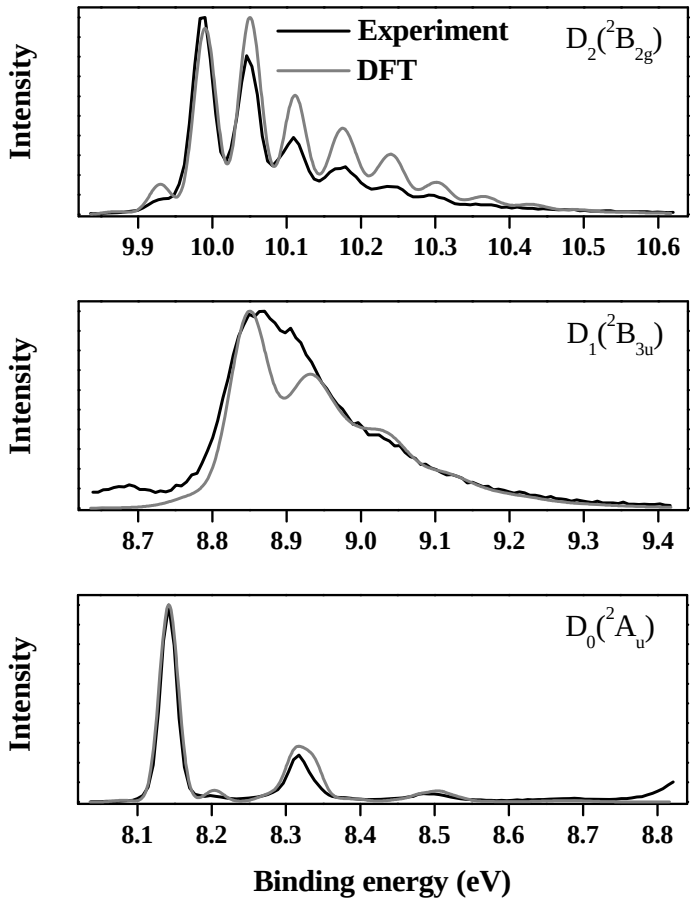

Figure 3.11 DFT/B3LYP simulations of the vibrational structure of the first three PE bands of naphthalene.

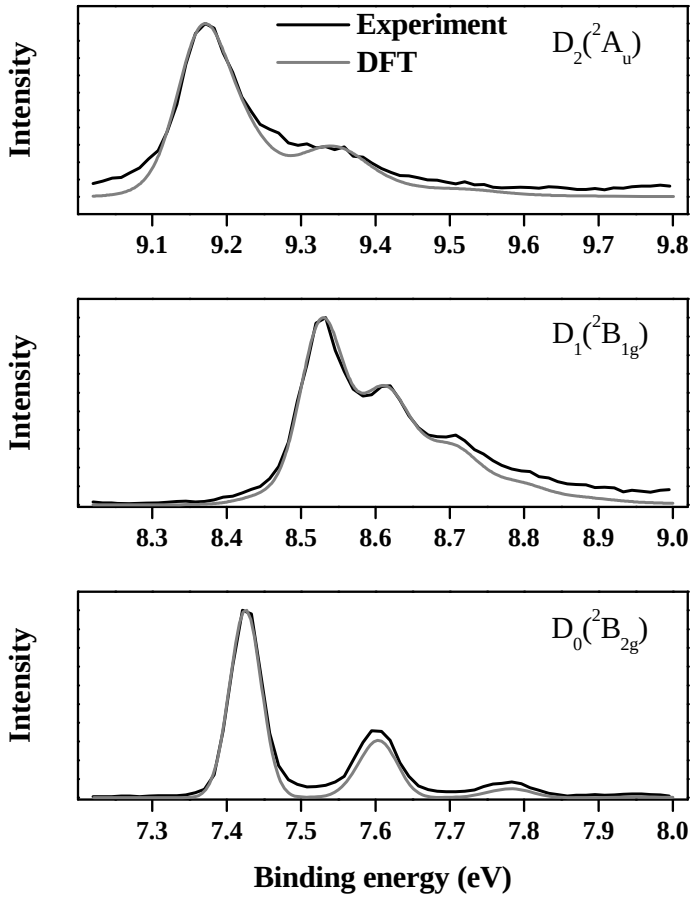

Figure 3.12 DFT/B3LYP simulations of the vibrational structure of the first three PE bands of anthracene.

In the case of D_0 states, the main contribution to the relaxation energy is coming from high-energy vibrations. The calculations and PE data reveal, however, a significant redistribution of the excited-state relaxation energy towards lower-frequency vibrations. In naphthalene, for instance, the contributions of the high-energy modes over 1200 cm^{-1} account for 95% of the relaxation energy of the D_0 state, while in the excited states D_1 and D_2 these vibrations account only for 33% and 50% of λ_{rel}, respectively. Accordingly, the contribution of low-energy modes increases on going from the ground to the second excited radical-cation state. As seen from Figure 3.13, the lowest-energy, totally

symmetric mode at 500 cm^{-1}, in agreement with the experimental observations, is predicted to be particularly active, accounting for about 50% of λ_{rel} in the D_2 state.

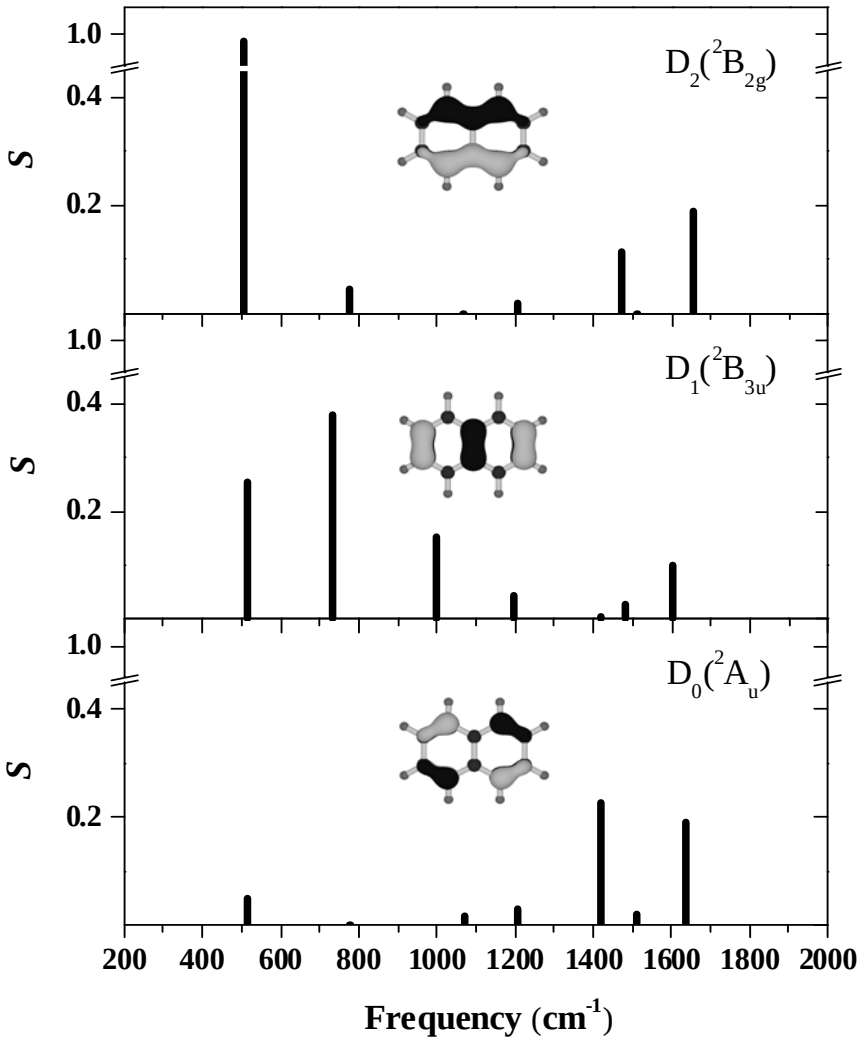

Figure 3.13 DFT/B3LYP estimates of Huang-Rhys factors, S, related to the first three ionizations bands of naphthalene.

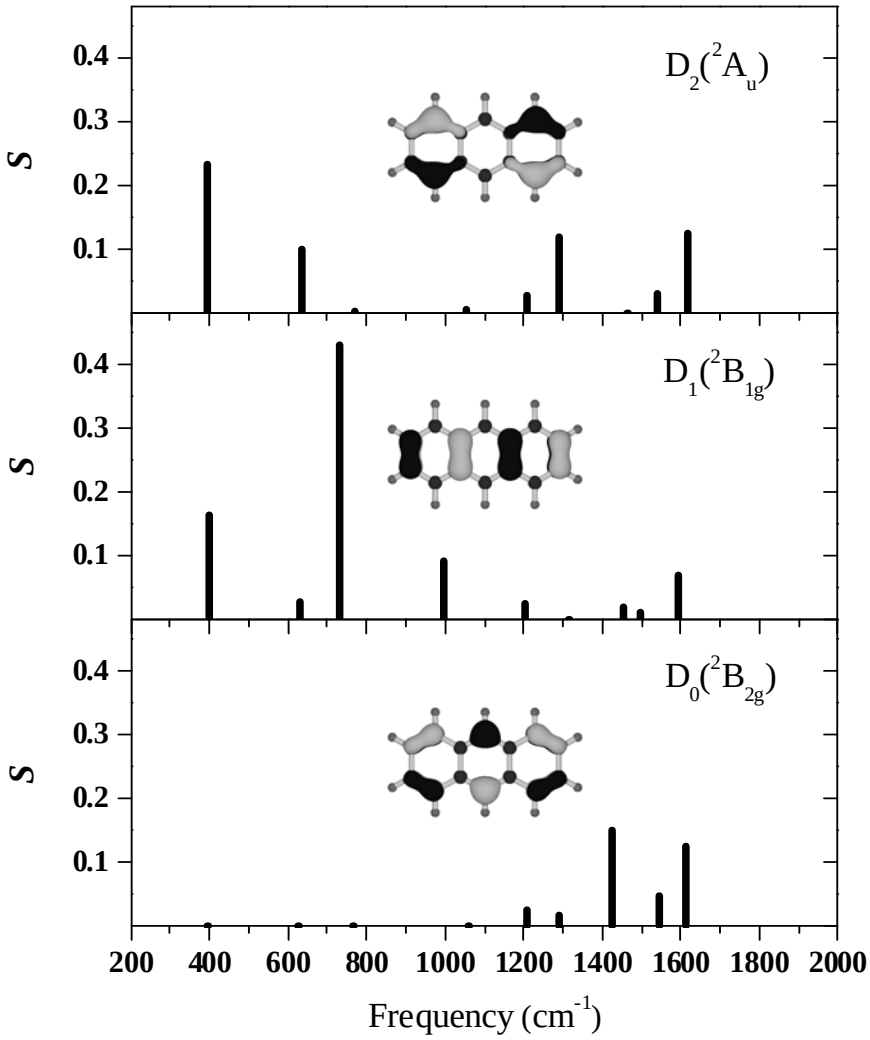

Figure 3.14 DFT/B3LYP estimates of Huang-Rhys factors, *S*, related to the first three ionizations bands of anthracene.

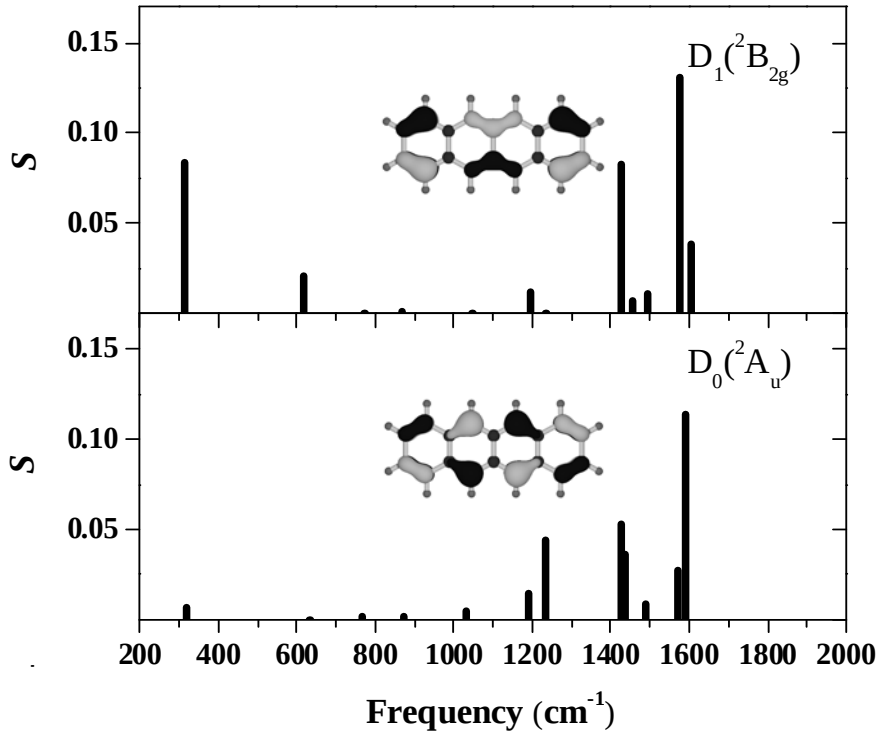

Figure 3.15 DFT/B3LYP estimates of Huang-Rhys factors, *S*, related to the first two ionizations bands of tetracene.

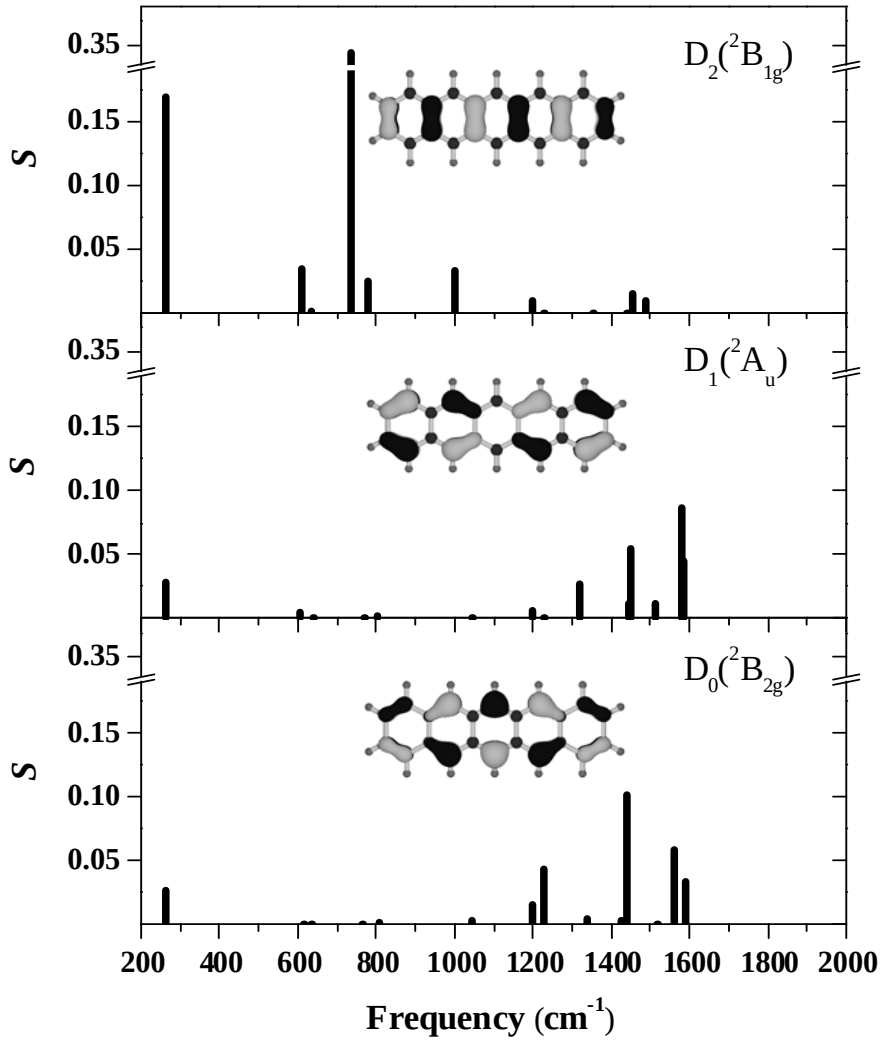

Figure 3.16 DFT/B3LYP estimates of Huang-Rhys factors, *S*, related to the first three ionization bands of pentacene.

The inspection of Figures 3.13-3.16 points to a direct correspondence between the nature of vibronic interaction and (*vide supra*) the electronic-structure pattern of the state. First, as already mentioned, the hole-vibrational interactions related to the first ionization bands (D_0 radical-cation state, *i.e.*, the type-I states) are dominated by high-energy vibrations. As seen from Figure 3.18, λ_{rel} for this group exhibits a linear evolution *versus* the inverse number of carbon atoms. The λ_{rel} of the type-II group of states ($^2B_{3u}$ and $^2B_{1g}$ states) exhibits the same linear dependence. As seen from Figures 3.13-3.16, the main contribution to the vibrational coupling in this group of states arises from a medium-frequency vibration (see Figure 3.17). The energy of this mode and the corresponding Huang-Rhys factor are comparable along the series (ω=734 cm^{-1}, S=0.38 in naphthalene; ω=730 cm^{-1}, S=0.44 in anthracene; ω=738 cm^{-1}, S=0.34 in pentacene). The vibronic interactions in the third set of states (excited $^2B_{2g}$ and ^2A_u states) come from both low-energy and high-energy vibrations; as the size of the system increases, the relative contribution of the low-frequency modes drops drastically. The evolution of the relaxation energy of these states as a function of molecular size therefore differs from the linear dependence observed for the other two sets of states.

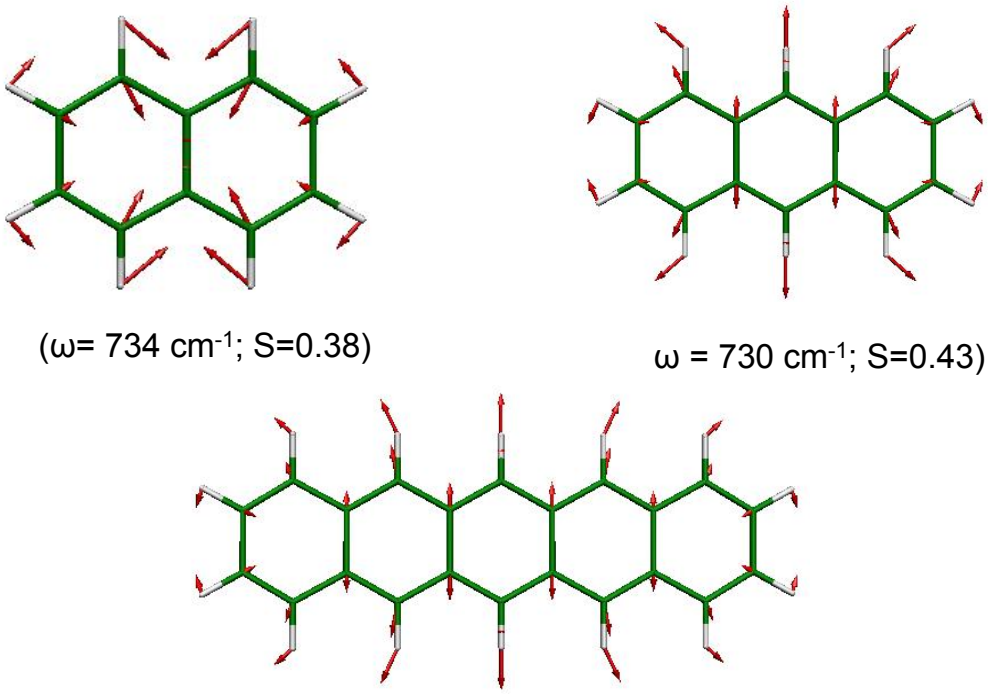

Figure 3.17 Sketch of the normal-mode that yields the largest vibrational coupling for type-II electronic states.

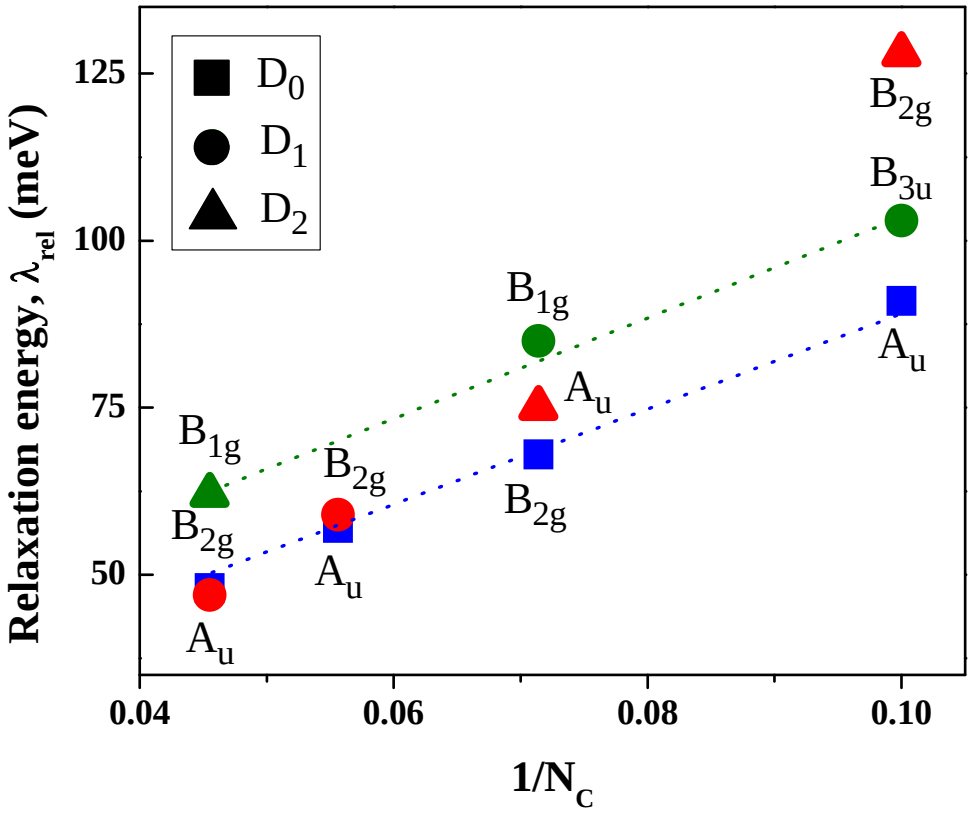

Figure 3.18 DFT/B3LYP estimates of the relaxation energies, λ_{rel}, of the first three cation states D_0, D_1, and D_2 upon ionization *versus* the inverse of the number of carbon atoms in naphthalene, anthracene, tetracene and pentacene. As in Figure 3.4, the blue, green and red colors are used to specify the three groups of states according to their type (I, II and III, respectively).

The pattern of vibronic interactions in a given electronic state can be rationalized in the framework of KT and the concept of orbital vibronic coupling.[43, 44] At the KT level of theory, the relaxation energies of the D_0, D_1, and D_2 radical-cation states are equal to the change in orbital energy of the corresponding frontier MOs (see Figure 3.4), which results from the geometry relaxation taking place after ionization. It is then clear that large variations in orbital energies (and thus large vibronic orbital couplings) result from geometry distortions along those vibrational modes that most strongly perturb the bonding/antibonding interactions within the MO. For instance, the strong vibronic

interactions with the 1420 and 1635 cm^{-1} vibrational modes in the D_0 state of naphthalene can be explained in the following way. A distortion following the 1420 and 1635 cm^{-1} modes (in the opposite direction or in the same direction as in Figure 3.19 for the 1420 and 1635 cm^{-1} modes, respectively) increases all bonding interactions (C_2-C_3, C_4-C_5, C_7-C_8 and C_9-C_{10}) and decreases all antibonding interactions (C_3-C_4 and C_8-C_9) in the HOMO, thus leading to a significant stabilization of the HOMO orbital energy. A distortion along these two high-energy modes also lead to a significant perturbation of the C_8-C_9, C_6-C_1, and C_4-C_3 bonding interactions present in HOMO-1. However, while the distortion along the 1635 cm^{-1} (1602 cm^{-1} in D_1) mode leads to in-phase changes of all three bonding interactions, in the case of the 1420 cm^{-1} (1418 cm^{-1} in D_1) mode, the change in the bonding interaction between the C_6 and C_1 carbons is in opposite phase to those in the C_8-C_9 and C_4-C_3 pairs. As a result, the Huang-Rhys factor for the 1602 cm^{-1} mode in the D_1 state (see Figure 3.13) is significantly larger than that of the 1418 cm^{-1} mode. Both high-frequency modes are also significantly coupled to the HOMO-2; this is in particular due to the strong impact of these modes on the antibonding interaction between the C_6 and C_1 atoms. As seen from Figures 3.4 and 3.19, the 515 and 777 cm^{-1} modes do not interact with the HOMO; however, there is a strong coupling between the mode at 777 cm^{-1} (734 cm^{-1} in D_1) and HOMO-1, and the mode at 515 cm^{-1} (506 cm^{-1} in D_2) and HOMO-2. The patterns of vibronic interactions in anthracene, tetracene, and pentacene can be rationalized in the same way.

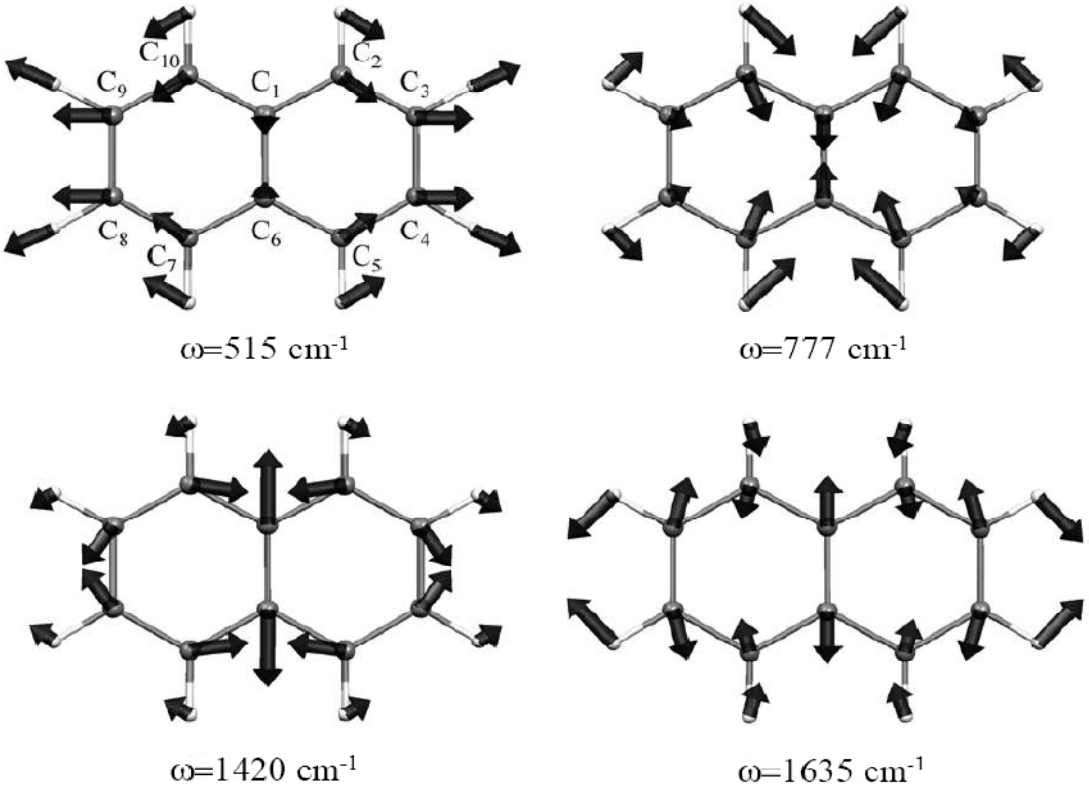

Figure 3.19 Sketch of the normal modes that yield the largest vibrational couplings in naphthalene.

3.4 Conclusions

The structural relaxations in the ground and excited states of naphthalene, anthracene, tetracene, and pentacene that appear after ionization have been investigated. The photoelectron measurements and DFT calculations show that there is a direct dependence between the nature of the vibronic interaction and the pattern of the electronic structure. The results reveal that while in the case of ground cation states the main contribution to relaxation energy is coming from high-energy vibrations, the excited-state relaxation energies show a significant redistribution towards lower-frequency vibrations.

Also, we have evaluated how the amount of "exact" Hartree-Fock exchange included in the hybrid functionals affect the DFT results. It was shown that, among the standard functionals, B3LYP provides the best description of geometry modifications upon ionization in oligoacenes for both ground and excided states.

3.5 References

(1) Malagoli, M.; Coropceanu, V.; da Silva Filho, D. A.; Brédas, J. L. *Journal of Chemical Physics* **2004**, *120*, 7490.

(2) Coropceanu, V.; Malagoli, M.; da Silva Filho, D. A.; Gruhn, N. E.; Bill, T. G.; Brédas, J. L. *Physical Review Letters* **2002**, *89*, 275503.

(3) Biennier, L.; Salama, F.; Allamandola, L. J.; Scherer, J. J. *Journal of Chemical Physics* **2003**, *118*, 7863.

(4) Hudgins, D. M.; Allamandola, L. J. *Journal of Physical Chemistry* **1995**, *99*, 8978.

(5) Le Page, V.; Keheyan, Y.; Snow, T. P.; Bierbaum, V. M. *Journal of the American Chemical Society* **1999**, *121*, 9435.

(6) Salama, F.; Allamandola, L. J. *Journal of Chemical Physics* **1991**, *94*, 6964.

(7) Sukhorukov, O.; Staicu, A.; Diegel, E.; Rouille, G.; Henning, T.; Huisken, F. *Chemical Physics Letters* **2004**, *386*, 259.

(8) Zhao, L.; Lian, R.; Shkrob, I. A.; Crowell, R. A.; Pommeret, S.; Chronister, E. L.; Liu, A. D.; Trifunac, A. D. *Journal of Physical Chemistry A* **2004**, *108*, 25.

(9) Bendikov, M.; Wudl, F.; Perepichka, D. F. *Chemical Reviews* **2004**, *104*, 4891.

(10) Brédas, J. L.; Beljonne, D.; Coropceanu, V.; Cornil, J. *Chemical Reviews* **2004**, *104*, 4971.

(11) Deng, W. Q.; Goddard, W. A. *Journal of Physical Chemistry B* **2004**, *108*, 8614.

(12) Katz, H. E.; Bao, Z. N.; Gilat, S. L. *Accounts of Chemical Research* **2001**, *34*, 359.

(13) Payne, M. M.; Parkin, S. R.; Anthony, J. E. *Journal of the American Chemical Society* **2005**, *127*, 8028.

(14) Payne, M. M.; Parkin, S. R.; Anthony, J. E.; Kuo, C.-C.; Jackson, T. N. *Journal of the American Chemical Society* **2005**, *127*, 4986.

(15) Troisi, A.; Orlandi, G. *Journal of Physical Chemistry B* **2005**, *109*, 1849.

(16) Andrews, L.; Friedman, R. S.; Kelsall, B. J. *Journal of Physical Chemistry* **1985**, *89*, 4016.

(17) Andrews, L.; Kelsall, B. J.; Blankenship, T. A. *Journal of Physical Chemistry* **1982**, *86*, 2916.

(18) Andruniow, T.; Pawlikowski, M. *Chemical Physics* **1998**, *236*, 35.

(19) Andruniow, T.; Pawlikowski, M. *Chemical Physics* **1998**, *236*, 25.

(20) Cockett, M. C. R.; Ozeki, H.; Okuyama, K.; Kimura, K. *Journal of Chemical Physics* **1993**, *98*, 7763.

(21) da Silva Filho, D. A.; Friedlein, R.; Coropceanu, V.; Öhrwall, G.; Osikowicz, W.; Suess, C.; Sorensen, S. L.; Svensson, S.; Salaneck, W. R.; Brédas, J. L. *Chemical Communications* **2004**, 1702.

(22) Dierksen, M.; Grimme, S. *Journal of Chemical Physics* **2004**, *120*, 3544.

(23) Dierksen, M.; Grimme, S. *Journal of Physical Chemistry A* **2004**, *108*, 10225.

(24) Gruhn, N. E.; da Silva Filho, D. A.; Bill, T. G.; Malagoli, M.; Coropceanu, V.; Kahn, A.; Brédas, J. L. *Journal of the American Chemical Society* **2002**, *124*, 7918.

(25) Kato, T.; Kondo, M.; Yoshizawa, K.; Yamabe, T. *Synthetic Metals* **2002**, *126*, 75.

(26) Kato, T.; Yamabe, T. *Journal of Chemical Physics* **2001**, *115*, 8592.

(27) Kato, T.; Yoshizawa, K.; Yamabe, T. *Chemical Physics Letters* **2001**, *345*, 125.

(28) Negri, F.; Zgierski, M. Z. *Journal of Chemical Physics* **1993**, *99*, 4318.

(29) Negri, F.; Zgierski, M. Z. *Journal of Chemical Physics* **1996**, *104*, 3486.

(30) Negri, F.; Zgierski, M. Z. *Journal of Chemical Physics* **1997**, *107*, 4827.

(31) Szczepanski, J.; Drawdy, J.; Wehlburg, C.; Vala, M. *Chemical Physics Letters* **1995**, *245*, 539.

(32) Szczepanski, J.; Vala, M.; Talbi, D.; Parisel, O.; Ellinger, Y. *Journal of Chemical Physics* **1993**, *98*, 4494.

(33) Yamane, H.; Nagamatsu, S.; Fukagawa, H.; Kera, S.; Friedlein, R.; Okudaira, K. K.; Ueno, N. *Physical Review B* **2005**, *72*, 153412.

(34) Zgierski, M. Z. *Journal of Chemical Physics* **1986**, *85*, 109.

(35) Frisch, M. J.; Trucks, G. W.; Schlegel, H. B.; Scuseria, G. E.; Robb, M. A.; Cheeseman, J. R.; Zakrzewski, V. G.; Montgomery, J., J.A.; Stratmann, R. E.; Burant, J. C.; Dapprich, S.; Millam, J. M.; Daniels, A. D.; Kudin, K. N.; Strain, M. C.; Farkas, O.; Tomasi, J.; Barone, V.; Cossi, M.; Cammi, R.; Mennucci, B.; Pomelli, C.; Adamo, C.; Clifford, S.; Ochterski, J.; Petersson, G. A.; Ayala, P. Y.; Cui, Q.; Morokuma, K.; Salvador, P.; Dannenberg, J. J.; Malick, D. K.; Rabuck, A. D.; Raghavachari, K.; Foresman, J. B.; Cioslowski, J.; Ortiz, J. V.; Baboul, A. G.; Stefanov, B. B.; Liu, G.;

Liashenko, A.; Piskorz, P.; Komaromi, I.; Gomperts, R.; Martin, R. L.; Fox, D. J.; Keith, T.; Al-Laham, M. A.; Peng, C. Y.; Nanayakkara, A.; Challacombe, M.; Gill, P. M. W.; Johnson, B.; Chen, W.; Wong, M. W.; Andres, J. L.; Gonzalez, C.; Head-Gordon, M.; Replogle, E. S.; Pople, J. A. Gaussian98, Revision A.11; Gaussian, Incorporated: Wallingford, CT, 1998.

(36) Reimers, J. R. *Journal of Chemical Physics* **2001**, *115*, 9103.

(37) Bally, T.; Carra, C.; Fülscher, M. P.; Zhu, Z. D. *J. Chem. Soc. Perkin Trans. 2* **1998**, 1759.

(38) Boschi, R.; Murrell, J. N.; Schmidt, W. *Faraday Discussions* **1972**, *54*, 116.

(39) Brogli, F.; Heilbronnner, E.; Kobayashi, T. *Helvetica Chimica Acta* **1972**, *55*, 274.

(40) Brundle, C. R.; Robin, M. B.; Keubler, N. A. *Journal of the American Chemical Society* **1972**, *94*, 1466.

(41) Schmidt, W. *Journal of Chemical Physics* **1977**, *66*, 828.

(42) Koopmans, T. *Physica* **1934**, *1*, 104.

(43) Bersuker, I. B. *Chemical reviews* **2001**, *101*, 1067.

(44) Kato, T.; Yamabe, T. *Journal of Chemical Physics* **2003**, *119*, 11318.

CHAPTER 4

NONLOCAL ELECTRON-PHONON COUPLING

In this chapter, DFT and empirical MM calculations are used to derive the nonlocal electron-phonon coupling constants arising from the interaction of charge carriers with the optical phonons in oligoacene crystals (naphthalene through pentacene). This chapter begins with a brief introduction to the nonlocal electron-phonon coupling and is followed by a discussion, from a molecular standpoint, of the parameters that impact charge carrier mobilities in ordered systems. It is found that the DFT and force field results for phonon frequencies and the hole- and electron-phonon coupling constants compare very well. Additionally, electronic band structure calculations were performed for the four molecular crystals; the respective effective masses for both holes and electrons were calculated as well. At the end of the chapter, a comparison of the standard deviations (σ) obtained from a quantum-mechanical treatment of the vibrational modes and from classical MDS is presented.

4.1 Introduction

As discussed in Chapter 2 (section 2.3), the nonlocal electron-phonon coupling represents the modulation of the transfer integrals by lattice phonons. Within the tight-binding approximation (Equation 2.65), the nonlocal electron-phonon interactions can be obtained by expanding the transfer integrals, t_{mn}, into a power series of the phonon

coordinates. In this representation, the potential energy (V_L) of the lattice vibrations and the dependence of the transfer integrals on the normal-mode coordinates are given by:

$$V_L = \sum_j \frac{\hbar\omega_j Q_j^2}{2} \tag{4.1}$$

$$t_{mn} = t_{mn}^{(0)} + \sum_j \upsilon_{jmn} Q_j \tag{4.2}$$

Here, ω_j is the frequency of j vibrational mode; $t_{mn}^{(0)}$ are the transfer integrals obtained at the equilibrium geometry; Q is the normal-mode coordinate; and υ_{jmn} are the nonlocal electron-phonon coupling constants. The systematic determination of the coupling constants υ_{jmn} represents the main focus of the present chapter. As in previous investigations,[1, 2] the dispersion of the vibrations was neglected and the strength of the nonlocal electron-phonon interaction for phonon frequencies was calculated at the Γ-point.

4.2 Theoretical methodology

The geometric and electronic-structure calculations of the oligoacene crystals were performed using DFT with the PBE[3] (Perdew-Burke-Ernzerhof) exchange-correlation functional and plane wave basis set as implemented in the VASP code.[4-6] Electron-ion interactions were described using the projector augmented wave (PAW) method.[7, 8] The kinetic energy cutoff on the wave function expansion was 300 eV. The self-consistent calculations were carried out with an 8×8×8 k-point mesh. The inverse effective mass tensor was calculated using Sperling's centered difference method at the

band edges with dk = 0.02 ($2\pi/$Å) for monoclinic crystals and dk = 0.025 ($2\pi/$Å) for triclinic crystals. The Γ-point lattice phonons were obtained by means of numerical derivation using a 0.03 Å atomic displacement step.

The lattice dynamics at the Γ-point was also investigated by means of MM simulations using the DMAREL program.[9] An empirical Buckingham (exp-6) model[10] was used for the repulsion-dispersion interactions and the atomic point charges were determined from the B3LYP/6-31G** calculations, using the CHelpG algorithm as implemented in the Gaussian03 package.[11] The MM calculations were carried out in the framework of the rigid-body approximation.[12, 13]

Transfer integrals for selected nearest-neighbor pairs of molecules were evaluated at both DFT and MM optimized crystal geometries by using a fragment orbital approach in combination with a basis set orthogonalization procedure.[14] These calculations were performed with the PW91 functional and Slater-type triple-ζ plus polarization basis sets for all atoms using the ADF package.[15]

Finally, MDS were carried out for the naphthalene crystal. The unit cell was replicated to build a 4×4×3 supercell containing 96 molecules. The dynamics of the system was studied with periodic boundary conditions employing the MM3 force field.[16] MDS were run at 300 K in the canonical NVT ensemble with a timestep of 1 fs, using the computer code TINKER.[17] A cutoff of 10 Å was adopted when evaluating both van der Waals and electrostatic interactions. The simulations lasted for 150 ps and atomic

coordinates were saved every 30 fs (*i.e.*, 5000 snapshots). For each snapshot, hole and electron transfer integrals were calculated for two distinctive molecular pairs (resulting in 20,000 electronic coupling evaluations for each molecular crystal). Due to the large number of required transfer integral evaluations, the transfer integrals were calculated at the semi-empirical Hartree-Fock INDO (Intermediate Neglect of Differential Overlap) level. Note that for this type of calculations the INDO method generally yields a good quantitative agreement when compared with results derived from more rigorous DFT approaches.[18]

4.3 Results and discussion

4.3.1 Crystallographic information

In fixed-cell periodic DFT calculations used to determine the vibrational modes of an oligoacene crystal at the Γ-point, the only required input is the measured crystal structure. For naphthalene[19] and anthracene,[20] the structure has been determined to be monoclinic in the space group $P2_1/a$, while tetracene[21] and pentacene[21] crystallize in the triclinic space $P\bar{1}$. Despite this difference, the arrangement of the molecules within the unit cell is very similar among the series of oligoacene single crystals. Two translationally inequivalent molecules per unit cell ($Z = 2$) are always present at positions (0,0,0) and (½, ½, 0). The crystallographic data used in the normal-mode calculations are listed in Table 4.1.

Table 4.1 Crystal constants and structures for oligoacenes.

Crystal constants	Naphthalene Monoclinic[19]	Anthracene Monoclinic[20]	Tetracene Triclinic[21]	Pentacene Triclinic[21]
a	8.098	8.414	6.057	6.275
b	5.953	5.990	7.838	7.714
c	8.652	11.095	13.010	14.442
α	90.0	90.0	77.1	76.8
β	124.4	125.3	72.1	88.0
γ	90.0	90.0	85.8	84.5

[a] Units in Å
[b] Units in degrees

4.3.2 Vibrational modes in oligoacene crystals

In this section, the lattice dynamical properties of the naphthalene crystal (which can be dubbed as the "hydrogen atom" of molecular crystals) are presented as computed at the Γ-point of the Brillouin zone. For the larger oligoacene members, only a few distinctive remarks with respect to their lattice dynamical properties will be discussed since there exist overall similarities in the frequencies and phonon eigenvectors at the Γ-point among the four molecular crystals studied here.

In the naphthalene crystal, there are two molecules in the primitive unit cell ($Z = 2$); this is also the case in the anthracene, tetracene, and pentacene crystals. Therefore, in these crystals, there are 12 degrees of freedom and thus 12 intermolecular modes (normal vibrations). Among these modes, three are acoustic modes and the other nine modes (*i.e.*, $6Z-3$) are optical. The intermolecular modes are well described by the rigid-body approximation in which the intramolecular geometries are frozen; such theoretical calculations are based on empirical potential energy models (force fields), in

which the intermolecular interactions are described by empirical atom-atom potentials. In this study, the intermolecular phonon frequencies at the Γ-point in oligoacenes were calculated using both a DFT approach and a rigid-molecule approximation.

The characteristics of the 9 intermolecular optical modes in the naphthalene crystal as derived from DFT and force field methods are collected in Table 4.2. Additionally, in Figure 4.1, the molecular motions of the 2 translationally inequivalent molecules in the unit cell are shown. A close inspection of Figure 4.1 shows that the intermolecular vibrations in naphthalene (and as well in anthracene, tetracene, and pentacene) correspond to 3 translational modes and 6 librational modes; the latter can be further categorized into 2 librations along the short molecular axes, 2 librations along the long molecular axes, and 2 librations about an axis approximately perpendicular to the molecular plane. The two lowest-frequency translational modes are characterized by a motion that shears the C−H···π interactions, while the highest-frequency translational modes present a continuous stretching of the edge-to-face contacts. Turning to librations, the two lowest-frequency librational modes (about an axis perpendicular to the molecular plane) present a continuous stretching of the edge-to-face contacts. The normal modes with frequency values of $\omega = 97\ cm^{-1}$ and $\omega = 102\ cm^{-1}$ show anti-symmetric and symmetric librations along the short molecular axis; these vibrations lead to a combined stretching and shearing effect of the C−H···π interactions. Finally, the two highest-frequency librational modes represent librations along the long molecular axis, decreasing or increasing the contact angle between the molecular planes of the two molecules.

Table 4.2 Phonon frequencies of the intermolecular optical modes in the naphthalene ($C_{10}H_8$) crystal obtained from DFT and MM calculations. Experimental results are included for comparison.[22]

Mode	Type	DFT (cm^{-1})	MM (cm^{-1})	Expt (77 °K) (cm^{-1})
$\nu_1(A_u)$	*translation*	51	50	44
$\nu_2(B_g)$	*libration*	56	54	56
$\nu_3(A_g)$	*libration*	63	59	67
$\nu_4(B_u)$	*translation*	76	63	75
$\nu_5(B_g)$	*libration*	97	82	83
$\nu_6(A_g)$	*libration*	102	99	88
$\nu_7(A_u)$	*translation*	121	117	106
$\nu_8(A_g)$	*libration*	126	152	121
$\nu_9(B_g)$	*libration*	150	153	141

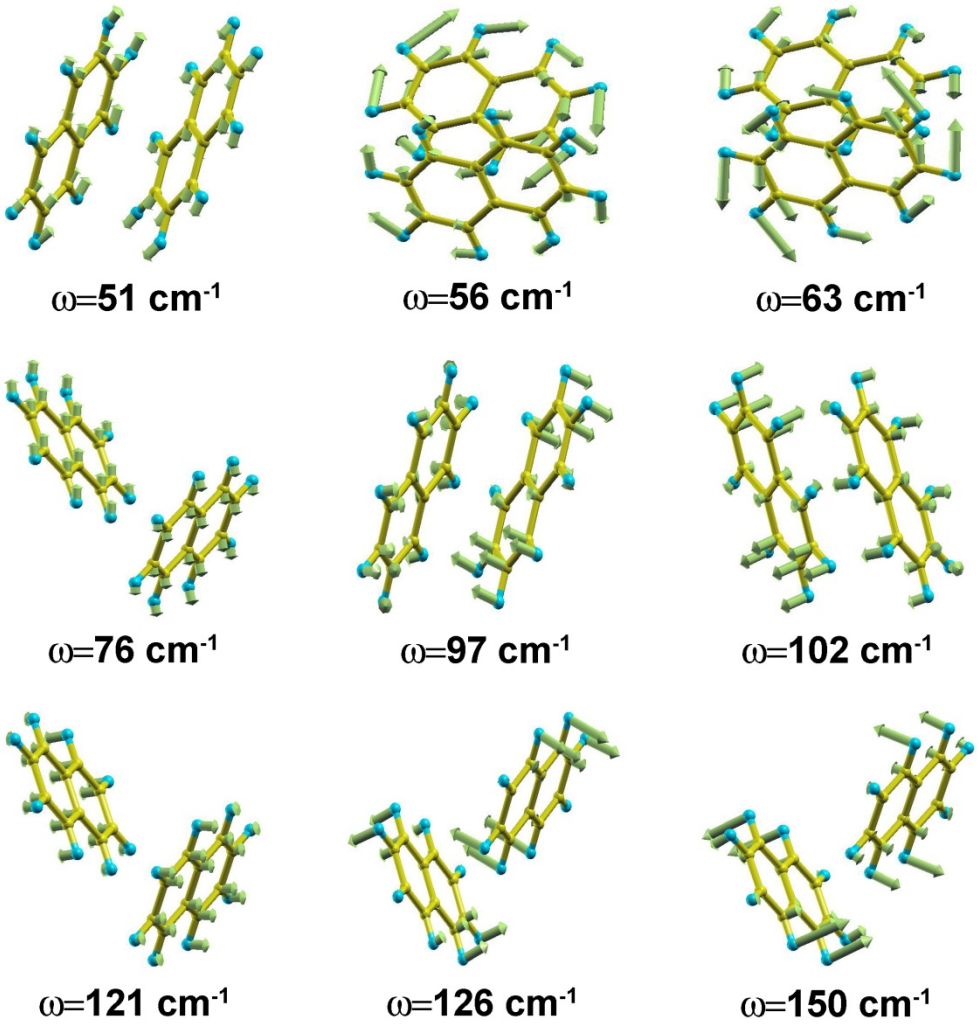

Figure 4.1 DFT calculated eigenvectors for the nine ($k = 0$) optical phonon modes in naphthalene. The phonon frequencies are also given.

In Tables 4.3-4.5 the characteristics of the 9 intermolecular optical modes in the anthracene, tetracene, and pentacene crystals derived from DFT and force field methods are displayed. It is important to note that for the larger oligoacenes, the qualitative description of the intermolecular modes becomes more complex than in naphthalene due to mixing among intermolecular and intramolecular modes. In principle, if a substantial frequency gap exists between the inter- and intramolecular motions, the two classes of

vibrations can be studied quite independently. In naphthalene, a clear but small frequency (~30 cm^{-1}) gap exists, with the lowest frequency for an intramolecular vibration at around 170 cm^{-1}.[23] This situation is different already in the anthracene crystal, for which there is no frequency gap between the inter- and intramolecular vibrations; the spectrum of the intramolecular vibrations in the anthracene crystal includes the region from 111 cm^{-1} to 3108 cm^{-1}.[23] DFT calculations show that two intramolecular modes for the isolated molecule of anthracene, two for tetracene, and several (more than five) for pentacene have lower frequencies than some of the intermolecular vibrations of their respective crystals. An example of such intramolecular modes (consistently found along the series of larger oligoacenes) includes the butterfly vibration, in which for the case of anthracene the outer benzene rings vibrate both above or both below the plane of the central ring. Such intramolecular vibrations are neither included in Tables 4.3-4.5 nor shown in Figures 4.2-4.4, but where explicitly included in the calculation of the electron-phonon coupling constants in the pentacene crystal (*vide infra*). In tetracene and pentacene crystals, the mixing of intermolecular and intramolecular modes is more evident leading to low-frequency (< 150 cm^{-1}) vibrations with a modest to significant intramolecular contribution. This behavior confirms that the interactions between inter- and intramolecular vibrations are important when describing the lattice dynamical properties of highly flexible molecules such as tetracene and pentacene (or even anthracene). Therefore, approaches that go beyond the rigid-body approximation might be more suitable for these types of molecular crystals; as observed from Tables 4.3-4.5, DFT calculations are in better (quantitative) agreement with the experimental phonon frequencies than results derived from MM calculations.

Table 4.3 Phonon frequencies of the intermolecular optical modes in the anthracene ($C_{14}H_{10}$) crystal obtained from DFT and MM calculations. Experimental results from deuterated anthracene are included for comparison.[24]

Mode	Type	DFT (cm^{-1})	MM (cm^{-1})	Expt (12 °K) (cm^{-1})
$\nu_1(A_u)$	*translation*	44	43	47
$\nu_2(A_g)$	*libration*	46	47	48
$\nu_3(B_g)$	*libration*	54	55	54
$\nu_4(B_u)$	*translation*	73	59	69
$\nu_5(B_g)$	*libration*	90	78	70
$\nu_6(A_g)$	*libration*	97	91	77
$\nu_7(A_u)$	*translation*	120	120	106
$\nu_8(A_g)$	*libration*	133	158	122
$\nu_9(B_g)$	*libration*	149	161	130

Table 4.4 Phonon frequencies of the intermolecular optical modes in the tetracene ($C_{18}H_{12}$) crystal obtained from DFT and MM calculations. The calculated data are compared with the corresponding experimental lattice frequencies (where available)[25, 26] and with data obtained from an atom-atom intermolecular potential.[27]

Mode	Type	DFT (cm^{-1})	MM (cm^{-1})	Expt (296 °K) (cm^{-1})
$\nu_1(A_u)$	*translation*	37	30	26[a]
$\nu_2(A_g)$	*libration*	48	46	44-45
$\nu_3(A_g)$	*libration*	52	50	49
$\nu_4(A_u)$	*translation*	72	55	48[a]
$\nu_5(A_g)$	*libration*	81	73	61
$\nu_6(A_g)$	*libration*	110	102	94
$\nu_7(A_u)$	*translation*	119	120	87[a]
$\nu_8(A_g)$	*libration*	132	153	120
$\nu_9(A_g)$	*libration*	146	161	132

[a] Calculated using an atom-atom intermolecular potential.

Table 4.5 Phonon frequencies of the intermolecular optical modes in the pentacene ($C_{22}H_{14}$) crystal obtained from DFT and MM calculations. The calculated data are compared with the corresponding experimental lattice frequencies (where available)[28] and with data derived from an atom-atom intermolecular potential.[29]

Mode	Type	DFT (cm^{-1})	MM (cm^{-1})	Expt (79 °K) (cm^{-1})
$\nu_1(A_u)$	*translation*	45	20	21[a]
$\nu_2(A_g)$	*libration*	48	35	45
$\nu_3(A_g)$	*libration*	63	57	66
$\nu_4(A_u)$	*translation*	74	53	61[a]
$\nu_5(A_g)$	*libration*	85	68	84
$\nu_6(A_g)$	*libration*	112	102	99
$\nu_7(A_u)$	*translation*	125	123	131[a]
$\nu_8(A_g)$	*libration*	139	156	144
$\nu_9(A_g)$	*libration*	153	162	150

[a] Calculated using an atom-atom intermolecular potential.

Figures 4.2-4.4 show the molecular motions of the two translationally non-equivalent molecules in the unit cell of anthracene, tetracene, and pentacene, respectively. In general, the qualitative description of the intermolecular modes is similar to that found in the naphthalene crystal, for which 3 translational and 6 librational modes were identified. However, the qualitative description of the normal modes is somewhat more complex for the larger oligoacenes, especially in the pentacene crystal. In this case, the lowest-frequency molecular librations do not occur along a single molecular axis, but involve librations along the molecular plane as well as librations along the short molecular axis. This situation is observed with both DFT and MM methods. It is important to note that in the monoclinic $P2_1/a$ space group, since the molecules lie on the crystallographic inversion centers, the translational and librational modes do not mix.[12, 13]

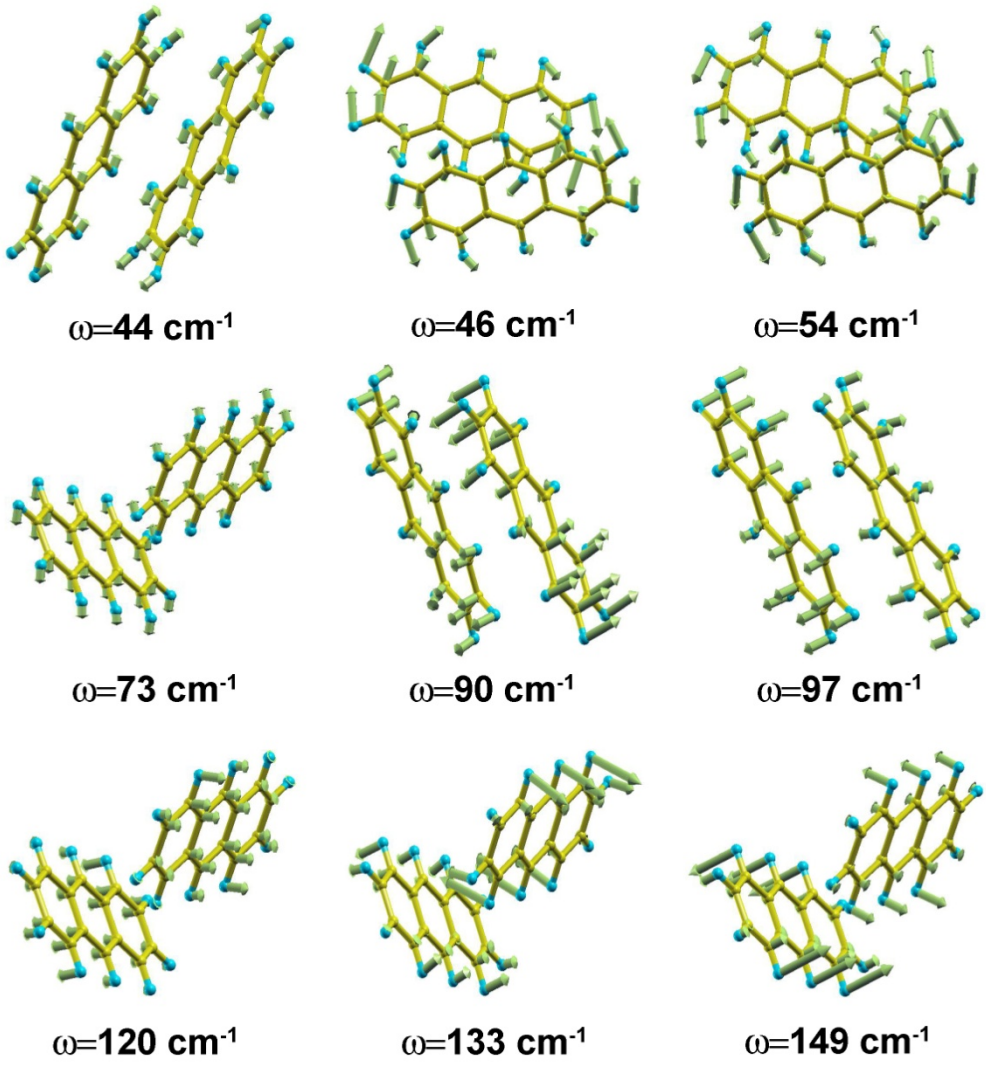

Figure 4.2 DFT calculated eigenvectors for the nine ($k = 0$) optical phonon modes in anthracene. The phonon frequencies are also given.

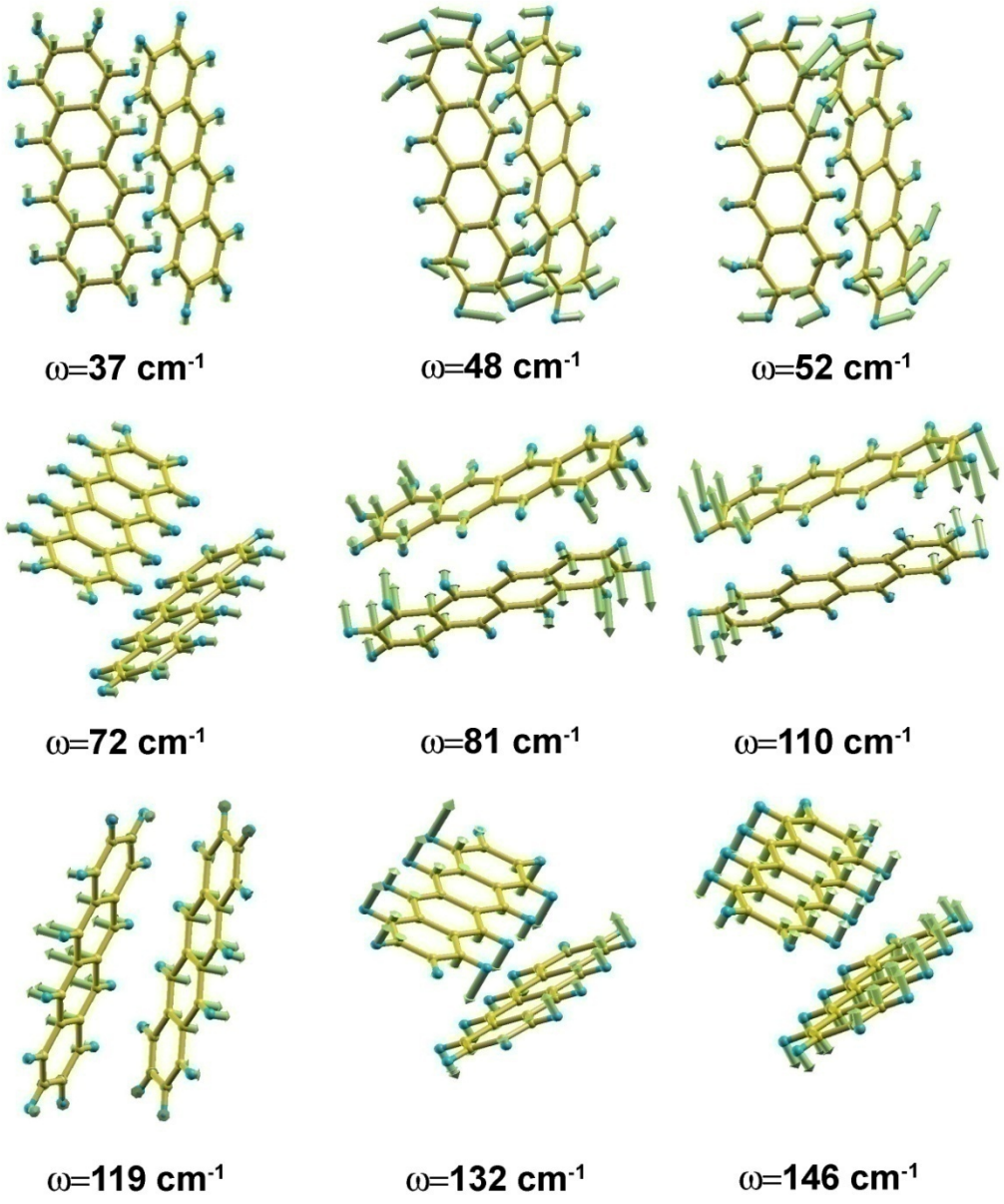

Figure 4.3 DFT calculated eigenvectors for the nine ($k = 0$) optical phonon modes in tetracene. The phonon frequencies are also given.

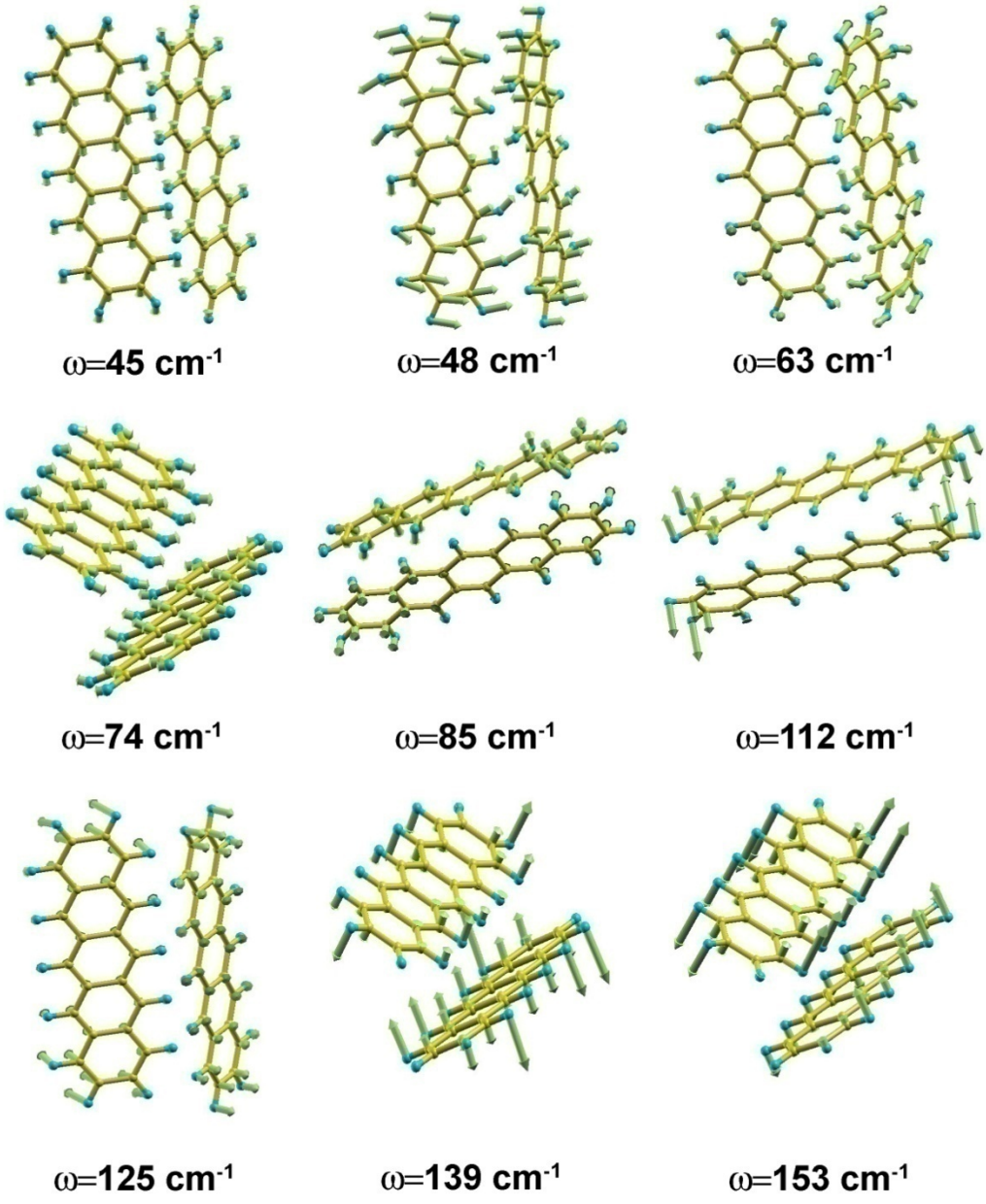

Figure 4.4 DFT calculated eigenvectors for the nine ($k = 0$) optical phonon modes in pentacene. The phonon frequencies are also given.

4.3.3 Electronic structure calculations

4.3.3.1 Transfer integrals

Table 4.5 reports the calculated transfer integrals for three different dimers in the naphthalene and anthracene crystals (see Figure 4.5 for definition of used molecular dimers). Table 4.6 contains the calculated transfer integrals in the tetracene and pentacene crystals for four different dimers (see Figure 4.6). As described elsewhere,[30, 31] significant hole and electrons interactions are found not only along the short crystal axis (b for monoclinic molecular crystals and a for triclinic ones) but also along the diagonal axes (pair 2 for naphthalene and anthracene and pair 3 and pair 4 for tetracene and pentacene). For the larger oligoacenes (tetracene and pentacene), vanishingly small transfer integrals are obtained from interactions among molecules located in adjacent layers (along c). For the smaller oligoacenes (naphthalene and anthracene), a medium-range coupling hole coupling is observed along the c axis; larger electronic interactions for both holes and electrons are only observed along the ab plane. This confirms that transport in oligoacene single crystals is mostly two-dimensional.[32] Therefore, the total bandwidths, W, of the valence and conduction bands in oligoacenes (especially in tetracene and pentacene) can be expressed from the transfer integrals calculated from the molecular dimers found in the ab crystallographic plane.

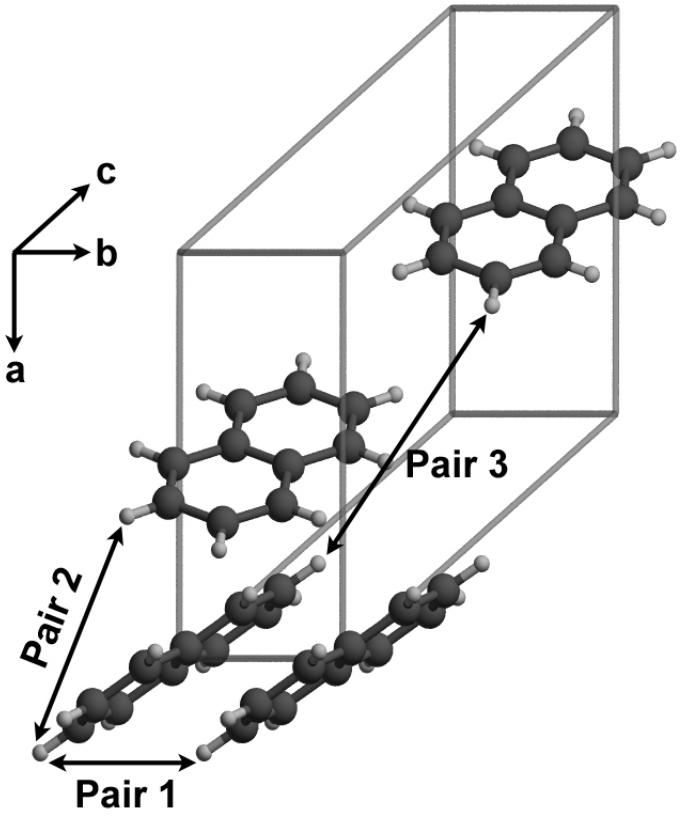

Figure 4.5 Illustration of the naphthalene (anthracene) molecular pairs with the largest transfer integrals as reported by Cheng *et al*.[31]

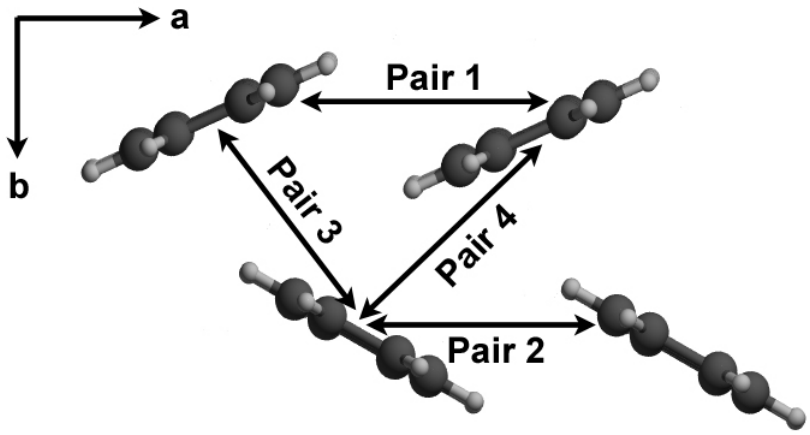

Figure 4.6 Definition of the tetracene and pentacene molecular pairs used to compute transfer integrals.

If the edge-to-face interactions are considered (*i.e.*, pair 2 for the smaller oligoacenes and pair 3(4) for the larger ones), an increase in transfer integrals (for both holes and electrons) is observed with the size of the oligoacene molecules. However, for cofacial dimers (*i.e.*, pair 1 for the smaller oligoacenes and pair 1(2) for the larger ones), the electronic coupling for holes is larger in the monoclinic molecular crystals than in the triclinic ones. This indicates that the size of the conjugated π system and the structure of the crystal are both important factors in determining the strength of the electronic interactions.[30]

Due to the subtle interplay between crystal packing and electronic couplings, the latter cannot be simply evaluated by only investigating the crystallographic interactions in the molecular crystal. Their determination (and impact on the hole and electron mobilities) requires investigating the three-dimensional band structure of the oligoacene crystals. As mentioned earlier in Chapters 1 and 2, the curvature at the top of the valence

band and at the bottom of the conduction can be used to calculate the effective mass, which is commonly used in band-like transport theories to estimate the relative magnitude of the mobility for holes and electrons. In the next section, the three-dimensional band structures of oligoacenes are discussed.

Table 4.6 DFT-calculated transfer integrals in naphthalene and anthracene (meV).

	Naphthalene		Anthracene	
	hole	electron	hole	Electron
Pair 1	-35.6	14.1	-44.9	36.9
Pair 2	-12.0	-35.3	-18.6	61.6
Pair 3	17.9	-5.7	18.6	-2.6

Table 4.7 DFT-calculated transfer integrals in tetracene and pentacene (meV).

	Tetracene		Pentacene	
	hole	electron	hole	electron
Pair 1	-5.1	-12.6	33.8	-43.1
Pair 2	13.2	-32.8	35.7	-44.8
Pair 3	17.1	63.9	47.3	-82.5
Pair 4	-69.5	-67.3	-85.2	83.5

4.3.3.2 Band structures

The electronic band structures and density of states spectra (DOS) for the naphthalene, anthracene, tetracene, and pentacene single crystals are shown in Figures 4.7-4.10. Since the effective mass can easily be computed from the band structures (see section 2.1.4), the calculated effective masses for the oligoacene series are also reported in Tables 4.8-4.11. The electronic bands were calculated along the standard Brillouin zone directions in the reciprocal space. Both the valence and conduction bands are composed of two sub-bands, which are well separated from the other bands and are due

to the presence of two inequivalent molecules per unit cell. A close look at the electronic band structure reveals that the band structures of naphthalene and anthracene are similar, but distinct from those of tetracene and pentacene, which are alike. The differences can be ascribed to the different crystal structures (monoclinic *versus* triclinic). All four compounds investigated here have continuous bandwidths, W, ranging from 300 to 700 meV for both holes and electrons. In this case, W is defined as the energy range covered by the continuous region in the DOS of the two uppermost and lowermost bands for the valence (W_{VB}) and conduction bands (W_{CB}), respectively. Along the oligoacene series from naphthalene to pentacene, the calculated bandwidths are 368, 347, 347, and 538 meV for W_{VB} and 326, 558, 531, and 694 for W_{CB}. While a clear trend cannot be defined for W_{VB} within the series, W_{CB} tends to increase; the pentacene single crystal displays the largest bandwidths for both holes and electrons.

The band dispersions (determined by a single sub-band) in oligoacenes were previously discussed using both semi-empirical[31] and *ab initio*[33] quantum-chemical methods. Therefore, in the following, we focus on the effective carrier masses. To estimate the effective masses, it is necessary to identify the band edges. In general, the valence and conduction band edges were found on the high symmetry points in the first Brillouin zone. The exception is pentacene whose valence band edge occurs at Δ_V (0.375, 0.5, 0.075); this contrasts with the tetracene crystal, in which the valence band edge is located at V (0.5, 0.5, 0.0), but it is clear from Figure 4.10 that the band near V (in pentacene) does not have a parabolic shape. However, the deviations between the two triclinic crystals are small.

The quantitative results in Tables 4.8-4.11 indicate that the effective masses for the electrons are smaller than those for the holes (at least along the ab plane), in agreement with the calculations reported in Reference 33. The smallest hole effective masses in naphthalene and anthracene are found along the short molecular axis, where cofacial interactions between molecules are favored. This result is consistent with the previously calculated transfer integrals (see Table 4.6). The smallest electron effective masses are found along the a-axis. This finding implies that the herringbone interactions (*i.e.*, pair 2 in monoclinic crystals) provide a path for electrons to move effectively along the a direction in spite of relatively large intermolecular distances (> 8 Å). For the tetracene and pentacene crystals, the smallest effective masses for both holes and electrons are found in the herringbone plane with the ones for pentacene smaller than those of tetracene (2.59 *versus* 1.94 and 2.04 *versus* 1.85 for holes and electrons, respectively). Heavier effective carrier masses are observed in the c direction for tetracene, but pentacene shows slightly lighter masses along this direction.

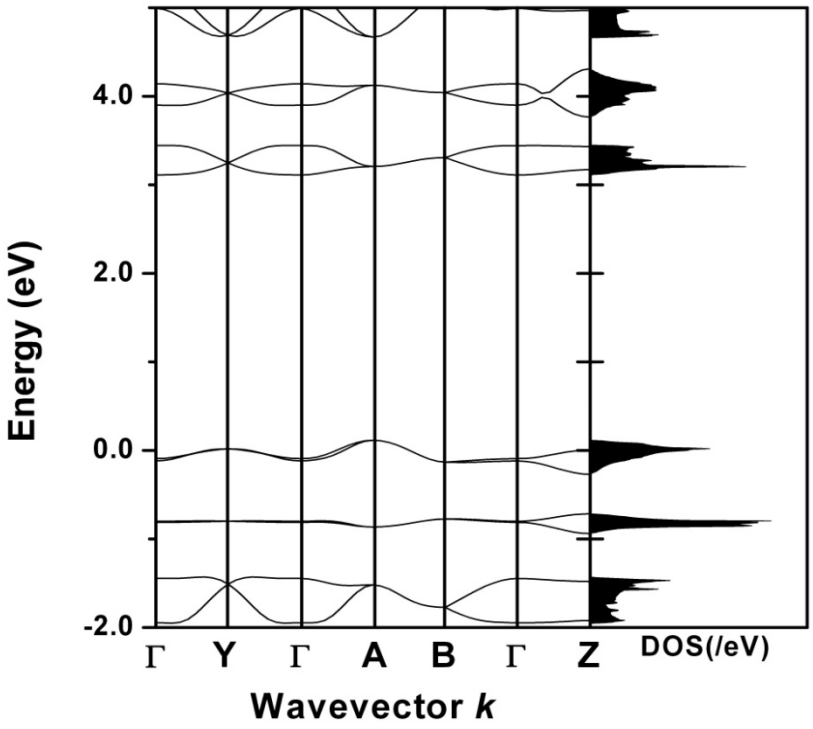

Figure 4.7 The band structure of crystalline naphthalene and density of states (DOS) spectrum. The energy is set to be zero at the top of the valence band. The energies are plotted along the directions in the first Brillouin zone, connecting the points Γ=(0,0,0), Y=(0,0.5,0), A=(0.5,0.5,0), B=(0.5,0,0) and Z=(0,0,0.5). DOS in states/eV per cell.

Table 4.8 Hole and electron effective masses m (in units of the free electron mass at rest, m_0) calculated at the band edges of the naphthalene crystal.

	m/m_0	parallel to
holes at A	2.86	$a + 0.57c$
	2.11	b
	9.63	$c + 0.09a$
electrons at Γ	1.70	$a + 0.27c$
	17.19 [a]	b
	7.56	$c + 0.27a$

[a] Due to the flatness of the band, it was not possible to derive an accurate value of the effective mass along this direction.

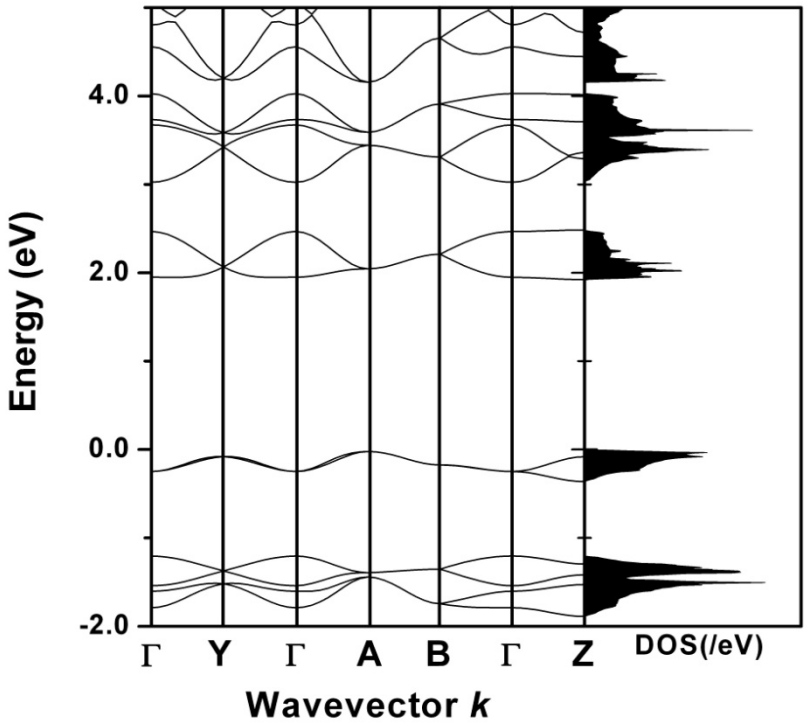

Figure 4.8 The band structure of single anthracene and density of states (DOS) spectrum. The energy is set to be zero at the top of the valence band. The energies are plotted along the directions in the first Brillouin zone, connecting the points Γ=(0,0,0), Y=(0,0.5,0), A=(0.5,0.5,0), B=(0.5,0,0) and Z=(0,0,0.5). DOS in states/eV per cell.

Table 4.9 Hole and electron effective masses m (in units of the free electron mass at rest, m_0) calculated at the band edges of the anthracene crystal.

	m/m_0	parallel to
holes at R	3.33	$a + 0.43c$
	1.97	b
	10.18	$c + 0.26a$
electrons at Z	1.48	$a + 0.58c$
	60.19 [a]	b
	8.06	$c + 0.10a$

[a] Due to the flatness of the band, it was not possible to derive an accurate value of the effective mass along this direction.

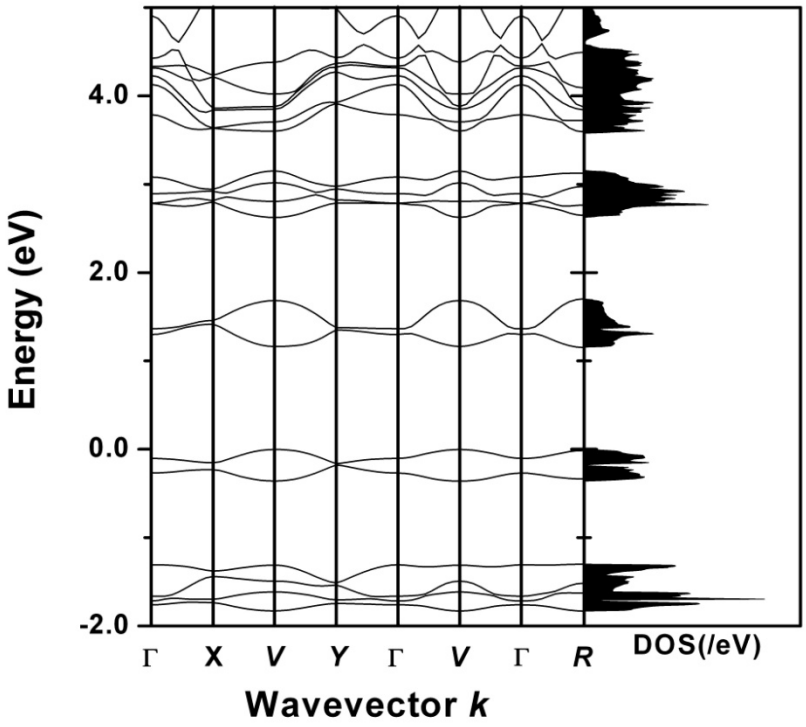

Figure 4.9 The band structure of crystalline tetracene and density of states (DOS) spectrum. The energy is set to be zero at the top of the valence band. The energies are plotted along the direction in the first Brillouin zone, connecting the points Γ=(0,0,0), R=(0.5,0.5,0.5), V=(0.5,0.5,0), X=(0.5,0,0), and Y=(0,0.5,0), all in crystallographic coordinates. DOS in states/eV per cell.

Table 4.10 Hole and electron effective masses m (in units of the free electron mass at rest, m_0) calculated at the band edges of the tetracene crystal.

	m/m_0	parallel to
holes at V	6.84	$a + 0.194b - 0.055c$
	2.59	$b - 0.413a - 0.096c$
	15.19	$c - 0.814a - 0.120b$
electrons at R	6.79	$a - 0.108b - 0.476c$
	2.04	$b + 0.083a - 0.205c$
	15.22	$c + 0.820a - 0.212b$

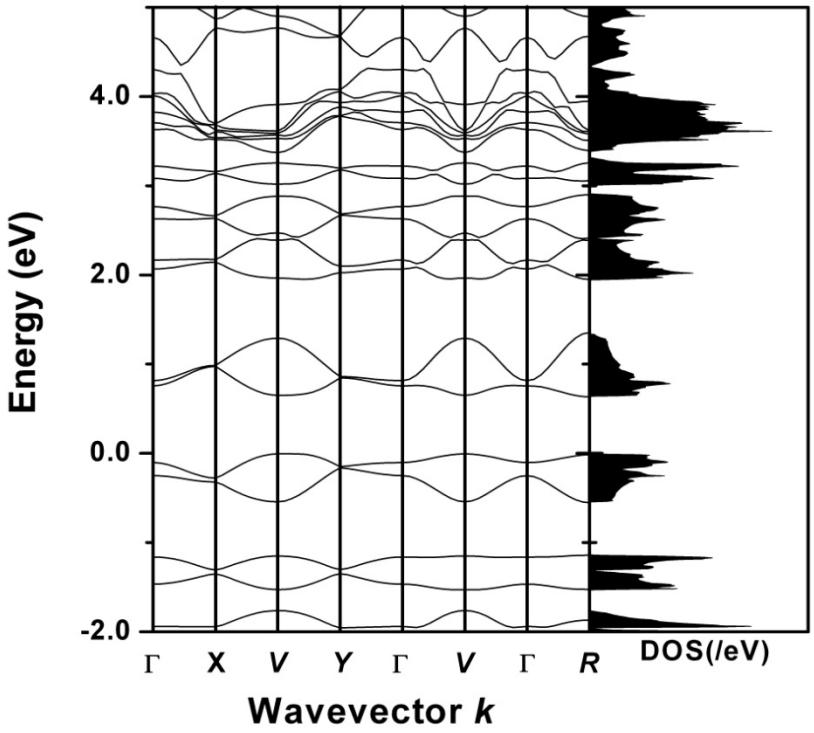

Figure 4.10 The band structure of crystalline pentacene and density of states (DOS) spectrum. The energy is set to be zero at the top of the valence band. The energies are plotted along the directions in the first Brillouin zone, connecting the points Γ=(0,0,0), R=(0.5,0.5,0.5), V=(0.5,0.5,0), X=(0.5,0,0), and Y=(0,0.5,0), all in crystallographic coordinates. DOS in states/eV per cell.

Table 4.11 Hole and electron effective masses m (in units of the electron mass at rest, m_0) calculated at the band edges of the pentacene crystal.

	m/m_0	parallel to
holes at Δ_V [a]	8.92	$a - 0.017b + 0.042c$
	1.94	$b - 0.114a - 0.238c$
	7.06	$c - 0.369a + 0.037b$
electrons at R	29.08	$a - 0.084b - 0.052c$
	1.85	$b - 0.007a - 0.176c$
	6.88	$c + 0.174a - 0.200b$

[a] Δ_V (0.375, 0.5, 0.075).

4.3.4 Hole- and electron-phonon coupling

As discussed above, the nonlocal electron-phonon coupling is related to the variations in transfer integrals due to modulations in the distances and relative orientations between molecules. In the rigid-body approximation, this mechanism is entirely due to interactions with the intermolecular (external) vibration modes. The nonlocal electron-phonon coupling constants were evaluated by computing the derivatives, $v_{\mathrm{jmn}} = \partial t_{mn}/\partial Q_j$. This was achieved first by distorting the crystal along all normal coordinates (Q_j) and computing the related transfer integrals at each distorted geometry; then, the derivatives of the transfer integrals with respect to normal coordinates were calculated numerically. This approach is similar to that used earlier to derive the local electron-phonon coupling constants in naphthalene.[34]

In order to quantify the effect of all modes, it is useful to introduce the following parameters G and L:

$$G_{mn} = \sum_j \frac{v_{jmn}^2}{2} \tag{4.3}$$

$$L_{mn} = \sum_j \frac{v_{jmn}^2}{2\hbar\omega_j} \tag{4.4}$$

G and L define the degree of thermal fluctuations in the related transfer integrals at low and high temperatures, respectively. The quantity L_{mn} represents as well the intermolecular relaxation energy that arises upon injecting a charge on a molecule in the crystal.

4.3.4.1 Nonlocal electron-phonon coupling constants derived from force field methods

The results obtained using MM normal modes are given in Tables 4.12-4.15 for naphthalene through pentacene. From Tables 4.12 and 4.13, it is clear that the coupling of the charge carriers in the naphthalene and anthracene crystals occurs mainly in the ab crystallographic plane, while along the c-axis the nonlocal coupling constants are rather modest. Interestingly, the electrons are more strongly coupled to the 9 normal modes derived from MM approaches than holes in all four molecular crystals. This finding is in agreement with recently published results by Wang *et al.*[35] for the naphthalene crystal. This observation can be rationalized by considering the differences in electronic interactions of the frontier molecular orbitals. That is, librations along an axis perpendicular to the molecular plane can result in a change in the relative phase (or sign of the molecular orbital) of the two interacting LUMO wavefunctions (electrons) when distorted along the normal mode; such modification is not observed for the HOMO wavefunctions (holes).

It is also evident that molecular dimers with a herringbone arrangement (that is, pair 2 in monoclinic crystals and pairs 3 and 4 in triclinic crystals) are more sensitive to the intermolecular vibrations than any of the other molecular pairs investigated in this study. Indeed, both charge carriers in such herringbone dimers are strongly coupled to the lowest-frequency vibrations in all four crystals. Relatively large nonlocal coupling constants are obtained for interactions of the carrier with the lowest-frequency translational vibration (50, 43, 30, and 20 cm^{-1} for naphthalene, anthracene, tetracene, and pentacene, respectively). This molecular vibration shears the C−H···π interactions because the molecules move in opposite directions along their long molecular axis, which in turn induces significant changes in the overlap of the frontier molecular orbitals. Finally, it is observed that the intermolecular relaxation energy (L) for both holes and electrons decreases with molecular size, the effect being more pronounced in the electron case. A similar behavior is found when including both inter- and intramolecular vibrations (*vide infra*). These findings suggest that the modulation of the transfer integrals by normal-mode vibrations (*i.e.*, L) can be considered to be a molecular size-dependent property, which is in agreement with the size dependence correlation of the intramolecular relaxation energies in oligoacene molecules.[36]

Table 4.12 Estimates of the electron (hole)-phonon coupling constants (in meV) of the 9 optical modes in the naphthalene crystal based on MM normal-mode calculations (see Figure 4.5 for a definition of pair 1, pair 2, and pair 3).

	Holes			Electrons		
$\omega\ (cm^{-1})$	v pair 1	v pair 2	v pair 3	v pair 1	v pair 2	v pair 3
50	0.0	10.0	3.3	0.0	11.8	-1.2
54	6.8	-6.2	-0.4	-14.0	-9.9	3.2
59	8.9	-6.1	1.0	-17.0	4.7	0.3
63	0.0	0.1	-1.0	0.0	-5.7	-2.2
82	-4.8	2.9	-0.1	8.9	4.4	-2.4
99	-0.8	-4.7	0.2	3.0	-12.9	2.5
117	0.0	-2.3	0.8	0.0	4.3	1.1
152	4.9	3.4	0.4	-1.8	0.0	-1.1
153	-5.2	4.2	-0.3	1.8	2.0	-0.5
$L\ (meV)$	11.3	15.8	1.1	38.8	30.6	1.8
$\sqrt{G}\ (meV)$	10.0	11.0	2.7	17.0	15.8	4.0

Table 4.13 Estimates of the electron (hole)-phonon coupling constants (in meV) of the 9 optical modes in the anthracene crystal based on MM normal-mode calculations (see Figure 4.5 for a definition of pair 1, pair 2, and pair 3).

	Holes			Electrons		
$\omega\ (cm^{-1})$	v pair 1	v pair 2	v pair 3	v pair 1	v pair 2	v pair 3
43	0.0	9.3	2.9	0.0	-7.2	-1.4
47	5.4	1.4	-0.9	9.4	1.0	-0.2
55	4.5	5.1	0.0	8.2	-6.0	-2.6
59	0.0	1.3	-0.8	0.0	4.7	-1.0
78	1.2	0.4	-0.4	2.3	-0.1	-0.6
91	-0.6	6.5	-0.6	-1.4	-6.9	-1.6
120	0.0	3.9	0.8	0.0	-6.1	0.5
158	3.0	-5.4	-0.3	0.2	3.2	0.1
161	2.3	-3.5	0.5	-0.6	-3.3	0.7
$L\ (meV)$	4.4	13.8	0.9	12.8	13.0	0.9
$\sqrt{G}\ (meV)$	5.7	10.4	2.4	9.0	10.4	2.6

Table 4.14 Estimates of the electron (hole)-phonon coupling constants (in meV) of the 9 optical modes in the tetracene crystal based on MM normal-mode calculations (see Figure 4.6 for a definition of pair 1, pair 2, pair 3, and pair 4).

	Holes				Electrons			
$\omega\ (cm^{-1})$	$v_{\text{pair 1}}$	$v_{\text{pair 2}}$	$v_{\text{pair 3}}$	$v_{\text{pair 4}}$	$v_{\text{pair 1}}$	$v_{\text{pair 2}}$	$v_{\text{pair 3}}$	$v_{\text{pair 4}}$
30	0.0	0.0	8.5	4.1	0.0	0.0	-6.7	2.4
46	4.7	4.0	2.2	-2.2	-5.8	-4.3	-2.1	-0.5
50	-2.3	4.7	1.1	0.3	2.9	-4.8	0.5	-0.9
55	0.0	0.0	-1.2	-1.9	0.0	0.0	-2.7	2.9
73	-2.1	-0.1	4.5	-0.2	2.4	0.3	5.2	-0.7
102	0.3	0.8	-0.5	0.0	-0.2	-0.7	0.1	-0.2
120	0.0	0.0	-0.9	8.0	0.0	0.0	4.9	5.5
153	1.4	0.5	-0.8	6.4	-0.2	0.2	-3.6	-0.6
161	0.4	-2.1	1.7	10.1	-0.1	-0.3	-1.6	4.9
$L\ (meV)$	2.7	3.3	11.5	8.7	3.9	3.4	9.6	3.1
$\sqrt{G}\ (meV)$	4.1	4.7	7.2	10.8	4.9	4.6	7.9	5.9

Table 4.15 Estimates of the electron (hole)-phonon coupling constants (in meV) of the 9 optical modes in the pentacene crystal based on MM normal-mode calculations (see Figure 4.6 for a definition of pair 1, pair 2, pair 3, and pair 4).

	Holes				Electrons			
$\omega\ (cm^{-1})$	$v_{\text{pair 1}}$	$v_{\text{pair 2}}$	$v_{\text{pair 3}}$	$v_{\text{pair 4}}$	$v_{\text{pair 1}}$	$v_{\text{pair 2}}$	$v_{\text{pair 3}}$	$v_{\text{pair 4}}$
20	0.0	0.0	8.7	5.7	0.0	0.0	0.8	0.5
35	-1.5	-2.4	1.5	3.0	1.7	2.1	1.5	-0.2
57	0.0	0.0	1.7	1.6	0.0	0.0	-3.2	-2.7
53	0.1	2.8	3.2	-0.3	0.0	-2.5	1.0	0.0
68	3.0	-0.8	2.0	0.1	-2.6	0.8	1.7	0.0
102	0.2	0.3	-0.9	0.4	-0.1	-0.1	0.1	0.0
123	0.0	0.0	-2.1	7.1	0.0	0.0	-5.8	5.4
156	-1.1	-1.1	-0.3	-2.5	-0.2	0.2	-4.0	1.9
162	-0.9	1.2	-4.5	-10.1	0.1	0.1	-3.2	-4.1
$L\ (meV)$	0.8	1.3	17.1	12.1	0.7	1.0	3.2	2.1
$\sqrt{G}\ (meV)$	2.6	2.9	7.7	10.1	2.2	2.4	6.2	5.4

4.3.4.2 Nonlocal electron-phonon coupling constants derived from *ab initio* methods

The results derived from DFT calculations provide comparable trends to those obtained from MM calculations. However, it is important to note that since DFT calculations go beyond the rigid-body approximation an evaluation of the coupling to intramolecular vibrations is also available. The nonlocal coupling constants derived from DFT calculations are summarized in Tables 4.16-4.19; the nonlocal coupling constants in the naphthalene crystal (with at least one value larger than 1.0 meV in any of three molecular pairs) are plotted in Figure 4.11. Due to the computationally demanding quantum-chemical evaluation of the transfer integrals, the nonlocal couplings with all the optical modes were only calculated for one representative system of the monoclinic and triclinic crystals (*i.e.*, naphthalene and pentacene, respectively). The results shown in Figure 4.11 reveal a significant coupling to intramolecular vibrations in the naphthalene crystal. The coupling of the carriers to the intermolecular vibrations is again more evident for the molecular pair that shows a herringbone pattern (*i.e.*, pair 2 in naphthalene) and is mainly observed in the ab crystallographic plane; coupling with high-frequency vibrations that would not be thermally activated at room temperature (modes at around 1600 cm^{-1}) was also found. These modes symmetrically stretch the C−C bonds, which in turn distort the HOMO and LUMO wavefuctions, leading to substantial modifications in the energy of the respective frontier molecular orbitals.

Table 4.16 Estimates of the electron (hole)-phonon coupling constants (in meV) of the 105 optical modes in the naphthalene crystal based on DFT normal-mode calculations (see Figure 4.5 for a definition of pair 1, pair 2, and pair 3).

	Holes			Electrons		
$\omega\ (cm^{-1})$	v pair 1	v pair 2	v pair 3	v pair 1	v pair 2	v pair 3
51	0.1	6.1	2.4	-0.4	-6.4	1.4
56	-2.8	-2.0	-0.1	7.0	4.0	-1.6
63	5.3	4.0	-0.5	-10.8	1.2	0.6
75	-0.1	-0.2	-0.7	0.3	3.0	0.9
97	1.5	-0.8	0.3	-4.7	3.6	-0.6
102	1.5	3.0	-0.5	-0.8	-7.8	2.4
121	0.0	-0.2	1.0	0.0	-2.9	-1.0
126	-2.9	1.9	0.2	0.9	0.8	0.8
150	2.3	1.3	-0.3	-0.5	0.0	0.6
180	0.0	2.1	0.1	0.0	4.6	-1.4
200	0.0	-1.7	-0.6	0.0	0.4	-2.3
215	0.0	-0.9	-0.1	0.0	-1.4	-0.3
220	0.0	-5.4	0.0	0.0	3.2	0.3
355	0.0	-0.5	0.2	0.0	-0.1	0.4
358	0.0	0.0	0.0	0.0	-0.2	0.1
386	3.1	1.5	-0.5	-1.9	-1.5	0.8
391	-2.3	-4.1	1.6	1.5	1.4	0.4
462	-0.3	2.3	0.1	-0.6	0.4	-2.1
467	0.0	-2.9	-1.4	0.0	-0.9	-0.1
469	-0.3	2.2	1.2	-0.5	-1.3	-1.0
477	0.0	-2.2	-0.6	0.0	-4.4	0.1
503	1.9	5.2	1.0	-0.1	-0.4	0.3
504	-1.6	0.4	0.0	0.1	-0.3	-0.2
510	-0.2	-0.3	0.0	0.1	2.3	0.1
511	0.2	0.4	-0.7	0.0	0.6	0.1
609	0.0	0.9	-0.1	0.0	-1.5	0.2
611	0.0	2.4	-0.5	0.0	-0.8	-0.2
621	0.0	-3.0	0.5	0.0	1.4	-2.0
626	0.0	4.4	-2.0	0.0	-1.8	1.2
715	-3.7	2.0	-1.1	4.5	-0.5	-0.5
717	1.9	-0.5	-1.3	-2.4	-0.8	-0.2
766	-0.4	1.6	0.9	-0.6	2.0	-1.0
768	-1.4	2.4	0.2	0.0	1.0	-1.8
768	-0.6	-0.3	0.8	0.1	1.7	0.1
768	1.9	-0.4	-0.2	-1.5	-0.9	0.1
772	-2.4	2.2	1.3	1.0	-0.4	-1.4
785	0.0	-0.2	-2.7	0.0	2.5	0.7

789	0.0	0.1	-0.3	0.0	-0.3	0.3
792	0.0	-0.6	0.7	0.0	-0.9	-0.1
837	0.0	2.3	-1.3	0.0	-0.1	0.3
843	0.0	-0.1	1.1	0.0	-1.2	-0.4
875	-1.9	0.7	0.8	0.2	-0.4	0.1
890	2.5	-1.1	0.2	-0.1	-1.1	0.0
920	1.4	1.5	-0.3	2.9	-1.6	-0.3
925	0.0	0.0	-0.1	-2.8	-4.3	1.5
938	3.3	1.1	-0.6	1.1	1.0	0.3
944	-2.8	0.9	1.5	-0.6	0.4	-1.1
952	0.0	1.6	0.6	0.0	-2.5	-0.2
954	0.0	-0.4	-1.3	0.0	0.0	0.6
971	0.0	-2.1	-0.2	0.0	0.5	-0.9
976	1.7	-1.8	0.0	-1.6	1.0	1.3
979	0.0	0.6	-2.0	0.0	-1.5	1.6
980	-1.1	1.2	1.9	1.1	-0.4	-1.5
1026	0.0	-0.8	0.2	0.0	0.1	-0.2
1026	0.0	0.9	-0.8	0.0	-1.0	0.8
1031	-0.2	-0.3	0.5	-0.6	-0.4	-0.6
1035	0.3	-0.2	0.1	0.5	0.3	-0.1
1118	0.0	-0.5	0.3	0.0	-0.2	0.0
1118	0.0	0.6	-0.2	0.0	1.1	0.1
1141	-0.2	0.3	0.0	-3.6	0.9	0.3
1144	0.0	2.4	1.1	3.8	4.1	-1.0
1145	0.0	-2.2	-0.1	1.2	-1.8	0.2
1145	0.0	0.4	0.2	4.3	0.0	-0.8
1154	0.0	-0.2	0.2	-0.2	-1.1	0.0
1154	0.5	1.1	0.3	2.1	2.5	-0.6
1227	0.0	2.5	-0.9	0.0	-1.1	0.3
1227	0.0	-1.9	0.9	0.0	1.6	-0.2
1238	1.1	3.9	0.3	1.3	1.2	-0.5
1241	-1.1	1.3	0.0	-1.2	0.6	0.1
1259	0.0	-0.2	0.2	0.0	-0.2	0.1
1264	0.0	-0.1	0.2	0.0	0.4	0.2
1374	0.0	0.3	-0.1	0.0	-0.4	-0.1
1374	0.0	0.5	-0.3	0.0	0.3	-0.3
1401	0.0	5.5	0.5	0.0	4.8	-0.9
1402	0.0	-0.2	-0.2	0.0	-3.6	0.2
1414	0.0	0.1	0.0	-0.1	-0.7	0.0
1416	0.0	0.2	-0.1	0.0	-0.2	0.5
1445	-0.2	-0.1	0.0	-0.6	0.5	0.0
1450	1.4	3.0	-0.6	0.2	1.1	-0.3
1451	0.3	-1.4	-0.1	0.5	-0.4	0.4

1454	1.0	-0.9	-0.1	-0.2	-0.5	-0.2
1514	0.0	-0.5	0.2	0.0	1.9	-0.2
1516	0.0	4.4	-0.7	0.0	1.5	-0.6
1579	-1.0	0.1	0.1	1.0	-0.3	0.8
1581	1.1	0.4	0.0	-0.8	-0.1	0.0
1600	0.0	-0.4	0.4	0.0	-0.3	-0.3
1600	0.0	2.0	-1.3	0.0	2.2	0.5
1634	-3.6	-11.7	-3.2	-8.6	-10.4	3.5
1635	-3.6	3.3	-0.3	-8.8	3.8	1.0
3110	0.0	0.0	0.1	-0.1	0.0	0.0
3111	0.0	-0.2	0.0	-1.4	0.5	0.2
3112	0.0	0.2	0.0	0.1	0.5	0.0
3113	0.0	0.2	0.1	-1.4	-1.6	0.5
3123	0.0	0.1	0.0	0.0	-0.3	0.0
3124	0.0	0.1	0.1	0.0	0.3	-0.1
3124	0.0	0.0	-0.1	0.1	0.6	-0.1
3124	0.0	-0.1	0.0	0.0	-0.3	-0.1
3133	-0.2	-0.5	0.0	0.7	0.9	-0.2
3134	0.0	-0.2	0.1	0.1	-0.5	-0.1
3134	0.2	0.3	-0.1	-0.6	0.1	0.1
3134	0.0	-0.1	-0.1	0.0	0.2	0.1
3137	0.0	0.3	-0.1	0.0	-0.3	0.1
3138	0.0	0.6	-0.2	0.0	0.1	0.0
3139	0.2	-0.1	0.0	-0.2	0.1	0.0
3141	-0.2	-0.1	0.1	0.2	0.0	0.0
$L\ (meV)$	3.6	7.3	0.8	12.9	10.0	1.1
$\sqrt{G}\ (meV)$	9.3	16.0	5.8	15.2	15.6	6.0

Table 4.17 Estimates of the electron (hole)-phonon coupling constants (in meV) of the 9 optical modes in the anthracene crystal based on DFT normal-mode calculations (see Figure 4.5 for a definition of pair 1, pair 2, and pair 3).

	Holes			Electrons		
$\omega\ (cm^{-1})$	v pair 1	v pair 2	v pair 3	v pair 1	v pair 2	v pair 3
44	-0.4	-5.5	2.0	0.6	3.4	1.2
46	3.4	-1.4	-0.4	-5.1	0.5	0.3
54	-2.2	2.5	0.2	3.9	-2.6	-1.6
73	0.0	1.5	0.7	-0.1	2.4	-0.7
90	1.0	1.9	0.1	-1.7	-1.7	0.1
97	0.4	-3.8	-0.9	0.1	4.4	1.1
120	0.0	-2.8	0.9	0.0	4.5	-0.3
133	-1.5	-1.8	0.0	0.1	-2.1	0.3
149	1.2	3.7	-0.3	-0.2	-2.3	0.0
$L\ (meV)$	1.6	5.1	0.5	3.6	3.8	0.4
$\sqrt{G}\ (meV)$	3.3	6.5	1.8	4.7	6.2	1.8

Table 4.18 Estimates of the electron (hole)-phonon coupling constants (in meV) of the 9 optical modes in the tetracene crystal based on DFT normal-mode calculations (see Figure 4.6 for a definition of pair 1, pair 2, pair 3, and pair 4).

	Holes				Electrons			
$\omega\ (cm^{-1})$	v pair 1	v pair 2	v pair 3	v pair 4	v pair 1	v pair 2	v pair 3	v pair 4
45	-0.2	0.1	5.3	2.2	0.2	-0.1	4.4	4.3
48	4.3	4.6	1.4	0.0	-5.1	-5.0	1.4	-1.2
63	-3.1	4.7	1.4	1.8	3.7	-5.2	0.3	-0.5
74	0.0	-0.1	1.5	1.2	0.0	0.1	-2.2	-2.5
85	-2.3	0.9	-3.1	1.0	2.7	-1.2	-4.1	-0.8
112	-0.6	-1.2	0.2	-0.4	0.6	1.2	-0.4	0.3
125	0.0	0.0	2.6	-6.5	0.0	0.0	4.2	-5.2
139	-0.9	-1.1	-0.1	-0.6	-0.4	0.1	-1.9	2.2
153	-0.7	1.2	-3.1	-9.1	-0.1	-0.2	-1.6	-2.6
$L\ (meV)$	2.5	3.3	3.8	4.4	3.4	4.0	3.7	3.3
$\sqrt{G}\ (meV)$	4.2	4.9	5.5	8.3	4.9	5.2	5.8	5.7

Table 4.19 Estimates of the electron (hole)-phonon coupling constants (in meV) of the 213 optical modes in the pentacene crystal based on DFT normal-mode calculations (see Figure 4.6 for a definition of pair 1, pair 2, pair 3, and pair 4).

	Holes				Electrons			
$\omega\ (cm^{-1})$	v pair 1	v pair 2	v pair 3	v pair 4	v pair 1	v pair 2	v pair 3	v pair 4
45	-0.2	-0.1	-4.1	-0.8	0.1	0.1	1.6	-1.7
48	-3.2	-2.1	1.1	0.2	2.7	1.7	-0.5	0.5
63	0.1	3.2	2.5	0.2	-0.3	-2.8	-1.5	0.1
74	0.0	0.0	-1.4	-0.8	0.0	0.0	-2.8	3.4
77	0.1	-0.1	1.2	0.3	0.0	0.1	0.7	-2.0
85	2.6	-1.8	1.2	-1.3	-2.2	1.4	-2.1	-0.2
111	0.1	0.0	-2.7	3.2	0.0	0.0	3.0	3.6
112	-0.9	-0.7	0.2	0.8	0.6	0.4	0.7	0.4
125	0.0	0.0	3.0	-5.8	0.0	0.0	-3.8	-3.5
126	0.0	0.0	-0.5	2.4	0.0	0.0	0.9	0.7
130	0.0	0.0	-2.2	2.7	0.0	0.0	1.9	2.5
134	0.5	-0.3	-0.1	0.6	-0.3	-0.4	0.3	0.7
139	0.5	0.5	-0.3	-1.6	0.1	0.1	-1.5	-2.6
142	0.0	0.0	-3.8	0.8	0.0	0.0	1.0	-0.1
148	0.3	0.0	0.2	-1.1	-0.1	0.2	1.7	0.7
153	0.5	-0.3	5.2	8.4	0.2	0.0	-2.2	2.0
159	0.0	0.0	0.8	0.5	0.0	0.0	0.0	0.0
188	-0.5	-1.0	-1.5	0.5	-0.5	-0.7	-0.1	-1.3
195	-0.9	0.5	3.7	4.2	-0.8	0.5	-2.2	2.3
202	0.0	0.0	0.3	0.1	0.0	0.0	-0.1	0.0
212	0.0	0.0	0.1	-0.5	0.0	0.0	-0.2	0.0
239	0.9	0.6	0.5	-0.1	-0.3	-0.2	0.2	0.1
240	0.6	-0.9	0.1	0.3	-0.3	0.4	-0.3	0.2
253	0.0	0.0	-0.9	0.2	0.0	0.0	0.4	0.0
259	0.0	0.0	0.9	0.1	0.0	0.0	0.2	-0.1
265	-0.3	0.4	-0.1	-0.2	0.4	-0.5	-1.2	1.5
267	0.4	0.3	0.2	0.1	-0.5	-0.4	0.1	0.2
298	0.0	-0.3	-0.3	-0.1	0.0	-0.1	-0.2	0.2
300	-0.3	-0.1	0.0	0.1	0.0	0.0	-0.1	0.0
350	0.0	-0.2	-0.2	0.3	-0.1	-0.3	0.1	0.0
351	0.0	0.0	-0.2	-0.3	0.0	0.0	-0.1	0.2
351	0.0	0.0	-0.4	-0.4	0.0	0.0	-0.2	0.0
353	0.1	0.0	-0.3	-0.1	0.3	-0.1	0.2	-0.5
385	0.0	0.0	0.3	-0.1	0.0	0.0	-0.5	0.1
386	0.0	0.0	0.1	-0.1	0.0	0.0	0.2	-0.4
437	-0.1	-0.1	-0.2	0.1	-0.1	-0.2	-0.2	-0.2
438	0.1	-0.1	0.2	0.0	0.2	-0.1	-0.1	0.1

452	0.0	0.0	2.9	-4.0	0.0	0.0	0.1	-0.5
460	-1.8	-2.3	-1.4	0.1	0.9	1.1	-0.2	0.2
464	0.0	0.0	-1.4	-2.8	0.0	0.0	-2.8	3.2
470	-2.2	1.6	1.9	0.4	1.1	-0.8	0.2	0.0
470	0.0	0.0	1.2	-1.0	0.0	0.0	-0.7	-1.0
473	0.0	0.6	0.6	0.1	0.1	-0.2	0.2	0.0
475	0.0	0.0	0.7	0.6	0.0	0.0	-0.4	0.4
478	-0.8	0.7	0.8	0.1	0.3	-0.3	0.1	-0.1
481	0.0	0.0	-0.2	0.2	0.0	0.0	0.2	0.0
483	0.0	0.0	-0.3	0.3	0.0	0.0	0.6	0.0
493	0.0	0.1	-0.1	0.2	0.0	-0.4	-0.1	-0.2
494	-0.1	-0.1	0.4	0.0	0.4	0.0	0.1	0.2
509	0.0	0.0	0.8	0.0	0.0	0.0	0.0	0.0
513	0.0	0.0	-0.6	-0.2	0.0	0.0	-0.2	0.0
543	0.0	-0.1	0.1	0.6	0.0	-0.3	0.2	-0.2
546	-0.2	0.0	-0.2	-0.1	-0.3	0.0	-0.1	0.7
566	0.0	0.0	-0.5	0.3	0.0	0.0	-0.3	-0.3
566	0.0	0.0	-1.3	-1.9	0.0	0.0	-0.8	0.9
594	-0.2	0.2	0.0	0.0	0.2	-0.2	0.0	0.1
596	0.1	0.2	-0.1	-0.1	-0.2	-0.2	0.0	-0.2
613	0.0	0.0	0.4	0.0	0.0	0.0	-0.2	-0.1
614	0.0	0.0	0.0	-0.1	0.0	0.0	-0.2	-0.1
618	0.0	0.0	0.0	0.0	0.0	0.0	-0.1	0.1
618	0.0	0.0	0.0	0.0	0.0	0.0	-0.1	0.0
696	0.0	0.0	-0.3	0.0	0.0	0.0	0.2	0.0
696	0.0	0.0	-0.2	-0.1	0.0	0.0	0.0	0.0
710	-0.2	0.0	-0.6	0.0	-0.8	-0.1	-0.4	-0.2
710	0.0	-0.2	-0.2	0.0	0.1	-0.8	0.0	-0.1
725	0.0	0.0	0.2	-0.2	0.0	0.0	-0.9	0.6
731	-0.1	-0.4	-0.1	-0.3	0.1	0.9	0.0	-0.1
737	-0.4	-0.1	0.3	0.2	0.6	0.1	0.0	-0.4
738	-0.1	0.2	0.7	1.2	0.2	-0.2	-0.1	-0.2
738	0.0	0.0	-0.3	-0.4	0.0	0.0	-1.1	-1.0
742	-0.2	0.1	-0.2	-0.2	0.7	-0.1	0.1	0.2
742	0.1	0.0	0.7	0.0	-0.2	0.0	-0.1	-0.4
743	0.0	0.0	0.7	0.1	0.0	0.0	0.3	0.0
753	-1.7	-1.5	-0.3	0.7	2.3	2.0	-0.2	-0.1
756	1.0	-1.2	-0.4	-0.5	-1.3	1.7	2.1	-2.0
757	0.0	0.0	-1.4	0.2	0.0	0.0	-0.2	-0.2
760	0.0	0.0	0.1	0.0	0.0	0.0	0.1	-0.1
765	1.0	1.2	0.5	-0.7	-1.3	-1.5	2.0	1.8
770	1.4	-1.5	-1.1	-1.2	-1.8	1.9	-0.9	0.7
791	0.2	-0.1	-0.1	-0.1	0.0	-0.1	-0.4	0.3

792	-0.2	-0.2	-0.1	0.1	0.0	0.0	-0.3	0.0
818	0.0	0.0	-0.2	-0.2	0.0	0.0	0.1	-0.2
818	0.0	0.0	0.1	0.2	0.0	0.0	-0.3	0.0
829	0.0	0.0	-0.2	0.0	0.0	0.0	0.1	0.1
831	-0.2	-0.4	-0.2	-0.2	0.0	-0.1	0.3	0.1
832	0.4	-0.2	0.1	-0.3	0.1	-0.1	0.2	-0.3
833	0.0	0.0	0.1	0.0	0.0	0.0	-0.1	-0.1
840	0.0	0.0	-0.3	0.0	0.0	0.0	-0.1	-0.1
841	0.0	0.0	0.3	-0.1	0.0	0.0	-0.1	0.2
860	0.1	0.0	0.0	0.1	-0.1	-0.2	0.2	0.1
862	0.0	-0.1	-0.2	0.0	-0.1	0.1	-0.2	-0.1
874	0.0	0.0	-0.1	0.0	0.0	0.0	0.1	0.0
875	0.0	0.0	0.0	0.0	0.0	0.0	-0.1	0.0
881	1.0	0.9	0.3	0.0	-0.2	-0.2	0.1	-0.1
883	1.0	-1.0	0.4	-0.2	-0.2	0.3	-0.3	-0.4
887	0.0	0.0	1.4	-0.5	0.0	0.0	-0.9	-0.5
891	0.0	0.0	0.3	0.3	0.0	0.0	0.0	0.2
896	0.0	0.0	0.4	-0.3	0.0	0.0	-0.5	-0.6
897	0.0	0.0	0.4	0.4	0.0	0.0	1.0	-1.3
905	0.1	0.1	0.7	-1.0	-0.1	-0.1	-1.8	-2.2
906	1.3	1.3	0.1	0.0	-1.7	-1.5	0.5	0.8
907	0.9	0.6	0.2	-0.2	0.0	-0.5	0.7	0.2
907	0.0	0.0	0.5	1.2	0.1	0.2	0.3	0.5
908	0.0	-0.4	-0.3	-0.1	0.2	-0.7	-0.1	-0.2
913	-1.5	1.5	-1.2	-2.1	1.6	-1.7	2.6	-2.9
949	0.5	2.2	0.1	-0.3	0.1	-0.2	0.0	-0.1
952	0.0	0.0	-0.2	0.1	0.0	0.0	0.1	0.5
953	-2.1	0.6	-0.6	-0.1	0.1	-0.1	0.0	-0.1
955	-0.1	0.0	-0.3	-0.2	0.0	0.0	0.5	-0.7
964	0.0	0.0	-0.3	0.0	0.0	0.0	0.4	0.1
967	-0.3	-0.6	0.0	-0.2	0.1	0.3	-0.3	0.3
969	0.0	0.0	-0.6	-0.1	0.0	0.0	0.0	-0.1
970	-0.6	0.3	-0.4	0.4	0.3	-0.2	0.6	-0.2
1015	0.0	0.0	0.5	0.1	0.0	0.0	0.3	-0.2
1016	0.0	0.0	0.5	0.1	0.0	0.0	0.2	0.0
1016	0.0	-0.2	-0.1	0.0	0.0	-0.2	-0.2	0.2
1019	-0.3	0.0	-0.2	-0.1	0.0	0.0	0.2	-0.5
1116	0.0	0.0	-0.4	-0.3	0.0	0.0	-0.2	0.1
1117	0.0	0.0	-0.3	-0.9	0.0	0.0	0.1	0.3
1132	-0.8	-0.3	-0.4	0.1	0.3	0.1	-0.2	-0.1
1135	0.3	-0.8	-0.4	-0.1	-0.1	0.4	-0.2	0.0
1142	0.0	0.0	0.9	0.1	0.0	0.0	0.6	-0.1
1144	0.0	0.0	-0.8	-0.1	0.0	0.0	-0.4	0.4

1151	0.2	0.2	0.1	-0.1	-0.1	-0.1	-0.2	-0.2
1155	0.0	-0.3	-0.2	0.1	0.0	0.1	0.1	0.2
1160	0.0	0.0	0.3	-0.2	0.0	0.0	0.6	0.3
1161	0.0	0.0	0.1	0.1	0.0	0.0	1.5	-0.2
1171	-0.2	-0.8	-1.1	0.4	-0.1	-0.5	-0.6	-0.3
1173	-0.8	0.2	-1.3	0.1	-0.6	0.1	-0.4	-0.4
1182	0.0	0.0	0.3	1.0	0.0	0.0	-1.3	0.9
1183	0.0	0.0	0.1	0.4	0.0	0.0	-0.3	1.4
1189	0.2	0.5	0.3	-0.2	-0.2	-0.4	-0.3	-0.5
1191	0.5	-0.2	0.0	-0.2	-0.4	0.2	-0.1	-0.2
1226	0.0	0.1	0.0	0.0	0.1	0.2	0.3	0.0
1227	0.1	-0.1	0.0	0.0	0.2	-0.1	0.0	0.0
1235	0.0	0.0	0.3	0.0	0.0	0.0	-0.1	0.0
1236	0.0	0.0	-1.2	-0.2	0.0	0.0	0.4	0.2
1264	0.0	0.0	0.2	0.6	0.0	0.0	0.2	-0.2
1265	0.0	0.0	-0.4	-0.2	0.0	0.0	-0.2	0.2
1266	0.1	0.3	-0.2	0.1	0.0	-0.3	0.1	0.0
1267	0.3	0.0	-0.6	0.0	-0.3	0.0	0.0	0.0
1277	-0.2	-0.3	0.3	-0.1	0.1	0.2	-0.2	-0.1
1278	-0.3	0.2	0.5	0.1	0.2	-0.1	0.0	-0.1
1285	0.0	0.0	-0.5	0.3	0.0	0.0	0.6	0.3
1289	0.0	0.0	-0.4	0.1	0.0	0.0	-1.2	1.1
1321	0.0	-0.1	-0.1	0.1	0.0	0.1	0.0	0.1
1321	-0.1	0.0	0.0	0.1	0.1	0.0	0.1	0.0
1337	0.0	0.0	-0.1	-0.2	0.0	0.0	-0.2	0.0
1339	0.0	0.0	-0.3	-0.7	0.0	0.0	0.1	0.1
1377	0.0	0.0	-1.4	-0.4	0.0	0.0	-2.3	0.9
1381	-0.3	0.0	0.1	0.0	0.0	0.0	-0.2	-0.1
1382	0.0	0.0	-0.3	0.2	0.0	0.0	-1.5	-0.4
1384	0.0	0.3	0.1	0.1	0.0	0.0	0.3	0.1
1410	0.0	0.0	-0.6	0.1	0.0	0.0	-0.2	0.0
1411	0.0	0.0	1.4	0.2	0.0	0.0	-0.4	-0.2
1415	0.4	0.4	0.5	-0.4	0.3	0.3	-0.1	-0.3
1418	0.4	-0.4	0.2	0.0	0.3	-0.3	-0.5	0.8
1419	0.0	0.0	0.6	0.3	0.0	0.0	-0.5	-0.1
1420	0.0	0.0	-1.9	-0.1	0.0	0.0	0.4	0.3
1424	-0.1	-0.2	-0.3	-0.2	0.1	0.2	-0.4	-0.2
1425	-0.1	0.1	-0.2	-0.1	0.3	-0.1	-0.3	0.2
1442	0.0	0.0	-1.8	0.0	0.0	0.0	0.1	0.2
1443	0.0	0.0	-1.0	-0.3	0.0	0.0	0.0	0.1
1447	0.0	0.0	0.1	0.0	0.0	0.0	-0.1	0.0
1447	0.0	0.0	-0.4	-0.2	0.0	0.0	0.1	0.3
1462	-0.1	-0.1	-0.2	-0.1	0.2	0.2	0.2	0.0

1462	0.1	-0.1	-0.1	-0.1	-0.2	0.2	0.4	-0.1
1511	0.0	0.0	-0.6	0.0	0.0	0.0	0.3	0.0
1512	0.0	0.0	1.1	0.2	0.0	0.0	-0.3	-0.1
1521	1.1	1.3	1.1	-0.8	-0.5	-0.6	-0.2	-0.7
1526	1.3	-1.1	0.0	-0.4	-0.6	0.5	-0.1	0.2
1545	0.0	0.1	-0.3	-0.2	-0.1	-0.5	-0.8	-0.4
1547	0.0	0.0	-2.0	0.2	0.0	0.0	-0.3	0.1
1548	0.1	-0.1	-0.3	-0.2	-0.4	0.2	-0.1	0.1
1549	0.0	0.0	-4.5	-0.7	0.0	0.0	0.6	0.6
1553	0.0	-0.2	-0.1	0.0	0.0	0.2	-0.1	0.0
1554	-0.2	0.0	-0.2	0.1	0.2	0.0	0.0	0.0
1597	1.8	2.4	5.0	-1.2	0.6	0.6	1.7	1.1
1598	-2.4	1.8	-2.4	-0.3	-0.7	0.5	-0.3	-0.2
1602	0.0	0.0	-0.2	-0.3	0.0	0.0	0.0	-0.1
1603	0.0	0.0	0.6	0.2	0.0	0.0	-0.1	0.2
1629	-0.1	-0.3	-0.5	0.0	0.2	0.7	0.7	0.1
1631	0.3	-0.1	0.4	-0.1	-0.8	0.3	-0.4	0.0
1631	0.0	0.0	-0.2	-2.8	0.0	0.0	1.5	-0.6
1632	0.0	0.0	-1.2	-3.0	0.0	0.0	2.3	-3.3
3110	0.0	0.0	0.2	0.2	0.0	0.0	0.2	-0.3
3112	0.0	0.0	-0.1	-0.2	0.0	0.0	-0.2	0.2
3112	-0.1	0.1	0.1	0.0	-0.2	0.0	0.0	-0.1
3113	0.0	0.1	0.1	0.0	0.1	0.1	0.1	0.0
3115	0.0	0.0	0.3	0.6	0.0	0.0	0.0	0.1
3116	-0.1	0.0	0.0	0.0	0.0	0.0	0.0	-0.1
3116	0.0	0.0	0.1	0.2	0.0	0.0	0.1	0.0
3117	-0.1	0.0	0.0	0.0	0.0	0.0	0.0	-0.1
3117	0.0	0.1	0.2	-0.1	0.0	-0.1	0.0	0.0
3117	0.0	0.0	0.3	-0.1	0.0	0.0	-0.1	-0.1
3118	0.0	0.0	0.0	0.0	0.0	0.0	0.1	0.0
3119	0.0	0.0	0.0	0.1	0.0	0.0	0.1	0.0
3120	0.0	0.2	0.1	0.0	0.0	0.0	-0.1	0.1
3120	0.0	0.1	0.2	0.1	0.0	0.0	0.2	-0.1
3121	-0.2	0.0	0.0	0.2	0.3	0.1	0.0	0.1
3122	-0.1	0.1	0.0	0.1	0.1	-0.2	-0.2	0.1
3122	0.0	0.0	-0.2	0.1	0.0	0.0	-0.1	0.3
3122	0.2	0.1	0.1	-0.3	-0.1	-0.1	0.2	-0.1
3123	0.0	0.0	0.1	0.1	0.0	0.0	0.2	-0.1
3124	0.0	-0.3	-0.2	0.0	0.0	0.2	0.2	-0.3
3128	-0.1	0.0	0.1	-0.1	0.1	0.0	0.0	-0.1
3128	0.2	0.0	0.1	-0.1	-0.1	0.0	0.0	-0.1
3130	0.0	0.0	0.0	0.0	0.0	0.0	-0.2	0.1
3131	0.0	-0.2	-0.2	0.0	0.0	0.2	0.1	0.0

3139	-0.1	0.0	0.1	0.1	0.1	0.0	0.0	0.1
3141	0.0	0.0	-0.2	-0.1	0.0	0.0	0.2	-0.1
3141	0.0	-0.1	-0.1	0.1	0.0	0.1	0.1	0.0
3143	0.0	0.0	0.3	0.0	0.0	0.0	-0.1	0.1
$L\ (meV)$	1.5	1.5	4.9	4.8	1.0	1.0	2.7	3.1
$\sqrt{G}\ (meV)$	5.6	5.7	10.7	10.5	4.5	4.5	8.0	8.2

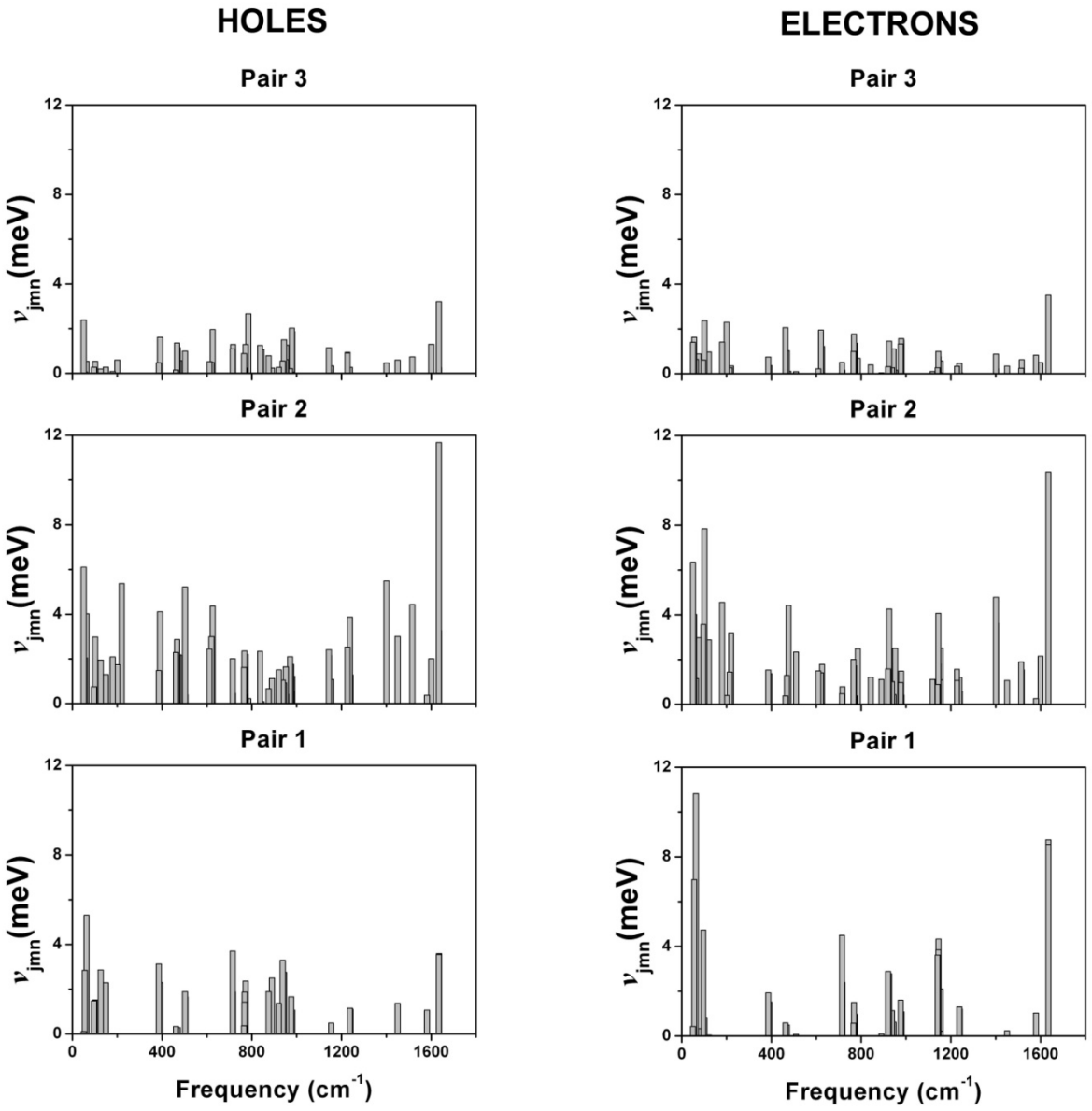

Figure 4.11 DFT estimates of the hole-phonon and electron-phonon couplings in the naphthalene crystal as a function of phonon energy.

Figures 4.12-4.14 show the contribution of each phonon frequency to the total intermolecular relaxation energy in the naphthalene and pentacene crystals, respectively. In naphthalene 83% and 93% of the total hole and electron intermolecular relaxation energies for pair 1 come from vibrational modes with phonon frequencies below 150 cm^{-1}. In pair 2, redistribution to normal modes with phonon frequencies in the range of 200-600 cm^{-1} is observed for both holes and electrons. In this case, such a redistribution reduces the contribution of the intermolecular vibrations (67% and 82% of the total coupling for holes and electrons, respectively). These findings again confirm the importance of including intramolecular vibrations in the investigation nonlocal coupling constants in organic molecular crystals. In pair 3, the values for the hole- and electron-phonon coupling are at least one order of magnitude smaller than those derived for pair 1 and pair 2. In pair 3, the intramolecular vibrations of the crystal have the largest contribution among the three pairs, reducing the contribution of the intermolecular modes to 65% for both holes and electrons. As shown by Figures 4.13 and 4.14, a similar picture holds in the pentacene crystal. Here, the contributions of the normal modes with phonon frequencies below 150 cm^{-1} to the total intermolecular relaxation energy for both holes and electrons are large for pair 1 and pair 2 (~80%) and decrease for pair 3 and pair 4 (~70%), due to a rather modest redistribution towards normal modes with larger phonon frequencies.

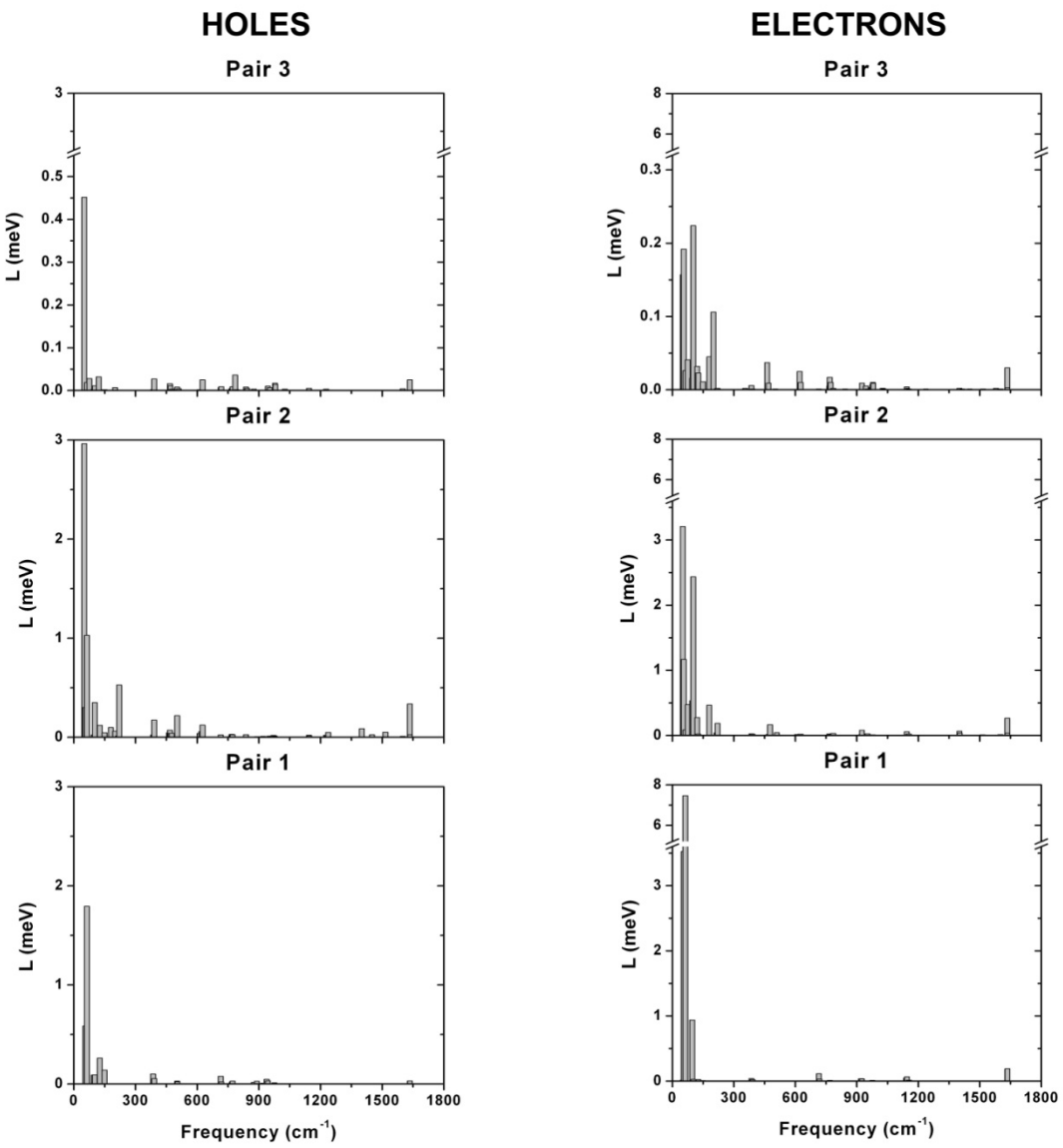

Figure 4.12 DFT estimates of the intermolecular relaxation energy (*L*) in the naphthalene crystal.

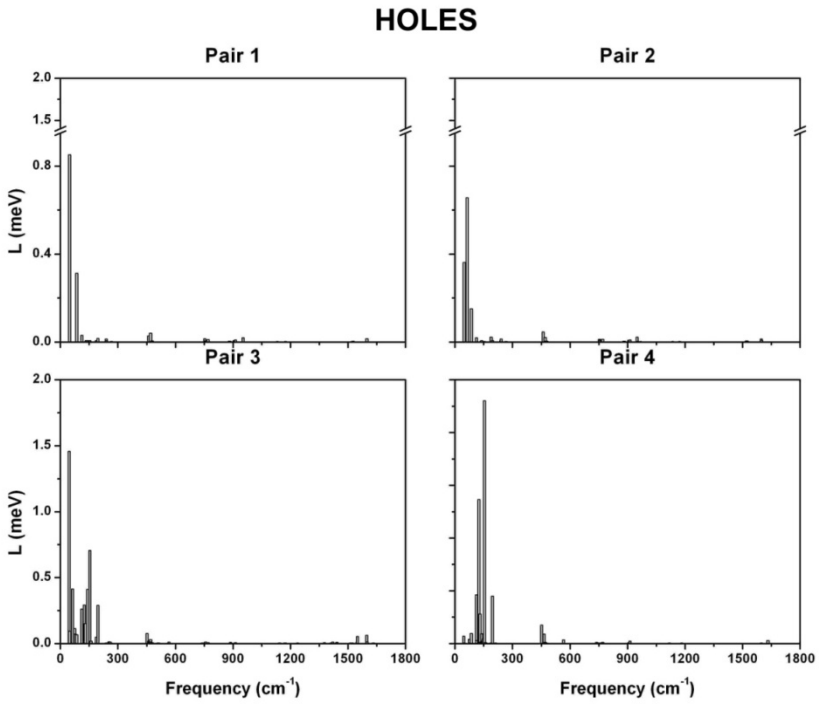

Figure 4.13 DFT estimates of the intermolecular relaxation energy (L) for holes in the pentacene crystal.

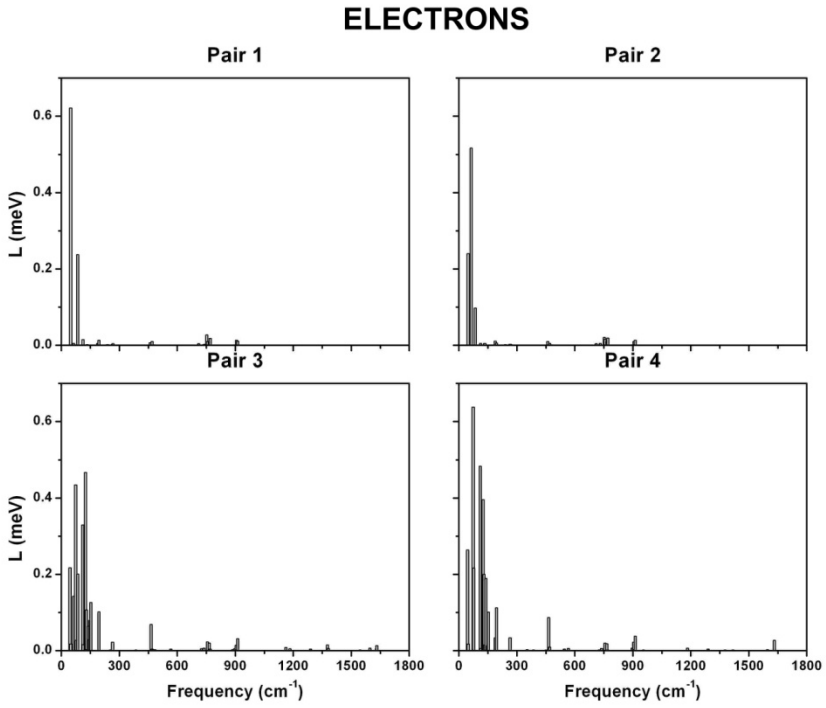

Figure 4.14 DFT estimates of the intermolecular relaxation energy (L) for electrons in the pentacene crystal.

4.3.4.3 Classical and quantum-mechanical distributions of the transfer integrals

In order to determine the dependence of the amplitude of a given normal mode by the temperature and its effect on the modulation of the transfer integral, classical (CM) and quantum-mechanical (QM) methods were used to sample the nuclear fluctuations. In classical dynamics, the potential energy of any normal mode is $\frac{\hbar\omega_j}{2}Q_j^2$ (where $\hbar\omega_j$ represents the energy of a phonon). In equilibrium at temperature T, the averages of the potential and kinetic energies are both equal to $\frac{k_BT}{2}$; they depend only on temperature and not on the frequency of the motions. Thus, the classical mean-square fluctuation of Q_j is:

$$\langle Q_j^2\rangle_{CM} = \frac{k_BT}{\hbar\omega_j} \tag{4.5}$$

In a quantum-mechanical dynamics context each normal mode will behaves as an harmonic oscillator with energy levels equally separated by $\hbar\omega_j$. The mean-square fluctuation of normal-mode Q_j is related to temperature via:

$$\langle Q_j^2\rangle_{QM} = \frac{1}{2}coth\left(\frac{\hbar\omega_j}{2k_BT}\right) \tag{4.6}$$

At 300 K, $\langle Q_j^2\rangle_{QM}$ tends to $\frac{k_BT}{2}$, which is the classical value. By using $coth(y) = (e^y + e^{-y})/(e^y - e^{-y})$, $\langle Q_j^2\rangle_{QM}$ can be rewritten as follows:

$$\langle Q_j^2\rangle_{QM} = \frac{1}{e^{\frac{\hbar\omega_j}{k_BT}} - 1} + \frac{1}{2} \tag{4.7}$$

Note also that the thermal energy of normal mode j is given by:

$$E_j^{th} = \left(v_j^{th} + \frac{1}{2}\right)\hbar\omega_j \tag{4.8}$$

where v_j^{th} is the average number of excited quanta in the oscillator and is given by the usual Bose-Einstein distribution, that is:

$$v_j^{th} = \frac{1}{e^{\frac{\hbar\omega_j}{k_B T}} - 1} \tag{4.9}$$

It is worth recalling that even at 0 K, $E_j^{th} = \frac{1}{2}\hbar\omega_j$; it is not zero as in the classical limit. This energy corresponds to the zero-point energy of the harmonic oscillator and is a direct result of the Uncertainty Principle.[37]

Here, the formalism discussed above is used to define the classical (σ_{CM}^2) and quantum-mechanical (σ_{QM}^2) variance of the transfer integrals as a function the temperature. The variance is represented by the square of the standard deviation, σ:

$$\sigma^2 = \langle (t_{mn} - \langle t_{mn} \rangle)^2 \rangle = \langle t_{mn}^2 \rangle - \langle t_{mn} \rangle^2 \tag{4.10}$$

By using Equation 4.2, the terms in this expression can be defined as follows:

$$\langle t_{mn} \rangle = t_{mn}^{(0)} \tag{4.11}$$

$$\langle t_{mn}^2 \rangle = \left(t_{mn}^{(0)}\right)^2 + \left(\sum_j v_{jmn} Q_j\right)^2 \tag{4.12}$$

The substitution of Equations 4.11 and 4.12 into Equation 4.10 leads to the following expression:

$$\sigma^2 = \left(\sum_j v_{jmn} Q_j \right)^2 \tag{4.13}$$

The subsequent substitution of Q_j^2 in Equation 4.13 by Equations 4.5 and 4.7 leads to the analytical expressions of the classical and quantum-mechanical variance:

$$\sigma_{CM}^2 = \sum_j v_{jmn}^2 \frac{k_B T}{\hbar \omega_j} \tag{4.14}$$

$$\sigma_{QM}^2 = \sum_j v_{jmn}^2 \left(\frac{1}{e^{\frac{\hbar \omega_j}{k_B T}} - 1} + \frac{1}{2} \right) \tag{4.15}$$

4.3.4.4 Temperature dependence of the hole- and electron-phonon interactions

Equations 4.14 and 4.15 and the nonlocal hole- and electron-phonon couplings constants reported in Tables 4.16 and 4.19 were used to investigate the interaction between the thermally-activated normal-mode vibrations and the charge carriers in the naphthalene and pentacene crystals. The calculated classical and quantum-mechanical standard deviations for the two molecular crystals are shown in Figures 4.15 and 4.16. We start our discussion with the naphthalene crystal.

As shown in Figure 4.15, the dependence of the vibronic couplings on the temperature is stronger for the case of the electrons and this effect is mainly observed along the ab plane (pairs 1 and 2). At room temperature, the differences between the classical and quantum-mechanical samplings are less than 3 meV for both holes and

electrons for the three pairs. It is also important to note that the quantum-mechanically calculated zero-point fluctuations are large when compared to those derived at room temperature. In fact, σ_{QM} at 300 K is on average 1.4 times larger than the deviation obtained at 0 K for the case of holes and 1.6 times larger for the electrons. From Figure 4.15, it is clear that a purely classical approach (σ_{CM}) would tend to overestimate the temperature dependence of the normal-mode vibrations and its effect on the modulation of the transfer integral.

The plots of the standard deviations as a function of the temperature for the pentacene crystal are shown in Figure 4.16. In the pentacene crystal, the σ_{CM} and σ_{QM} values show the largest temperature dependence for the edge-to-face molecular dimers (*i.e.*, pair 3 and pair 4). However, in this molecular crystal the temperature has a stronger effect on the holes than on the electrons (in contrast to the naphthalene case). At room temperature the differences between σ_{CM} and σ_{QM} are less than 1 meV. The zero-point fluctuations have a similar effect as in the naphthalene crystal; in pentacene, σ_{QM} at 300 K is on average 1.6 times larger than that at 0 K for both electrons and holes.

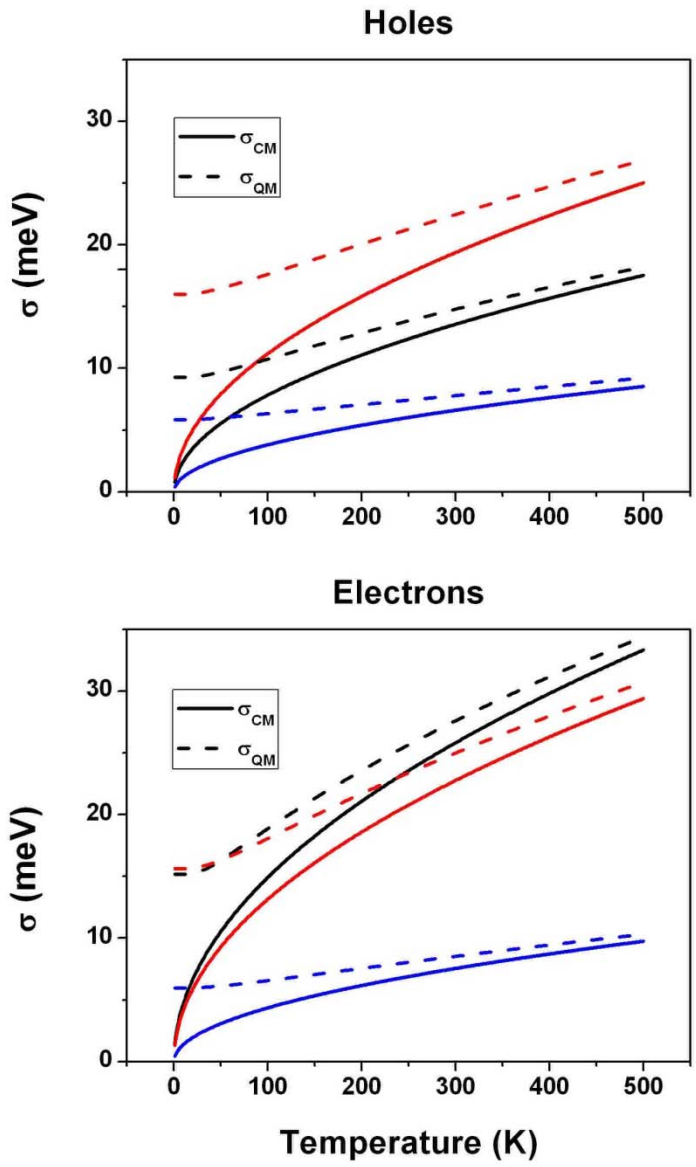

Figure 4.15 Classical and quantum-mechanical standard deviations of the hole-phonon coupling (top) and electron-phonon coupling (bottom) as a function of temperature for pair 1 (black), pair 2 (red), and pair 3 (blue) in the naphthalene crystal.

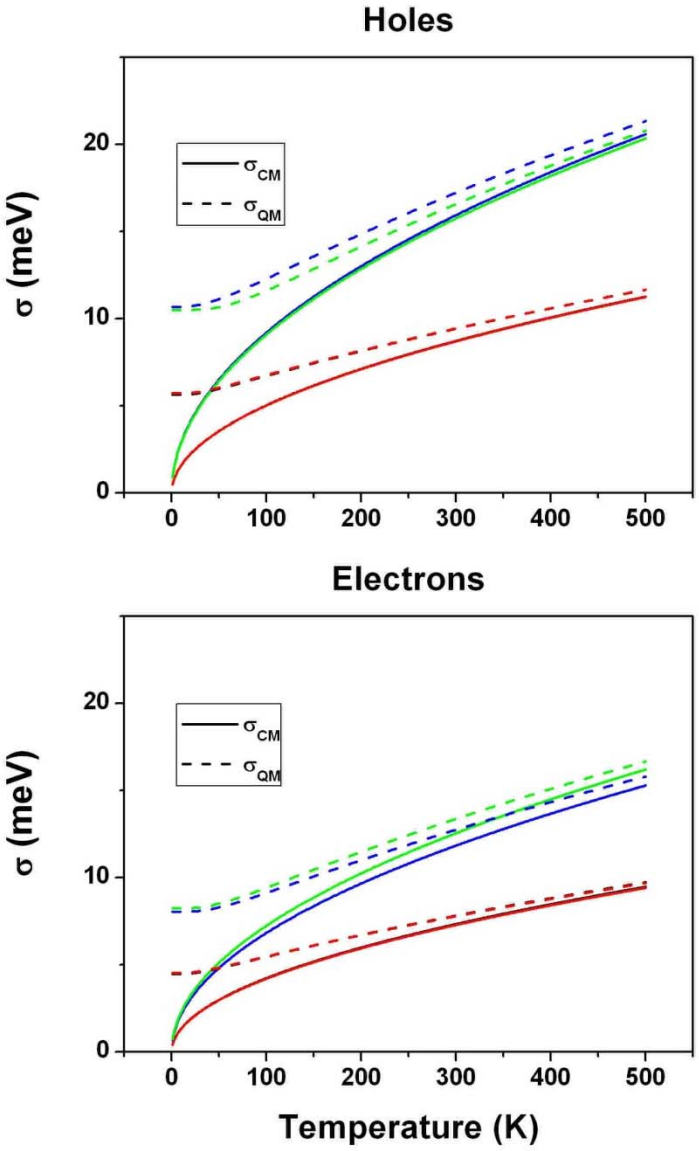

Figure 4.16 Classical and quantum-mechanical standard deviations of the hole-phonon coupling (top) and electron-phonon coupling (bottom) as a function of temperature for pair 1 (black), pair 2 (red), pair 3 (blue), and pair 4 (green) in the pentacene crystal. Note: the standard deviations for holes and electrons in pairs 1 and 2 display the same evolution as a function of the temperature; therefore, the red curves appear on top of the black ones.

4.3.4.5 Intermolecular relaxation energies from MDS

Inspection of Figures 4.15 and 4.16 reveals a close agreement between the classical and quantum-mechanical standard deviations at 300 K (σ_{CM} and σ_{QM}, respectively) for the naphthalene and pentacene crystals. This finding suggests that, in principle, simulation techniques that use a classical dynamics approach should be appropriate to investigate the modulation of transfer integrals by thermally-activated vibrations in organic molecular crystals. In this context, a mixed quantum-chemical and MDS methodology was used to provide further computational evidence of the role played by normal-mode vibrations in defining the charge-transport properties in organic molecular crystals; note that the main advantage of MDS is to encompass all vibrational modes of the system instead of a few effective modes, as is typically done in phenomenological models.[1, 2] The combined methodology used here represents an extension of the work reported by Troisi and co-workers, in which it was demonstrated that the transfer integrals are strongly modulated by thermal vibrations at room temperature.[38, 39] When applied to molecular crystals of pentacene and rubrene,[38, 40] this approach yields a quasi-Gaussian distribution of the transfer integrals for holes and, in a number of instances, the standard deviation is found to be as large as the value of the transfer integral obtained from undistorted molecular dimers. More importantly, the combination of Equations 4.4 and 4.14 leads to an expression that correlates the standard deviation (σ) with the intermolecular relaxation energy (L), that is:

$$\sigma = \sqrt{2 \cdot L \cdot k_B T} \tag{4.16}$$

By using Equation 4.16 and the fact that transfer integrals for holes and electrons have a nearly Gaussian distribution, a comparison between the values of L derived from DFT approaches and from MDS can be established.

In Figure 4.17, the distributions for the transfer integrals of holes and electrons in pair 1 and pair 2 of the naphthalene crystal are presented. The standard deviations of the transfer integrals are also indicated (assuming a complete Gaussian distribution) as inset in the figure. In the case of DFT, the standard deviations are derived from Equation 4.16 and values of L reported in Table 4.16. A reasonable correspondence in the standard deviations of the transfer integrals for holes in pairs 1 and 2 is found between the DFT and MDS methods, *i.e.*, in pair 1 $\sigma_{MDS} = 23.9\ meV$ *versus* $\sigma_{DFT} = 13.4\ meV$ and in pair 2 $\sigma_{MDS} = 23.1\ meV$ *versus* $\sigma_{DFT} = 19.1\ meV$. The validity of the comparison can be understood upon the assumption that in DFT methods, only optical vibrations at the Γ-point are considered while in MDS dispersive vibrations both acoustic and optical are present (*i.e.*, the standard deviation obtained from MDS should be larger than that of DFT). For electrons, the situation is different since the standard deviations derived from DFT methods are on average 5 meV larger than those derived with MDS approaches. A reason for that discrepancy can be attributed to the lesser ability of the semi-empirical methods to estimate transfer integrals for electrons. In this study, it was observed that in case of the naphthalene crystal the transfer integral values for holes calculated using semi-empirical methods are in good agreement with those obtained from *ab initio* methods (see Table 4.6); however, the transfer integrals for electrons do not present the same agreement, especially for pair 2 where $t_{pair2}^{el} = -14\ meV$ *versus* $t_{pair2}^{el} = 35\ meV$

for semi-empirical and *ab initio* methods, respectively. At this point, a clear correspondence between DFT and MDS methods to estimate the values of intermolecular relaxation energy cannot be established yet. To achieve a better understanding of the respective merits of the two proposed methods, it will be helpful to evaluate the transfer integrals at a high level of theory for the molecular configurations obtained from MDS. While this clearly represents a computationally demanding task, it can be planned at least for the naphthalene crystal and on those dimers that show significant coupling with lattice vibrations (*i.e.*, pair 1 and pair 2).

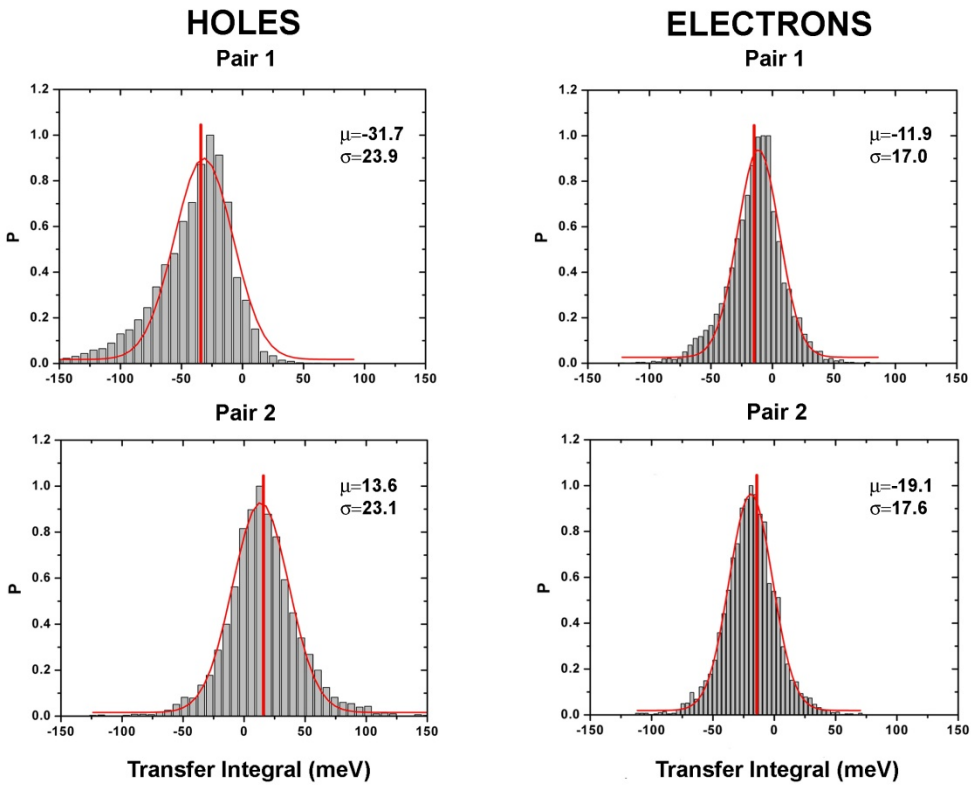

Figure 4.17 Normalized probability distribution of the transfer integrals for holes and electrons in pair 1 and pair 2 of the naphthalene crystal. The average value μ and the standard deviation σ are also reported. The vertical lines (in red) correspond to the transfer integrals of the two molecular dimers obtained from the optimized geometry at the MM3 force field level.

4.4 Conclusions

In this study, a first-principles methodology to characterize the interaction between holes/electrons and the low-frequency optical phonons at the Γ-point has been developed. It was found that holes and electrons in oligoacenes are substantially affected by both intermolecular and intramolecular vibrations. This vibronic coupling effect, quantified in terms of the intermolecular relaxation energy L, is more significant in naphthalene than in pentacene and is mainly dominated by intermolecular vibrations. In addition, it was also observed that the contributions of zero-point vibrations are larger in small organic molecular crystals. The electronic-structure calculations performed in this study further confirm that transport in oligoacene single crystals is mostly two-dimensional. Also, standard deviations of the transfer integrals in the naphthalene crystal were obtained from both DFT and MDS methods. Our preliminary results open the possibility of evaluations of the transfer integrals at a high level of theory in studies that evaluate the effect of nuclear dynamics on the modulation of the transfer integrals between neighboring molecules. Finally, it is our aim to extend this fully integrated methodology to other organic molecular crystals in order to more completely characterize the charge-transport properties of organic semiconductors.

4.5 References

(1) Hannewald, K.; Stojanovic, V. M.; Schellekens, J. M. T.; Bobbert, P. A.; Kresse, G.; Hafner, J. *Physical Review B* **2004**, *69*, 075211.

(2) Wang, L. J.; Peng, Q.; Li, Q. K.; Shuai, Z. *Journal of Chemical Physics* **2007**, *127*, 044506.

(3) Perdew, J. P.; Burke, K.; Ernzerhof, M. *Physical Review Letters* **1996**, *77*, 3865.

(4) Kresse, G.; Furthmuller, J. *Computational Materials Science* **1996**, *6*, 15.

(5) Kresse, G.; Hafner, J. *Phys. Rev. B* **1993**, *47*, 558.

(6) Kresse, G.; Hafner, J. *Phys. Rev. B* **1994**, *49*, 14251.

(7) Blochl, P. E. *Physical Review B* **1994**, *50*, 17953.

(8) Kresse, G.; Joubert, D. *Physical Review B* **1999**, *59*, 1758.

(9) Willock, D. J.; Price, S. L.; Leslie, M.; Catlow, C. R. A. *Journal of Computational Chemistry* **1995**, *16*, 628.

(10) Cox, S. R.; Hsu, L. Y.; Williams, D. E. *Acta Crystallographica Section A* **1981**, *37*, 293.

(11) Frisch, M. J. T., G. W.; Schlegel, H. B.; Scuseria, G. E.; Robb, M. A.; Cheeseman, J. R.; Montgomery, Jr., J. A.; Vreven, T.; Kudin, K. N.; Burant, J. C.; Millam, J. M.; Iyengar, S. S.; Tomasi, J.; Barone, V.; Mennucci, B.; Cossi, M.; Scalmani, G.; Rega, N.; Petersson, G. A.; Nakatsuji, H.; Hada, M.; Ehara, M.; Toyota, K.; Fukuda, R.; Hasegawa, J.; Ishida, M.; Nakajima, T.; Honda, Y.; Kitao, O.; Nakai, H.; Klene, M.; Li, X.; Knox, J. E.; Hratchian, H. P.; Cross, J. B.; Bakken, V.; Adamo, C.; Jaramillo, J.; Gomperts, R.; Stratmann, R. E.; Yazyev, O.; Austin, A. J.; Cammi, R.; Pomelli, C.; Ochterski, J. W.; Ayala, P. Y.; Morokuma, K.; Voth, G. A.; Salvador, P.; Dannenberg, J. J.; Zakrzewski, V. G.; Dapprich, S.; Daniels, A. D.; Strain, M. C.; Farkas, O.; Malick, D. K.; Rabuck, A. D.; Raghavachari, K.; Foresman, J. B.; Ortiz, J. V.; Cui, Q.; Baboul, A. G.; Clifford, S.; Cioslowski, J.; Stefanov, B. B.; Liu, G.; Liashenko, A.; Piskorz, P.; Komaromi, I.; Martin, R. L.; Fox, D. J.; Keith, T.; Al-Laham, M. A.; Peng, C. Y.; Nanayakkara, A.; Challacombe, M.; Gill, P. M. W.; Johnson, B.; Chen, W.; Wong, M. W.; Gonzalez, C.; and Pople, J. A. Gaussian 03, Revision C.02 Gaussian, Inc., Wallingford CT, 2004.

(12) Brüesch, P. *Phonons, theory and experiments*; Springer-Verlag: Berlin ; New York, 1982.

(13) Day, G. M.; Price, S. L.; Leslie, M. *Journal of Physical Chemistry B* **2003**, *107*, 10919.

(14) Valeev, E. F.; Coropceanu, V.; da Silva Filho, D. A.; Salman, S.; Brédas, J. L. *Journal of the American Chemical Society* **2006**, *128*, 9882.

(15) *ADF, 2005.01*, Scientific Computing and Modeling NV: Amsterdam.

(16) Allinger, N. L.; Li, F. B.; Yan, L. Q. *Journal of Computational Chemistry* **1990**, *11*, 848.

(17) Ponder, J. W. TINKER: Software Tools for Molecular Design, 4.2 ed.; Washington University School of Medicine: Saint Louis, MO, 2004.

(18) Coropceanu, V.; Cornil, J.; da Silva Filho, D. A.; Olivier, Y.; Silbey, R.; Brédas, J. L. *Chemical Reviews* **2007**, *107*, 926.

(19) Ponomarev, V. I.; Filipenko, O. S.; Atovmyan, L. O. *Kristallografiya* **1976**, *21*, 392.

(20) Brock, C. P.; Dunitz, J. D. *Acta Crystallographica Section B-Structural Science* **1990**, *46*, 795.

(21) Holmes, D.; Kumaraswamy, S.; Matzger, A. J.; Vollhardt, K. P. C. *Chemistry-a European Journal* **1999**, *5*, 3399.

(22) Suzuki, M.; Yokoyama, T.; Ito, M. *Spectrochimica Acta Part a-Molecular Spectroscopy* **1968**, *A 24*, 1091.

(23) Schwoerer, M.; Wolf, H. C. *Organic molecular solids*; Wiley-VCH: Weinheim, 2007.

(24) Dorner, B.; Bokhenkov, E. L.; Chaplot, S. L.; Kalus, J.; Natkaniec, I.; Pawley, G. S.; Schmelzer, U.; Sheka, E. F. *Journal of Physics C-Solid State Physics* **1982**, *15*, 2353.

(25) Jankowiak, R.; Kalinowski, J.; Konys, M.; Buchert, J. *Chemical Physics Letters* **1979**, *65*, 549.

(26) Tomkiewi.Y; Groff, R. P.; Avakian, P. *Journal of Chemical Physics* **1971**, *54*, 4504.

(27) Filippini, G.; Gramaccioli, C. M. *Chemical Physics Letters* **1984**, *104*, 50.

(28) Della Valle, R. G.; Venuti, E.; Farina, L.; Brillante, A.; Masino, M.; Girlando, A. *Journal of Physical Chemistry B* **2004**, *108*, 1822.

(29) Venuti, E.; Della Valle, R. G.; Brillante, A.; Masino, M.; Girlando, A. *Journal of the American Chemical Society* **2002**, *124*, 2128.

(30) Brédas, J. L.; Calbert, J. P.; da Silva Filho, D. A.; Cornil, J. *Proceedings of the National Academy of Sciences of the United States of America* **2002**, *99*, 5804.

(31) Cheng, Y. C.; Silbey, R. J.; da Silva Filho, D. A.; Calbert, J. P.; Cornil, J.; Brédas, J. L. *Journal of Chemical Physics* **2003**, *118*, 3764.

(32) Karl, N.; Marktanner, J. *Molecular Crystals and Liquid Crystals* **2001**, *355*, 149.

(33) Hummer, K.; Ambrosch-Draxl, C. *Physical Review B* **2005**, *72*, 205202.

(34) da Silva Filho, D. A.; Friedlein, R.; Coropceanu, V.; Ohrwall, G.; Osikowicz, W.; Suess, C.; Sorensen, S. L.; Svensson, S.; Salaneck, W. R.; Brédas, J. L. *Chemical Communications* **2004**, 1702.

(35) Wang, L. J.; Li, Q. K.; Shuai, Z. *Journal of Chemical Physics* **2008**, *128*, 194706.

(36) Coropceanu, V.; Malagoli, M.; da Silva Filho, D. A.; Gruhn, N. E.; Bill, T. G.; Brédas, J. L. *Physical Review Letters* **2002**, *89*, 275503.

(37) McQuarrie, D. A.; Simon, J. D. *Physical chemistry : a molecular approach*; University Science Books: Sausalito, Calif., 1997.

(38) Troisi, A.; Orlandi, G. *Journal of Physical Chemistry A* **2006**, *110*, 4065.

(39) Troisi, A.; Orlandi, G. *Physical Review Letters* **2006**, *96*, 086601

(40) Troisi, A. *Advanced Materials* **2007**, *19*, 2000.

CHAPTER 5

CHARGE TRANSPORT PARAMETERS OF THE PENTATHIENOACENE CRYSTAL

In this chapter, the focus of the discussion is shifted to the description of the charge transport properties in organic molecular crystals. By using DFT, the microscopic charge-transport parameters of the pentathienoacene crystal are investigated. It is observed that the valence band exhibits a stronger dispersion than in the pentacene and rubrene single crystals with marked uniaxial characteristics within the molecular layer due to the presence of one-dimensional π-stacks; a small hole effective mass is also found along the direction perpendicular to the molecular layers. In the conduction band, strong intermolecular sulfur–sulfur interactions give rise to a significant inter-stack electronic coupling whereas the intra-stack dispersion is greatly reduced. The intramolecular vibronic coupling (reorganization energy) is stronger than in pentacene but comparable to that in sexithienyl; it is larger for holes than for electrons, as a result of low-frequency modes induced by the sulfur atoms. Charge transport is discussed in the framework of both band and hopping models.

5.1 Introduction

Oligothiophenes and oligoacenes are two prototypical organic semiconductors actively pursued for use in thin film transistors (TFTs).[1-3] Well-defined crystal structures, combined with improved purification and film deposition techniques, have made these

oligomers and their derivatives the most studied classes of organic semiconductors (see Figure 5.1). As indicated earlier, recent breakthroughs in solution processing that enable roll-to-roll printing now place small-molecule-based devices close to commercialization for low-cost, large-area electronic and optoelectronic applications.[4, 5]

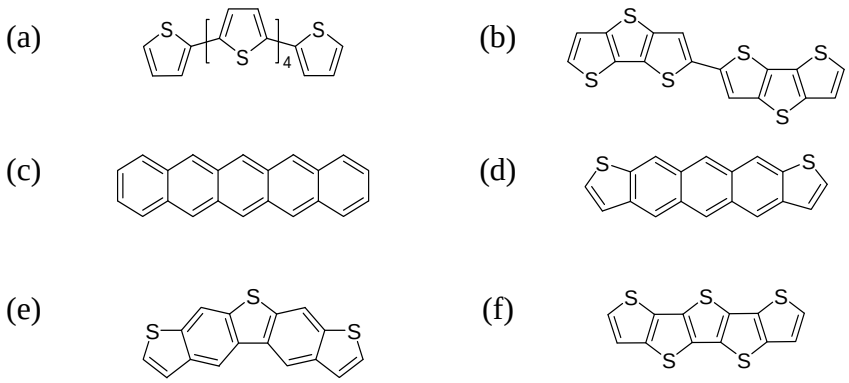

Figure 5.1 Chemical structures of actively investigated π-conjugated organic semiconductors: (a) sexithienyl (6T), (b) bisdithienothiophene (BDT), (c) pentacene, (d) *syn*-anthradithiophene (*syn*-ADT), (e) *syn*-thienobisbenzothiophene (*syn*-TBBT), and (f) pentathienoacene (5TA).

Efforts have been directed toward enhancing intramolecular π-conjugation in oligothiophenes by bridging adjacent β-carbon atoms with a sulfur linkage, thereby fusing the rings; this is the case, for example, in bisdithienothiophene (BDT: quaterthiophene with two bridges)[6] and oligothienoacenes (*n*TA: fully fused oligothiophenes).[7-11] The ring fusion can also be accompanied by changes in molecular packing, for instance, from a less favorable herringbone packing to the desired π-stacking. Numerous attempts have also been made to overcome the shortcomings of pentacene, the five-ring member of the oligoacene family that presents among the highest hole mobilities for organic crystals.[12] These approaches include a functionalization of the molecular backbone with sulfur, as in anthradithiophene (ADT: the end benzene rings are

each replaced with a thiophene ring)[13, 14] and thienobisbenzothiophene (TBBT: the central and two end rings are replaced);[15-17] these compounds display improved environmental stability and solubility, and modified crystal packing. It is therefore no surprise that pentathienoacene (5TA), which can be viewed either as a thiophene equivalent of pentacene or as a fully fused terthiophene, has received special attention. It has recently become even more appealing, as new synthetic routes are now available[10, 11] and 5TA-based TFTs have promising characteristics[11] (the thin-film field-effect mobility of 0.045 $cm^2/V \cdot s$ can be compared to the reported value of 0.02 $cm^2/V \cdot s$ for sexithienyl (6T)[18, 19]).

Here, a series of oligothienoacenes with a focus on 5TA were investigated by using DFT methods. In particular, the electronic and vibronic couplings in these systems were examined; these electron-vibration interactions dictate the charge transport properties in the crystal.[20]

5.2 Theoretical methodology

Geometry optimizations and normal-mode calculations of isolated *n*TA molecules (*n* = 3–7) were performed at the B3LYP/6-31G(d,p) level using the Gaussian package.[21] The normal-mode frequencies and Huang–Rhys factors were obtained with the DUSHIN code[22] and used to simulate the vibrational structure of the first ionization peak within the framework of the Born–Oppenheimer and Franck–Condon approximations (see Chapter

3, section 3.2). The frequencies were scaled down by a factor of 0.9613, which has been shown to reproduce very well the experimental IR frequencies.[23]

The calculations on the 5TA crystal were performed on an orthorhombic unit cell containing four molecules. The molecular coordinates determined by X-ray diffraction on the single crystal[11] were used with and without further geometry optimization (the cell constants were fixed at the experimental values during optimization). The wavefunctions were obtained using plane waves via a direct inversion in the iterative subspace (DIIS) method[24] at special k-points with a Monkhorst–Pack mesh[25] of 4×2×12. The electronic band structure was constructed in a non-self-consistent manner from the optimized electron density with an iterative Lanczos diagonalization method.[26] The inverse effective mass tensor was calculated using Sperling's centered difference method at the band edges with dk = 0.0017 (2π/Bohr). Norm-conserving numerical pseudopotentials generated with the procedure of Troullier and Martins[27] were used for C and S, and a local analytic pseudopotential for H, with a plane-wave energy cutoff of 70 Ry. The plane wave DFT calculations reported here were carried out at the BLYP level with the CPMD (Car–Parrinello Molecular Dynamics) code.[28] In addition, the transfer integrals for nearest-neighbor pairs of molecules in the geometry-optimized crystal were calculated by using a fragment orbital approach[29] in combination with a basis set orthogonalization procedure.[30] Transfer integrals for the diagonal pair in the 6T crystal[31] were computed for comparison. These calculations were performed with the PW91 functional and Slater-type triple-ζ plus polarization (TZP) basis sets, using the ADF (Amsterdam Density Functional) package.[32]

5.3 Results and discussion

5.3.1 Geometric structure

The optimized geometries of the isolated *n*TA molecules in the neutral state show that the C=C bonds lengthen and the C−C bonds shorten in going from the periphery to the center (see Figure 5.2, top panel for the C−C bonds). The gradual evolution of the bond lengths is still visible all the way to the molecular center even in 7TA. On the other hand, the C−S bond lengths alternate and converge already at the fourth bond from the periphery. Similar trends are found in the experimental crystal structures of 3TA[34] and 4TA[8] for the C=C and C−S bonds.

The optimized molecular geometry of 5TA in the crystal indicates that the spatial evolution of the bond lengths remains unaffected by intermolecular interactions with the exception of the C−C bond lengths. The calculated C−C bond lengths increase sharply in the first inner thiophene ring before heading down to follow the evolution of the isolated case. The experimental crystal data, on the other hand, show the opposite trend (see Figure 5.2, bottom panel). This apparent discrepancy is believed to be due to the uncertainty in the X-ray data of 5TA as a result of polycrystallinity in the sample.[11] Indeed, the sharp increase in C−C bond length in going from the outer ring to the next is clearly seen experimentally in the better resolved crystal structures of 3TA[32] and 4TA;[8] the standard deviation there is less than 0.004 Å whereas it is as large as 0.02 Å (*i.e.*, the full axis length in the figure) in the case of 5TA[11] (see also Figure 5.2, bottom panel). The

trend calculated with DFT is also seen in the experimental crystal structures of TIPS-5TA and TIPS-7TA[11] (both ends are substituted by triisopropylsilyl groups at the α-positions). It is worth mentioning that, despite the inability of DFT to describe van der Waals interactions,[33] a number of studies have shown that constraining the lattice constants to experimental values effectively compensates the missing attractive interactions so that such DFT calculations reproduce not only the geometry of the molecules in the unit cell, but also their pressure-dependent molecular orientation[34] and vibrational properties.[35, 36] It is important to note that recent studies have demonstrated that when DFT is modified with an empirical interatomic dispersion term (the so-called DFT-D method), it leads to an accurate description of the intermolecular interactions; results are even comparable to those derived from high level *ab initio* methods.[37, 38] It is also observed that (i) the geometry optimization of the 5TA crystal leads to a slight change in the stacking distance from 3.517 to 3.527 Å (both values are smaller than the experimental stacking distance of 3.576 Å for 4TA); and (ii) the crystal packing of 5TA is similar to that of α-terthiophene (3T)[39] in having a double-layered unit cell.

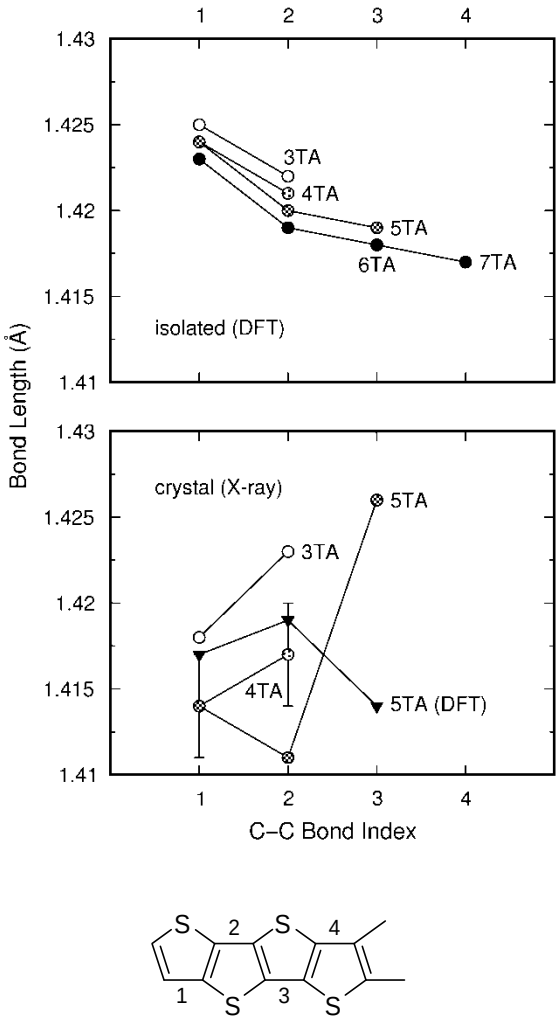

Figure 5.2 Evolutions of the C−C bond lengths in going from the end to the center of the molecule: (top panel) DFT calculations on isolated molecules and (bottom panel) experimental crystal data. In the top panel, three data points of 6TA overlap with those of 7TA. In the bottom panel, DFT values are also given for the 5TA crystal.

In the following, the geometric relaxation upon oxidation or reduction of an isolated molecule (see Figure 5.3 for the case of 5TA) is discussed. The C=C and C−C bonds undergo geometric changes to a greater extent in the cationic state than in the anionic state; the bond relaxations occur over the entire molecule and are more pronounced toward the molecular center. For the C−S bond, on the other hand, the geometric relaxations are more pronounced toward the molecular periphery and occur

predominantly upon reduction (as seen below in Figure 5.4, the HOMO wavefunctions have nodes on the sulfur atoms); the weak geometric changes in the cationic state are localized to the molecular ends (1.5 thiophene rings at each end). The role of the sulfur atoms in transport will be discussed further when the electronic structure and vibronic coupling is examined in the following subsections.

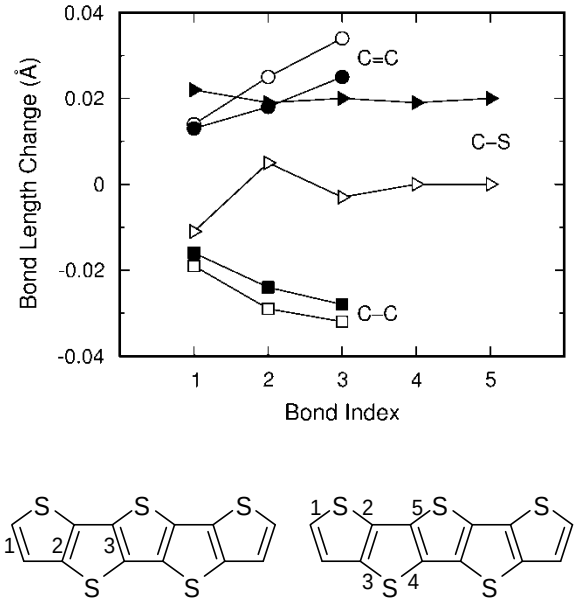

Figure 5.3 Calculated bond length changes in isolated 5TA upon oxidation (open symbols) and reduction (filled symbols).

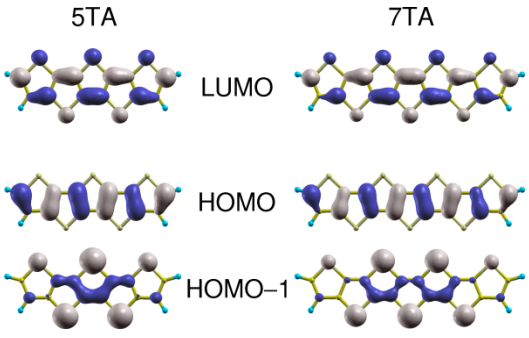

Figure 5.4 Wavefunctions of the frontier molecular orbitals in isolated 5TA and 7TA.

5.3.2 Crystal electronic structure

Figure 5.5 illustrates the X-ray crystal structure of 5TA obtained by Zhang et al.[11] A displacement of 1.650 Å [1.629 Å as calculated with DFT] along the short molecular axis (or a *roll* according to the terminology of Curtis et al.[40]) and a small stacking distance of 3.517 [3.527] Å are indicative of π-stacks along the *c*-axis. This one-dimensional π-stacking is in contrast to the herringbone packing found in pentacene. The "rolled" π-stacks in the 5TA crystal can be compared to the "pitched" π-stacks found in the rubrene crystal[41] that also exhibits very high mobilities[42] (the *pitch* is defined by Curtis et al.[40] as the displacement along the long molecular axis). The crystal unit cell of 5TA consists of four translationally inequivalent molecules.

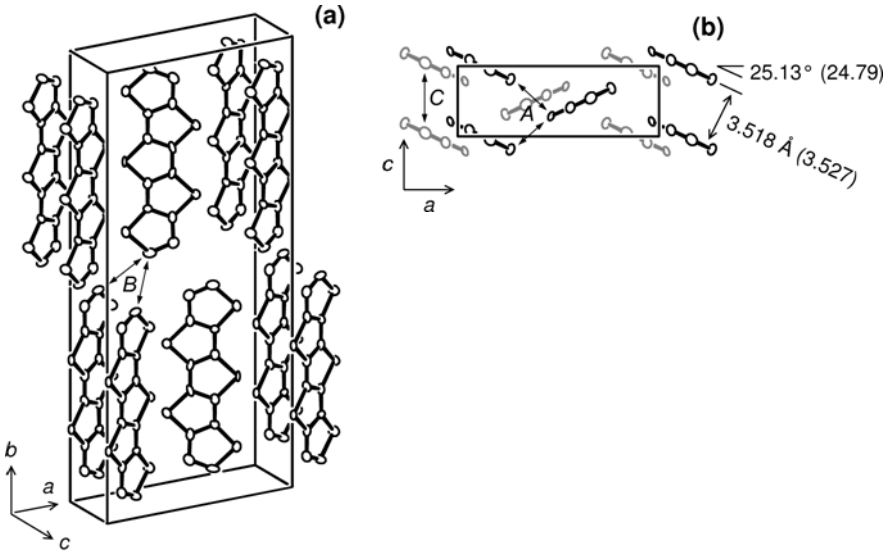

Figure 5.5 Crystal structure of 5TA.[10] The experimental lattice constants of the orthorhombic unit cell (*Pnma*) are a = 11.171, b = 25.098, and c = 3.8852 Å. Shown in (b) is a view from the bottom along the b-axis, where the molecules in gray belong to the top layer of the double-layered unit cell. Rolled π-stacks (displaced along the short molecular axis) are clearly seen along the c-axis. Values in parentheses refer to the DFT-optimized structure. The nearest-neighbor pairs *A*, *B*, and *C* considered for calculation of the transfer integrals are indicated by arrows.

The electronic band structure of the 5TA crystal is shown in Figure 5.6 along various orientations in reciprocal space. The valence band consists of four nearly degenerate π-subbands and has a width W of 0.77 eV. Importantly, when comparison is made among DFT results, this valence bandwidth is larger than that of pentacene[43, 44] and almost twice as large as that of rubrene.[45] The strongest dispersion responsible for the large bandwidth is found along the c-axis (in the ΓZ section of the Brillouin zone), as expected from the π-stacking in this direction. A flat band is observed along the a-axis (ΓX); in rubrene, by contrast, a moderate dispersion was observed along the other in-layer crystal axis. A weakly dispersive band is found along the b-axis (ΓY), that is, in the direction perpendicular to the molecular layers.

The quasi-degeneracy of the valence band indicates that interactions at the HOMO level among the translationally inequivalent molecules are very weak. This conclusion, obvious from the strong orientational anisotropy of the band dispersion, is also supported by direct calculations of the transfer integrals; among the three molecular pairs highlighted in Figure 5.5, a significant electronic coupling only occurs for pair *C*, *i.e.*, along the c-axis (note that the nearest neighbors in pair *C* are translationally equivalent whereas those in pairs *A* and *B* are not). The transfer integral for pair *C*, t_h^C, is 179 meV, to be compared to $t_h^A = 2\ meV$ for pair *A* and $t_h^B = 6\ \ meV$ for pair *B*. The valence band can therefore be represented by a superposition of four weakly interacting subbands that are one-dimensional in character, and it is not surprising that the bandwidth from the band structure (0.77 eV) is in good agreement with the value derived from a one-dimensional tight-binding model ($4t_h^C = 0.72\ eV$).

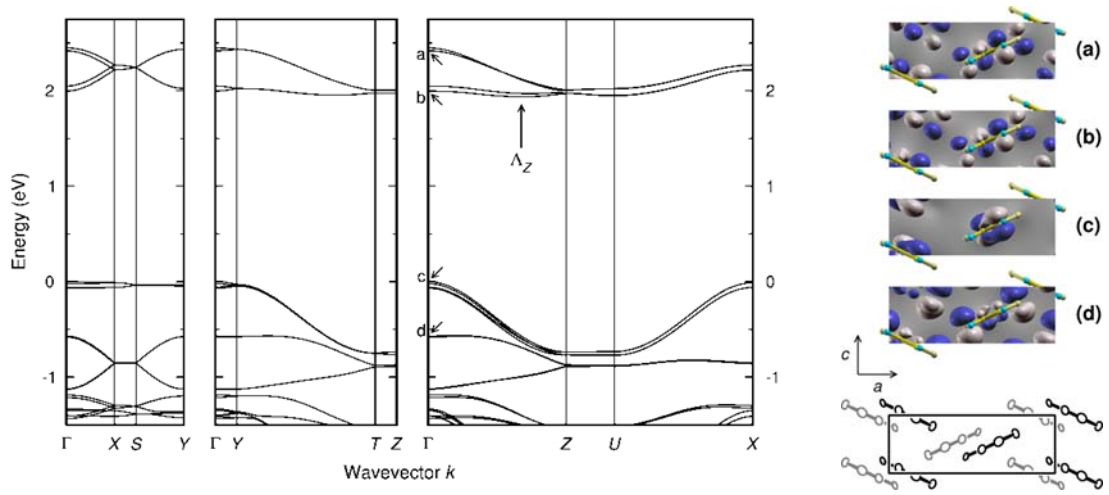

Figure 5.6 Electronic band structure of the geometry-optimized 5TA crystal. Points of high symmetry in the first Brillouin zone are Γ=(0, 0, 0); X=(0.5, 0, 0); Y=(0, 0.5, 0); Z=(0, 0, 0.5); S=(0.5, 0.5, 0); T=(0, 0.5, 0.5); and U=(0.5, 0, 0.5), all in crystallographic coordinates. The energy levels are shifted such that the valence band edge at the Γ-point aligns at 0 eV. The conduction band edge denoted by Λ_Z (0, 0, 0.337) is located 59 meV below the Γ-point. The wavefunctions of the crystal orbitals at the Γ -point (for the bottom molecular layer) are shown on the right, with each corresponding to a labeled arrow in the band structure plot.

The very weak dispersion along the a-axis occurs despite the close proximity of the neighboring molecules; S···S distances in pair *A* are only ~3.55 Å, less than the sum of the van der Waals radii, whereas C···C distances are > 4.9 Å. This is due to the presence of nodes on the sulfur atoms in the HOMO, which effectively decouples the HOMOs from one another along the a-axis (see Figure 5.6c for the crystal wavefunction of the topmost π-subband).

The conduction band, like the valence band, arises from the interactions of only one type of molecular orbitals, the LUMOs in this case. A reduced full bandwidth of 0.51 eV for the four subbands but with a significant subband splitting indicates that the

pattern of electronic coupling is markedly different in the conduction states. (Actually, the shape of the conduction band is similar to that of the valence band; the notable difference is due to the strong subband splitting in the former). As expected from the band dispersion in ΓZ, the transfer integral calculations give again the largest value for pair C ($t_e^C = 63\ meV$); this value, however, is nearly three times as small as that for holes. The major reduction results from a mutual cancellation of bonding and antibonding interactions of the LUMO wavefunctions between the molecules in the pair (see Figure 5.7 for the interplay between the roll in the stack and the wavefunction pattern that changes, or does not change, phase across the short molecular axis).

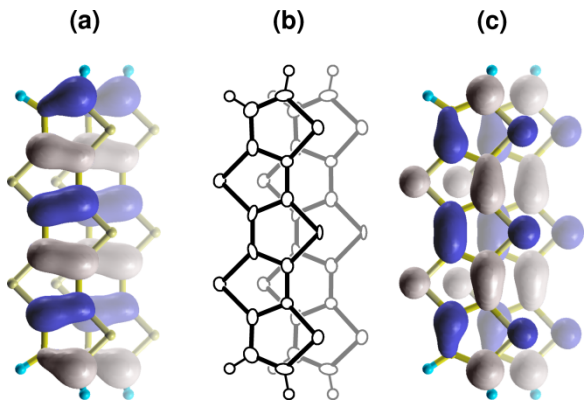

Figure 5.7 Illustration of rolled π-stacking and of the HOMO and LUMO interaction patterns: (b) two adjacent molecules from the unit cell along the c-axis as viewed down the molecular plane normal; and (a) the HOMO and (c) LUMO wavefunctions of isolated 5TA from Figure 5.4 laid over each of the molecules in (b). The wavefunction overlap between the two molecules is significant; however, the LUMO electronic coupling is greatly reduced by the roll in the stack which, in combination with the alternating LUMO phase along the short molecular axis, creates both in-phase and out-of-phase interaction patterns.

Another feature, which is directly relevant to the subband splitting, is the significant electronic coupling between translationally inequivalent molecules along the

a-axis, as manifested by the splitting in ΓX; the electronic coupling in pair *A* ($t_e^A = 42\ meV$) is now comparable to that in pair *C*. The difference in electronic interactions between the LUMO and HOMO levels for pair *A* can be explained by their charge density patterns; unlike the latter, the former carries a significant charge density on the sulfur atoms, which promotes effective electronic interactions through short S···S contacts spaced at about 3.55 Å (see Figure 5.4 and compare 5.6b and 5.6c). On the other hand, the electronic coupling between adjacent molecular layers (or in pair *B*) remains very small ($t_e^B = 7\ meV$) and similar to that found for holes.

Importantly, the LUMO interactions along the a- and c-axes do not work in a constructive manner. That is, the splitting via pair *A* separates the subbands along ΓZ at Γ, so that the top two subbands become more dispersive and the bottom two become less dispersive. As will be discussed below, it is the bottommost subbands that are of interest with regard to charge transport. The conduction band edge is shifted away from the zone boundary Z to Λ_Z (0, 0, 0.337); the energy at Λ_Z is 59 meV lower than at Γ, making the states around Γ less accessible (see Figure 5.6).

The theoretical derivation of the crystal properties requires, in general, an integration over the entire Brillouin zone. In the case of wide bands (or at low temperature), where the only populated states are those around the band edges, the description of many properties including charge transport can be simplified by using the effective mass approximation. The calculated effective masses are reported in Table 5.1. Holes in 5TA are light with the smallest hole effective mass equal to 1.26 m_0, a value

smaller than in pentacene[43, 44] (for comparison, the effective masses in silicon are 0.69 m_0 for a hole and 0.26 m_0 for an electron[46]). Electrons are much heavier than the holes; the smallest electron effective mass at the band edge is 3.15 m_0.

Table 5.1 Hole and electron effective masses m (in units of the electron mass at rest, m_0) at the band edges of the 5TA crystal.

	$m/\,m_0$	parallel to
holes at Γ	1.26	c
	1.78	b
	38.5	a
electrons at Λ_Z	3.15	b
	7.46	$a - 0.176c$
	8.26	$0.021a + c$
electrons at U[b]	1.42	b
	4.44	$0.133a + c$
	7.14	$0.912a - c$
electrons at Γ	1.01	a
	1.85	b
	-10.8[c]	c

[a] Taken from the diagonal components of the inverse effective mass tensors in principal axis coordinates and normalized by the free electron mass at rest m_0. [b] U located 10 meV above the conduction band edge Λ_Z. [c] The negative value reflects that the Γ-point is not a local energy minimum.

Interestingly, the effective mass displays a less pronounced orientational anisotropy than the band dispersion. That is, the hole effective mass along the b-axis (1.78 m_0), despite the very flat band along this direction, is a mere 40 % larger than that along the c-axis (1.26 m_0). The unexpected hole behavior arises from the fact that the effective mass not only depends on the band dispersion but also scales with the unit cell

dimensions in reciprocal space. This dependence can be illustrated by a one-dimensional tight-binding model, where the effective mass is given by:[51]

$$m = \frac{\hbar^2}{2td^2} \tag{5.1}$$

That is, the effective mass decreases linearly with the electronic coupling t and quadratically with the intermolecular distance (or cell length) d. Similar behavior can be expected for electrons and the effect is more dramatic. At the conduction band edge and a higher energy valley at U (10 meV above the band edge), an electron attains the smallest effective mass along the b-axis.

5.3.3 Local vibronic coupling

As mentioned before (see Chapter 3), the strength of the local vibronic coupling is measured by the polaron binding energy E_{pol} or, in the context of electron transfer theory, by the reorganization energy λ_{reorg} $\left(\approx 2E_{pol}\right)$. In Table 5.2, the intramolecular reorganization energies for the *n*TA series are presented. The results were obtained from adiabatic potential energy surfaces and from normal-mode calculations.[20] The hole reorganization energy of 5TA is slightly larger than that of 6T (301 and 255 meV for the non-planar and planar neutral geometries, respectively),[47] about twice as large as that of *syn*-TBBT (148 meV),[15] and three times as large as that of pentacene (97 meV).[48] 5TA, like 6T, shows a stronger vibronic coupling for holes than for electrons, in contrast to TBBT and pentacene.

Table 5.2 Calculated intramolecular reorganization energies for hole (λ_h) and electron (λ_e) transfer in the *n*TA series (energies in meV).

	λ_h AP[a] (NM)[b]	λ_e AP (NM)
3TA	352 (352)	324 (325)
4TA	325 (325)	293 (292)
5TA	306 (308)	270 (270)
6TA	291 (292)	252 (252)
7TA	279 (279)	237 (237)

[a] From adiabatic potential energy surfaces. [b] From normal-mode analysis.

Decomposition of the intramolecular reorganization energy into individual contributions from the relevant vibrational modes shows that large values of the Huang–Rhys factor for hole transfer are found mostly at low frequencies (see Figure 5.8). In fact, 41 % of the relaxation energy in 5TA (44 % in 7TA) originates from low-frequency modes below 500 cm^{-1} (~2.5 times the thermal energy). This is in marked contrast to the pentacene case, where there is almost no contribution from low-frequency vibrations.[48]

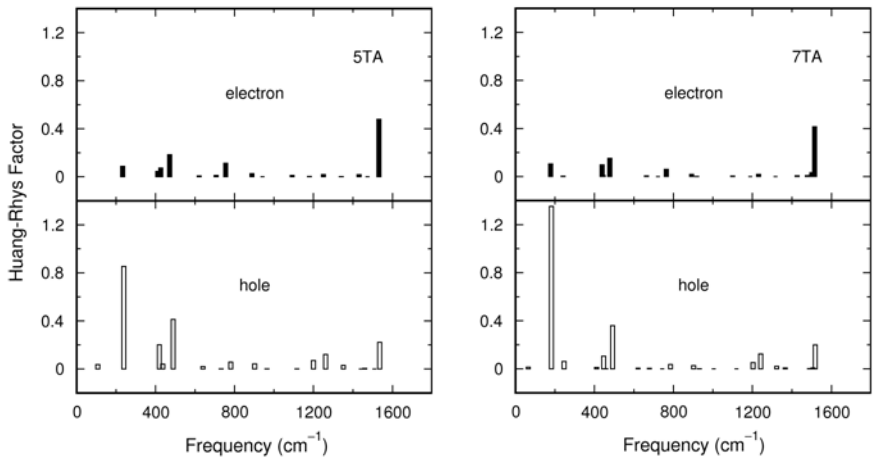

Figure 5.8 Huang–Rhys factors S_i of 5TA and 7TA. The relaxation energy λ_{rel} contributed by each normal mode at frequency ω_i is obtained by $\lambda_{rel} = \hbar\omega_i S_i$.

For electron transfer, on the other hand, 73 % [78 % for 7TA] of the total relaxation involves vibrational modes at about 1200 cm^{-1} or higher, and less than 7 % [7 %] comes from modes below 500 cm^{-1}. A similarly large contribution of high-frequency vibrations was found in TBBTs (over 70 %);[15] the corresponding value in pentacene is about 61 %.[13]

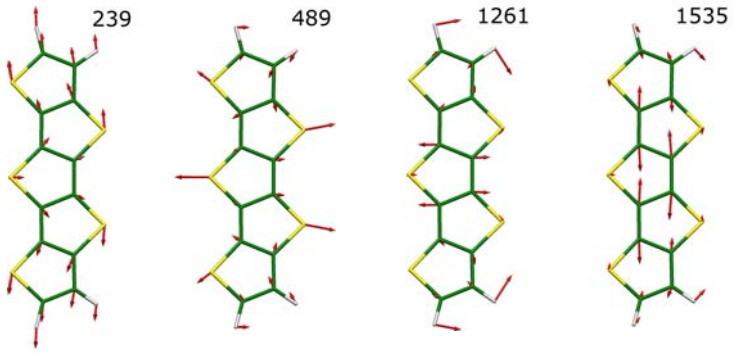

Figure 5.9 Normal modes with strong vibronic coupling in cationic 5TA. The low-frequency modes at 239 and 489 cm^{-1} involve mostly sulfur atoms whereas the high-frequency modes at 1261 and 1535 cm^{-1} involve carbon atoms. All modes are in-plane.

Further comparison of 5TA with TBBTs[15] indicates that the low-frequency vibronic coupling for holes grows with increasing sulfur content, although in TBBTs the low-frequency coupling is not strong enough to result in a larger reorganization energy for holes than for electrons. The most strongly coupled modes are illustrated in Figure 5.9. The 239 cm^{-1} mode is characterized by C−S−C bending in the three inner thiophene rings, which leads to a stretching motion of the 5TA cation as a whole along the long molecular axis (the two outer rings move more or less as a rigid body). The 489 cm^{-1} mode stretches the molecule along the short axis via C−S−C bending in the inner rings. The high-frequency modes with strong vibronic coupling for holes involve carbon atoms only. The 1261 cm^{-1} mode consists of C=C stretching in the central ring (and two

adjacent rings in the case of 7TA), and the 1535 cm^{-1} mode represents C−C stretching within the three inner rings. The latter mode is also found in the 5TA anion at 1531 cm^{-1} and provides the largest Huang–Rhys factor.

5.3.4 Band-like *versus* hopping transport

Using Equation 1.13 and the effective masses from Table 5.1, it is found that the hole mobility of 5TA is two-dimensional in the bc-plane with the highest along the c-axis and the lowest along the b-axis. The hole mobility of 5TA is greater than that of pentacene, if it is assumed that both have the same τ (where τ represents the carrier relaxation time). The fact that the mobility plane is perpendicular to the molecular layer may have implications for TFT applications. The intrinsic hole mobility may be much greater than the reported value of 0.045 $cm^2/V \cdot s$ measured on thin films on the a-SiO_2 surface, in which the molecular layer is parallel to the substrate[10] and thus the conduction is an average over the randomly oriented *c*-axes of individual grains. The orientation of the molecular layer relative to the substrate depends on the substrate material and/or deposition method (for example, pentacene on Ag[49] and graphite[50] forms molecular layers perpendicular to the substrate). Therefore, growing a thin film of 5TA with the bc-plane, instead of the ac-plane, parallel to the substrate could improve the field-effect mobility, which would then correspond to an average of biaxial grain mobilities.

The complex behavior of the conduction band allows no easy prediction for the electrons in the band regime. There are additional energy levels close to the conduction

band edge (U and Γ) which can be populated even at moderate temperature. All these contributions are to be taken into account to calculate the conductivity effective mass tensor, which is beyond the scope of this investigation. However, it seems reasonable to conclude that the electron mobility is uniaxial along the b-axis. Since the highest electron mobility is found perpendicular to the transport direction probed in TFTs, this may explain, at least partly, the experimental observation of p-channel-only field-effect behavior.[10]

When vibronic coupling becomes comparable to or stronger than electronic coupling, band-like transport is expected to take place only in perfectly ordered systems at very low temperature. Increasing temperature gradually reduces the bandwidth, leading to an increase in effective mass and subsequently to localization of the charge. Motion of the charge carrier can then be modeled by a sequence of uncorrelated hops.[51, 52] The hopping transport can be described as a self-exchange electron transfer from a charged molecule to a nearby neutral molecule. The carrier mobility is then expressed by means of Equation 1.18. At high temperature, the electron transfer or hopping rate takes its semiclassical form of Marcus theory given by:

$$k_{ET} = A \cdot exp\left[-\frac{E_a}{k_B T}\right] = A \cdot exp\left[-\frac{(\lambda - 2t)^2}{4\lambda k_B T}\right] \tag{5.2}$$

This expression represents a simplified version of Equation 1.16. Here, the prefactor A depends on the strength of the electronic coupling; that is, in the case of weak coupling, $A \sim t^2$; in the case of strong coupling, A is equal to the frequency of the nuclear motion along the reaction coordinate. E_a is the activation energy barrier; this parameter is used in the next paragraph to understand the hole and electron mobility in 5TA.

In the hopping regime, the hole mobility of 5TA becomes uniaxial along the c-axis; the large transfer integral leads to a negligibly small activation energy barrier of less than 10 meV (t = 179 and λ = 460 meV). The other two axes are close to the classical limit for weak electronic coupling with an energy barrier ($\approx \lambda/4$) of 110 meV. Also, the highest hole mobility in 5TA is expected to be greater than that of 6T, the energy barrier of which is estimated to be 60 meV (t = 35 and λ = 370 meV). Additionally, the hopping model predicts the electron mobility to be much smaller than the hole mobility. The largest electron mobility is found along the c-axis with an energy barrier of 50 meV, and the next along the a-axis (70 meV).

5.4 Conclusions

The key molecular parameters governing charge transport in the 5TA crystal have been identified by using DFT calculations. The main results can be summarized as follows. The 5TA crystal presents: (i) an exceptionally strong dispersion in the valence band (W = 0.77 eV, t = 179 meV, m = 1.26 m_0) due to one-dimensional π-stacks; (ii) a much reduced dispersion in the conduction band (W = 0.51 eV, t = 63 meV) due to cancellation of bonding and antibonding interactions by the roll in the π-stacks; (iii) a significant electronic coupling between π-stacks in the conduction band (t = 42 meV) via intermolecular S···S interactions; (iv) a very small hole effective mass (1.78 m_0) in the direction perpendicular to the molecular layers; and (v) larger intramolecular reorganization energy for holes (306 meV) than for electrons (270 meV) due to low-frequency vibrations induced by sulfur atoms. Interestingly, the transport parameters

calculated here in the context of both the band and hopping models suggest that the intrinsic hole mobility in the 5TA crystal might be higher than in two benchmark high-mobility organic crystals in their representative transport regimes: larger than pentacene in the band regime and larger than sexithienyl in the hopping regime.

5.5 References

(1) Dimitrakopoulos, C. D.; Malenfant, P. R. L. *Advanced Materials* **2002**, *14*, 99.

(2) Horowitz, G. *Advanced Materials* **1998**, *10*, 365.

(3) Katz, H. E. *Journal of Materials Chemistry* **1997**, *7*, 369.

(4) Mushrush, M.; Facchetti, A.; Lefenfeld, M.; Katz, H. E.; Marks, T. J. *Journal of the American Chemical Society* **2003**, *125*, 9414.

(5) Payne, M. M.; Parkin, S. R.; Anthony, J. E.; Kuo, C. C.; Jackson, T. N. *Journal of the American Chemical Society* **2005**, *127*, 4986.

(6) Li, X. C.; Sirringhaus, H.; Garnier, F.; Holmes, A. B.; Moratti, S. C.; Feeder, N.; Clegg, W.; Teat, S. J.; Friend, R. H. *Journal of the American Chemical Society* **1998**, *120*, 2206.

(7) Mazaki, Y.; Kobayashi, K. *Tetrahedron Letters* **1989**, *30*, 3315.

(8) Mazaki, Y.; Kobayashi, K. *Journal of the Chemical Society-Perkin Transactions 2* **1992**, 761.

(9) Sato, N.; Mazaki, Y.; Kobayashi, K.; Kobayashi, T. *Journal of the Chemical Society-Perkin Transactions 2* **1992**, 765.

(10) Xiao, K.; Liu, Y. Q.; Qi, T.; Zhang, W.; Wang, F.; Gao, J. H.; Qiu, W. F.; Ma, Y. Q.; Cui, G. L.; Chen, S. Y.; Zhan, X. W.; Yu, G.; Qin, J. G.; Hu, W. P.; Zhu, D. B. *Journal of the American Chemical Society* **2005**, *127*, 13281.

(11) Zhang, X. N.; Cote, A. P.; Matzger, A. J. *Journal of the American Chemical Society* **2005**, *127*, 10502.

(12) Goldmann, C.; Haas, S.; Krellner, C.; Pernstich, K. P.; Gundlach, D. J.; Batlogg, B. *Journal of Applied Physics* **2004**, *96*, 2080.

(13) Kwon, O.; Coropceanu, V.; Gruhn, N. E.; Durivage, J. C.; Laquindanum, J. G.; Katz, H. E.; Cornil, J.; Brédas, J. L. *Journal of Chemical Physics* **2004**, *120*, 8186.

(14) Laquindanum, J. G.; Katz, H. E.; Lovinger, A. J. *Journal of the American Chemical Society* **1998**, *120*, 664.

(15) Coropceanu, V.; Kwon, O.; Wex, B.; Kaafarani, B. R.; Gruhn, N. E.; Durivage, J. C.; Neckers, D. C.; Brédas, J. L. *Chemistry-a European Journal* **2006**, *12*, 2073.

(16) Wex, B.; Kaafarani, B. R.; Kirschbaum, K.; Neckers, D. C. *Journal of Organic Chemistry* **2005**, *70*, 4502.

(17) Wex, B.; Kaafarani, B. R.; Schroeder, R.; Majewski, L. A.; Burckel, P.; Grell, M.; Neckers, D. C. *Journal of Materials Chemistry* **2006**, *16*, 1121.

(18) Dodabalapur, A.; Torsi, L.; Katz, H. E. *Science* **1995**, *268*, 270.

(19) Torsi, L.; Dodabalapur, A.; Rothberg, L. J.; Fung, A. W. P.; Katz, H. E. *Science* **1996**, *272*, 1462.

(20) Brédas, J. L.; Beljonne, D.; Coropceanu, V.; Cornil, J. *Chemical Reviews* **2004**, *104*, 4971.

(21) Frisch, M. J.; Trucks, G. W.; Schlegel, H. B.; Scuseria, G. E.; Robb, M. A.; Cheeseman, J. R.; Zakrzewski, V. G.; Montgomery, J., J.A.; Stratmann, R. E.; Burant, J. C.; Dapprich, S.; Millam, J. M.; Daniels, A. D.; Kudin, K. N.; Strain, M. C.; Farkas, O.; Tomasi, J.; Barone, V.; Cossi, M.; Cammi, R.; Mennucci, B.; Pomelli, C.; Adamo, C.;

Clifford, S.; Ochterski, J.; Petersson, G. A.; Ayala, P. Y.; Cui, Q.; Morokuma, K.; Salvador, P.; Dannenberg, J. J.; Malick, D. K.; Rabuck, A. D.; Raghavachari, K.; Foresman, J. B.; Cioslowski, J.; Ortiz, J. V.; Baboul, A. G.; Stefanov, B. B.; Liu, G.; Liashenko, A.; Piskorz, P.; Komaromi, I.; Gomperts, R.; Martin, R. L.; Fox, D. J.; Keith, T.; Al-Laham, M. A.; Peng, C. Y.; Nanayakkara, A.; Challacombe, M.; Gill, P. M. W.; Johnson, B.; Chen, W.; Wong, M. W.; Andres, J. L.; Gonzalez, C.; Head-Gordon, M.; Replogle, E. S.; Pople, J. A. Gaussian98, Revision A.11; Gaussian, Incorporated: Wallingford, CT, 1998.

(22) Reimers, J. R. *Journal of Chemical Physics* **2001**, *115*, 9103.

(23) Wong, M. W. *Chemical Physics Letters* **1996**, *256*, 391.

(24) Hutter, J.; Lüthi, H. P.; Parrinello, M. *Computational Materials Science* **1994**, *2*, 244.

(25) Monkhorst, H. J.; Pack, J. D. *Physical Review B* **1976**, *13*, 5188.

(26) Pollard, W. T.; Friesner, R. A. *Journal of Chemical Physics* **1993**, *99*, 6742.

(27) Troullier, N.; Martins, J. L. *Physical Review B* **1991**, *43*, 1993.

(28) *CPMD, 3.9.2, IBM Corp (Copyright 1990-2004) and Max-Planck Institut für Festkörperforschung Stuttgart (Copyright 1997-2001): 2005*.

(29) Senthilkumar, K.; Grozema, F. C.; Bickelhaupt, F. M.; Siebbeles, L. D. A. *Journal of Chemical Physics* **2003**, *119*, 9809.

(30) Valeev, E. F.; Coropceanu, V.; da Silva Filho, D. A.; Salman, S.; Brédas, J. L. *Journal of the American Chemical Society* **2006**, *128*, 9882.

(31) Siegrist, T.; Fleming, R. M.; Haddon, R. C.; Laudise, R. A.; Lovinger, A. J.; Katz, H. E.; Bridenbaugh, P.; Davis, D. D. *Journal of Materials Research* **1995**, *10*, 2170.

(32) *ADF, 2005.01*, Scientific Computing and Modeling NV: Amsterdam.

(33) Zhao, Y.; Truhlar, D. G. *Journal of Chemical Theory and Computation* **2005**, *1*, 415.

(34) Hummer, K.; Puschnig, P.; Ambrosch-Draxl, C. *Physical Review B* **2003**, *67*, 184105.

(35) Hermet, P.; Bantignies, J. L.; Rahmani, A.; Sauvajol, J. L.; Johnson, M. R.; Serein, F. *Journal of Physical Chemistry A* **2005**, *109*, 1684.

(36) Kearley, G. J.; Johnson, M. R.; Tomkinson, J. *Journal of Chemical Physics* **2006**, *124*, 044514.

(37) Antony, J.; Grimme, S. *Physical Chemistry Chemical Physics* **2006**, *8*, 5287.

(38) Grimme, S.; Antony, J.; Schwabe, T.; Muck-Lichtenfeld, C. *Organic & Biomolecular Chemistry* **2007**, *5*, 741.

(39) Vanbolhuis, F.; Wynberg, H.; Havinga, E. E.; Meijer, E. W.; Staring, E. G. J. *Synthetic Metals* **1989**, *30*, 381.

(40) Curtis, M. D.; Cao, J.; Kampf, J. W. *Journal of the American Chemical Society* **2004**, *126*, 4318.

(41) Jurchescu, O. D.; Meetsma, A.; Palstra, T. T. M. *Acta Crystallographica Section B-Structural Science* **2006**, *62*, 330.

(42) Podzorov, V.; Menard, E.; Borissov, A.; Kiryukhin, V.; Rogers, J. A.; Gershenson, M. E. *Physical Review Letters* **2004**, *93*, 086602.

(43) de Wijs, G. A.; Mattheus, C. C.; de Groot, R. A.; Palstra, T. T. M. *Synthetic Metals* **2003**, *139*, 109.

(44) Hummer, K.; Ambrosch-Draxl, C. *Physical Review B* **2005**, *72*, 205205.

(45) da Silva Filho, D. A.; Kim, E. G.; Brédas, J. L. *Advanced Materials* **2005**, *17*, 1072.

(46) Sze, S. M. *Semiconductor devices, physics and technology*, 2nd ed.; Wiley: New York, 2002.

(47) da Silva Filho, D. A.; Coropceanu, V.; Fichou, D.; Gruhn, N. E.; Bill, T. G.; Gierschner, J.; Cornil, J.; Brédas, J. L. *Philosophical Transactions of the Royal Society a-Mathematical Physical and Engineering Sciences* **2007**, *365*, 1435.

(48) Malagoli, M.; Coropceanu, V.; da Silva Filho, D. A.; Brédas, J. L. *Journal of Chemical Physics* **2004**, *120*, 7490.

(49) Casalis, L.; Danisman, M. F.; Nickel, B.; Bracco, G.; Toccoli, T.; Iannotta, S.; Scoles, G. *Physical Review Letters* **2003**, *90*, 206101.

(50) Koch, N.; Vollmer, A.; Salzmann, I.; Nickel, B.; Weiss, H.; Rabe, J. P. *Physical Review Letters* **2006**, *96*, 156803.

(51) Holstein, T. *Annals of Physics* **1959**, *8*, 325.

(52) Holstein, T. *Annals of Physics* **1959**, *8*, 343.

CHAPTER 6

CHARGE TRANSPORT PARAMETERS IN IODO-FUNCTIONALIZED ORGANIC MOLECULAR CRYSTALS

In this chapter, on the basis of a DFT study, the electronic and charge transport properties of the crystals of 1,4-diiodobenzene (DIB), dithieno[3,2-*b*:2',3'-*d*]thiophene (DTT), and 2,6-diiodo-dithieno[3,2-*b*:2',3'-*d*]thiophene (DTT-2I) are investigated. In the case of the DIB crystal (room-temperature hole mobility > 10 $cm^2/V \cdot s$), the high mobility is primarily associated with the heavy iodine atoms. In the DTT and DTT-2I crystals, the dominant charge-transport properties are determined by π-π interactions along their respective molecular plane. Interestingly, the presence of iodine atoms in DIB and DTT-2I leads to a significant decrease in the local hole-vibration coupling compared to benzene and DTT, respectively. In marked contrast, the polaron binding energy in the case of electrons is found to be significantly higher than the electronic coupling; this implies that electrons in DIB and DTT-2I are strongly localized even at room temperature.

6.1 Introduction

Recently, many attempts have been made to enhance the charge-transport properties of oligoacenes via substitution or functionalization.[1-5] Following this strategy, several halogen-substituted[6-9] systems have been prepared and investigated. For instance, the chlorosubstitution of tetracene to obtain 5,11-dichlorotetracene, transforms the

characteristic herringbone packing motif of tetracene into a slipped π-stacking motif[9] and leads to a slightly larger field-effect mobility (1.6 *versus* 1.3 $cm^2/V \cdot s$). As well, perfluorination can convert pentacene from a p-channel to an n-channel semiconductor.[6, 7] More importantly, the largest impact of halogenation on charge-transport properties has been reported over four decades ago for 1,4-diiodobenzene (DIB, see Figure 6.1),[10] a derivative of benzene (the building unit of the acenes). Photoconductivity measurements[10] revealed that DIB exhibits a room-temperature hole mobility as large as 12 $cm^2/V \cdot s$. In spite of this promising finding,[10] charge transport in DIB was revisited only very recently by Ellman *et al.*[11, 12] These authors confirmed the earlier data regarding large hole mobility. In addition, the analysis of the electronic density of states derived from band-structure calculations[11] underlined the role played by the iodine atoms in the charge transport. Here, a detailed quantum-mechanical study of the electronic and vibrational couplings in DIB demonstrates that the iodine atoms have a strong effect on the transfer integrals and that there is a marked difference between the electron-vibration and hole-vibration couplings.

Additionally, in order to obtain a more comprehensive picture on the role of halogenations on the charge-transport properties, similar quantum-mechanical studies were performed on 2,6-diiodo-dithieno[3,2-*b*:2',3'-*d*]thiophene (DTT-2I) crystal. This molecular crystal represents an important addition to the family of ambient stable and easy to functionalize oligothienoacene semiconductors. DTT-2I combines the π-stacking properties[13] of its building block, dithieno[3,2-*b*:2',3'-*d*]thiophene (DTT), with a halogen substitution of two of the thiophene peripheral protons, which promotes extended

wavefunctions.[11] In this study, these two structural features were investigated by performing a systematic comparison of the electronic properties in DTT and DTT-2I molecular crystals. This investigation represents an extension of the work on the DIB crystal; comparisons between the DIB and DTT-2I crystals are made where possible.

6.2 Theoretical methodology

The geometric and electronic structure of the isolated DIB and benzene molecules were obtained at the density functional theory (DFT) level by performing geometry optimizations with the B3LYP functional and the 6-31G(d,p) basis set for the carbon and hydrogen atoms and the 3-21G(d,p) basis set for the iodine atoms, as implemented in the Gaussian package.[14] Additional calculations, using the 6-311++G(d,p) diffuse functions for C and H atoms and the 6-311G basis set augmented[15] by two polarization (d and f) and two (s and p) diffuse functions for the iodine atoms, were also carried out in the case of the radical-anion states. The results of vibration calculations, performed at the B3LYP/6-31G(d,p) level of theory, were used to calculate the relaxation energy with the DUSHIN code.[16]

The geometry optimization and the derivation of the crystal electronic band structure of the α and β crystalline structures in DIB (with the lattice constants fixed at the experimental values) were performed using the CRYSTAL06 package.[17] The calculation of the optical vibrations at the Γ–point for the crystal structure of the α-phase of DIB was performed with the same computational package. In these calculations, the

B3LYP functional, the 6-31G basis set (3-21G for the iodine atoms), and a uniform 4×6×8 Monkhost-Pack k-point mesh were employed. Additional DFT/BLYP calculations using the Troullier-Martins pseudopotentials and plane wave basis sets with an energy cutoff of 70 Ry were also performed on the α-phase with the CPMD (Car–Parrinello Molecular Dynamics) code.[18] The inverse effective mass tensor was calculated by means of a numerical differentiation approach.

The electronic-structure calculations of the DTT and DTT-2I crystals were performed using DFT with the PBE[19] (Perdew-Burke-Ernzerhof) exchange-correlation functional and plane-wave basis set as implemented in the VASP code.[20-22] Electron-ion interactions were described using the projector augmented wave (PAW) method.[23, 24] The kinetic energy cutoff on the wave function expansion was 300 eV. The self-consistent calculations were carried out with a 6×6×12 k-point and a 6×14×4 k-point meshes for DTT and DTT-2I, respectively. The inverse effective mass tensor was calculated using Sperling's centered difference method at the band edges with dk = 0.02 (2π / Å) in both molecular crystals.

Finally, the transfer integrals for nearest-neighbor pairs of molecules at the optimized crystal geometry were evaluated by using a fragment-orbital approach[25] in combination with a basis set orthogonalization procedure.[26] These calculations were performed with the PW91 functional and Slater-type triple-ζ plus polarization (TZP) basis sets for all atoms, using the ADF (Amsterdam Density Functional) package.[27]

6.3 Results and discussion

6.3.1 Crystallographic information

DIB forms two orthorhombic crystalline phases, denoted α and β, which belong to space groups *Pbca* and *Pccn*, respectively,[28] and contain four molecules per unit cell (see Figure 6.1). The α phase (with lattice parameters[28] a = 16.9697 Å, b = 7.3242 Å, and c = 6.156 Å) is stable up to 326 K, where a transition to the β phase (a = 17.047 Å, b = 7.4370 Å, and c = 6.1548 Å) occurs. Figure 6.2 illustrates the crystalline structure of DTT[29] and DTT-2I.[30] The crystallographic data for DTT are as follows: $P\ 2_1/n$ space group, a=12.746, b=10.614, c=6.005 Å, and β=97.53°; the crystallographic data for DTT-2I are: $P\ 2_1/n$ space group, a=13.200, b=4.140, c=19.760 Å, and β=96.354°. Both crystalline unit cells consist of four translationally inequivalent molecules. In DTT, identical π-stacking dimers are found along two different reciprocal lattice vectors, *i.e.*, b^* and c^*, respectively. These dimers show the shortest distance (3.773 Å) between sulfur atoms in the DTT crystal. In the DTT-2I crystal significant π-stacking is also observed along the $b(b^*)$-axis. The shortest S···S distances are found along this direction (4.140 Å). As a comparison, in the pentathienoacene crystal the shortest S···S distance is 3.527 Å.[31]

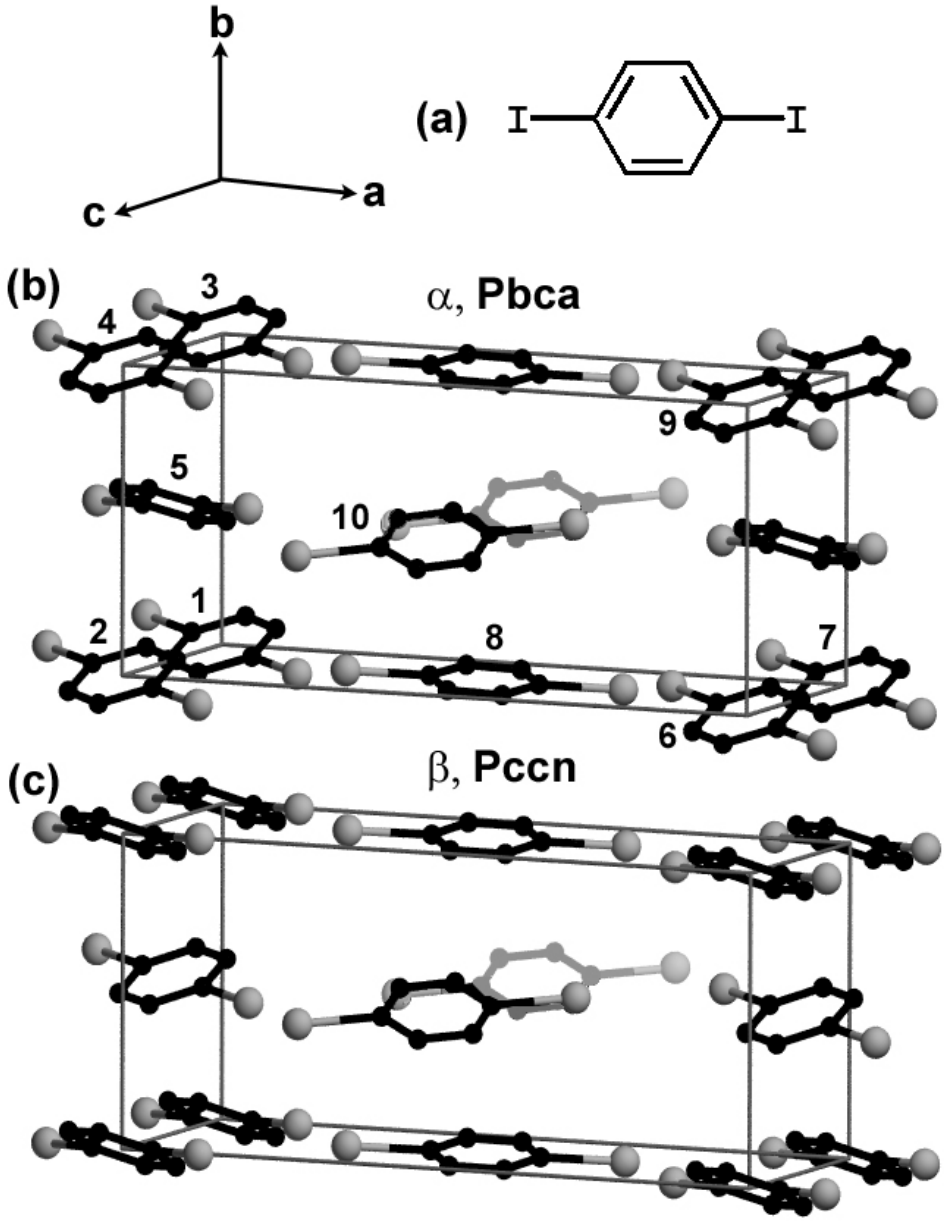

Figure 6.1 a) Chemical structure of DIB. b) Crystal structure of the α-phase of DIB[28] (*Pbca* space group, *a*=16.9697, *b*=7.3242, and *c*=6.156 Å; the labeling of the DIB molecules as used in the calculations of the transfer integrals is also shown). c) Crystal structure of the β-phase of DIB[28] (*Pccn* space group, *a*=17.047, *b*=7.4370, and *c*=6.1548 Å).

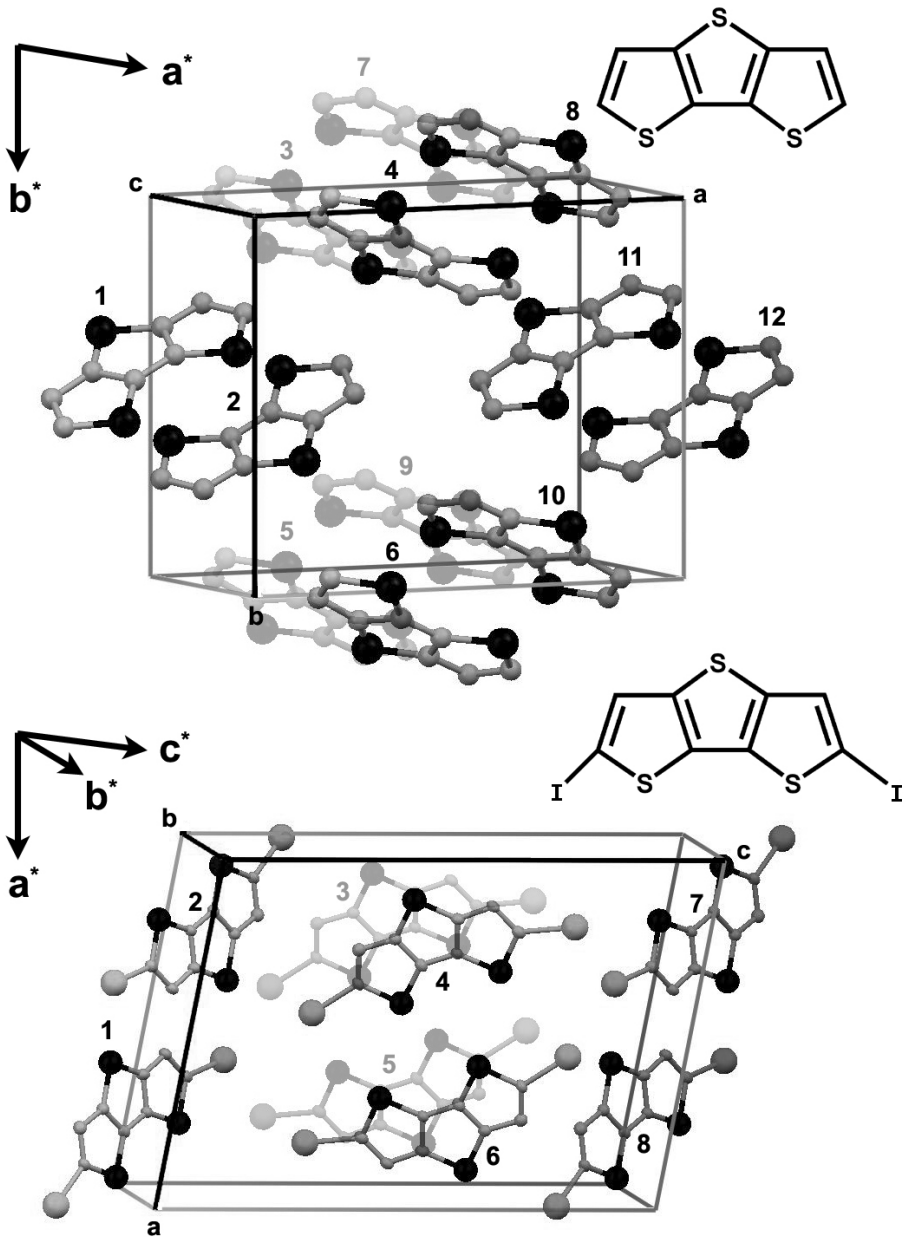

Figure 6.2 (top) Crystal structure of DTT ($P\,2_1/n$ space group, a=12.746, b=10.614, c=6.005 Å, and β=97.53°. (bottom) Crystal structure of DTT-2I ($P\,2_1/n$ space group, a=13.200, b=4.140, c=19.760 Å, and β=96.354°. Chemical structures of the DTT and DTT-2I molecules are drawn in the top right corner of each crystal structure, respectively. The labeling of the DTT and DTT-2I molecules as used in the calculations of the transfer integrals is also shown. The reciprocal lattice vectors for each crystal are included as well.

6.3.2 Molecular electronic structure

The frontier molecular orbitals (MOs) of DIB along with those of benzene are shown in Figure 6.3. As a result of iodine substitution, the D_{6h} symmetry of benzene is reduced to D_{2h} in DIB, which lifts the two-fold orbital degeneracy of the frontier orbitals found in the parent benzene. The calculations show that while the HOMO level in the DIB molecule is well separated (by about 0.8 eV) from the lower-lying MOs levels, the energy difference between the LUMO and higher unoccupied MO levels is only about 0.3 eV. As seen from Figure 6.3, the wave functions of the frontier levels all display a significant electronic density on the iodine atoms; this suggests that the iodine atoms should contribute significantly to intermolecular electronic interactions for both electrons and holes. The HOMO–LUMO gap in DIB is reduced with respect to benzene by 1.4 eV, which is mainly due to the stabilization of the LUMO level.

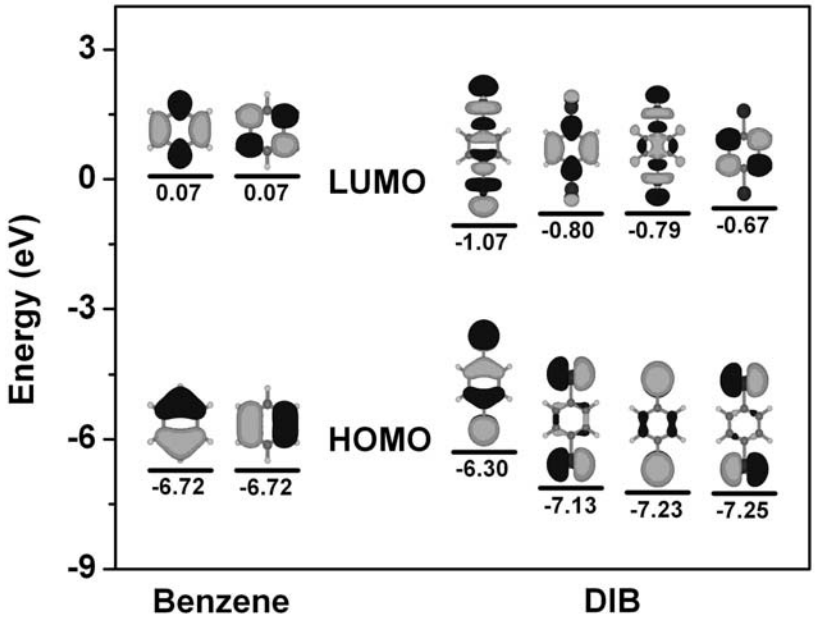

Figure 6.3 Illustration of the frontier molecular orbitals of benzene and DIB.

The frontier MOs of DTT and DTT-2I are shown in Figure 6.4. The substitution of the thiophene peripheral protons with iodine induces a slight decrease between the HOMO and LUMO energy levels. The HOMO-LUMO gap in DTT-2I is reduced with respect to that of DTT by 0.4 eV, which results from the stabilization of the LUMO level due to the presence of electron-withdrawing substituents. As observed from Figure 6.4, the presence of iodine atoms in the molecular backbone results in an extended HOMO wavefunction with significant electron density on the halogen atoms. It is important to note that electronic density of the iodine atoms in DTT-2I molecule is less pronounced than that found in DIB molecule.

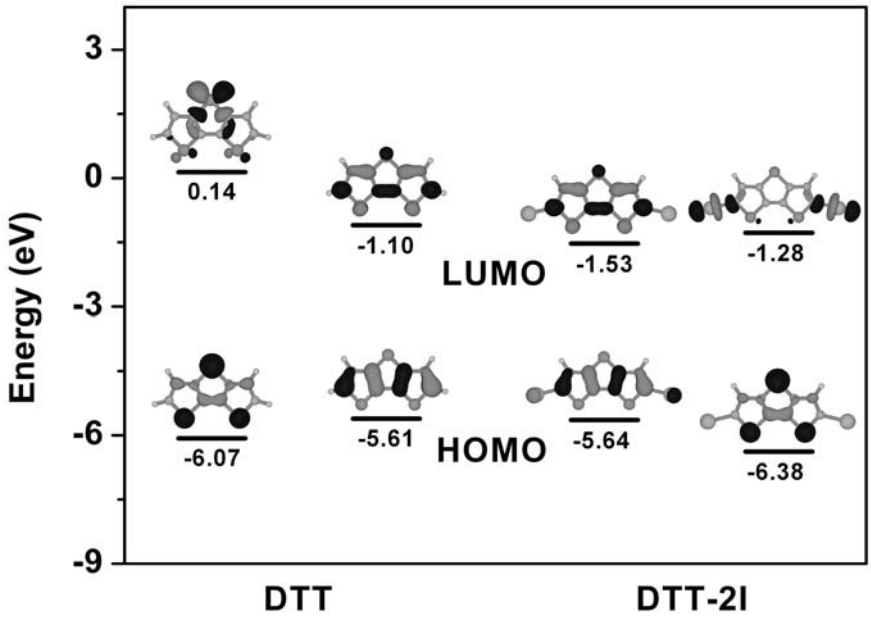

Figure 6.4 Illustration of the frontier molecular orbitals of DTT and DTT-2I.

6.3.3 Electronic-structure calculations

6.3.3.1 The DIB crystal

The results of the band-structure calculations along various directions in the α and β crystalline phases of DIB are shown in Figures 6.5 and 6.6, respectively. In both cases, the valence band consists of four sub-bands arising primarily from the interactions among the HOMO levels of the four translationally inequivalent molecules present in the unit cell. This is confirmed by a comparison of Figures 6.5 and 6.7, which shows that the electron density of the four sub-bands at the Γ-point resembles that of the HOMO level. The upper valence sub-band has nearly the same structure in both crystalline phases. Its maximum is located at the Γ-point and the largest dispersion is observed along the a-axis (along ΓX) followed by a relatively weaker dispersion along the b-axis (ΓY), while the dispersion along the c-axis (ΓZ), albeit smaller, remains significant.

Interestingly, the largest dispersion is observed along the direction where the intermolecular distance between adjacent molecules along the crystal axis is about 17 Å. Since such a large intermolecular distance precludes any direct electronic coupling,[26] it is clear that the significant band dispersion seen along the a-axis is due to mediation of the electronic coupling by other molecules located in the ab and/or ac crystal planes. In order to shed more light on this issue, transfer integrals between all relevant neighboring molecules were computed; the calculations were limited to the transfer integrals involving only the HOMO's for holes and the LUMO's for electrons. The results

obtained for the α crystalline phase are collected in Table 6.1. As expected, the coupling between two consecutive molecules along the a-axis (molecules 1 and 7 in Figure 6.1) is zero. The transfer integrals along other two crystallographic directions are also very small. However, moderate coupling was found between adjacent molecules along the diagonal directions of both ab and ac planes, 46 and 33 meV, respectively. If a DIB molecule is replaced with a benzene one while keeping the same intermolecular distances, the transfer integrals would decrease by at least one order of magnitude; this confirms that the electronic coupling in DIB is largely dominated by iodine-iodine interactions.

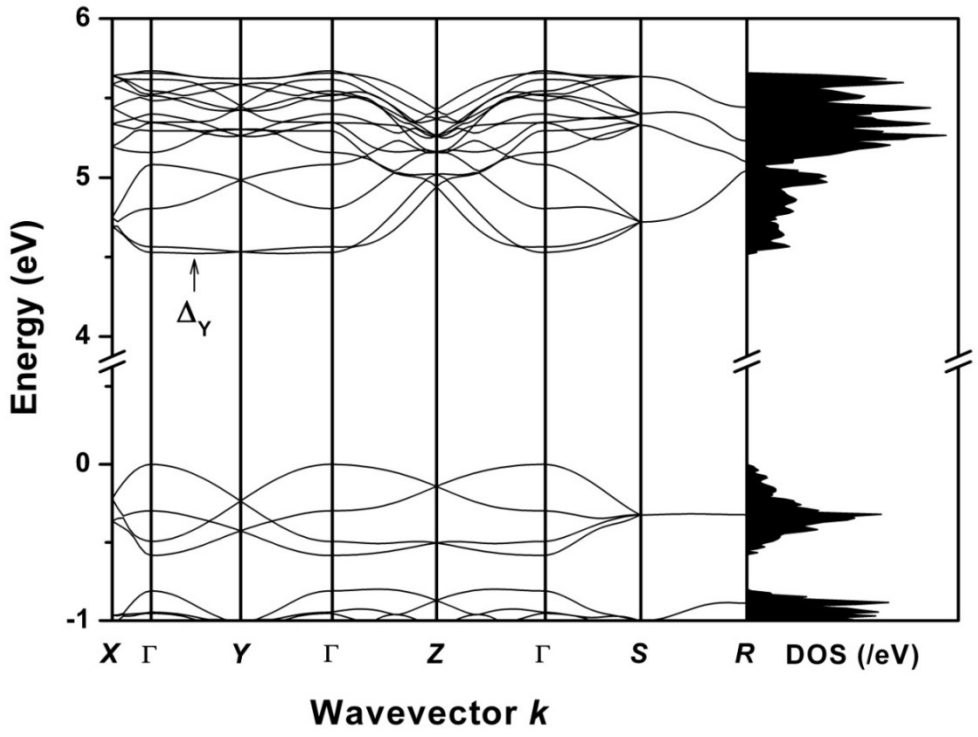

Figure 6.5 Electronic band structure of the α-phase of DIB. Points of high symmetry in the first Brillouin zone are labeled as follows: Γ=(0,0,0), X=(0.5,0,0), Y=(0,0.5,0), Z=(0,0,0.5), S=(0.5,0.5,0), and R=(0.5,0.5,0.5), all in crystallographic coordinates. The zero of energy levels corresponds to the valence band edge. The conduction band edge denoted by Δ_Y=(0,0.25,0) is located about 4 meV below the Γ-point. The right panel illustrates the corresponding density of states.

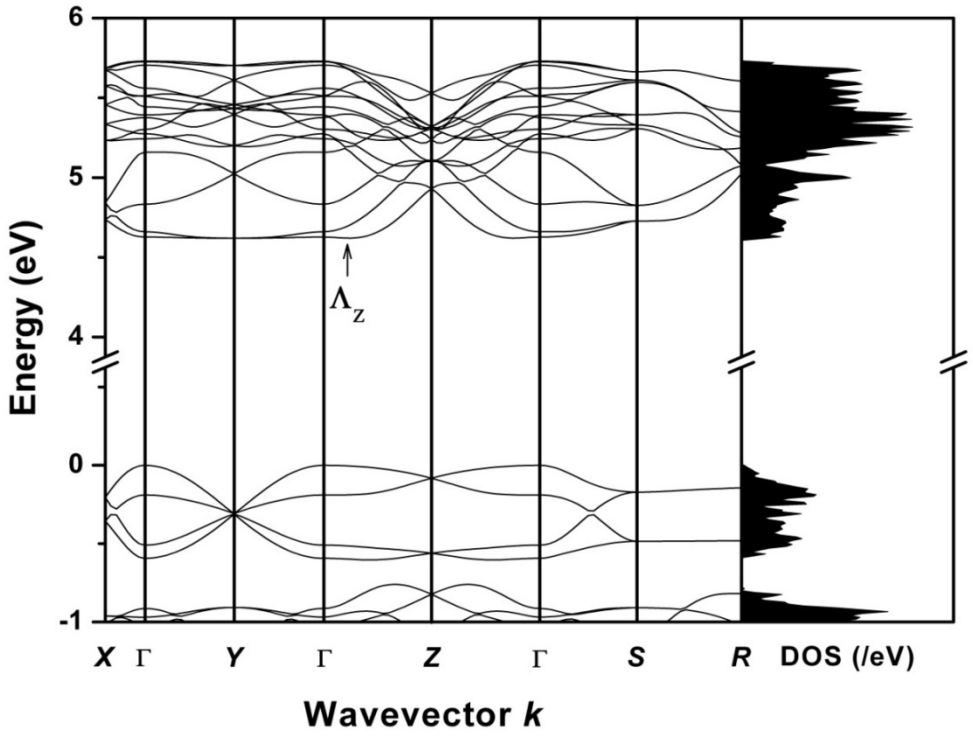

Figure 6.6 Electronic band structure of the β-phase of DIB. The labeling scheme for the points of high symmetry is the same as in Figure 6.5. The conduction band edge denoted by Λ_Z=(0,0,0.125) is located about 7 meV below the Γ-point.

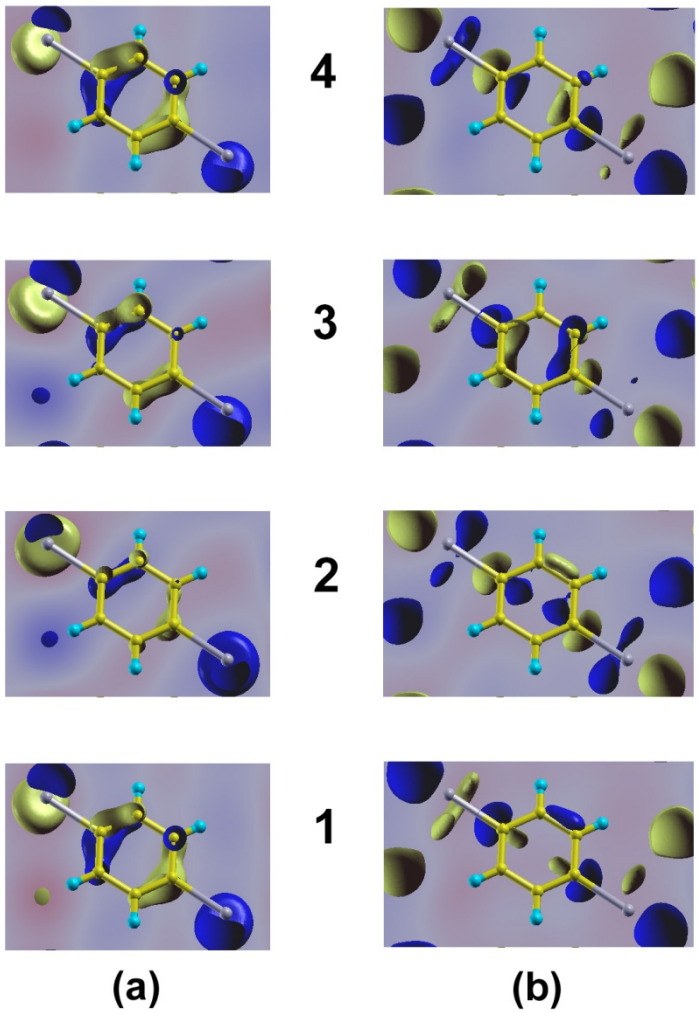

Figure 6.7 Wavefunctions of (a) the four valence sub-bands; and (b) the four lowest conduction sub-bands at the Γ-point. in the α-crystalline phase (the frontier orbitals are denoted as 1). Due to the periodic boundary conditions, portions of the electron density appear as fragmented throughout the unit cell.

Table 6.1 DFT Estimates of the transfer integral for molecular pairs in the α-phase of DIB.

	hole (meV)	electron (meV)
$t_{1,2}$	-5	10
$t_{1,3}$	3	-5
$t_{1,7}$	0	0
$t_{1,5}$; $t_{4,5}$	-12	-20
$t_{2,10}$; $t_{9,10}$	46	9
$t_{1,8}$; $t_{6,8}$	-33	-104

As in the case of the valence band, the structure of the conduction band is very similar for both crystalline phases. The conduction band is in general more complex than the valence band. As discussed above, the LUMO level in DIB is separated from the next molecular levels by a very small energy gap; as a result, these upper-lying states are also expected to contribute to the conduction band. This is confirmed by the comparison of Figures 6.3 and 6.7, which indicates a significant contribution of the LUMO+2 state to the lower two conduction sub-bands. Furthermore, inspection of Figures 6.5 and 6.6 reveals that the conduction band consists of a larger number of sub-bands than the valence band. The conduction band minimum in both crystalline phases is shifted from the Γ-point and is located at Δ_Y=(0,0.25,0) and Λ_Z=(0,0,0.125) for the α- and β-phases, respectively.

The dispersion of the lowest conduction sub-band is largest along the *a*-axis where its bandwidth is comparable to that of the highest valence sub-band (165 *versus* 235 meV). At first glance, this would appear to contradict the results obtained for the transfer integrals in Table 6.1. Indeed, the largest transfer integrals coming from the LUMO interactions are at least twice as large as those derived for the HOMO's; one would then expect the conduction band to be significantly wider than the valence band. However, as was already mentioned, the conduction band arises from interactions among several molecular levels. Thus, the transfer integrals related to the LUMO's are not sufficient to rationalize the dispersion of the conduction band (this result again warns against a naive use of just HOMO's and LUMO's for the interpretation of charge-transport properties).

In the case of wide bands where the thermally populated levels remain close to the band edges, the description of charge transport can be simplified by using the electron effective mass approximation. The calculated effective masses along the principal axes are shown in Table 6.2 and Table 6.3 for the α and β crystalline phases, respectively. As expected, the holes are found to be very light along the a-axis, with an effective mass of about 0.6 m_0 in both crystalline phases. The hole effective mass is about four times larger for the α phase and three times larger for the β phases along the b axis, and is very large along the c-axis (8 m_0 and 14 m_0, for the α and β phases, respectively). For the sake of comparison, it was observed that the rubrene crystal (about 0.8 m_0)[32] has the smallest effective mass for holes among the members of the oligoacenes family.

Table 6.2 Hole and electron effective masses m (in units of the electron mass at rest, m_0) calculated at the band edges of the α-phase of DIB.

	$m/\,m_0$	parallel to
holes at Γ	0.56	a
	2.55	b
	8.07	c
electrons at Δ_Y	0.50	a
	6.06	b
	0.96	c

Table 6.3 Hole and electron effective masses m (in units of the electron mass at rest, m_0) calculated at the band edges of the β-phase of DIB.

	$m/\,m_0$	parallel to
holes at Γ	0.58	a
	1.73	b
	13.83	c
electrons at Λ_Z	0.79	a
	4.57	b
	>10[a]	c

[a]Due to the flatness of the band, it was not possible to derive an accurate value of the effective mass along this direction.

According to band-like charge transport theory (see Chapter 1) the orientational anisotropy of the mobility is governed by that of the effective mass. In this context, it is interesting to note that the measured anisotropy of the hole mobility in DIB (the experimental hole mobilities at room temperature along the a, b and c-axes are reported to be 12, 4 and 1.7 $cm^2/V \cdot s$, respectively[10]) follows the same pattern as the calculated anisotropy of the hole effective mass.

The temperature dependence of mobility is determined (in the absence of chemical and physical defects) by the nature and strength of the electron-phonon (vibration) interactions. In the general case of the band model, mobility decreases as temperature increases. In the case of DIB, temperature-dependent measurements were performed only at elevated temperatures (above 200 K)[10, 12] and the hole mobility was observed to decrease with increasing temperature. This feature does not prove that charge transport in DIB is band-like since at high temperatures a decrease in mobility with temperature could also take place in the hopping regime (in the so-called residual

scattering limit where thermal energy exceeds the energy of the activation barrier[33]). However, this temperature dependence, taken together with the similarity between the orientational anisotropy of the mobility and the anisotropy of the effective mass, strongly points towards the band-like nature of hole transport in DIB.

As in the case of holes, the smallest effective mass for electrons is obtained along the a-axis (0.5 m_0 and 0.8 m_0 for the α and β phases, respectively). Thus, the effective mass for electrons in the α phase is even slightly smaller than that for holes. This result suggests that if the relaxation time of electrons were to be comparable to that of holes, their charge-transport properties should be also comparable, in particular along the a-axis. However, as described in section 6.3.4, the electron transport in DIB is expected to suffer from strong polaronic effects, which might explain why no charge transport has been observed or reported for electrons.

6.3.3.2 The DTT and DTT-2I crystals

Considering the high-symmetry reciprocal space directions illustrated in Figure 6.8, the electronic band structures of DTT and DTT-2I are presented in Figures 6.9 and 6.10. The high-symmetry points in units of $(2\pi/a,2\pi/b,2\pi/c)$ are Γ=(0,0,0), A=(0.5,0.5,0), B=(0.5,0,0), C=(0,0.5,0.5), Y=(0,0.5,0), and Z=(0,0,0.5). Note that ΓB, ΓY, and ΓZ are parallel to the reciprocal crystalline axes a*, b*, and c*, respectively. The ΓA and ΓC correspond to the a*+ b* and b*+ c* directions, respectively. The energy zero is set to the valence-band maximum. In both crystals, the conduction bands are less

dispersive than the valence bands. This indicates that hole transport should be favored as compared to electron transport. Therefore, the main focus of our discussion is oriented towards a theoretical understanding of the hole-transport properties in these molecular crystals.

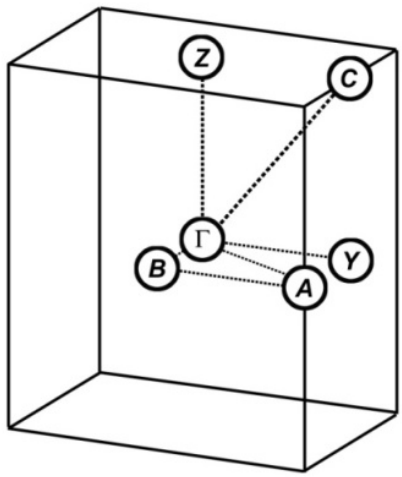

Figure 6.8 Illustration of the standard Brillouin zone directions used to generate the band structure plots of Figures 6.9 and 6.10.

In the DTT crystal, the four uppermost valence bands have a bandwidth W of 0.43 eV; when compared with other DFT results, this valence bandwidth is smaller than that of pentathienoacene crystal, where $W = 0.77\ eV$ (see Chapter 5 or Reference 34). The valence-band dispersion (determined by a single band) along the reciprocal axes shows the following trend: c^* (ΓZ) $>$ b^* (ΓY) $>$ a^* (ΓB). Note that along the c^* direction the intermolecular distance between DTT molecules is 6 Å; this might a priori preclude any significant orbital interaction, and therefore any band dispersion. In this case, the observed band dispersion is attributed to the presence of an intermediate layer of molecules along the c^* axis. As seen in Figure 6.2, the molecules 1, 2, 11, and 12 are sandwiched by two layers of molecules; one layer is formed by molecules 4, 6, 8, and 10

and the second layer is formed by molecules 3, 5, 7, and 9. Large band dispersions for the uppermost valence band in DTT are found along the b^*+c^* and a^*+b^* directions. Along the b^*+c^* direction, short interatomic distances between carbon atoms are present (~3.5 Å) and along the a^*+b^* direction π-stacking interactions are observed; these two crystallographic features are thought to be responsible for the moderate dispersion (as compared with larger oligothienoacene family members) in the valence band of the DTT crystal.

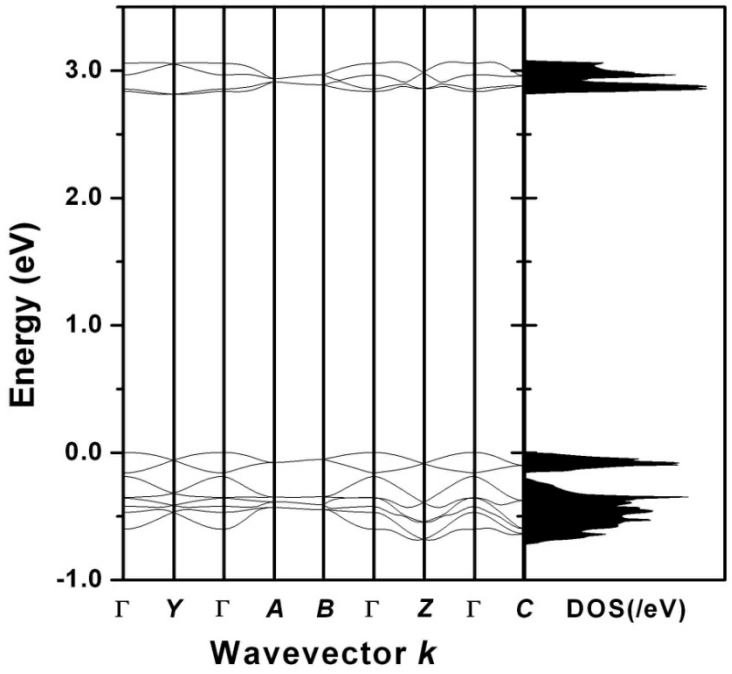

Figure 6.9 Electronic band structure of the DTT crystal. The valence band edge is located at the Γ-point. The right panel illustrates the corresponding density of states (see text for definition of the high-symmetry k-points in the first Brillouin zone).

The electronic characteristics discussed above are also supported by direct calculations of the transfer integrals between all relevant neighboring molecules. The DFT-calculated transfer integrals for DTT are presented in Table 6.4. As expected, the

coupling between molecules that lead to π-stacking interactions (for example, dimers composed of molecules 1 and 2 or 6 and 10) or that favor C···C interactions (*i.e.*, dimers formed by molecules 2 and 3 or 10 and 11) show the largest HOMO transfer integrals (-138 meV and 54 meV, respectively). Also, it is important to note that the large values of the transfer integral for dimers composed of molecules 2 and 3 (10 and 11) provide another evidence for the valence band dispersion found along the c*-axis.

Table 6.4 DFT estimates of the transfer integral for molecular pairs in the DTT crystal (see Figure 6.2 for labeling).

	hole (meV)	electron (meV)
$t_{1,2}$; $t_{3,7}$; $t_{4,8}$; $t_{5,9}$; $t_{6,10}$; $t_{11,12}$	-138	18
$t_{1,4}$	19	39
$t_{2,3}$; $t_{10,11}$;	54	21
$t_{2,11}$	-1	3
$t_{3,4}$; $t_{5,6}$; $t_{7,8}$; $t_{9,10}$	6	1

In the DTT-2I crystal, the situation is more simple than in the DTT crystal because the characteristics of its electronic band structure involve fewer crystallographic coordinates. The valence band consists of four nearly degenerated sub-bands and has a bandwidth W of 0.47 eV. The width results from a strong wavevector dispersion along π-stacking directions, *i.e.*, the a*+b* and b*+c* directions or the b*-axis. A flat band is observed along the a*-axis (ΓB); along this direction, the molecules are packed in a sidewise arrangement with respect to their short molecular axis, leading to relatively large distances ($>$ 4.0 Å) between the atoms that carry significant electron density in the HOMO wavefunctions of DTT-2I molecule. The flattest band is found along the c*-axis (ΓZ). In this case, neither π-stacking nor I···I interactions are favored. In complete

contrast, we recall that the DIB crystal shows the largest valence-band dispersion along this crystallographic direction (*i.e.*, along the long molecular axis).

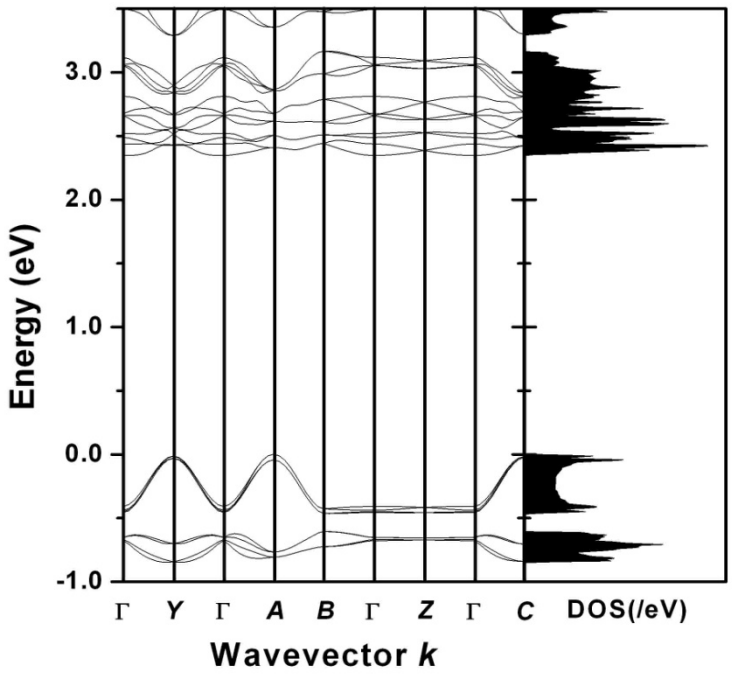

Figure 6.10 Electronic band structure of the DTT-2I crystal. The valence band edge is located at A=(0.5,0.5,0). The right panel illustrates the corresponding density of states (see text for definition of the high-symmetry k-points in the first Brillouin zone).

The DFT-calculated transfer integrals for molecular dimers of the DTT-2I crystal are collected in Table 6.5. We note that the bandwidth obtained from the band-structure calculation ($W = 0.47\ eV$) is fully consistent with the value derived from a one-dimensional tight-binding model ($4t_{3,4} = 4t_{5,6} = 0.47\ eV$) taking into account the π-stacking direction. In this case, the transfer integral for holes is 122 meV, which is much larger than that for neighboring dimers (less than 10 meV). Such a disparity in the values of the transfer integrals opens the possibility to perform systematic modifications of the crystalline packing to enhance other types of intermolecular interactions in DTT-2I,

namely halogen interactions. Interestingly, it is found that a small rotation ($< 15°$) along the short molecular axis of molecule 7 in a dimer formed by molecules 5 and 7, leads to a significant increase (over two orders of magnitude, $t_{5,7} > 100\ meV$) in the transfer integral for holes of this dimer (see Figure 6.11). This finding indicates that the functionalization of the molecular backbone to maximize the S···S interactions or/and I···I interactions is a rational step towards the production of organic materials with enhanced charge-transport properties.

Table 6.5 DFT estimates of the transfer integral for molecular pairs in the DTT-2I crystal.

	hole (meV)	electron (meV)
$t_{1,2}$; $t_{7,8}$	-7	1
$t_{1,3}$; $t_{6,7}$	5	-4
$t_{1,4}$; $t_{5,7}$	-1	10
$t_{2,4}$; $t_{6,8}$	-1	5
$t_{3,4}$; $t_{5,6}$	-122	1
$t_{4,7}$	-7	-1

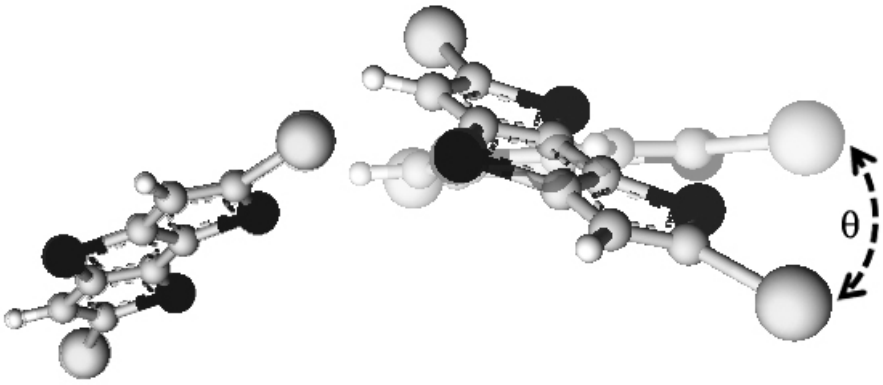

Figure 6.11 Illustration of the rotation of molecule 7 along its short molecular axis in a dimer formed by molecules 5 and 7 (see Figure 6.2 for a definition of the given molecule numbers).

The calculated effective masses for the DTT and DTT-2I crystals are shown in Table 6.6 and Table 6.7, respectively. The lightest hole in DTT, with an effective mass of about 3.7 m_0, is found along the ac plane in which π-stacking interactions are observed. This effective mass is heavier than that of other organic molecular crystals used in semiconducting applications, such as the pentathienoacene[34] or pentacene[35] crystals. Also, relatively large hole effective masses are observed along the $b(b^*)$-axis, but they are not as large as to preclude any charge-carrier transport; this finding is supported by the band dispersions and transfer integrals of the DTT crystal along the $b(b^*)$-axis (*vide supra*). As a comparison, in the pentathienoacene crystal (see Chapter 5 or Reference 34), hole effective masses along the a-axis are in the order of 35 m_0 and the calculated hole transfer integral values are equal to 2 meV; in this case, it is more clear that hole transport is hindered. In the DTT-2I crystal, the lightest holes (2.0 m_0) are found as expected along the b-axis. Heavy charge carriers are calculated for the c-axis; however, as previously discussed small rotations along the short molecular axis in one of the DTT-2I molecules decrease the distance between the halogen moieties and enhance the HOMO wavefunctions overlap. Calculations of the phonon modes would be useful to determine whether such vibrations might be presented and potentially lead to lighter hole effective masses.

Table 6.6 Hole effective masses m (in units of the electron mass at rest, m_0) calculated at the band edges of the DTT crystal.

	$m/\,m_0$	parallel to
holes at Γ	3.73	$a\,+\,0.813c$
	7.16	b
	12.10	$c\,-\,0.152a$

Table 6.7 Hole effective masses m (in units of the electron mass at rest, m_0) calculated at the band edges of the DTT-2I crystal.

	m/m_0	parallel to
holes at A	8.47	$a + 0.095c$
	1.99	b
	75.52	$c + 0.035a$

6.3.4 Electron-vibration coupling

6.3.4.1 DIB

In this section, a discussion of electron-vibration interactions is presented. The DFT estimates for hole-vibration coupling in DIB are collected in Table 6.8. For the sake of comparison, the hole-vibration coupling in benzene was also calculated; the benzene and DIB results are illustrated in Figure 6.12. The intramolecular polaron binding energy calculated for DIB is about 88 meV, which is nearly 40% smaller than that in benzene (143 meV). The estimate for E_{pol} in benzene is in good agreement with the value of 122 meV derived by Kato and Yamabe in the framework of the one-electron approximation.[36]

As seen from Figure 6.12, the decrease of E_{pol} in DIB *versus* benzene results mostly from a significant drop in hole-vibration interaction for the high-frequency mode at 1600 cm^{-1}; the coupling with all other modes is also reduced to some extent. The significant decrease in hole-vibration interaction with the 1600 cm^{-1} mode can be rationalized in terms of orbital vibronic coupling constants.[37, 38] According to this model, the hole-vibration coupling is large when the molecular deformation along the corresponding normal coordinate considerably distorts the electron density of the related

MO (HOMO in the present case), leading to a large variation in the MO energy. The inspection of the normal coordinate for the 1600 cm^{-1} mode shows that the iodine atoms are not involved in this vibration (they stay motionless). Since part of the electron density in the case of the diiodobenzene HOMO is located on the iodine atoms, the energy of this molecular state is comparatively less affected by this vibration than for benzene; thus, the hole-vibrational coupling constant is smaller in the case of DIB.

In general, the charge-transport properties of a particular system results from the interplay between a charge localization effect due to electron-phonon coupling and a charge delocalization effect due to the electronic coupling. We point out that in the case of complex systems, it is incorrect to take the bandwidth of the entire valence or conduction band as a measure of the delocalization energy; rather, only those sub-bands that are thermally populated and contribute to charge transport should be considered. For the understanding of hole transport in DIB only the upper valence sub-band is relevant; in the α-crystalline phase (the results for the β-phase are similar), the related bandwidths are 218, 235 and 141 meV for the a-, b-, and c- directions, respectively. All these values are significantly larger than the polaron binding energy (88 meV). Thus, it can be concluded that at low temperature local electron-vibration coupling would not lead to the formation of molecular-type (localized) polarons in DIB. However, it is important to bear in mind that even if charge transport in DIB falls in a band-like regime at low temperature, the local hole-phonon coupling is large enough to result in substantial polaronic effects which can lead to a renormalization of the effective mass. A complete description of this issue can be obtained only in the framework of a microscopic approach that treats the

whole Hamiltonian self-consistently (*i.e.*, including first-principles calculations of the electronic and electron-phonon interactions); this challenging task is beyond the scope of our thesis.

Table 6.8 B3LYP/6-31G(d,p) (B3LYP/3-21G(d,p) for iodine) estimates of intramolecular frequencies (ω) and polaron binding energy (relaxation energy) related to hole transport in DIB.

Neutral		Cation	
$\omega\ (cm^{-1})$	$E_{pol}\ (meV)$	$\omega\ (cm^{-1})$	$E_{pol}\ (meV)$
159	33.2	165	35.6
700	0.3	710	0.1
1074	23.9	1054	31.6
1217	8.4	1231	4.3
1614	21.8	1605	15.8
3226	0.1	3238	0.0
total	87.6	total	87.5

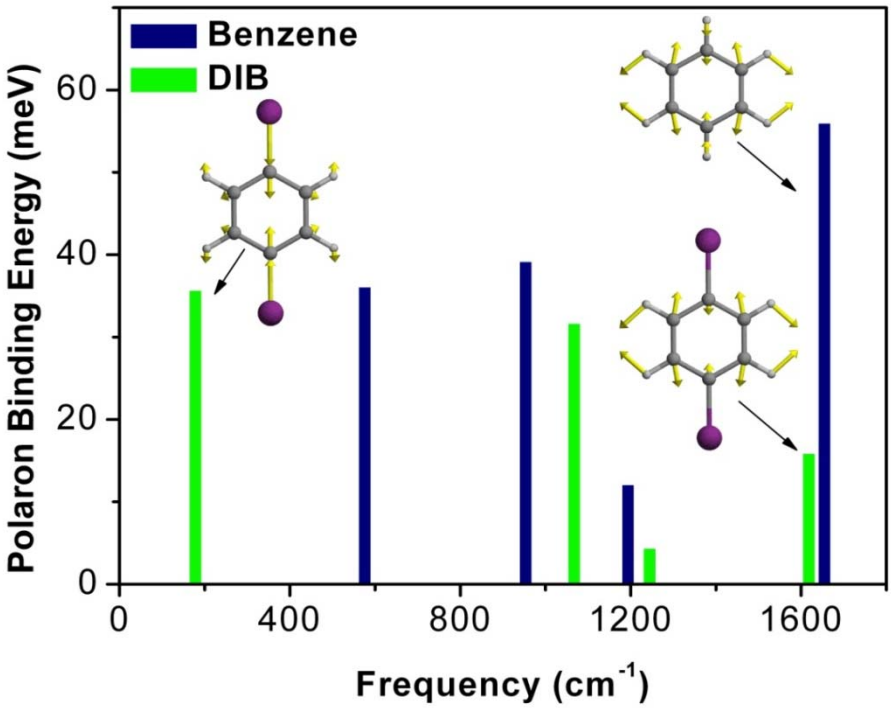

Figure 6.12 Contributions of the vibrational modes to the polaron binding energy (relaxation energy) in DIB and benzene.

As discussed before, there is growing consensus in the literature[33, 39-41] that both local and nonlocal couplings should be taken into account in order to obtain a coherent description of charge transport in organic molecular crystals. In the case of DIB, the preliminary results suggest that nonlocal interactions are weak. This is consistent with the fact that, since the iodine atoms are heavy, the amplitudes of DIB molecular motions are in general very small and the modulation of the transfer integrals due to intermolecular vibrations can be expected to be small as well. The only modes characterized by large displacements correspond to librations around the I−I axis. Since the electronic coupling in DIB is dominated by iodine-iodine interactions, these modes are also expected to have only a small impact on the transfer integrals.[12] An example of the dependence of the transfer integral on the coordinate of the libration mode at 110 cm^{-1} is shown in Figure 6.13. For a geometric distortion of the dimer along this mode corresponding to the mean-squared displacement ($Q = \pm 2$) at room temperature, the transfer integral varies just by 10%, which supports the above arguments. Thus, nonlocal vibrational coupling appears not to be strong enough to lead to radical changes in the nature of hole transport in DIB, even if this term is expected to affect the relaxation time and consequently the temperature dependence of the mobility.

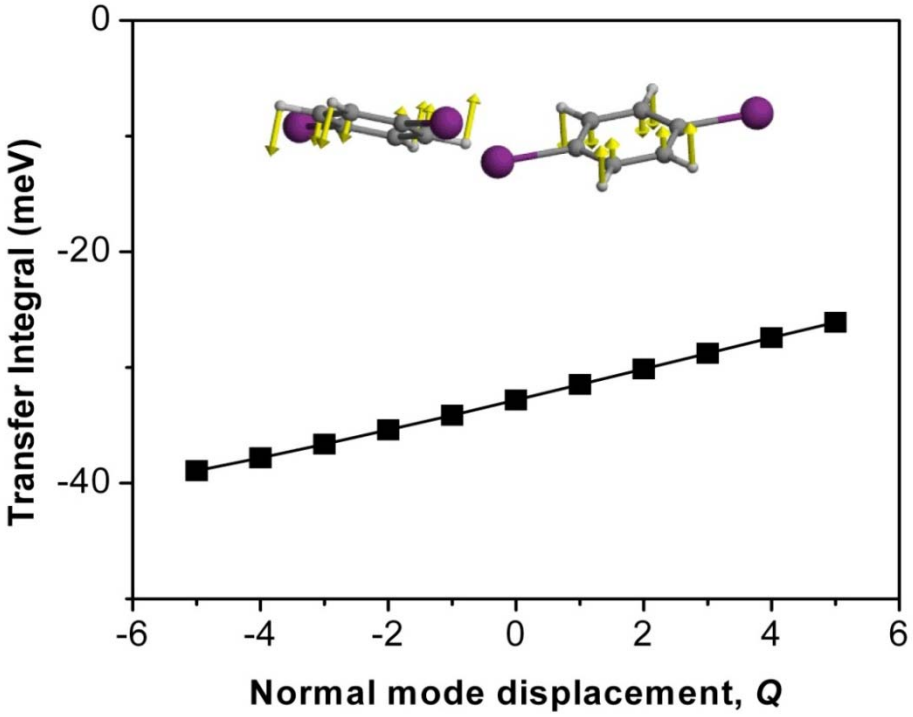

Figure 6.13 Evolution of the HOMO transfer integral for a DIB dimer composed of molecules 1 and 8, as a function of the dimensionless normal coordinate of the ω = 110 cm^{-1} libration mode (here, the mean-square displacement at room temperature approximately corresponds to $Q = \pm 2$ since thermal energy at room temperature is ~200 cm^{-1}).

While the iodine substitution of benzene results in a significant reduction in hole polaron binding energy, the situation is markedly different for electrons. It is well established that the electrochemical reduction of aromatic halides can cause the cleavage of the carbon-halogen bonds in the generated radical-anions.[42, 43] Electronic-structure calculations on mono-iodobenzene have shown that the lowest potential surface exhibits a minimum along the C−I dissociation coordinate characterized by a very elongated C−I bond and with the negative charge localized on the halogen atom.[44] Similar results for the radical-anion of DIB (see Figure 6.14) were obtained. As seen from Figure 6.14, in contrast to the oxidized (radical-cation) state where the symmetric geometry of the

neutral state is preserved, the reduction of DIB results in extreme elongation (by about 0.8 Å) of one of the C−I bonds (a broken-symmetry effect). Such a large geometry deformation results in a very large polaron binding energy for electrons, 1.3 eV *versus* 0.088 eV for holes (in comparison, the polaron binding energy for electrons in benzene is about 0.2 eV).

The calculated electron-polaron binding energy in DIB is much larger than the bandwidth of the lowest conduction sub-band. This result strongly suggests that in this case electron-phonon coupling leads to the formation of localized molecular polarons. In such an instance, charge transport can be described as a sequence of uncorrelated hops. The corresponding activation energy is very large (half the polaron binding energy,[45, 46] *i.e.*, about 0.6 eV); according to the hopping model, the electron mobility in DIB should be vanishingly small even at room temperature. It would also be of interest to find out whether, upon electron injection, molecular fragmentation of DIB takes place in the solid state as well; such a fragmentation would obviously lead to the formation of chemical defects.

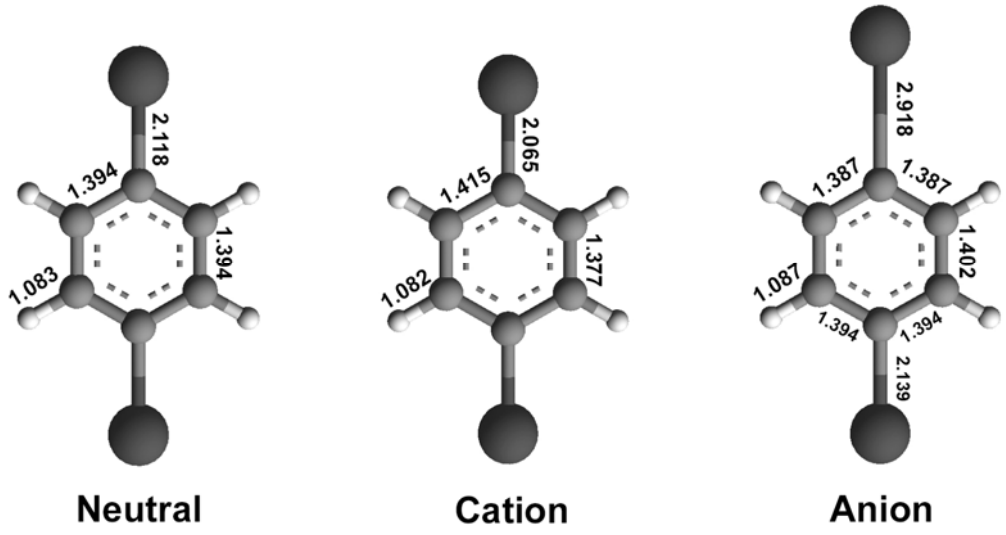

Figure 6.14 DFT geometries (bond lengths are given in Å) for the neutral, radical-cation, and radical-anion states of DIB.

6.3.4.2 DTT and DTT-2I

Tables 6.9 and 6.10 collect the DFT estimates for the hole-vibration coupling in DTT and DTT-2I, respectively. The intramolecular polaron binding energy calculated for DTT-2I is about 134 meV, which is nearly 20% smaller than that in DTT (174 meV). The decrease of E_{pol} in DTT-2I *versus* DTT comes mainly from a drop in hole-vibration interaction for the low-frequency mode at around 480 cm^{-1}; the coupling with all other modes is also somewhat reduced. The decrease in hole-vibration interaction with the 481 cm^{-1} mode can be understood in terms of the orbital vibronic coupling constants, as discussed for the case of DIB in the previous section. A close inspection of the 481 cm^{-1} normal mode in DTT reveals pronounced geometry distortions along the short molecular axis, which distorts the electron-density pattern of the HOMO. This low-frequency mode stretches the molecule via C−S−C bending in the inner rings. Also, in DTT-2I, a normal-mode that stretches the short molecular axis is found at 474 cm^{-1} (see Figure 6.15);

however, in this case, the iodine atoms remain motionless. Since part of the electron density of the HOMO wavefunction of DTT-2I is located on the iodine atoms, the energy of this molecular level is less affected by this vibration, leading to a smaller hole-vibration coupling constant in the DTT-2I molecule as compared to the DTT molecule.

Table 6.9 B3LYP/6-31G(d,p) estimates of intramolecular frequencies (ω) and polaron binding energy (relaxation energy) related to hole transport in DTT.

Neutral		Cation	
$\omega\ (cm^{-1})$	$E_{pol}\ (meV)$	$\omega\ (cm^{-1})$	$E_{pol}\ (meV)$
195	2.1	201	2.2
439	16.2	445	13.6
485	44.2	481	47.1
656	2.5	667	3.3
793	13.1	773	9.7
906	5.6	899	7.1
1115	1.3	1107	1.7
1201	2.3	1199	11.6
1343	29.8	1318	29.0
1402	0.0	1431	2.6
1487	45.8	1480	3.8
1531	15.8	1555	42.3
3232	0.1	3246	0.1
3268	0.1	3259	0.1
total	178.7	total	174.2

Table 6.10 B3LYP/6-31G(d,p) (B3LYP/3-21G(d,p) for iodine) estimates of intramolecular frequencies (ω) and polaron binding energy (relaxation energy) related to hole transport in DTT-2I.

Neutral		Cation	
$\omega\ (cm^{-1})$	$E_{pol}\ (meV)$	$\omega\ (cm^{-1})$	$E_{pol}\ (meV)$
151	32.0	153	32.6
477	9.5	474	10.7
537	9.6	542	7.9
659	1.2	664	1.2
832	0.0	816	0.1
962	0.0	968	0.1
1317	28.8	1173	0.3
1388	3.2	1271	40.3
1479	35.5	1418	0.3
1517	17.6	1470	7.8
3248	0.0	1526	32.1
total	137.4	total	133.5

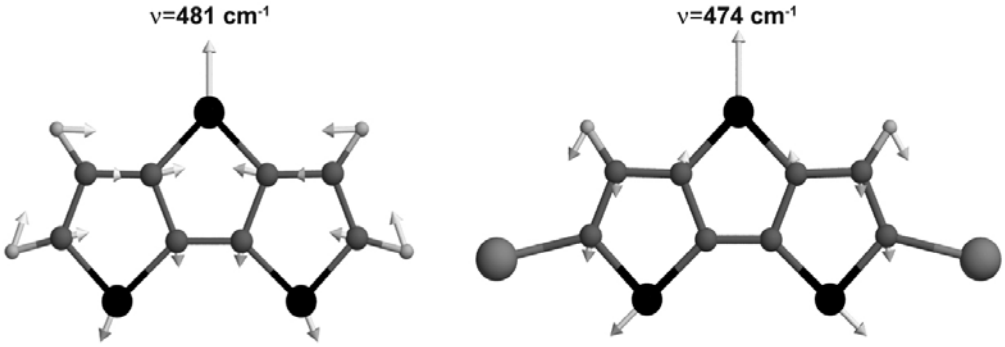

Figure 6.15 Low-frequency normal modes involving sulfur atoms in cationic DTT and DTT-2I, respectively.

As shown in Tables 6.9 and 6.10, the peripheral halogen substitution of DTT reduces the hole polaron binding energy by 40 meV. However, this situation is markedly different for the case of electrons, where a notably large polaron binding energy is found. As in the case of DIB (see previous section). Recent theoretical calculations demonstrate that peripheral halogen substitution of DTT significantly elevates the polaron binding energy for electrons.[47] Here, DFT calculations show an elongation (by about 0.7 Å) for

one of the C−I bonds (a broken-symmetry effect) upon reduction of the DTT-2I molecule (see Figure 6.16). Such large geometry deformation results in a very large polaron binding energy for electrons, 1.7 eV vs. 0.134 eV for holes, which will prevent any significant charge-transport activity for electrons.

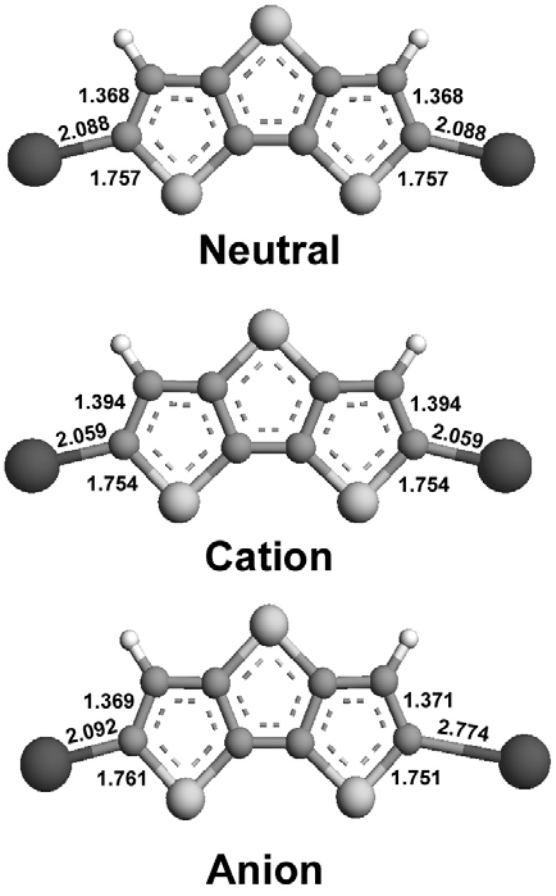

Figure 6.16 DFT geometries (bond lengths are given in Å) for the neutral, radical-cation, and radical-anion states of DTT-2I.

6.4 Conclusions

The electronic and electron/hole-vibration interactions in the crystals of 1,4-diiodobenzene, dithieno[3,2-*b*:2',3'-*d*]thiophene, and 2,6-diiodo-dithieno[3,2-*b*:2',3'-*d*]thiophene were investigated. In the 1,4-diiodobenzene crystal, transfer-integral and band-structure calculations confirm that the electronic coupling for both holes and electrons is dominated by iodine-iodine interactions. It was found that both types of charge carriers are characterized by a very small effective mass of about 0.5 m_0 (along the a-axis). On the other hand, the calculations of the band structure and transfer integrals for hole transport in the dithieno[3,2-*b*:2',3'-*d*]thiophene and 2,6-diiodo-dithieno[3,2-*b*:2',3'-*d*]thiophene crystals show that the π-π interactions determine the dominant transport direction.

Interestingly our results indicate that the iodine substitution of both benzene and dithieno[3,2-*b*:2',3'-*d*]thiophene leads to a significant decrease in the local hole-vibration coupling. Estimates of the electron-phonon coupling in DIB suggest that the transfer integrals for holes are only moderately affected by intermolecular vibrations. This finding and the estimated values for bandwidth along with the results from effective mass calculations and temperature-dependent measurements all concur to suggest a band-like transport regime for holes in DIB. However, low-temperature mobility measurements and additional theoretical investigations would be useful to reach a more complete description of hole transport in DIB. In the DTT-2I crystal, the situation appears to be different since the intermolecular interactions (*i.e.*, I-I or π-π interactions) that determine the main

transport direction are sensitive to phonon-assisted mechanisms, as indicated by the preliminary investigation of vibrations such as the one described in section 6.3.3.2. However, in order to confirm this conclusion, further theoretical calculations to investigate the role of the lattice vibrations and experimental measurements of the mobilities in the DTT-2I crystal are required.

For the case of electron transport, DFT calculations for both the DIB and DTT-2I molecules point to a very large polaron binding energy, suggesting that electrons would be completely localized even at room temperature. The large relaxation energy (local electron-vibration coupling) calculated for the radical-anion of DIB and DTT-2I is consistent with the previous findings that upon reduction iodobenzenes[43] are prone to cleavage of the carbon-iodine bonds. Recent theoretical calculations on halogen-substituted oligothienoacenes have shown a similar trend.[47]

To summarize, quantum-chemical calculations on DIB indicate that iodine substitution could yield new organic semiconductors with large hole mobilities; however, these materials are likely to be less suitable as electron transport materials. The theoretical work done on DTT-2I opens the route for new synthetic efforts to systematically control halogen interactions, which could lead to a new generation of organic semiconductors.

6.5 References

(1) Anthony, J. E. *Chemical Reviews* **2006**, *106*, 5028.

(2) Anthony, J. E. *Angewandte Chemie, International Edition* **2008**, *47*, 452.

(3) Bendikov, M.; Wudl, F.; Perepichka, D. F. *Chemical Reviews* **2004**, *104*, 4891.

(4) Coropceanu, V.; Kwon, O.; Wex, B.; Kaafarani, B. R.; Gruhn, N. E.; Durivage, J. C.; Neckers, D. C.; Brédas, J. L. *Chemistry-a European Journal* **2006**, *12*, 2073.

(5) Kwon, O.; Coropceanu, V.; Gruhn, N. E.; Durivage, J. C.; Laquindanum, J. G.; Katz, H. E.; Cornil, J.; Brédas, J. L. *Journal of Chemical Physics* **2004**, *120*, 8186.

(6) Sakamoto, Y.; Suzuki, T.; Kobayashi, M.; Gao, Y.; Fukai, Y.; Inoue, Y.; Sato, F.; Tokito, S. *Journal of the American Chemical Society* **2004**, *126*, 8138.

(7) Sakamoto, Y.; Suzuki, T.; Kobayashi, M.; Gao, Y.; Inoue, Y.; Tokito, S. *Molecular Crystals and Liquid Crystals* **2006**, *444*, 225.

(8) Perepichka, D. F.; Bendikov, M.; Meng, H.; Wudl, F. *Journal of the American Chemical Society* **2003**, *125*, 10190.

(9) Moon, H.; Zeis, R.; Borkent, E. J.; Besnard, C.; Lovinger, A. J.; Siegrist, T.; Kloc, C.; Bao, Z. N. *Journal of the American Chemical Society* **2004**, *126*, 15322.

(10) Schwartz, L. M.; Ingersoll Jr., H. G.; Hornig, J. F. *Molecular Crystals* **1967**, *2*, 379.

(11) Ellman, B. *Journal of Chemical Physics* **2006**, *125*, 074702.

(12) Ellman, B.; Nene, S.; Semyonov, A. N.; Twieg, R. J. *Advanced Materials* **2006**, *18*, 2284.

(13) Li, X. C.; Sirringhaus, H.; Garnier, F.; Holmes, A. B.; Moratti, S. C.; Feeder, N.; Clegg, W.; Teat, S. J.; Friend, R. H. *Journal of the American Chemical Society* **1998**, *120*, 2206.

(14) Frisch, M. J. T., G. W.; Schlegel, H. B.; Scuseria, G. E.; Robb, M. A.; Cheeseman, J. R.; Montgomery, Jr., J. A.; Vreven, T.; Kudin, K. N.; Burant, J. C.; Millam, J. M.; Iyengar, S. S.; Tomasi, J.; Barone, V.; Mennucci, B.; Cossi, M.; Scalmani, G.; Rega, N.; Petersson, G. A.; Nakatsuji, H.; Hada, M.; Ehara, M.; Toyota, K.; Fukuda, R.; Hasegawa, J.; Ishida, M.; Nakajima, T.; Honda, Y.; Kitao, O.; Nakai, H.; Klene, M.; Li, X.; Knox, J. E.; Hratchian, H. P.; Cross, J. B.; Bakken, V.; Adamo, C.; Jaramillo, J.; Gomperts, R.; Stratmann, R. E.; Yazyev, O.; Austin, A. J.; Cammi, R.; Pomelli, C.; Ochterski, J. W.; Ayala, P. Y.; Morokuma, K.; Voth, G. A.; Salvador, P.; Dannenberg, J. J.; Zakrzewski, V. G.; Dapprich, S.; Daniels, A. D.; Strain, M. C.; Farkas, O.; Malick, D. K.; Rabuck, A. D.; Raghavachari, K.; Foresman, J. B.; Ortiz, J. V.; Cui, Q.; Baboul, A. G.; Clifford, S.; Cioslowski, J.; Stefanov, B. B.; Liu, G.; Liashenko, A.; Piskorz, P.; Komaromi, I.; Martin, R. L.; Fox, D. J.; Keith, T.; Al-Laham, M. A.; Peng, C. Y.; Nanayakkara, A.; Challacombe, M.; Gill, P. M. W.; Johnson, B.; Chen, W.; Wong, M. W.; Gonzalez, C.; and Pople, J. A. Gaussian 03, Revision C.02; Gaussian, Inc., Wallingford CT, 2004.

(15) Glukhovtsev, M. N.; Pross, A.; Mcgrath, M. P.; Radom, L. *Journal of Chemical Physics* **1995**, *103*, 1878.

(16) Reimers, J. R. *Journal of Chemical Physics* **2001**, *115*, 9103.

(17) Dovesi, R.; Saunders, V. R.; Roetti, C.; Orlando, R.; Zicovich-Wilson, C. M.; Pascale, F.; Civalleri, B.; Doll, K.; Harrison, N. M.; Bush, I. J.; D'arco, P.; Llunell, M. CRYSTAL06; University of Torino, Torino, 2006.

(18) *CPMD, 3.9.2, IBM Corp (Copyright 1990-2004) and Max-Planck Institut für Festkörperforschung Stuttgart (Copyright 1997-2001): 2005*.

(19) Perdew, J. P.; Burke, K.; Ernzerhof, M. *Physical Review Letters* **1996**, *77*, 3865.

(20) Kresse, G.; Furthmuller, J. *Computational Materials Science* **1996**, *6*, 15.

(21) Kresse, G.; Hafner, J. *Phys. Rev. B* **1993**, *47*, 558.

(22) Kresse, G.; Hafner, J. *Phys. Rev. B* **1994**, *49*, 14251.

(23) Blochl, P. E. *Physical Review B* **1994**, *50*, 17953.

(24) Kresse, G.; Joubert, D. *Physical Review B* **1999**, *59*, 1758.

(25) Senthilkumar, K.; Grozema, F. C.; Bickelhaupt, F. M.; Siebbeles, L. D. A. *Journal of Chemical Physics* **2003**, *119*, 9809.

(26) Valeev, E. F.; Coropceanu, V.; da Silva Filho, D. A.; Salman, S.; Brédas, J. L. *Journal of the American Chemical Society* **2006**, *128*, 9882.

(27) *ADF, 2005.01*, Scientific Computing and Modeling NV: Amsterdam.

(28) Alcobe, X.; Estop, E.; Aliev, A. E.; Harris, K. D. M.; Rodriguez-Carvajal, J.; Rius, J. *Journal of Solid State Chemistry* **1994**, *110*, 20.

(29) Bertinelli, F.; Palmieri, P.; Stremmenos, C.; Pelizzi, G.; Tallani, C. *Journal of Physical Chemistry* **1983**, *87*, 2317.

(30) Kinnibrugh, T. L.; Odom, S. A.; Barlow, S.; Timofeeva, T.; Marder, S. R. *Unpublished work*.

(31) Zhang, X. N.; Cote, A. P.; Matzger, A. J. *Journal of the American Chemical Society* **2005**, *127*, 10502.

(32) Li, Z. Q.; Podzorov, V.; Sai, N.; Martin, M. C.; Gershenson, M. E.; Di Ventra, M.; Basov, D. N. *Physical Review Letters* **2007**, *99*, 016403.

(33) Coropceanu, V.; Cornil, J.; da Silva Filho, D. A.; Olivier, Y.; Silbey, R.; Brédas, J. L. *Chemical Reviews* **2007**, *107*, 926.

(34) Kim, E. G.; Coropceanu, V.; Gruhn, N. E.; Sánchez-Carrera, R. S.; Snoeberger, R.; Matzger, A. J.; Brédas, J. L. *Journal of the American Chemical Society* **2007**, *129*, 13072.

(35) Kitamura, M.; Arakawa, Y. *Journal of Physics-Condensed Matter* **2008**, *20*, 184011.

(36) Kato, T.; Yamabe, T. *Journal of Chemical Physics* **2001**, *115*, 8592.

(37) Bersuker, I. B. *The Jahn-Teller effect*; Cambridge University Press: Cambridge, UK ; New York, 2006.

(38) Kato, T.; Yamabe, T. *Journal of Chemical Physics* **2005**, *123*, 024301.

(39) Della Valle, R. G.; Brillante, A.; Farina, L.; Venuti, E.; Masino, M.; Girlando, A. *Molecular Crystals and Liquid Crystals* **2004**, *416*, 145.

(40) Hannewald, K.; Bobbert, P. A. *Applied Physics Letters* **2004**, *85*, 1535.

(41) Hannewald, K.; Stojanovic, V. M.; Schellekens, J. M. T.; Bobbert, P. A.; Kresse, G.; Hafner, J. *Physical Review B* **2004**, *69*, 075211.

(42) Andrieux, C. P.; Blocman, C.; Dumasbouchiat, J. M.; Saveant, J. M. *Journal of the American Chemical Society* **1979**, *101*, 3431.

(43) Sanecki, P. *Computers & Chemistry* **2001**, *25*, 521.

(44) Pierini, A. B.; Vera, D. M. A. *Journal of Organic Chemistry* **2003**, *68*, 9191.

(45) Holstein, T. *Annals of Physics* **1959**, *8*, 325.

(46) Holstein, T. *Annals of Physics* **1959**, *8*, 343.

(47) Zhang, Y. X.; Cai, X.; Bian, Y. Z.; Li, X. Y.; Jiang, J. Z. *Journal of Physical Chemistry C* **2008**, *112*, 5148.

CHAPTER 7

SUMMARY AND PERSPECTIVES

7.1 Synopsis

In this thesis, a theoretical investigation of the major microscopic parameters involved in the description of charge-transport processes in organic semiconductors has been presented. The results of our calculations reveal that the theoretical description of the electronic and transport properties of organic materials requires the inclusion of both electron-electron and electron-phonon interactions. This generalized picture is more complex than in conventional inorganic materials, in which the transport properties are well described via one-electron (band-like model) approaches.

The results presented in Chapters 3 and 4 indicate that the local and nonlocal electron-phonon couplings are system- and size-dependent parameters that need to be incorporated in theoretical models whose goal is to predict the transport properties in organic semiconductors. More specifically, in Chapter 3, the structural relaxations in the ground and excited states of oligoacene molecules showed that: (i) the intramolecular vibronic coupling (local coupling) evolves with system size; and (ii) while the hole coupling constant in the ground cation states is dominated by high-frequency vibrations, the coupling constants of the excited states tend to redistribute towards low-frequency vibrations. In Chapter 4, a combined DFT and MM investigation of the nonlocal electron-

phonon interactions in the oligoacene crystals revealed that the electronic couplings for both holes and electrons are significantly affected by intermolecular- and intramolecular lattice vibrations, with the major contribution coming from intermolecular vibrations. The coupling of the charge carriers with lattice vibrations was estimated by means of the intermolecular relaxation energy, L. In the oligoacene crystals, L decreases with system size and is larger in the case of electrons with respect to holes. To study the role of the nonlocal coupling mechanism on the charge transport, the variance of the electronic couplings due to thermal fluctuations was systematically investigated. The results underline that thermal vibrations (even the zero-point vibrations at 0 K) significantly modulate the hole- and electron-phonon coupling constants; the contribution of low-temperature vibrations to the respective charge-carrier coupling constants is larger in the molecular crystal of naphthalene than in pentacene.

In Chapters 5 and 6, the focus of our studies shifted towards systematic investigations of the microscopic charge-transport parameters in a series of organic molecular crystals functionalized with sulfur and/or iodine atoms. In Chapter 5, the key molecular parameters that govern charge transport in the pentathienoacene crystal (the thiophene equivalent of pentacene) were investigated. It was found that the main charge-transport properties can be associated to the nature of the intermolecular interactions present in this molecular crystal, *i.e.*, the π-stacking and S···S interactions for holes and electrons, respectively. Estimated hole mobilities in the band and hopping regimes for the pentathienoacene crystal are comparable to those obtained for the pentacene and sexithienyl crystals.

In Chapter 6, on the basis of electronic-structure calculations, it was demonstrated that the high hole mobility in the 1,4-diiodobenzene (DIB) crystal is associated with the iodine atoms. Similar theoretical calculations were performed on the 2,6-diiodo-dithieno[3,2-*b*:3',2'-*d*]thiophene (DTT-2I) crystal, a new addition to the family of thiophene organic semiconductors. In contrast to the DIB case, the intermolecular π-π interactions in DTT-2I have precedence over the I-I interactions; our results suggest negligible hole transport along the direction where the I-I interactions are dominant. However, it remains to be seen whether lattice vibrations could provide a path for hole transport along the long molecular axis, where the iodine atoms are located. In the case of electron transport, our calculations for both the DIB and DTT-2I molecules point to a very large polaron binding energy and, as a result, insignificant charge mobility for electrons.

7.2 Future considerations

In the past, the nature of the local electron-vibration coupling and its impact on charge-transport processes in organic materials (at a molecular level) has been extensively characterized. This is in part related to the reliability of current quantum-chemical methods to accurately describe the vibrational spectra of organic molecules of medium to relatively large size. However, the description of the vibrational modes in organic molecular crystals, a key element in the analysis of the role of the nonlocal coupling in charge-transport processes, is a much more complicated proposition. This is mainly due to the fact that first-principles methods fail to adequately describe weak

intermolecular interactions. In the near future, it can be expected that the inclusion of non-covalent interactions into DFT methodologies (for example, DTF-D methods) will stimulate the accurate prediction of the vibrational modes over a much larger range of systems than those investigated in this thesis. Therefore, a rapid and a reliable description of the vibrational properties in a series of organic molecular crystals represents the first step towards the calculation of the vibrational couplings and subsequently towards a better understanding of the role of nonlocal electron-phonon interactions and their impact on charge transport. Once this first step is completed and on the basis of our theoretical calculations, it will be important to develop new polaron models that explicitly take into account the impact of lattice vibrations on the description of charge-carrier dynamics in organic materials. A more comprehensive approach will come with the development of models that allow the inclusion of the vibrational couplings with all the modes, optical and acoustical, and at different k-points in the reciprocal space.

On a separate basis, high-level *ab initio* calculations of the electronic couplings (*i.e.*, transfer integrals) can be used to benchmark results obtained from semi-empirical methods on a variety of crystals. If significant agreement is found, the calculation of the nonlocal electron-phonon coupling constants can be substantially accelerated. In the same context, the quality of the correspondence between DFT and MDS methods to estimate the intermolecular relaxation energy, L, remains to be assessed. It will be helpful to evaluate the transfer integrals at a high-level of theory for those molecular configurations obtained from MDS. While we are aware that this represents a computationally demanding task, we believe that it can be carried out at least for the naphthalene crystal

and on those dimers that show significant coupling with lattice vibrations (*e.g.*, interactions along the ab plane in the naphthalene crystal).

Finally, it is expected that future theoretical characterizations (at the molecular level) of the microscopic charge-transport parameters in organic semiconductors will fully include the nonlocal coupling constants in their derivation. It is worth noting that the magnitude of the nonlocal electron-phonon coupling in naphthalene is comparable ot that of the electronic coupling, which illustrates its importance in further theoretical studies which aim at predicting new materials with high carrier mobility. In principle, the methodology used to estimate the nonlocal coupling in oligoacenes can be extended to members of the oligothienoacene family (*i.e.*, the pentathienoacene crystal) or, as an extension to Chapter 6, the effect of the lattice vibrations can be also investigated in the 2,6-diiodo-dithieno[3,2-*b*:3',2'-*d*]thiophene crystal. The theoretical work on the 1,4-diiodobenzene crystal, which attributes the high mobility in this crystal to the heavy iodine atoms, opens the route for new synthetic efforts to systematically control the intermolecular halogen interactions, in addition to the well-known π-π interactions. This could potentially lead to a new generation of organic semiconductors.

LIST OF PUBLICATIONS

1) V. Coropceanu, D. A. da Silva Filho, O. Kwon, R. S. Sánchez-Carrera, J. L. Brédas. "Impacts of Hole-and Electron-Vibrational Couplings on Charge Transport in Organic Semiconductors". *Proc. Int. Symp. Super-Functionality Organic Devices*. *6*: 15-18, **2005**.

2) R. S. Sánchez-Carrera, V. Coropceanu, D. A. da Silva Filho, R. Friedlein, W. Osikowicz, R. Murdey, C. Suess, W. R. Salaneck, and J. L. Brédas. "Vibronic Coupling in the Ground and Excited States of Oligoacene Cations". *J. Phys. Chem. B 110 (38)*: 18904-18911, **2006**.

3) E. G. Kim, V. Coropceanu, N. E. Gruhn, R. S. Sánchez-Carrera, R. Snoeberger, A. J. Matzger, and J. L. Brédas. "Charge Transport in the Pentathienoacene Crystal". *J. Am. Chem. Soc. 129 (43)*: 13072-13081, **2007**.

4) R. S. Sánchez-Carrera, V. Coropceanu, E. G. Kim, and J. L. Brédas. "Charge Transport Properties of the 1,4-Diiodobenzene Crystal: A Quantum-Mechanical Study". *Chem. Mat.* Accepted.

5) N. Martinelli, Y. Olivier, M. C. Ruiz-Delgado, K. Pigg, D. A. da Silva Filho, R. S. Sánchez-Carrera, E. Venuti, R. G. Della Valle, J. L. Brédas, D. Beljonne, and J. Cornil. "Influence of Intermolecular Vibrations on the Electronic Coupling and Charge-Transport Properties of Organic Semiconductors: A Molecular Dynamics and Quantum-Chemical Study of the Anthracene and Perfluoropentacene Molecular Crystals". *To be submitted*.

6) V. Coropceanu, R. S. Sánchez-Carrera, G. Day, P. Paramonov, and J. L. Brédas. "The Interaction of Charge Carriers with Optical Phonons in Organic Molecular Semiconductors: the Study Case of Naphthalene". *To be submitted*.

7) M. C. Ruiz-Delgado, D. A. da Silva Filho, V. Coropceanu, K. Pigg, R. S. Sánchez-Carrera, N. E. Gruhn, Y. Sakamoto, R. Malavé Osuna, J. Casado, V. Hernández, J. T. López Navarrete, T. Suzuki, and J. L. Brédas. "Impact of Perfluorination on the Charge Transport Parameters of Oligoacene Crystals". *To be submitted.*

8) R. S. Sánchez-Carrera, V. Coropceanu, P. Paramonov, and J. L. Brédas. “The Interaction of Charge Carriers with Optical Phonons in the Oligoacene Crystals”. *Manuscript in preparation*.

9) R. S. Sánchez-Carrera, S. A. Odom, T. L. Kinnibrugh, E. G. Kim, V. Coropceanu, S. Barlow, T. Timofeeva, S. Marder, and J. L. Brédas. “Charge Transport Parameters in Iodo-Functionalized Organic Molecular Crystals: the Case of 2,6-diiodo-dithieno[3,2-*b*:2’,3’-*d*]thiophene”. *Manuscript in preparation*.

10) I. Rudra, R. S. Sánchez-Carrera, V. Coropceanu, and J. L. Brédas. “Polarization Energy in Naphthalene: A DFT-based Approach”: *Manuscript in preparation*.